PhD Thesis

Jakob Ejler Sørensen

Mass-Selected Model System Characterization in Catalysis

Rastered deposition, LEIS and TPD

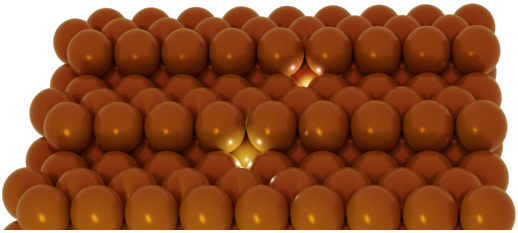

Supervisor: Professor Ib Chorkendorff
Co-supervisor: Associate Professor Jakob Kibsgaard

Technical University of Denmark
Department of Physics, SurfCat
December, 2020

Abstract

The study of catalysts is motivated by giving a short overview of the huge and growing energy demand which, at present, is based mostly on a polluting and limited resource. A transition to sustainable energy is therefore needed and catalysis plays an important role in balancing out the intermittent nature of the truly renewable energy sources.

This thesis deals with model systems of catalysts in order to elucidate the mechanisms responsible for their activity. Two submethods have been implemented to improve the method of preparing model system catalysts, and two catalytic systems for splitting water have been investigated with isotope studies.

Rastered depositions: It is shown how the distribution of nanoparticles can vary quite a lot across the surface after a deposition. To fix this, stepper motors now control movement of the sample during depositions so it can be rastered. This smooths out any variations in the beam of nanoparticles, but introduces an uncertainty in the calculation of loading. Simulations are used to show how this uncertainty can be understood and minimized.

Isotope studies: Electrocatalytic water splitting is a sustainable way of storing energy as chemical bonds, but the reaction is expensive. Nickel-iron based catalysts are commonly used in alkaline electrolyzers because of the stability and activity, but the nature of the active site is still under

debate. Through isotope studies, we show that lattice oxygen is not exchange during oxygen evolution from which we conclude that the active sites are only located on the surface of the nanoparticles. Thereby, our well-defined 5.4 nm Ni_3Fe nanoparticles have a turnover frequency of $6.2 \pm 1.6\,s^{-1}$ at 300 mV overpotential, which is the highest reported in the literature. For polymer electrolyte membrane electrolysis, thin film electrodes of RuO_2 are compared to IrO_2 in an ongoing investigation to provide mechanistic insights for oxygen evolution. We find evidence of oxygen evolution down to 60 mV overpotential on a RuO_2 foam, which is experimentally unprecedented. Comparing to thin films show that there is nothing special about the intrinsic activity, but the record owes to the high surface area of the catalyst and the sensitivity of the measurement setup. Initial results from isotope studies indicate that lattice oxygen exchange is much lower than dissolution processes on RuO_2 and that the exchanged oxygen remains close to the surface. On hydrous IrO_2, however, the lattice oxygen exchange is larger than in the RuO_2 system. The dissolution processes are on the same scale as the oxygen exchange. These results are only based on a small subset of the data, though.

Liquid nitrogen-cooled TPD: LN_2-cooled temperature-programmed desorption has been implemented so CO-TPD can be performed on copper nanoparticles. This is to have a characterization method which probes the reactivity of the prepared model systems for a more complete characterization. The technique is illustrated by three examples: 1) A copper foil provides a reference that is comparable with the literature. 2) Overlapping 5 nm mass-selected copper nanoparticles show a new peak, which may be due to unique sites from overlapping nanoparticles, or simply an up-concentration of natural under-coordinated sites. 3) Intermetallic charge transfer is shown to weaken the reactivity of palladium atoms in palladium-tin bimetallic alloys. Slightly more than 50 % tin content leaves the palladium sites with binding energies similar to copper.

Resumé

Studiet af katalysatorer bliver motiveret ved at give et kort overblik over det kæmpe og stadig voksende energibehov, som for tiden mest er baseret på en forurenende og begrænset ressource. Der er derfor brug for en overgang til vedvarende energi, og katalyse spiller en vigtig rolle i at afbalancere de vedvarende energikilders sporadiske karakter.

Denne afhandling tager sig af modelsystemer af katalysatorer for at opklare mekanismerne bag deres aktivitet. Der er implementeret to undermetoder som forbedrer metoden at danne modelsystemer af katalysatorer, og to katalytiske systemer til at splitte vand er blevet undersøgt med isotopstudier.

Rasteret deponeringer: Det er vist hvordan fordelingen af nanopartikler kan variere en hel del henover overfladen efter en deponering. For at fikse det, styrer to steppermotorer nu prøvens bevægelse under deponeringer, så den kan blive rasteret. Dette udligner enhver variation i nanopartikelstrålen, men introducerer en usikkerhed i udregning af katalysatormængden. Simuleringer bliver brugt til at vise hvordan denne usikkerhed kan forstås og minimeres.

Isotopstudier: Elektrokatalytisk splitning af vand er en bæredygtig måde at gemme energi i form af kemiske bindinger, men reaktionen er dyr. Katalysatorer baseret på nikkel og jern bliver almindeligt brugt i alkalinske elektrolysatorer på grund af deres stabilitet og aktivitet, men karakteren af det katalytiske

aktive sted er stadig under debat. Vi viser gennem isotopstudier, at ilt fra krystalgitteret ikke udveksles under iltudvikling. Fra dette konkluderer vi, at det katalytisk aktive sted kun befinder sig på overfladen af nanopartiklerne. Derved har vores veldefinerede 5,4 nm Ni_3Fe nanopartikler en omdannelsesfrekvens på $6.2 \pm 1.6\,s^{-1}$ ved 300 mV overpotentiale, hvilket er det højeste rapporteret i litteraturen. For polymer-elektrolyt-membran-elektrolyse er tyndfilm af RuO_2 sammenlignet med IrO_2 i en igangværende undersøgelse af at fremdrive indblik i mekanismerne bag iltudvikling. Vi ser bevis på iltudvikling på RuO_2-skum ned til 60 mV overpotentiale, som eksperimentelt er uden fortilfælde. Sammenlignes dette med tyndfilm, ses det, at der ikke er noget specielt ved den intrinsiske aktivitet, men at rekorden skyldes det høje overfladeareal og sensitiviteten af måleudstyret. Første resultater fra isotopstudier indikerer at krystalgitteriltombytning er meget lavere end opløsningsprocesser for RuO_2, og at det ombyttede ilt forbliver tæt ved overfladen. På hydreret IrO_2 er krystalgitteriltombytningen dog større end i RuO_2-systemet. Opløsningsprocesserne er på samme størrelse som iltombytning. Disse resultater er dog kun baseret på en lille delmængde af dataen.

TPD kølet med flydende kvælstof: Temperaturprogrammeret desorption kølet med flydende kvælstof er blevet implementeret så CO-TPD kan blive udført på kobbernanopartikler. Dette er for at have en karakteriseringsmetode, som prober reaktiviteten af de forberedte modelsystemer for at give en mere udførlig karakterisering. Denne teknik er illustreret med tre eksempler: 1) en kobberfolie giver os en reference, som kan sammenlignes med litteraturen. 2) Overlappende masse-selekterede 5 nm kobbernanopartikler udviser en ny top, som kan være på grund af unikke steder fra de overlappende nanopartikler eller simpelt en opkoncentration af naturlige underkoordinerede steder. 3) Intermettalisk ladningsoverførsel er vist at svække reaktiviteten af palladium-atomer i bimetalliske legeringer af palladium og tin. Lidt over 50 % tinindhold efterlader palladium-stederne med bindingsenergier tilsvarende kobber.

Preface

This thesis is written as one of the final requirements for obtaining a PhD degree in physics at the Technical University of Denmark (DTU). The work was carried out in the Department of Physics, Section of Surface Physics and Catalysis (SurfCat) from March 2017 to November 2020 under the supervision of Professor Ib Chorkendorff and Associate Professor Jakob Kibsgaard. The project was funded through grant 9455 from VILLUM FONDEN through the VILLUM Center for the Science of Sustainable Fuels and Chemicals (V-SUSTAIN).

First and foremost, I would like to thank my supervisors Ib Chorkendorff and Jakob Kibsgaard. I am truly grateful for having done my PhD at SurfCat under their good-natured, honest and expert guidance. They have inspired a great atmosphere that motivated me to work way too much and learn all kinds of interesting things.

Second, I would like to specially thank my lab-companion, Niklas Secher for the time we spent alone in the lab figuring out how to fix broken equipment. His sense of humour, calm behaviour, and valuable discussions has been a real asset over the years. I am not afraid to jinx it when I say that everything will just work from now on.

I would also like to mention Søren Scott whose enthusiasm for science is unparalleled. The discussions and uncountable late hours we have shared in

the pursuit will be remembered. The floor managers Kenneth Nielsen, Robert Jensen, Brian Knudsen, and Patrick Strøm-Hansen for sharing office space, interesting discussions (sometimes related to physics and solving problems), and in general for being very supportive and teaching me a lot. Birgit Bohn for always helping with a smile, and Bela Sebok and Anders Bodin for the all too brief introduction to UHV in the small overlap we had. Ezra Clark and Degenhart Hochfilzer for their valuable discussions on copper nanoparticles.

Special thanks to my initial neighbor-by-setup, Ann-Louise Christoffersen with whom I enjoyed many conversations over coffee breaks. A three-fold thanks to Andrea Crovetto, first for organizing the Christmas band where I actually learned to do a solo on the ukulele, second for karaoke, and third for making a project of me. Claudie Roy for patiently waiting on ISS. Erlend Bertheussen for keeping a well-organized friday bar. Suzanne Andersen for being a hard-working joy and organizing many a SurfCat event. And thanks to all the other colleagues at SurfCat over the past years. The people I mentioned are only a very small fraction of all the people who daily contribute to a busy and happy atmosphere, but I have to stop somewhere.

Lastly I would like to thank my friends and family who made it possible for me to get here. And finally a heart-felt thanks to my girlfriend Amanda Boye who wanted to spend her time with me. She taught me the merits of a proper work-life balance and was very understanding when I threw said work-life balance away again for the last 3-6 months of my PhD.

Jakob Ejler Sørensen

List of Papers

Paper I

https://doi.org/10.1021/acs.jpcc.7b11089

Ambient Pressure Hydrodesulfurization of Refractory Sulfur Compounds in Highly Sensitive μ-Reactor Platform Coupled to a Time-of-Flight Mass Spectrometer

Ann-Louise N. Christoffersen, Anders Bodin, Christian F. Elkjær, Jakob E. Sørensen, Jakob Kibsgaard, and Ib Chorkendorff

J. Phys. Chem. C 2018, 122, 1669-1705

Paper II

https://doi.org/10.1038/s41929-018-0162-x

Impact of nanoparticle size and lattice oxygen on water oxidation on $NiFeO_xH_y$

Claudie Roy, Bela Sebok, Søren B. Scott, Elisabetta M. Fiordaliso, Jakob E. Sørensen, Anders Bodin, Daniel B. Trimarco, Christian D. Damsgaard, Peter C.K. Vesborg, Ole Hansen, Ifan E.L. Stephens, Jakob Kibsgaard, and Ib Chorkendorff

Nat Catal **1**, 820-829 (2018)

Paper III

https://dx.doi.org/10.1021/acscatal.0c00779

Particle Size Effects on Platinum Dissolution: Considerations for Accelerated Stability Testing of Fuel Cell Catalysts

Daniel J.S. Sandbeck, Niklas M. Secher, Florian D. Speck, Jakob E. Sørensen, Jakob Kibsgaard, Ib Chorkendorff, and Serhiy Cherevko

ACS Catal. 2020, 10, 6281-6290

Paper IV

https://dx.doi.org/10.1149/1945-7111/abc767

The Dissolution Dilemma for low Pt Loading Polymer Electrolyte Membrane Fuel Cell Catalysts

Daniel J.S. Sandbeck, Niklas M. Secher, Masanori Inaba, Jonathan Quinson, Jakob E. Sørensen, Jakob Kibsgaard, Alessandro Zana, Francesco Bizzotto, Florian D. Speck, Michael T.Y. Paul, Alexandra Dworzak, Carsten Dosche, Mehtap Oezaslan, Ib Chorkendorff, Matthias Arenz, and Serhiy Cherevko

Journal of The Electrochemical Society, 2020, **167** 164501

Paper V

Kinetics of oxygen evolution in acid on RuO2 down to 60 mV overpotential

Reshma Rao, Søren B. Scott, Choongman Moon, Jakob E. Sørensen, Jakob Kibsgaard, Yang Shao-Horn, and Ib Chorkendorff

In preparation

Paper VI

Comparison of lattice oxygen evolution and metal dissolution in RuO2 and IrO2 films at low overpotential

Reshma Rao, Søren B. Scott, Choongman Moon, Jakob E. Sørensen, Jakob Kibsgaard, Yang Shao-Horn, and Ib Chorkendorff

In preparation

Paper VII

The importance of potential control during immersion of Cu catalysts on the picogram scale

Degenhart Hochfilzer*, Jakob E. Sørensen*, Jakob Kibsgaard, Ib Chorkendorff... (not the final author list)

In preparation

* these authors contributed equally

Paper VIII

Transient methane production on mass-selected Cu nanoparticles explained as an effect in buffered solutions

Degenhart Hochfilzer*, Jakob E. Sørensen*, Jakob Kibsgaard, Ib Chorkendorff... (not the final author list)

In preparation

* these authors contributed equally

Contents

Introduction

Chapter 1

My PhD studies were conducted in the SurfCat group at the Technical University of Denmark. In this group, we study catalysis for sustainable energy. This chapter is intended to give you, the reader, perspective on why we study this, and what it is. At the end of the chapter is an outline for the rest of the thesis.

1.1 World energy and catalysis

In 2005, Richard Smalley gave a talk in which he identified the biggest problem to focus on fixing: the energy problem.[1] Oil is an excellent energy carrier, and due to its use for more than a hundred years, it is very efficient. But not only does it pollute the atmosphere with excess amounts of CO_2 that is beginning to affect the climate on a global scale, it is also a limited resource which will run out in the nearer future if the current use of oil is continued. Considering these two aspects, the switch to a cheap and sustainable energy source should be done sooner rather than later.[1]

The problem is, that the energy industry is huge. On a global scale, almost 20 TW of energy is used on average, which is expected to increase to 30 TW by 2050.[2,3] This means that for any energy technology to be considered a

viable replacement for the burning of fossil fuels, the scale of production has to reach 1 TW - aptly called "the Terawatt Challenge" by Smalley.[1] The only truly viable source of energy on this scale is harvesting the energy coming from the sun whether directly using solar cells, or indirectly like using wind mills.

While this now is at a potential that can be scaled up, another problem remains to be fixed: storing electrical energy. Since wind and solar energy is intermittent in nature, for an economy to rely on it, we would need to produce more energy than we need when the sun shines and the wind blows, and then store it for use when it is dark and still outside. There are many different options for energy storage and I will here consider only two: batteries and chemical bonds. *Batteries* are well known in everyday household appliances for powering of small units like remote controls, flashlights and cell phones to name a few. The problem with batteries is the energy density - they simply get impractically big and heavy when considered for bigger scales. In recent years, the battery technology improved to the point where cars can be fully electrified thanks to the lighter lithium-ion batteries. While a large fleet of electric vehicles is being considered as a link in smoothing the intermittency of sustainable energy sources, simply the scale of materials needed for this fleet[4], makes it impossible for this to be the single solution to energy storage. *Chemical bonds* as energy storage is the what we mostly use now when burning fossil fuels. Since hydrocarbons are liquid at room temperature, this form of energy is easily stored. A form of clean energy stored in chemical bonds can be found by splitting water in electrolyzers to produce hydrogen and oxygen. By feeding electricity and water into the electrolyzer, the energy is now stored in the hydrogen-hydrogen bonds and the oxygen-oxygen bonds. The electricity can then be extracted at a later point by running the reverse process in a fuel cell where hydrogen and oxygen combine to form water again. This is described in a little more detail in chapter 4. There are mainly two problems with this solution: 1) hydrogen is difficult to store in its pure form, requiring very high pressures or very low temperatures, and 2) every time we convert the electricity to chemical bonds or back, we lose some of the energy. For this reason, Smalley did not believe in an economy built solely on hydrogen.[1]

There are however ways around this, as described nicely by Seh et al.[5] One example is the decentralization of chemicals where clean electricity can be used to form hydrogen which can immediately be used to form other chemicals which may either be used directly (such as ammonia for fertilizer) or is stored more easily (like hydrocarbons). (Electro)catalysts are used to enable all these conversion pathways, and the efficiency of the processes depends intrinsically on the catalyst and extrinsically on the final engineered system. In this group, we focus mainly on the different aspects of the hydrogen economy by figuring out how catalysts work so we can make them better and use the knowledge to discover new catalysts.

As a final note to the preceding discussion: given the availability of materials[4] needed to meet the Terawatt challenge, it is unlikely for one single technology to be the solution to the world energy problem. Most likely, it will be the concerted contribution of many different technologies that will meet the energy demands of the world.

What is catalysis

A catalyst is something that increases the rate of a reaction without itself being consumed by the reaction. There are various forms of catalysis, and we focus mainly on metallic heterogeneous catalysts. Figure 1.1 illustrates a reaction that takes place on the surface of a catalyst compared to the case where the catalyst is absent. For two reactants, A and B, to form a product, P, they must physically meet and interact long enough to overcome the energy barrier that is between their initial state (A and B) and their final state (P). By adding a catalyst which reacts strongly enough with the reactants that they adsborb on its surface, another reaction pathway is now possible in which the adsorbed reactants react to form a product. This new catalytic pathway has the benefit that it is easier for reactant to meet on a two-dimensional surface than in a three-dimensional space, and, more importantly, the catalyst weakens the electronic structure of the reactants[7,8] which decreases the energy barrier to the final state of the product. The optimal catalyst will be the one that binds the reactants just right.[9] If the catalyst binds the reactants too weakly, they will never stick

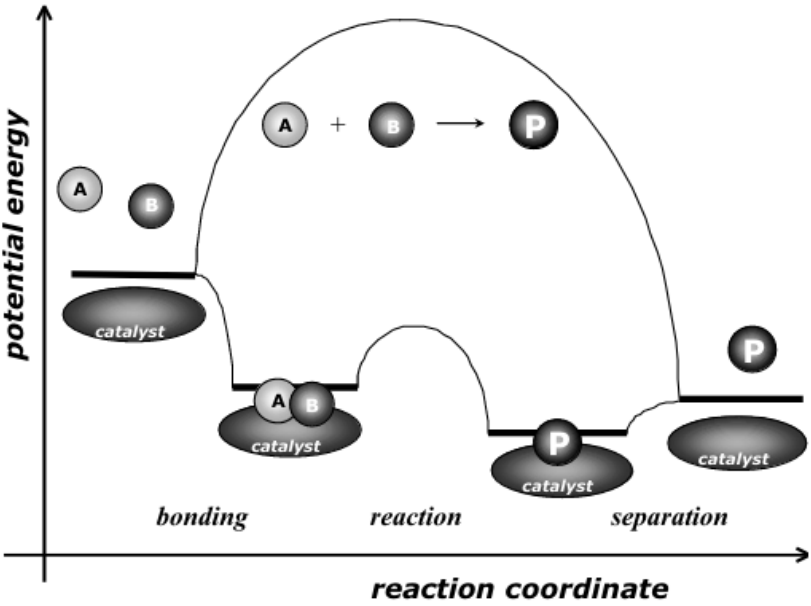

Figure 1.1: Illustration of a catalytic reaction. Two reactants, A and B, meet on the surface of a catalyst where they react to form the product, P. The energy barrier for the reaction to proceed on the surface of the catalyst is much lower than if the reaction was to proceed in the absence of the catalyst. Reprinted from [6].

to the surface and react to form the products. Alternatively, if the catalyst binds the reactants too strongly, they will definitely stick to the surface, but the formed products will also bind so strongly to the surface that they will not leave it again. Thus, no new reactants can come to the surface and the reaction rate is just as bad as for the weakly binding catalyst.

Since catalysis takes place on the surface of materials, understanding of how catalysis works came through surface science studies which were able to pinpoint the *active sites* where the reaction proceeds on catalysts. This, coupled with density functional theory (DFT) being able to explain current trends and predict new ones, has really sped up the process of properly understanding catalysts.[10]

1.2 Structure of the thesis

The majority of my work has been focused on the synthesis and characterization of nanoparticle model systems using a gas-aggregation source coupled to a ultra-high vacuum (UHV) system in order to provide useful insight to the mechanisms of catalysis so that new and better catalysts can be developed. It is fairly complex to fully understand all the details of this system and utilize its full potential within a single PhD study. During my studies, I have strived to better understand the model systems we prepare with the cluster source and to improve the method.

This thesis will not go through every paper I have published during my studies, but will be presented in a way that better reflects my attention and contributions.

Chapter 2 introduces the UHV system and the associated techniques which I have used to produce the results for the following chapters.

Chapter 3 is technical and focuses on rastered depositions: the implementation of a new technique at the setup which improves the quality of the model systems we produce. This was a necessary step to initiate a collaboration with mainly Daniel Sandbeck and Serhiy Cherevko at the Friedrich-Alexander-University Erlangen-Nürnberg. With two different model systems of mass-selected Pt nanoparticles, we discern the dissolution effect depending on the distance between nanoparticles as well as their size. My biggest contribution was implementing the method of rastering in collaboration with Niklas Mørch Secher. The Pt stories (paper III and IV) are appended at the end of the thesis and the main chapter focuses on the method.

Chapter 4 is devoted to isotope studies where I used LEIS to distinguish between ^{16}O and ^{18}O and discern their involvement in reactions for two studies: 1) mass-selected Ni_3Fe nanoparticles for alkaline oxygen evolution, and 2) sputter deposited thin films of RuO_2 and IrO_2 for acidic oxygen evolution. The first (paper II) was led by Claudie Roy and Bela Sebok. I took over sample synthesis and

characterization for Bela as he finished his PhD, but my main contribution is the isotope study in collaboration with Søren Scott. The second project (paper V and VI) is led by Reshma Rao and Søren Scott in a collaboration with Reshma Rao and Yang Shao-Horn of MIT.

Chapter 5 is devoted to temperature-programmed desorption (TPD). It was necessary to design a dedicated chamber to do CO-TPD on copper. This chapter first details the implementation, then describes some experimental procedures, and finally shows some preliminary results on 1) Cu foils as a reference to the literature, 2) 5 nm mass-selected Cu nanoparticles in search of higher binding energies, and 3) Pd_xSn sputter deposited thin films in search of copper-like binding energies. Anders Bodin guided the implementation in the initial phase during my Master's thesis, Julius Needham did the synthesis and measurements on Cu nanoparticles under my guidance as part of his Master's thesis, and Ezra Clark prepared the Pd_xSn thin films.

Chapter 6 provides a brief summary of the chapters.

I wanted to include the story on the electrocatalytic behaviour of Cu nanoparticles that make up paper VII and VIII. It has been a main project in my PhD since the beginning and has been fraught with instability and frustration. In the last half year, Degenhart Hochfilzer and I finally figured out why the system behaved as it did. After the details of chapters 3 to 5, however, I realize that I neither have the time or space to include it in this thesis.

Method

Chapter 2

In this chapter, I present primarily the methods I have used to synthesize and characterize model systems of nanoparticles throughout my projects. This is to build you a foundation for understanding the results presented in the following chapters. A short introduction to electrocatalysis is included at the end as the main method used by my colleagues for measuring the catalytic performance of the nanoparticles.

2.1 "Omicron" UHV system

The setup commonly referred to as "Omicron" in our group, is a Multiscan Lab XP ultra-high vacuum system shown in figure 2.1. It consists of two main chambers: a preparation chamber and an analysis chamber - each pumped by a turbo pump, ion pump, and titanium sublimation pump. The analysis chamber holds a sample storage carousel with space for 12 samples along with characterization techniques XPS, LEIS, SEM, and TPD described in more detail after this. Auger and scanning Auger spectroscopy (AES/SAM) and scanning tunneling microscopy (STM) are in principle also available, but it was not deemed worth the effort to get up and running for the projects during my PhD. The ion gun for LEIS is differentially pumped by its own small turbo pump and is connected to a small bottle of helium.

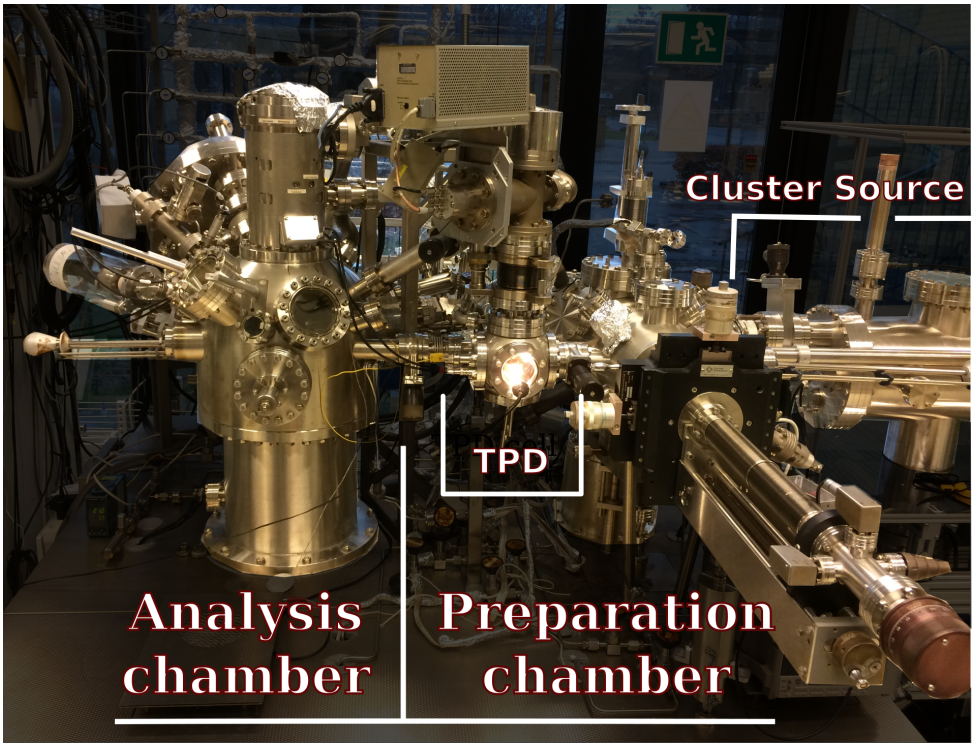

Figure 2.1: Overview of the setup called "Omicron". On the left: Analysis chamber with a 12-slot sample stage, XPS, LEIS, SEM, AES/SAM, and STM. On the right: Preparation chamber with TPD, cluster source, ion gun, and a 3-sample fast entry loadlock.

On the preparation chamber is a coarser ion gun mainly used for sputter cleaning samples with argon. A lecture bottle of ammonia is also connected for experiments at creating nitrogen-terminated defect sites. The chamber has an antechamber for TPD, a fast-entry loadlock for three samples, and a nanoparticle generator commonly referred to as "cluster source". The turbo pump is shared between the preparation chamber and loadlock. It is possible to dose $(^{18}O)_2$ and $^{12}C^{18}O$ into the preparation chamber via leak valves. A gas wall is also connected to the setup, but as for AES/SAM/STM, we never dedicated time to revive it.

2.1.1 Sputtering

Sputtering can be translated to "bombardment with ions". Generating the ions may vary from method to method, but generally the ions are then accelerated in an electrostatic field to a desired energy and then directed at a surface. The two ion guns on Omicron generate the ions by admitting the gas to be ionized into a small chamber where a filament emits low-energy electrons. These will then collide with the gas atoms and knock free electrons to leave a positively charged ion. The ions are then accelerated, extracted and focused with electrostatic lenses.

The ion gun on the preparation chamber is an ISE 10 gun that is not differentially pumped. It is connected to Ar and NH_3 via leak valves and is generally used for sample preparation in sputter cleaning the entire surface with Ar ions og using ionized NH_3 to create nitrogen defects. The ion gun on the analysis chamber is a ISE 100 Fine Focus gun and is differentially pumped and connected to He, which is used to generate the signal for low-energy ion scattering spectroscopy. The ISE 10 is used for coarser beams and rough treatments that involve the entire sample, while the ISE 100 Fine Focus produces a very focused beam ($\sim 140\,\mu$m) which can be scanned across the sample.

Whether intentional or unintentional, sputtering removes material from the surface and it is very useful to estimate this amount. The *sputter yield*, Y, is a term that denotes how many atoms are sputtered per incoming sputter ion and depends on the projectile and its energy and the target surface material. Table 2.1 lists estimated sputter yields for the various projectile/target combinations used in my projects. Assuming a generic ion current density $i = 1\,\mu A/cm^2$ and a sputter yield $Y = 1$, the rate of which surface atoms are removed is given by

$$R = \frac{i\,Y}{e\,N_A} = \frac{10^{-6}\frac{\mathrm{C}}{\mathrm{s\,cm^2}} \cdot 1}{1.602 \cdot 10^{-19}\frac{\mathrm{C}}{\mathrm{ion}} \cdot 6.022 \cdot 10^{23}\frac{\mathrm{ions}}{\mathrm{mol}}} = 10\frac{\mathrm{pmol}}{\mathrm{s\,cm^2}} \tag{2.1}$$

The removal rate expressed in terms of (pico)meter per second depends on the mass and density of the sputtered material, X: $r_X = R\,M/\rho$. For

Y	He	Ar		Generic sputter rate
	1000 eV	1000 eV	2000 eV	(pm/s)
Ti	0.065	0.731	1.023	1.06
Fe	0.150	1.704	2.359	0.71
Ni	0.145	1.682	2.336	0.66
Cu	0.254	2.821	3.851	0.71
Ru	0.089	1.632	2.320	0.82
Pd	0.177	2.389	3.288	0.89
Sn	0.107	1.337	1.823	1.62
Ir	0.055	1.492	2.147	0.85
Pt	0.067	1.542	2.197	0.91

Table 2.1: Sputter yields for various combinations of projectile and targets used throughout this project. Data retrieved from ref[11] which is based on ref[12]. Generic sputter rates are calculated assuming a current density of $1\,\mu\mathrm{A\,cm^{-2}}$ and a sputter yield of 1 atom/ion. Elemental densities and molar masses are from an online periodic table[13].

Projectile	Energy	Emission current	Sample current*
He	1000 eV	0.1 mA	4.1 nA
		0.3 mA	11.85 nA
		0.4 mA	15.5 nA
		1.0 mA	41.85 nA
		3.0 mA	104 nA
		4.0 mA	116 nA
		10.0 mA	177 nA
Ar	1000 eV	10.0 mA	0.8 μA
	2000 eV	10.0 mA	5 μA

Table 2.2: Sputter currents measured for various settings. *Note that the sample current is the total neutralization current when the sample is at ground potential and is a one-time measurement for He. The asymptotic value is used for Ar.

example, for copper

$$r_{Cu} = \frac{R\,M_{Cu}}{\rho_{Cu}} = \frac{10\frac{\mathrm{pmol}}{\mathrm{s\,cm^2}} \cdot 63.55\frac{\mathrm{g}}{\mathrm{mol}}}{8.96\frac{\mathrm{g}}{\mathrm{cm^3}}} = 71 \cdot 10^{-12}\,\frac{\mathrm{cm}}{\mathrm{s}} = 0.71\,\frac{\mathrm{pm}}{\mathrm{s}} \qquad (2.2)$$

These rates are added to the last column in table 2.1 for the individual elements. Seah and Nunney present work on the sputtering of oxide compounds[14], but for the calculations in this thesis, I will assume oxide sputter rates to equal their metallic counterparts.

Sputter element:	He	Ar	
Energy (V)	1000	1000	2000
Chamber pressure (mbar)	$5 \cdot 10^{-8}$	$1 \cdot 10^{-6}$	$3.3 \cdot 10^{-6}$
Focus 1 (V)	745	1	1200
Focus 2 (V)	153	-	-
Extract (V)	947	903	1709

Table 2.3: Settings used throughout the project for the three different sputter conditions.

The effective beam size of helium sputtering depends on the size of the raster pattern. This is a square with variable side lengths of 0.5 mm, 1.0 mm (default), 2.0 mm, 4.0 mm, or 6.0 mm. Argon sputtering was conducted with the conditions described in table 2.3. From a very long sputtering time with 1 keV Ar (the sample in figure B.1), the sampleholder next to the sample was visibly cleaned, and the beam area is roughly estimated from this to be $(1.5\,\mathrm{cm})^2$. The beam profile for 2 keV Ar has not been measured, but is assumed to be similar to 1 keV Ar based on not having to move the sample much in either direction before the sample current would start to drop.

The sputter rate can now be estimated matching the experimental conditions to the information in these tables. For example, sputtering copper with 1 keV helium rastered $(1.0\,\mathrm{cm})^2$ with 1.0 mA emission current, I estimate the sputter rate:

$$r = r_{Cu} \cdot \frac{i}{\mu\mathrm{A\,cm^{-2}}} \cdot Y = 0.71 \frac{\mathrm{pm}}{\mathrm{s}} \cdot \frac{41.85 \cdot 10^{-3}}{0.1^2} \cdot 0.254 = 0.75 \frac{\mathrm{pm}}{\mathrm{s}} = 2.3 \frac{\text{Å}}{5\,\mathrm{min}} \tag{2.3}$$

or in words: a little less than a monolayer is sputtered every five minutes. In chapter 4, depth profiles are conducted on two different samples to assess the assumptions concerning these sputter rates.

2.1.2 XPS - X-ray Photoelectron Spectroscopy

X-ray photoelectron spectroscopy (XPS) is a surface-sensitive technique allowing us to probe the electronic binding energies of the outer layers of a surface.

By accelerating high-energy electrons towards an anode - usually magnesium or aluminum - core electrons will be knocked out of the material, and, as anode relaxes, a spectrum of photons in the range of 0 to 1500 eV are emitted. Almost 100 % of the intensity of this spectrum is dominated by the $K_{\alpha_{1,2}}$ line - 1253.6 eV for Mg and 1486.6 eV for Al. These photons will penetrate 1-10 μm of the sample[15] where they will be absorbed by core electrons of the sample by photoemission with a kinetic energy:

$$E_k = h\nu - E_b - \phi \tag{2.4}$$

$h\nu$ is the energy of the photons, E_b is the binding energy of the core electron, and ϕ is the work function between the sample and analyzer. X-rays at Omicron are generated by a XR 50 X-ray gun with an unmonochromatized twin Al/Mg anode. Typically the magnesium anode is used at a power of 12 kV / 20 mA. The detector is a NanoSAM 7-channel hemispherical energy analyzer.

By scanning across the spectrum of kinetic energies of electrons emitted from the sample, you will get a finger print of the sample consisting of its core electron peaks mapped as a function of binding energy. The spectrum electron core energy levels for a single element will depend uniquely on the number of protons and the oxidative state of the atom. This allows us to gather information about what elements are present and their chemical state. Data analysis is complicated by background subtraction from inelastically scattered electrons, overlapping peaks, Auger lines, satellites and shake-up features. Unmonochromatized laboratory X-ray sources are characterized by a broad band of photons - Bremsstrahlung - superimposed on the main K_α line which gives rise to a background. Furthermore, several smaller spectral lines besides the main one is also present which gives rise to satellite peaks. This means that core electron peaks are duplicated with smaller intensity and energy. However, only the α_3 and α_4 lines are intense

enough to be visible in most spectra (8 and 4 % intensity relative to the main K_α peak)[15]. Auger lines are shake-up features in which two electrons will work together to relax an electron into a core state with the other being expelled from the material with the excess energy. These lines are therefore purely dependent of the chemical state of the atom and not the excitation energy of the photons. These lines are often complex and take up a rather large portion of the spectrum. Some core electron peaks exhibit strong shake-up features following the resonance peak, but the background of inelastically scattered electrons is nearly constant for many peaks and so a Shirley background is often a fine approximation.[16] In the other cases, one would have to calculate a response matrix to account for the energy losses. For quantifying the ratio of elements on the surface, one need relative sensitivity factors which in principle are setup-dependent, but using a standard database like in CasaXPS gives decent results.

The inelastic mean free path of electrons depend on the kinetic energy, which for XPS is below 1500 eV. This means that *all* the measured electrons originate from within a maximum depth of a few nanometers from the surface.[17]

2.1.3 LEIS - Low-Energy Ion Scattering Spectroscopy

Low-energy ion scattering spectroscopy (LEIS) also referred to simply as ion scattering spectroscopy (ISS) is an extremely surface sensitive technique allowing us to probe the atomic mass of the elements in the single top atomic layer(s) of a surface.

The signal from LEIS originates from sputtering a target surface with ions (usually noble gas ions like He^+, Ne^+,, Ar^+, Kr^+) and monitoring the energy of reflected ions at a specific scattering angle. The collision between the incident ion and surface atom can be described by a classical elastic binary collision model. The incident ion of a certain energy, E_0, impinges on the surface where it will collide with a single atom and scatter in a random direction. The energy retained by the incident ion after the collision, E_1, will depend on the angle it was scattered, θ, and the mass of

the surface atom, m_s, relative to its own, m_i:

$$E_1 = \left(\frac{\cos\theta \pm \sqrt{\left(\frac{m_s}{m_i}\right)^2 - \sin^2\theta}}{1 + \frac{m_s}{m_i}} \right)^2 \cdot E_0 \tag{2.5}$$

The scattering angle is determined by the setup and you choose the type of incident ion and acceleration voltage, so by measuring the kinetic energy of the scattered ion, you know all the variables in order to solve equation (2.5) for the mass of the surface atom, m_s. This relation means that you will not be able to detect elements lighter than the ion you probe with and the mass resolution decreases drastically the bigger the difference in mass between the colliding atoms. The big strength of LEIS comes with its surface sensitivity: When the ions get close to atoms in a solid, there is a very large probability the ions will be neutralized. This means

The best effort at fitting peaks and backgrounds I have seen so far, is following the semiempirical model by Nelson[18], which uses a mix of a Gaussian and Lorentzian to fit the peak shape

$$I_p = \frac{A \exp\left(-2.77259 \cdot (1-R) \cdot \left(\frac{E-E_0}{W}\right)^2\right)}{R(E-E_0)^2 + \left(\frac{W}{2}\right)^2} \tag{2.6}$$

where A is an amplitude, R is a factor between 0 and 1 determining the Gaussian/Lorentzian character of the peak, E_0 is the peak position at its maximum, and W is the full width at the half maximum.

The background is modeled similar to core peaks in XPS[16] with the background from inelastic scattering being proportional to the integral peak signal. This gives a constant background signal from inelastic scattering of the main peak. This is modulated by an exponential decay $\exp(-\kappa/E)$ to capture the neutralization behavior of the inelastically scattered ions. κ, here, is the exponential decay factor. This is 5 parameters to fit per peak: A, R, E_0, W, and κ although the width will be relatively constant for a given experimental setup and the peak position will lie within a narrow range per element depending on the magnitude of the signal. The peak

width for Omicron is around 27 eV. Initial efforts at this fitting method gave good results when applying it manually to a single spectrum, but less well trying to do it automatically for multiple spectra. Quantification of peaks in this thesis has therefore been done by subtracting a linear background and either: 1) integrate the bare signal above the background, or 2) fit a reference peak to the background-subtracted spectrum. The second method requires more work, but works wonders at matching the peak shapes.

The sensitivity of LEIS on Omicron, can roughly be estimated to 100 ppm or 0.01 % of a monolayer. This estimate is based on the following: Pure clean copper gives a signal of 300000 to 500000 cps (counts per second) when dosing He into the analysis chamber at a pressure of $5 \cdot 10^{-8}$ mbar and drawing a 1.00 mA emission current from the ionizing filament. If we need about 50 cps to say with certainty that we have a peak, then the sensitivity under these conditions is $50/500000 = 0.01\,\%$. The sensitivity thus derived, will depend on the substrate, the element, and the fluence. The substrate will the tailing background of inelastically scattered ions: a 50 cps peak on top of this might very well drown in the background noise. At energies higher than the substrate peak, however, there is no signal at all (assuming the substrate is clean, of course). This means that LEIS is very good at detecting small traces of elements heavier than your substrate. The relative sensitivity between elements also differs a bit. Usually they are within a factor two of each other and for some elements it may depend strongly on the ion beam energy.[19] Especially lighter elements seem to be closer to a tenth of the sensitivity of copper. You may then lower the fluence to reduce the sputter damage on your sample at the expense of sensitivity, while increasing the fluence will make you more sensitive to the low signals at expense of more sputter damage. When working with high ion beam currents, take care that you don't make the analyzer measure signals higher than 500 kcps.

2.1.4 SEM/TEM - Scanning/Transmission Electron Microscopy

In electron microscopy, the sample under investigation is bombarded by high-energy electrons to generate a bunch of signals either one of which can

be used to generate a map of the sample. The volume in which the electrons interact with the sample is tear shaped with a narrow region close to the surface and a bulky part deeper in the sample. Any signal that is measured is generated in this interaction volume and the size depends on the energy of the electron beam. Increasing the energy makes the near-surface neck narrower, but extends the bulky part into the surface.

In scanning electron microscopy (SEM), electrons of low energy (5 - 30 keV) are used since these electrons have a rather small interaction volume close to the surface. By scanning a focused beam, three signals are often used to map the surface: secondary electrons, primary electrons, and X-rays. Secondary electrons are electrons of low-energy that escape the surface and can easily be pulled in by a weak electrostatic field. They originate from the top few nanometers of the interaction volume[17] and are therefore more sensitive to surface geometries, i.e. edges where more sample surface is close to the interaction volume. Primary electrons on the other hand, are electrons that penetrate into the sample and back-scatter off a single atom and escapes from the surface with most of its original energy. These are directional and require the detector to be placed close to the incoming beam. The signal is generated in most of the interaction volume and is more sensitive to the mass of the scattered atom than any local geometries. X-rays are generated in the entire interaction volume and can be used to make an elemental map of the surface. This technique is called EDX. The resolution of the UHV Gemini on Omicron is nominally 3 nm, but requires the table to float. This requires disconnecting and realigning the cluster source and is not done without a good reason. The best resolution achieved without floating the air table is 8 nm and can be used to check substrates and verify dispersion of particles across the surface.

If the primary energy is increased to 100 - 300 keV, the neck of the interaction volume gets extremely long and narrow. For thin samples (¡ 100 nm), this means that most of the electrons are simply transmitted. Transmission electron microscopy (TEM) in bright-field mode is mapping the directly transmitted signal of a parallel beam of electrons through a sample. Dark areas will thus correspond to either thick or heavy areas on the sample with subnanometer resolution. A typical use of TEM with the

cluster source is to prepare mass-selected nanoparticles on dedicated TEM grids to get images for a size distribution.

2.1.5 TPD - Temperature-Programmed Desorption

In temperature-programmed desorption (TPD), you let a gas mixture adsorb on your sample at a temperature, T_0. The gas molecules will adsorb to various specific sites on the surface with a binding strength that depends on the electronic configuration of the specific site(s) of adsorption. Under-coordinated sites tend to bind more strongly, and so molecules adsorbed to these sites will require more energy to desorb again and the rate of change in surface coverage, θ can in general be described by the following equation[6]

$$r = -\frac{\mathrm{d}\theta}{\mathrm{d}t} = \nu(\theta)\,\theta^n \cdot exp\left(-\frac{E_{des}(\theta)}{RT}\right) \tag{2.7}$$

Here, r is the rate of desorption, θ is the surface coverage of a specific site, ν is a preexponential factor, E_{des} is the desorption energy and R is the gas constant. ν and E_{des} may furthermore depend on the coverage making the equation difficult to solve exactly. But qualitatively, when increasing the temperature of the surface linearly $T = T_0 + \beta\, t$, the rate of desorption increases rapidly when the temperature gets close to the desorption energy. With a high rate of desorption, the surface coverage will quickly decrease thereby reducing the rate of desorption again. This means that the signal from each site will show up as peaks located at specific temperatures as shown in figure 2.2. Illustrated in the same figure is the effect of varying the heating rate, β. One can fit the experimental spectrum to an assumed distribution of sites, but if the heating rate is not constant, a single peak in the ideal case will instead show up as multiple adjacent peaks. This effect is even worse if the desorption energy decreases with coverage as this will make the peak much broader.

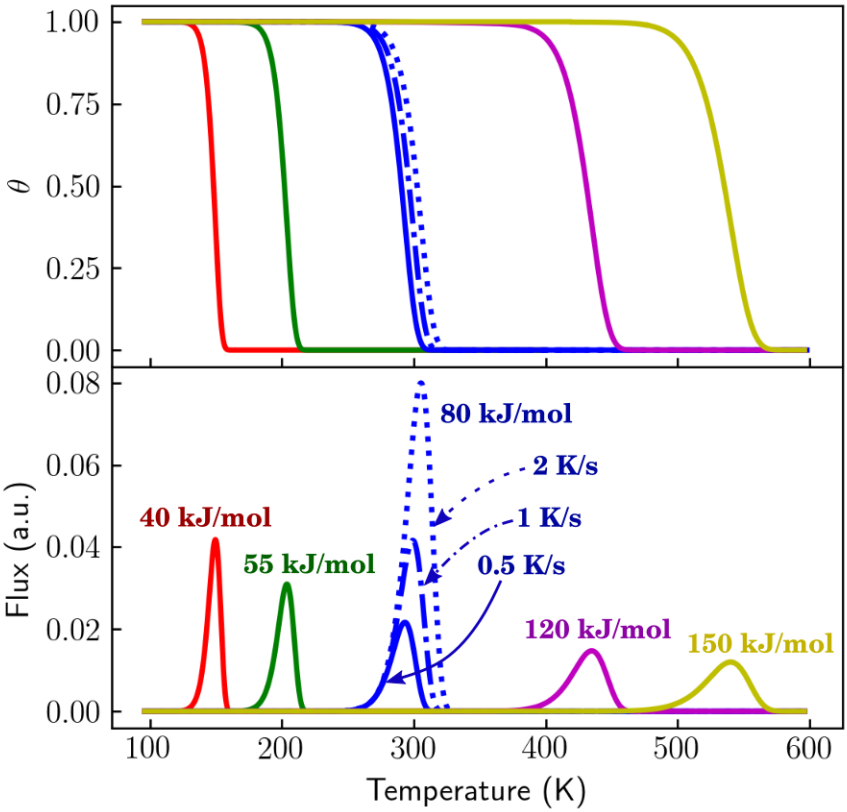

Figure 2.2: Modelled desorption for various E_{des} with $\beta = 0.5\,\mathrm{K/s}$ unless specified otherwise, $\nu = 10^{13}\,\mathrm{s}^{-1}$, and $n = 1$ for first-order desorption.

2.1.6 QMS - Quadrupole Mass Spectrometry

A quadrupole mass spectrometer (QMS) can be used for residual gas analysis and requires high vacuum or better to work. A filament emits electrons which ionizes the gas molecules near the QMS entrance. By mixing applying a varying potential across four rods inside the QMS, only

particles with a specific m/z ratio has a stable path through the rods. By changing the potentials, the transmitted m/z ratio can be varied. The transmitted ions can then be measured with a detector. When the gas is ionized, a fraction of the species will fragment into ionized subspecies resulting in a cracking pattern that is more or less unique for each compound.

The mass spectrometer is operated in one of two modes: obtaining a mass spectrum, or tracking a predefined set of m/z ratios over time. Only one m/z ratio can be transmitted at a time, so a mass spectrum is obtained by detecting one m/z ratio and then slowly scanning up to another m/z ratio to get a spectrum. This takes a little time (depending on the desired resolution) and is not useful if you expect the gas composition to vary within the time it takes to get a spectrum. Instead, a set of m/z ratios can be predefined, which the QMS will track over time by scanning each m/z a fraction of time before moving to the next in the list. The list is then repeated continuously until terminated by the user. One has to know what to look for in order to find a good optimum between tracking enough masses (m/z ratios) to notice unexpected things and getting a good resolution for the expected signals. A typical mass spectrum of the UHV chamber background towards the end of the project is shown in figure 2.3 after having replaced a broken filament with a "homemade" one (see appendix A).

2.2 Nanoparticle generator

The nanoparticle generator or "cluster source" used throughout my PhD projects is a Nanobeam2011 from Birmingham Instruments and is shown in figure 2.4. It consists of three main chambers each pumped by its own turbo pump: an aggregation chamber where the nanoparticles are formed, a lateral time-of-flight mass filter (TOF-MF) where the nanoparticles are separated according to their mass, and a small ion optics chamber in between where the beam of nanoparticles is accelerated and focused into the TOF-MF which exits into the Omicron preparation chamber. When dormant, the chamber pressure is logged by an ion gauge in the TOF-MF

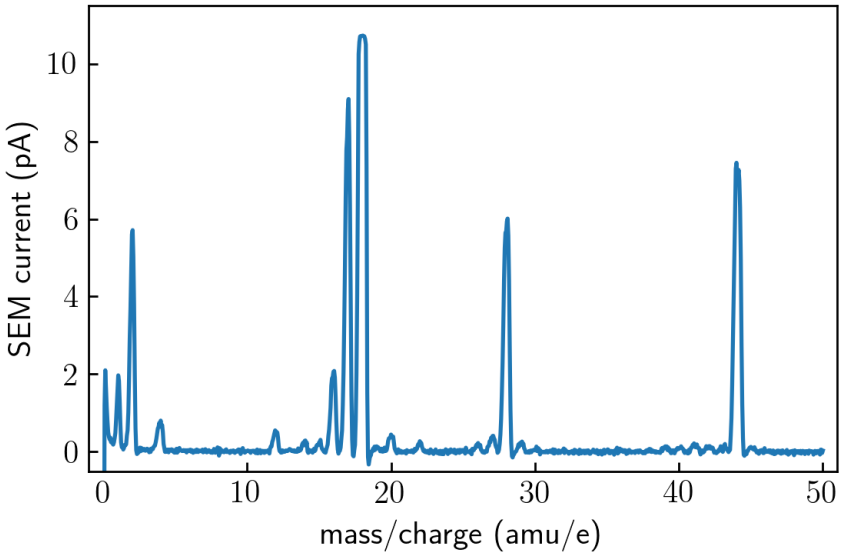

Figure 2.3: Typical mass spectrum of the chamber background towards the end of the project. Note that $m/z = 18$ is capped at $1.2 \cdot 10^{-11}$ A because of the full scale range for the detector chosen to better resolve weak signals.

with a normal base pressure of mid-10^{-10} to low-10^{-9} mbar. The cluster source uses standard sputtering targets: discs of 2.00" in diameter and 0.125" to 0.250" thick. The sizes produced by the cluster source ranges from single atoms up to nanoparticles around 10 nm in size. The region between trimers and nanoparticles of around 2 nm, however, we have not been able to find any working conditions for synthesis.

2.2.1 Formation of nanoparticles

Magnetron-sputtered, gas-aggregated clusters are formed in the aggregation zone as depicted in figure 2.5a and described in [21]. You load the magnetron sputter head with a sputtering target (referred to as just the *target*) consisting of the elements you want to form clusters from. A stream

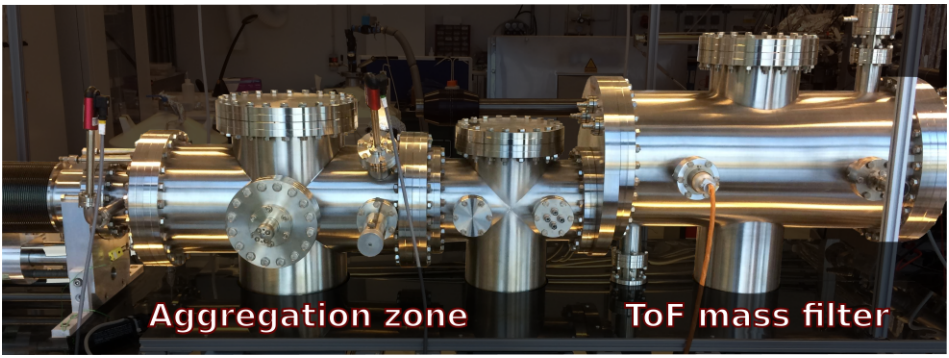

Figure 2.4: "Cluster source" used to generate mass-selected nanoparticles: Nanobeam 2011 from Birmingham Instruments. Nanoparticles are formed in the aggregation zone by magnetron sputtering and gas-aggregation. The charged particles are then guided into a lateral time-of-flight mass filter where only the portion of nanoparticles with a specific mass-to-charge ratio will be transmitted to the Omicron preparation chamber. Figure adapted from [20].

of argon is led into the aggregation zone from behind the target on which a high potential ($\sim 200\,\mathrm{V}$) is applied. The short distance between the target and the grounded chimney surrounding the target, between which the argon flows, has a very intense electric field. When an argon atom spontaneously ionizes, instead of naturally recombining, the argon ion and electron are pulled away from each other where collisions with other argon atoms will induce further ionization providing a cascade effect. In this way, a plasma is very quickly ignited when applying the high voltage on the target. A ring of magnets behind the target produces field lines that localize the electrons from the plasma in a ring in front of the target. These electrons continuously ionize new argon ions, which are accelerated into the target surface thereby sputtering it while the ejected electrons help to generate new argon ions. The plasma is thus sustained and localized on the target by a flow of argon, the ring of magnets and the neutralization current from the high voltage supply on the target. The argon sputtering "liberates" atoms from the target and ejects them into the aggregation zone. Here, the metal atoms are thermally equalized with the gas in the chamber and via collisions in the gas, they aggregate into clusters and nanoparticles. Haberland et al.

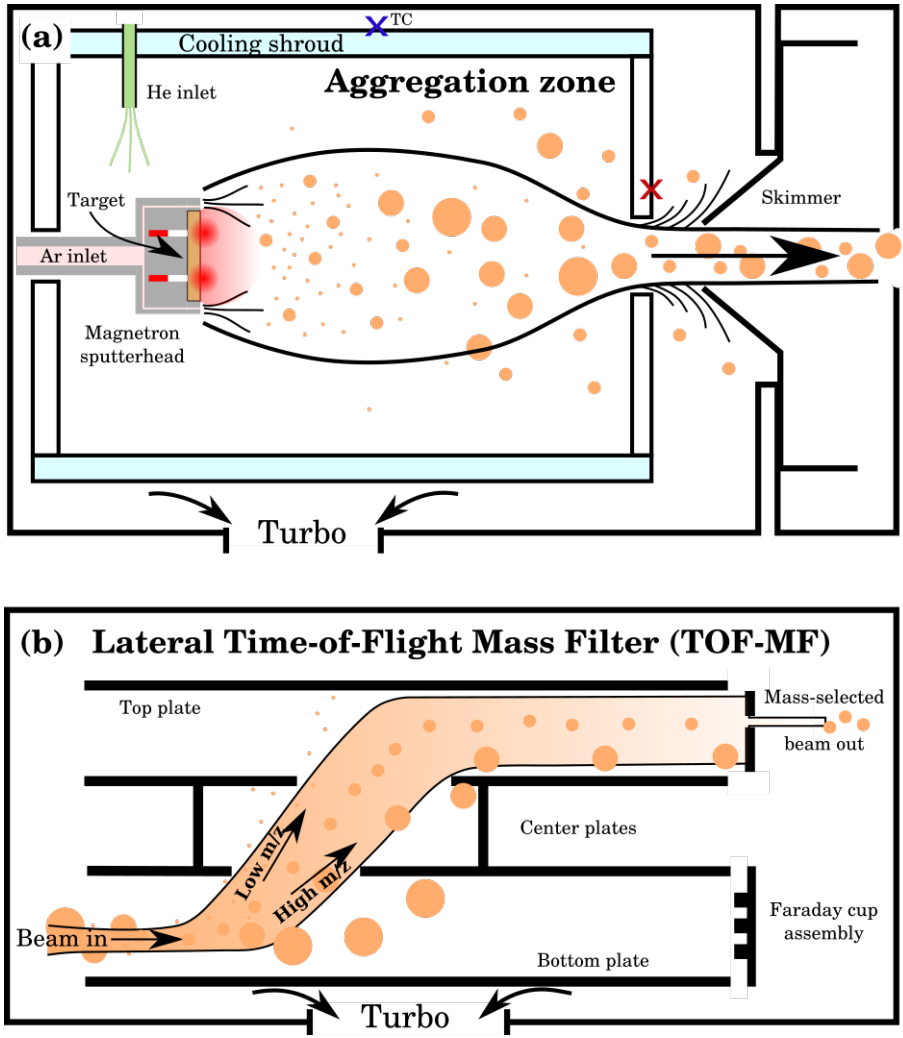

Figure 2.5: Illustration of the working principle of the cluster source. (a) Formation of nanoparticles in the aggregation zone, and (b) size selection of the beam of nanoparticles by separation in a lateral time-of-flight mass filter (TOF-MF) according the mass/charge ratio (m/z). See main text for detailed descriptions. Figure adapted from [20].

explain that cluster growth is nucleated via dimerization which due to conservation laws of energy and momentum requires at least a third atom in a collision between two metal atoms in order for a metal dimer to form:[22]

$$M + M + \mathrm{Ar} \rightarrow M_2 + \mathrm{Ar} \tag{2.8}$$

where M represents the metal atoms in the collision. Through multiple collisions in the aggregation zone, the dimers continue growing into nanoparticles.[21,22] The aggregation zone is an inner chamber with an exit aperture leading into the UHV chamber that is pumped by a turbo pump. This reduced pumping leads to a higher pressure inside the aggregation zone which induces more collisions. Py pumping liquid nitrogen (LN_2) through walls of the aggregation zone, heat is drawn out of the system which assists the growth of particles. The flow of gas and nanoparticles undergoes a supersonic expansion when it exits the aggregation zone via the aperture because of the great pressure difference between the two zones - usually a factor 20 or more. This means that the beam of particles is "pulled apart from itself" and is no longer self-interacting: no further collisions between particles in the beam.

The size of the nanoparticles is thereby controlled by the conditions in the aggregation zone, while the following zones is "simply" manipulating the beam of nanoparticles onto the sample. A benefit of magnetron sputtering is that a very large fraction of the particles is charged[22], whereby the particles can be manipulated in vacuum by electrostatic lenses according to their mass-charge (m/z) ratio.

Controlling the size of the nanoparticles can roughly be boiled down to: 1) how many atoms are sputtered from the target, and 2) how many collisions a sputtered target atom in average experience on its journey through the aggregation zone, and 3) the temperature of the system. The parameters we can tune to control this is: 1) by varying the flow of argon in combination with restricting the neutralization current on the target (sputter power). 2) The pressure inside the aggregation zone can be varied by adjusting the flow into the zone (mass flow controllers) or restricting the flow out the zone (size of the exit aperture). Furthermore the distance of the aggregation zone can be tuned by moving the magnetron sputter head

further in so the particles need to travel a shorter distance. Helium can also be introduced from the back of the chamber via another mass flow controller. As it does not sputter as effectively as argon does (see table 2.1), helium mainly serves to induce more collisions and nucleate more dimers. Adding a little helium then tends to move the size distribution towards lower masses. Adding too much helium, however, affects the sputtering plasma since this is controlled via the total neutralization current. 3) In principle, the temperature of the aggregation zone could be controlled by pulsing or at least controlling the flow of liquid nitrogen through the cooling shroud, or by circulating another cooling medium. In practice, however, this is difficult to control, since the resulting size distributions are very sensitive to temperature variations. The temperature is measured by a thermocouple attached to the side of the cooling shroud (**X** in figure 2.5a). Really, the relevant temperature is near the exit aperture (**X** in figure 2.5a), and it takes two to three hours of cooling before the system is in thermal equilibrium - which then changes when you start flowing gases and sputtering the target. Physical changes to the target as sputtering progresses also changes the optimum conditions of the aggregation zone.

In practice, this means that we more or less have to retune the cluster source every time before use. The tuning process is based on trial-and-error, but modulated by the above concepts.

2.2.2 Selection of masses

Exiting the aggregation zone, the first electrostatic lens is a skimmer which selects the semi-laminar part of the nanoparticle beam. This helps reduce self-interaction and gives a better focused beam. The beam is then accelerated to 500 eV and focused into the mass filter for size selection.

The mass filter is a lateral time-of-flight mass filter developed by Issendorff and Palmer in 1999.[23] Its working principle is illustrated in figure 2.5b. The focused beam of nanoparticles enters the mass filter between the bottom plate and the center plates. A high voltage pulse is then applied between the two plates to give the charged particles a fixed amount of momentum upwards. The resulting lateral speed will thus physically separate the beam

of particles in space with the smaller particles reaching the top of the mass filter faster than the heavier particles. A grid in the center plates allow the beam to pass through to the upper region of mass filter. By applying an opposite high voltage pulse between the upper plate and the center plate, the lateral movement is negated and the beam is "straightened out". If the beam is perfectly focused before the filtering, only one specific m/z ratio will be aligned with the exit aperture of the mass filter when the beam is straightened out.

It is important to note that the mass filter filters according to the mass-per-charge ratio and not the absolute mass. While most of the particles carry only a single charge, a fraction of them may be doubly charged. So if the mass-selected size distribution from the aggregation zone contains a significant amount of masses double that which you are interested in, a fraction of these will pass unnoticed through the mass filter under the same criteria as the desired mass. Therefore when tuning the conditions of the aggregation zone, you not only has to optimize the signal of the desired mass, you have to simultaneously deoptimize the double mass current. The distribution of masses resulting from the conditions in the aggregation zone can be imaged by scanning the mass filter to get a spectrum. Such a spectrum is shown in figure 2.6, where the aggregation zone and ion optics has been tuned to deposit 350,000 amu copper nanoparticles (~ 5 nm). After a few depositions (an hour), the size distribution from the aggregation zone has developed a tail towards higher masses

2.2.3 Depositing the nanoparticles

Guiding the mass-selected nanoparticles safely onto the substrate is done by *soft landing*: The substrate is biased so the energy of the particles is reduced to below the general cohesive energy of the atoms, i.e. less than 1 eV per atom, allowing nondestructive landing of the nanoparticles.[24–26] In practice, this is achieved by biasing the substrate to 45 V by connecting five 9 V batteries in series. The 50 pA peak current reported in figure 2.6 is a decently high current for nanoparticles, but virtually no current for a battery. Batteries are therefore a convenient means of providing a stable

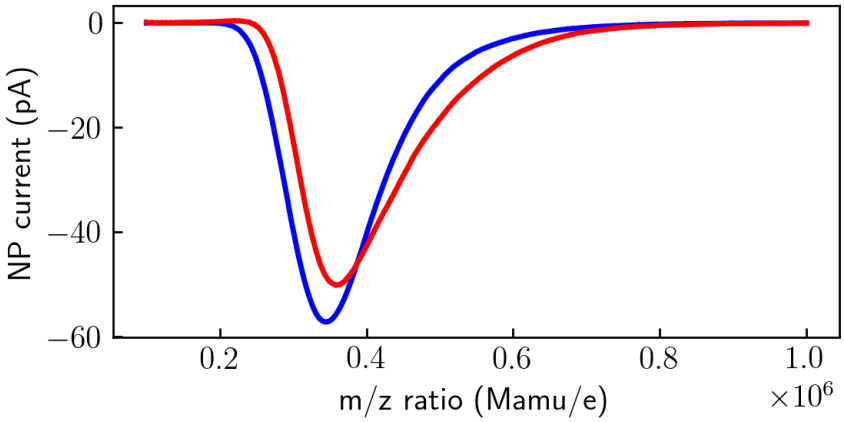

Figure 2.6: Example mass spectra before (blue) and after (red) deposition of 350,000 amu Cu nanoparticles. The mass profile has drifted slightly developing a more intense tail towards higher masses.

and noise-free potential. Since every particle that land on the substrate will have had to pass through the TOF mass filter, the total amount of nanoparticles can be calculated by simply measuring the neutralization current of the substrate and integrating it. If the ceramics isolating the substrate from ground potential are slightly dirty, a finite current will leak to ground and this will be added to any particle flux current measured by the Keithley 6514 Electrometer. Subtracting this background first is therefore strictly necessary. The leak current has caused trouble several times during my PhD and some notes about it can be found in appendix A. Example data for deposition of 350,000 amu Cu nanoparticles is shown in figure 2.7. Note that even if the deposited nanoparticles contain a large number of double-mass particles, the total mass loading is still estimated correctly with this method. The beam of nanoparticles is deposited on the substrate through an circular aperture 4.5 mm in diameter situated right in front of the sample in order to deposit on a well defined area.

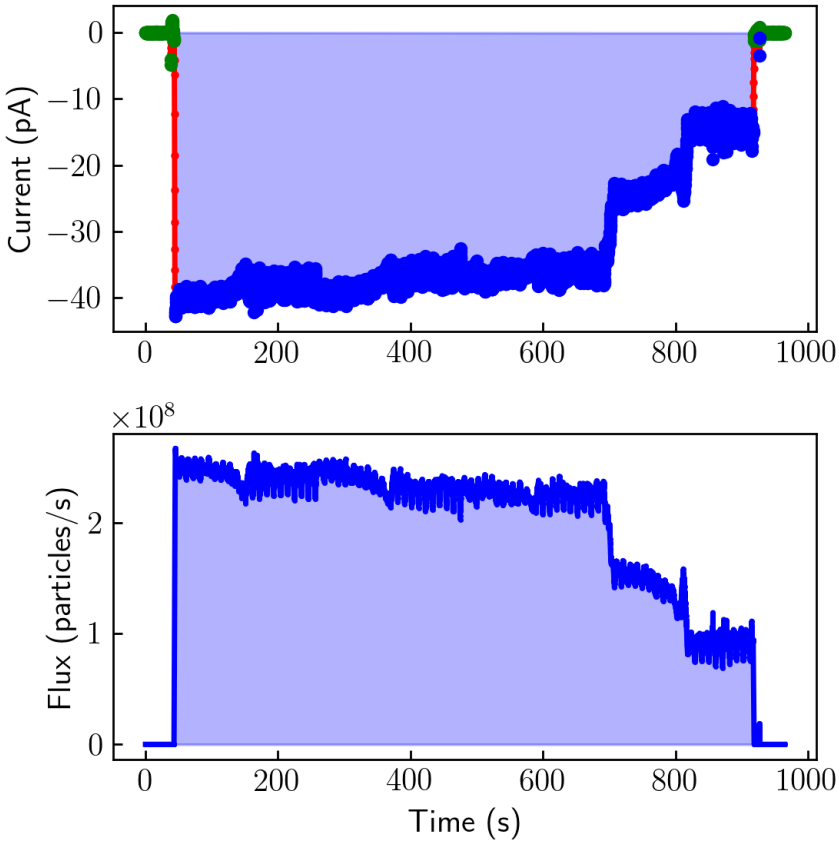

Figure 2.7: Example deposition current of 350,000 amu Cu nanoparticles. Note that the particles are negatively charged, so the raw neutralization current (top panel) is measured as a negative current. Bottom panel shows the flux of nanoparticles after automatically detecting background measurements (leak current - green) and subtracting the extrapolated background. The total mass loading is found by integrating flux of nanoparticles multiplied with the mass per particle (charge) as set by the TOF-MF.

2.2.4 "Coverage" and "loading"

When deciding on the total amount of nanoparticles to deposit on a sample, we use the term *coverage* [unit: %] as an alternative to *loading* [unit:

$g\,cm^{-2}$]. What we actually mean with coverage is *projected coverage*, and throughout this thesis, I will continue to be lazy and simply use the term *coverage*. Unless specified otherwise, *coverage* (θ) is the projected coverage of nanoparticles of a surface and is calculated by the equation

$$\theta = N \cdot \phi_M \tag{2.9}$$

where N is the total number of nanoparticles and ϕ_M is the relative coverage per particle using model M. For nanoparticles, the relative coverage per particle is simply the ratio of nanoparticle cross-sectional area, A_{NP}, to the deposition area, $A_{deposition}$

$$\phi_{NP} = \frac{A_{NP}}{A_{deposition}} = \frac{\pi d_{NP}^2}{4\,A_{deposition}} \tag{2.10}$$

where d_{NP} is the diameter of (spherical) nanoparticles calculated from the pure metal bulk density. For smaller entities where this is a poor descriptor, one can instead describe the surface as the number of sites describing one monolayer. For example, relative to a Pt(111) surface with lattice parameter 3.92 Å, the density of sites per area is

$$\rho_{2D}^{Pt(111)} = \frac{4\,\text{sites/unit cell}}{2 \cdot 3.92^2 \cdot \sin(60^\circ)\,\text{Å}^2/\text{unit cell}} = 0.15\,\frac{\text{sites}}{\text{Å}^2} \tag{2.11}$$

and thus for a single atom model where each particle occupies one site on a Pt(111) lattice, we would have

$$\phi_{SA} = \frac{1\,\text{site}}{A_{deposition}\rho_{2D}^{Pt(111)}} \tag{2.12}$$

From above relations, it is clear that the relative coverage depends on the deposition area and equation 2.9 can be rewritten as

$$\theta(A_{deposition}) = N \cdot \phi_M(A_{deposition}) \tag{2.13}$$

For simple depositions where the sample is not rastered, this is trivial to state since it is a constant depending on the aperture that is used between the sample and beam. However, when introducing rastering of the sample, the deposition area suddenly depends on the combination of aperture, chosen raster pattern and the cluster beam profile. How to handle this problem is discussed in detail in chapter 3.

2.3 Electrochemistry and EC-MS

Most of the catalysts presented in this thesis are electrocatalysts. This means that the reactions they catalyze are redox (reduction-oxidation) coupled reactions that involve the transfer of electrons. The two half-reactions can be confined to separate electrodes by connecting them with wires. One electrode will thereby be the anode where the oxidation reactions take place, and the other electrode is the cathode for the reduction reactions. The electrons produced by the one flow through the wire where they are consumed by the other. For charge balance, ions in electrolyte move from one electrode to the other. By forcing a potential difference between the two electrodes, you can tune the natural equilibrium of electrochemical products. The absolute potential is controlled by measuring it against an electrode that is in known equilibrium with the solution (i.e. does not partake in the reaction) - this is known as the reference electrode, RE. Current between the redox reactions flow between the working electrode, WE, and the counter electrode, CE. The catalyst under investigation is deposited on the working electrode where the reaction of interest happens. The counter electrode is there to provide charge balance by providing the other half-reaction. A simple version of this is known as a three-electrode setup and is the common way to test electrocatalysts. Variations such as the rotating disc electrode (RDE) setup and electrochemistry-mass spectrometry (EC-MS) exist to serve specific purposes. In RDE, the working electrode is mounted in a holder that can be rotated up to 1600 revolutions per minute. This increases convective flow of electrolyte to the catalyst on the electrode surface, so the reaction can be probed at higher currents/potentials without the process becoming limited by the diffusion of reactants to the catalyst. The directly measurable quantity here is the redox current versus the potential needed to drive it, but different reactions as well as corrosion processes can contribute to the total current, so it is necessary to measure the reaction products as well. This can be done by sampling the composition of the electrolyte or the gas in the headspace at regular intervals when the concentrations are high enough for detection, e.g. with a gas-chromatograph.

Recent advances in microchip fabrication technology has enabled the real-time detection of volatile species by connecting a small well-defined electrochemical working volume to a UHV mass spectrometer via a specialized silicon membrane chip developed previously in the group.[27,28] A 100 μm thick PTFE gasket separates the working electrode from the membrane chip which is hydrophobic, but has small pores that allow volatile products to escape from the liquid through the membrane while keeping the electrolyte in the working volume. The setup is illustrated in figure 2.8. Since a mass spectrometer is used for the product detection, the method is not only live, but also sensitive to isotope labeled experiments as is utilized in chapter 4. Furthermore, because of the well-defined electrolyte volume, the setup has a 100 % collection efficiency meaning that the measured mass spectrometer signals can be quantified. In figure 2.9 is an example of cyclic voltammetry (CVs) on a sputter deposited RuO_2 thin film shown as EC-MS plots: mass spectrometer signals are easily correlated with the electrochemical current and potential. In this case the oxygen evolution signal can easily be distinguished from the otherwise dominating capacitive charging current of the system. Lastly, the very high sensitivity of EC-MS makes it ideal for testing of cluster source samples that usually have very low loading (10 to 1000 ng catalyst), which makes direct product detection difficult for many conventional setups.

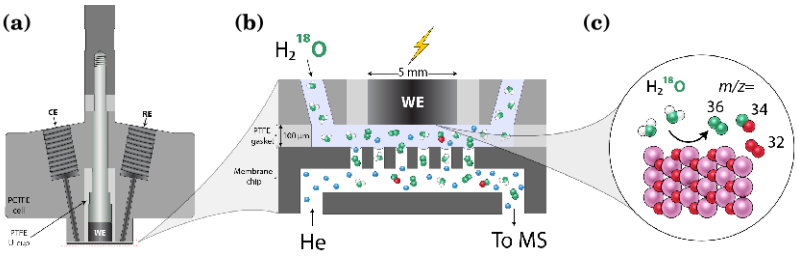

Figure 2.8: Diagram of the EC-MS setup. (a) side-view of the PTFE cell that holds the working electrode (WE), counter electrode (CE) and reference electrode (RE) and is mounted on the interface block holding the membrane chip. (b) The working volume consisting of WE, electrolyte layer, membrane chip and gas channel. The WE is separated from the membrane chip by a 100 μm thick PTFE gasket. (c) Example of surface reaction. Since volatile products are detected with a QMS, the method is sensitive to isotope scrambling effects. Diagram by Jakob Kibsgaard for paper V.

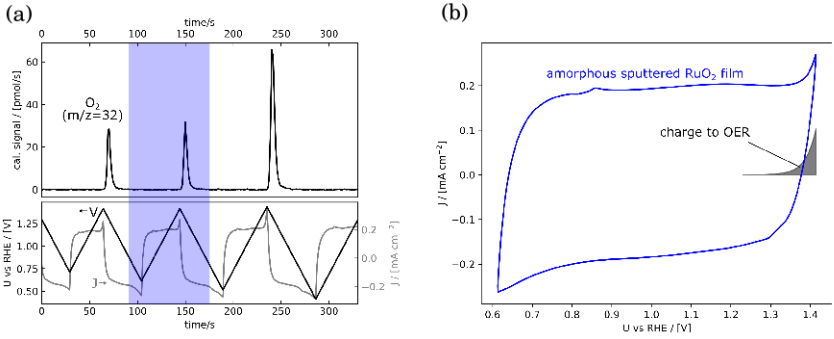

Figure 2.9: Oxygen evolution on RuO_2 thin film. (a) EC-MS plot of $m/z = 32$ ($^{16}O_2$) during CVs with the highlighted region shown in (b) wrapped as a conventional current-vs-potential CV. The current corresponding to the calibrated rate of measured oxygen is marked in gray. The OER current is only a small portion of the total measured current. Images by Søren Scott for paper V.

Rastered Depositions

Chapter 3

In this chapter, I go into details about a new method for the preparation of mass-selected nanoparticle model systems, which I developed in close collaboration with my colleague Niklas Secher. The method involves rastering the sample in front of the beam of mass-selected nanoparticles in order to smooth out any unevenness in the beam profile that would otherwise be projected directly unto the sample. Without rastering, for a sample of nanoparticles with an average coverage of 5 %, the local coverage on the sample can in extreme cases be up to 4000 % located in a very small spot while being zero on most of the sample. This could help explain and solve some issues with reproducibility that has previously been a problem in our group.

The implementation of this method enabled us to conduct a study in collaboration with Daniel Sandbeck and Serhiy Cherevko at the Helmholtz-Institute Erlangen-Nürnberg for Renewable Energy. This involved the coverage effect of Pt dissolution in the scope of polymer electrolyte membrane fuel cells and led to paper IV[29] with the spin-off paper III[30] elucidating the size effect of these mass-selected Pt nanoparticles in the same topic.

Since my major contribution to the papers was through the development of the method, I choose to focus only on presenting the method and

investigate how much you can push it. The scientific results are kept to the individual papers and are appended to the end of the thesis. It is my belief, that the implementation of this method at the setup will improve the quality of its output.

The chapter is divided into four main sections: the first section motivates the implementation of the method by showing some examples of bad depositions. The second section describes how the method is implemented, while the third section deals with how the method is properly used. The chapter concludes with a brief summary.

3.1 Background

Figure 3.1 shows (a) an image pieced together from individual SEM images of a standard 5 mm glassy carbon stub on which Niklas Secher and I deposited 6 nm Pt nanoparticles for a projected coverage of 20 %. Trusting in the Z-contrast between heavy Pt nanoparticles and the light carbon substrate, we immediately attributed the very bright region the bottom right corner to a higher local coverage of nanoparticles. This was confirmed by "walking the SEM" across this bright region from one side of the sample to the other in a series of images. The collected string of images are pieced together in (b). This indeed showed that the darker regions of the sample did have 6 nm Pt particles distributed across the surface, but in a much lower scale than in the bright regions. Although, in principle, this could be caused by an unintentional configuration of electrostatic potentials (misaligned lenses, proximity of a grounded object..) resulting in a focusing effect on the beam of nanoparticles, it is very clear that the effect is a direct consequence of an (intentionally) over-focused beam. Since both beam and substrate is kept stationary during deposition, the local coverage will be directly proportional to the local intensity of the beam. Hence, what we see with the SEM is a projection of the mass-selected beam profile (intensity distribution orthogonal to its axis of travel). If there had been a sharp cutoff with no nanoparticles detected in the dark regions, the issue might have been a misalignment of the sample. The "mouse bites" on the bottom

and right edge of the bright spot, on the other hand, are because of some local field effects on the edge of the particle beam - probably rough edges on the aperture in front of the sample. This possibility of over-focusing the beam obviously poses a problem if you intend to investigate whether or not the distance between particles has an effect on their catalytic properties or stability. Even disregarding the intentional study, ensuring a homogeneous projected coverage of nanoparticles across individual samples minimizes any activity/stability variations stemming from a coverage effect that might translate into larger than necessary standard errors and reproducibility issues. Tuning is done on a daily basis as needed in order to maximize the beam current to reduce the deposition time. In the beginning of my studies, it was common to get around 5 pA of nanoparticles through a 4.5 mm aperture in front of a substrate. For 5 nm particles, this corresponds roughly to 20 minutes to cover 5 % of a 5 mm stub for a rotating disc electrode. This is not a long time, but would require pushing the limits of the Einzel lens in front of the sample. The advice was to leave the lenses close to beam potential for a defocused beam, but even in this case the beam variation is unknown and, especially for new operators, the degree to which you focus the beam too much is an unknown parameter that weighs against the prospect of creating a model system. The cluster source was also not properly aligned with the substrate in the deposition chamber, meaning that a well-focused beam was pointing somewhere off to the corner of the 9 mm aperture. Rather than try to physically reposition Omicron or the cluster source, we installed an XY-translator between the preparation chamber and aperture flag. By aligning the aperture flag after the maximum flux of nanoparticles through the aperture, it was possible to get up to 30 to 40 pA current of nanoparticles (well-focused) through the aperture out of 50 pA total current.

To ensure homogeneity by rastering, two options were possible: raster the beam of nanoparticles in front of the aperture, or raster the sample behind the aperture. The first option would require fitting an extra electrostatic lens between the Einzel lens and the sample and acquiring four high voltage channels than can perturb the individual lens elements rapidly. Seeing that the combined geometry of Einzel lens, preparation chamber and aperture flag made it difficult to fit in an extra lens, we went with the second simpler

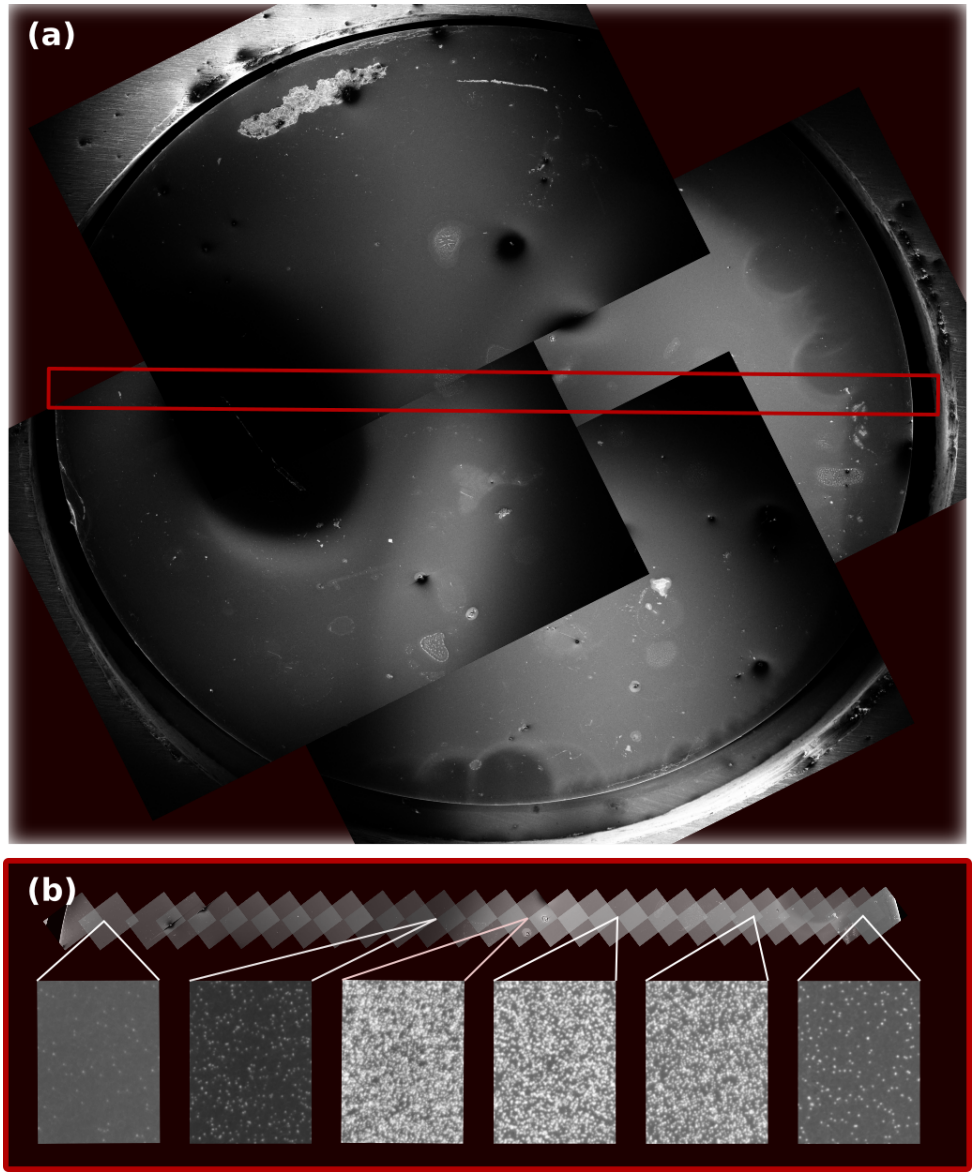

Figure 3.1: A Frankenstein SEM mosaic of a 5 mm glassy carbon stub with 20 % projected coverage of 6 nm Pt nanoparticles. The red box in (a) indicates the line traversed to get the close-ups in (b). An inhomogeneous beam profile clearly skews the local projected coverage on the sample.

option of rastering the sample.

3.2 Implementation

Rastering of depositions at Omicron cluster source was implemented by fitting two VEXTA ASX66A stepper motors from Oriental Motors to the Z- and Y-axis linear drives (orthogonal to the beam of nanoparticles) for computer controlled motion. The computer control is managed by a Raspberry Pi, and a standard keypad and small display secured to a piece of plexiglass constitutes a user interface that can be placed by the viewport most convenient for manipulating the sample. Figure 3.2 shows the user interface for easy control of the motors. The display is divided into three regions: the top region always displays the coordinates of the two motors, while the bottom region is dedicated to special short messages and for accepting custom user input. The larger middle region is the main part of the screen and has three levels the user can navigate between. The controller starts up with the screen in the lowest level: the splash screen (a) where a few brief help messages are displayed. The second level (b) is the main menu where the user can choose which type of program to run: 1 - incremental mode; 2 - absolute mode (c); 3 - change speed; 9 - raster programs (d). This group of subroutines is the highest level. Navigation proceeds via the controls displayed in (e). NumLock (red) is the most important button: it serves as panic button to abort any motion that may have been started accidentally - the only alternative panic reaction to pushing this button is pulling the power plug for the motors. When the NumLock LED is deactivated, the controller disregards input from the keypad until NumLock is reactivated. User input can be classified as "general input mode" and "custom input mode". The latter is only used when the user is prompted to type a given value. In this case, any number can be written with the numbered keys and decimal/Del to add a decimal point. Backspace (purple) deletes the most recent character, and the input is submitted with Enter (blue). Submitting an empty input returns the controller to the previous menu. In general input mode, the star (pink) will always send the controller to the main menu, while backspace (purple)

Figure 3.2: User interface for controlling ZY-axis motion of the preparation chamber manipulator using the two stepper motors implemented for rastering. Four main graphical user interfaces feed information back to the user: (a) start-up/splash screen, (b) main menu, (c) motor control - absolute mode, and (d) raster program menu. A keypad (e) feeds user input back to the controller. NumLock (red) is the panic button to abort any unwanted motion as an alternative to pulling the power plug. When the NumLock LED is off, the keypad is also locked to prevent accidental inputs. Remaining highlighted keys are explained in the main text.

always sends the controller back one level. The only command from the splash screen apart from going to the main menu is by pressing the slash key (white), which prompts the user for special codes (see *calibrating position* below). In the main menu, pressing a numbered key corresponding to a subroutine will go there. In *Incremental mode*, the motor is moved in increments defined by the displayed value. The arrow keys (green) are used to choose a digit and increment its value. ± (orange) sets the direction, slash (white) toggles the selection between the Y or Z motor. Motion is started by Enter (blue). In *Absolute mode*, the selected motor is moved to the coordinate corresponding to the displayed value. Motors in this mode are controlled similarly to the incremental mode except that, here, ±

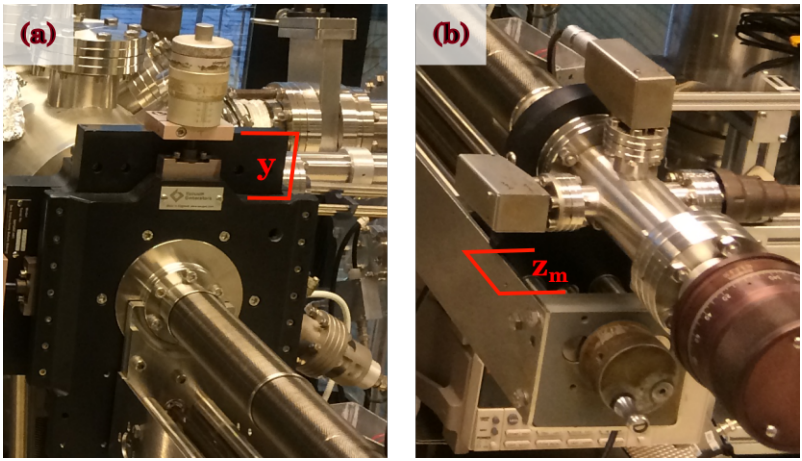

Figure 3.3: Illustration of the distances measured for calibration of motor position. (a) the position y of the Y motor, is defined as the distance in mm between the two upward pointing faces of the XY sliders. (b) The position z of the Z motor can be measured as $z = 340\,\text{mm} - z_m$ where z_m is the gap indicated on the image measured in mm. Images show the manual knobs from before the motors were attached.

(orange) prompts the user to type a coordinate to display on the screen. Hitting Enter again will send the controller to that coordinate. In *Change speed* mode, the current speed settings of each motor are displayed in unit mm/s. By hitting Enter, the user will be prompted to change these. The last mode, *Raster programs*, allows the user to choose from a list of raster programs using the arrow keys and Enter. The chosen raster pattern will keep repeating itself until the user aborts by pressing NumLock.

3.2.1 Calibrating the motor positions

The motors are not connected to physical contact switches that define hard movement limits. Instead, the physical limits of the motors are hardcoded into the Python controller. The Z motor can move between 25 mm and 325 mm with the coordinate axis defined by the ruler that is permanently mounted on the side of Z-motion bellow support. The Y motor can move

between 46.5 mm and 65.0 mm with the coordinate axis defined by the vertical distance between the top surfaces of the two sliders in the XY-axis drive. User inputs outside of these ranges are denied. To ensure that the motors are mounted by qualified personnel, the controller starts up with initial position coordinates for $ZY = (-9999.000, -9999.000)$ which ensures that the controller program crashes if one of the motor movement routines are activated without the position being calibrated first. To calibrate the position: go to the splash screen and type "/" to be prompted for a special command. Then type the very secret command "123" and hit Enter. The user will now be prompted for the coordinates of each motor and be set accordingly. To measure the Z motor position, use a caliper to measure the distance, z_m, of the gap between the block that moves about the threaded movement rod and the end piece where the motor is attached (see figure 3.3b). The position is then $z = (340 - z_m)$ mm. If the motor is initialized at a coordinate below 300 mm, using the caliper is impractical. Instead, read a rough value off the ruler for calibration, then move the motor to 320 mm and recalibrate using the caliper. The Y motor is calibrated using a caliper to measure the height that defines the coordinate axis (see figure 3.3a). The Y calibration is prone to vary with ± 0.5 mm, but the most important part for accuracy is when aligning the sample for deposition, and this is done by eye for the Y coordinate anyway.

3.2.2 Defining raster patterns

The raster pattern that was used to produce homogeneous samples for paper III and IV is shown in figure 3.4 as an example of how they are designed. Lines beginning with # are ignored and can be used to insert useful comments in the document. The section following `<<<DATA>>>` sets the relevant parameters for the raster script: `step_size` defines the scale for the raster pattern [unit in mm]; `speed` defines how fast [mm/s] the sample should be moved during rastering. The section between `<<<PATTERN>>>` and `<<<END>>>` defines the raster pattern using the scale set above. The pattern is created by a set of individual sample movement commands indicated by the colon-separated syntax (one command per line): `<axis>:<sign><distance>`. If the pattern is to be offset from the sample

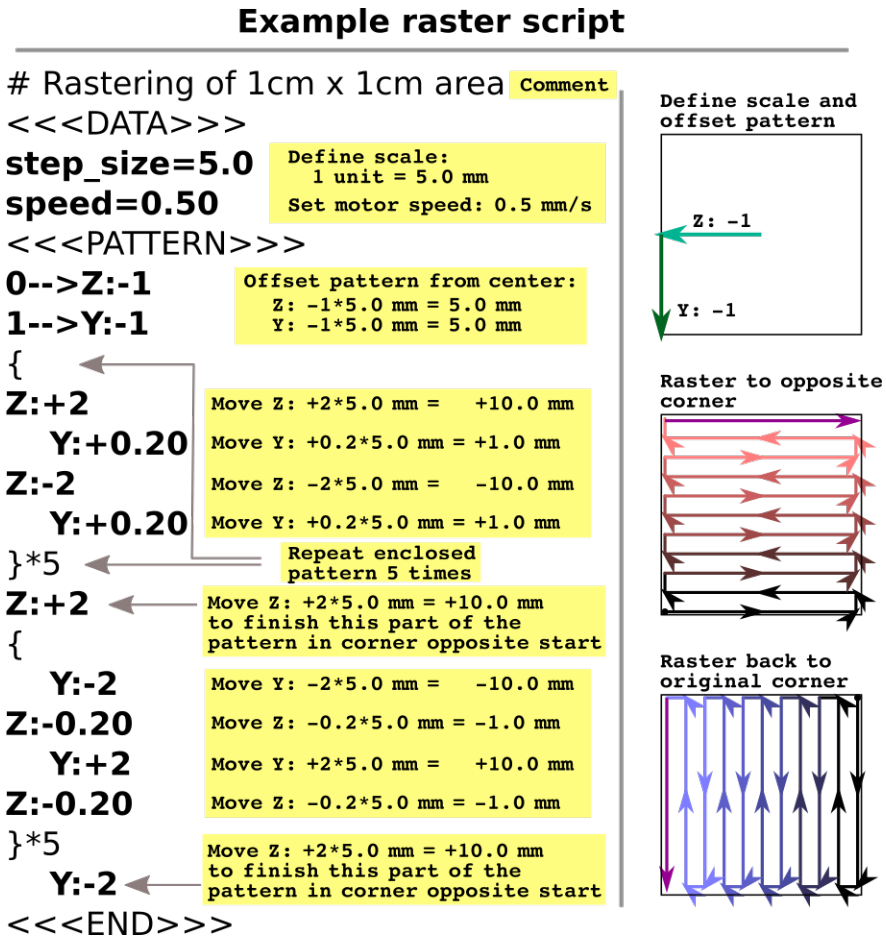

Figure 3.4: Example of a raster script. The pattern contains three sections: a header for comments, a configuration section, and a section for describing the repeating pattern including an offset from start position. The pattern shown here was used to produce homogeneous samples for paper III and IV.

start point, this is done first by indicating a numbered arrow followed by a movement command like `0-->Z:-1`, which would start by moving the sample $(-1) \cdot$ `<step_size>` mm along the Z-axis. In the shown script, the sample is moved to the bottom left corner from where the repeating pattern is defined. A subpattern can be repeated a number of times by enclosing it in brackets and doing a multiplication. Aligning the two axes to different columns is not necessary, but it improves the human readability of the code. There must only be one command per line for the interpreter to read it, but surrounding whitespace is ignored. These rules can be combined to create a raster pattern to suit a specific need. The speed can not be varied during the rastering, and the two motors can not move at the same time. The latter would require some careful thinking on the synchronization of commands to/from the motors. If this is implemented at a later time, be aware that currently a single power supply is shared between the two motors, but it is only dimensioned to sustain one running motor at a time.

3.3 Estimating the projected coverage

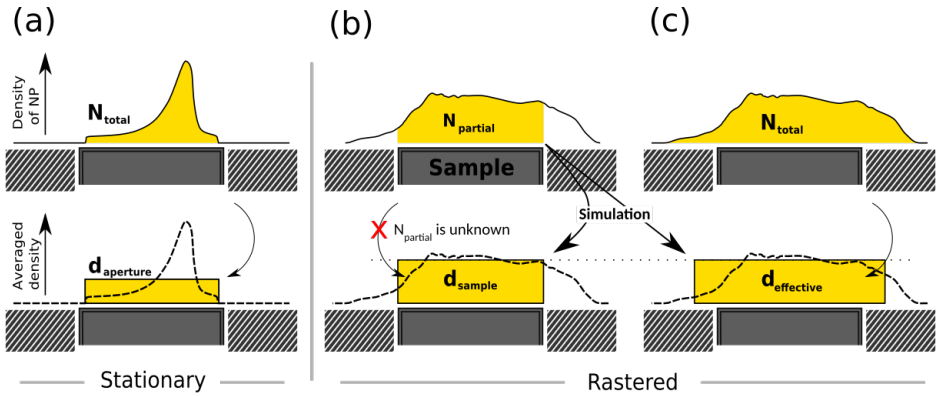

Figure 3.5: Conceptual illustration of how the projected coverage of nanoparticles is estimated. In the stationary case (a), it the calculation is straightforward. The rastered case (b) and (c) relies on assumptions which to some degree can be simulated.

This section deals with the implications of rastering the sample behind the aperture: how can we get a good estimate of the coverage, and when is a raster pattern designed well?

Figure 3.5 compares the conventional coverage calculation in (a) for a sample that is stationary behind the aperture during deposition to the rastered case in (b) and (c). For the stationary case, we know that all the measured current is being deposited on the sample surface through a well-defined aperture slightly smaller than the sample. If the nanoparticle size is known, it is straightforward to calculate an average coverage across the deposition area. While the local coverage may vary a lot depending on the profile of the nanoparticle beam, the average coverage in terms of total mass loading and total catalyst surface area is accurate (neglecting substrate-catalyst interactions and overlapping nanoparticles). For the situation in figure 3.5a, equation (2.13) translates to

$$\theta_{NP}^{nominal} = N_{total}\frac{A_{NP}}{A_{aperture}} = N_{total}\frac{d_{NP}^2}{d_{aperture}^2} \tag{3.1}$$

which I call the *nominal coverage* when discussing rastering. $d_{aperture}$ is the diameter of the aperture. When the samples are rastered, some of the nanoparticles will be deposited on the sampleholder instead of the substrate, and the average coverage on the sample should be calculated by

$$\theta_{NP}^{sample} = N_{partial}\frac{A_{NP}}{A_{sample}} = N_{partial}\frac{d_{NP}^2}{d_{sample}^2} \tag{3.2}$$

However, since we can only measure the total current, we cannot immediately calculate the average coverage across the sample surface since this requires knowledge of the fraction of nanoparticles landing on the sample as illustrated in figure 3.5b. We know with certainty the maximum deposition area from the programmed raster path and the size of the aperture, but averaging the total number of nanoparticles to this area will by far underestimate the actual coverage on the sample. For our initial rastered depositions, I roughly simulated how the coverage distribution across the sampleholder would look like assuming some beam profile. As expected, there was a region in the middle of the raster pattern where the

coverage is more constant and then it falls off to zero at the far edges of the pattern. An area was roughly estimated somewhere between the edge of the constant coverage region and the edge of the zero coverage region which was used as an effective area in order to reproduce the average coverage across the sample surface by using the total number of deposited nanoparticles as illustrated in figure 3.5c. Since then, I have improved the simulation method in order to provide more details on the effects of rastering including the direct correlation between the partial number of nanoparticles on the sample and the effective area needed to correctly calculate the average coverage. If a raster pattern is used to scan the sample wide in very small increments, there will be a region in the middle where the coverage is independent of the beam profile. If this area is larger than the region of interest (the sample), then, for this raster pattern, the total number of particles landing on the region of interest will be a constant fraction of the total number of particles deposited through the aperture. This allows us via the simulation to calculate the coverage by equation (3.2) as in figure 3.5b.

With this information, it is now possible to calculate an effective deposition area that produces the same coverage when calculated from the total number of deposited particles

$$\theta_{NP,rastered}^{sample} = N_{partial}\frac{A_{NP}}{A_{sample}} = N_{total}\frac{A_{NP}}{A_{effective}} \tag{3.3}$$

or

$$A_{effective} = \frac{N_{total}}{N_{partial}}A_{sample} \tag{3.4}$$

where A_{sample} is the region of interest containing $N_{partial}$ number of nanoparticles. The tool we use to automatically integrate the deposition current and simultaneously convert it to an average coverage requires that the user provides information about the diameter of both particles and the aperture used. It is therefore useful to describe the effective deposition area as the diameter of the corresponding circular area:

$$A_{effective} = \pi\frac{d_{effective}^2}{4} \tag{3.5}$$

which for circular samples reduces to

$$d_{effective} = \sqrt{\frac{N_{total}}{N_{partial}}} \cdot d_{sample} \tag{3.6}$$

This has a more versatile form when expressed in terms of coverage via equations (3.1) and (3.2)

$$A_{effective} = \frac{N_{total}}{N_{partial}} \cdot A_{sample} = \frac{\theta_{NP}^{nom} \cdot \frac{A_{aperture}}{A_{NP}}}{\theta_{NP}^{sample} \cdot \frac{A_{sample}}{A_{NP}}} \cdot A_{sample} \tag{3.7}$$

which can be freely converted to

$$d_{effective} = \sqrt{\frac{\theta_{NP}^{nom}}{\theta_{NP}^{sample}}} \cdot d_{aperture} \tag{3.8}$$

The effective diameter (of the aperture), $d_{effective}$, can thereby be supplied to the automatic integration tool instead of the aperture diameter to directly calculate the sample coverage for your raster pattern as in figure 3.5c.

3.3.1 Assessing a raster pattern

The simulation script serves two purposes: to help design new raster patterns that produce homogeneous coverages in a specific region, and to extract relevant descriptive parameters for an existing design. The boundary between the two purposes is most clear when the simulation is run after a deposition using it to create a coverage map - especially if extra information about the beam profile is available. The accuracy of the simulation depends entirely on the assumption of the beam profile shape. Therefore the criteria for a well designed raster pattern is that it gives consistent coverage results independent of which beam profile you assume. In the following, I will use two different raster patterns to show how the simulation works and how to interpret the results.

The raster patterns are simulated by stretching a grid between -10 mm to +10 mm (a 500x500 grid produces cells roughly 0.05 mm of length). A

hypothetical beam profile is then calculated and scanned along the path of the raster pattern until one full lap has been completed. The resulting intensity map is then scaled to show the local coverage given inputs on how many particles were deposited in total and the size per particle as per equation (2.9). Intensity maps for the raster pattern in figure 3.4 is shown in figure 3.6 (**Raster 1**) for three different assumed beam profiles visualized in the upper section of figure 3.6. The coverage maps for a given raster pattern is aligned underneath the beam profile that was used to produce it. The beam profiles are made by one or two added gaussian distributions cut off by the aperture. They are described as:

1 **Even:** A beam profile which is considered the best case scenario for stationary depositions where the beam is as defocused as possible to give a somewhat even distribution of particles across the sample.

2 **Off-center:** This is considered a reasonable worst-case scenario of a beam profile inspired by figure 3.1. It is not unreasonable to expect that lenses are tuned aggressively to produce a beam with this focus, but fairly simple measures can be taken to check that the beam is not this misaligned before starting deposition.

3 **Spot:** An extreme case where the beam has been focused to a point only about 0.5 mm wide. To my knowledge, something like this has only been achieved when depositing single atoms and maximizing the focusing potential of the Einzel lens. Even so, this profile is considered an extreme case that is easy to prevent from happening without sacrificing much particle current.

Raster 1 was designed to produce a more homogeneous coverage across a 1x1 cm^2 glassy carbon square. The simulated coverage maps are quantified by considering three different centered regions of the samples as drawn with black lines in figure 3.6: a circular area 5 mm in diameter (solid line) and two squares with side length 8 mm (dash-dotted line) and 10 mm (dotted line). Within these regions, the quantified parameters are the average coverage along with the spread, $\mu \pm 2\sigma$, the maximum and minimum coverage, and the effective aperture diameter, d_{ap}^{eff} [mm], needed to

Table 3.1: Simulation results based on different scenarios for two raster patterns. **Raster 1** is the pattern shown in figure 3.4 and used for the platinum dissolution stories[29,30]. **Raster 2** is the pattern designed for rotating disc electrode stubs used for rastered samples in paper VII and VIII. Coverage numbers are calculated using a total of 5.1095 pmol nanoparticles with diameter 6 nm.

	Beam profile:		Even	Off-center	Spot
Stationary	Area	Param.			
	4.5 mm ◯	$\mu \pm 2\sigma$	71.995 ± 4.208	71.995 ± 119.59	71.995 ± 757.83
		max/min	75.7 / 68.4	365.2 / 30.9	4131.7 / 0.0
		d_{ap}^{eff}	4.500	4.500	4.500
Raster 1	5 mm ◯	$\mu \pm 2\sigma$	72.538 ± 3.394	72.550 ± 3.564	73.526 ± 60.291
		max/min	76.1 / 69.2	76.5 / 66.6	136.2 / 15.9
		d_{ap}^{eff}	12.357	12.356	12.274
	8 mm ■	$\mu \pm 2\sigma$	71.926 ± 5.367	71.926 ± 7.284	72.550 ± 60.527
		max/min	79.2 / 56.7	85.1 / 40.2	136.2 / 15.9
		d_{ap}^{eff}	12.410	12.410	12.356
	10 mm ■	$\mu \pm 2\sigma$	65.520 ± 19.545	64.531 ± 25.660	72.215 ± 64.880
		max/min	79.2 / 28.7	85.1 / 16.1	177.1 / 15.9
		d_{ap}^{eff}	13.002	13.101	13.136
Raster 2	5 mm ◯	$\mu \pm 2\sigma$	121.816 ± 2.830	121.873 ± 3.216	122.108 ± 4.110
		max/min	124.1 / 114.9	125.6 / 110.4	131.3 / 119.9
		d_{ap}^{eff}	9.536	9.534	9.524
	8 mm ■	$\mu \pm 2\sigma$	100.502 ± 42.150	98.489 ± 52.442	122.977 ± 8.509
		max/min	125.0 / 38.0	126.7 / 21.3	152.3 / 61.2
		d_{ap}^{eff}	10.498	10.605	9.491
	10 mm ■	$\mu \pm 2\sigma$	80.082 ± 66.067	79.235 ± 72.216	86.651 ± 105.05
		max/min	125.0 / 7.8	126.7 / 4.3	152.3 / 0
		d_{ap}^{eff}	11.761	11.824	11.306

reproduce the average coverage using the total particle current. In order to show the effects of varying the raster pattern, the pattern designed to produce homogeneous coverage samples for paper VII and VIII is shown for comparison with the same total number of deposited particles. The quantified results are shown in table 3.1.

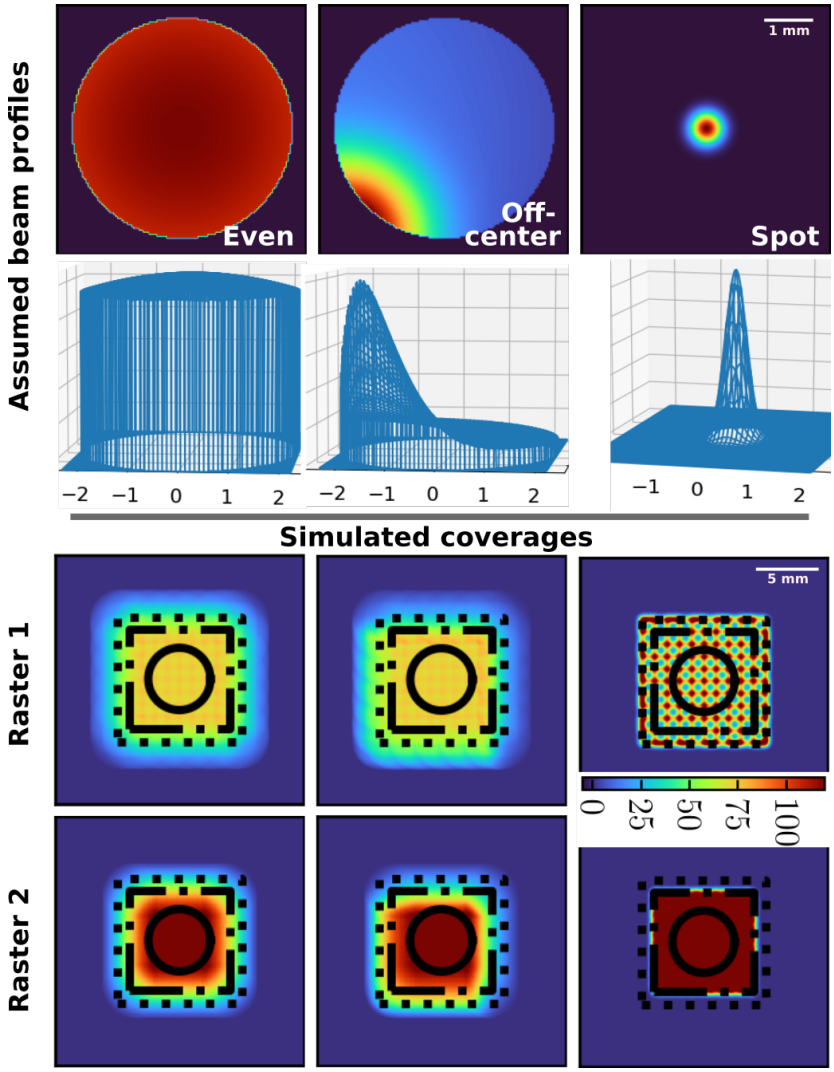

Figure 3.6: Simulated intensity or coverage maps for two raster patterns using three different beam profiles arbitrarily chosen to represent a best case scenario (even) along with a realistic worst-case scenario (off-center) and an extreme worst-case scenario (spot). The upper half shows the shape of the beam profiles – the color map is scaled to the minimum and maximum value in each case. For the simulated raster patterns, the color bar indicates local coverage (%) and is shared between all six different cases.

Stationary deposition reference

The first section in table 3.1 is to show the need for rastering in the same quantified manner that is used to assess the validity of designed raster patterns. The area of interest is fixed by the aperture: a disc of 4.5 mm diameter. The color mapping for the beam profiles in figure 3.6 is scaled individually for each type, while the intensity maps for the two raster patterns share a common color map.

Looking at the results, all beam profiles produce an average coverage of 72 %, but the spread is huge and depends entirely on the beam profile. The "best case scenario" has local coverage varying between 68 % and 76 %. The extreme scenario has all the particles localized in the center region with a peak coverage of 4132 %, but zero coverage on most of the area of interest. The worst case scenario is somewhere in between the two. It should be clear from the results and figures that rastering is needed if well-dispersed samples are needed. Alternatively, the only option to ensure this is to hope you get a very defocused beam profile and then to verify it after the deposition with SEM or XPS/AES mappings. Also, while the even beam profile will provide a reasonable coverage distribution through the 4.5 mm aperture, maintaining the quality while depositing on larger areas will be nearly impossible.

Comparing patterns with different beam profiles

Considering the 5 mm area for raster pattern 1, near-identical results are produced from the two realistic beam profiles with a mean coverage of roughly 72.5 % with a spread of 3.4 - 3.6 % coverage. For the more extreme spot beam profile, however, the results deviate yielding close to the same mean coverage (73.5 %), but with peak coverage of 136 % and areas with as low as 16 % coverage. This is evident by the grid-like coverage map in figure 3.6 which occurs because the width of the beam is much smaller than the raster increments used to advance across the sample. For comparison, raster pattern 2 handles this case much better because of its smaller steps during rastering. The same grid shape is still discernible for the two first

beam profiles, but here the beams are wide enough that the rastering acts to smooth out the signal. When we consider the 8 mm area, we get a slightly lower mean value of 72 % coverage, but the spread starts to increase because we now include part of the outer region where the local coverage starts sloping from the homogeneous coverage region towards zero. For the larger 10 mm area, we now include significantly more of the inhomogeneous boundary, and the simulated mean coverage now takes a significant dip showing a mean coverage of 65 %, which is not representative of the more homogeneous coverage on the larger part of the sample. Despite the large variations in coverage for the more extreme spot beam profile, it is still a huge improvement over the unrastered case.

To pick a number from here, it depends on the usage of the sample. Whichever effective aperture is chosen to guide the deposition, the integrated deposition current can be fed back into the simulation script to produce a map of that specific sample. If an activity measurement would involve the entire surface, then the $65\,\% \pm 22\,\%$ coverage is the right number to use in order to normalize to the total mass loading. In the case of the samples for paper III and IV, Daniel Sandbeck would probe 1 mm areas a couple different locations on the sample with a SFC-ICP-MS flow cell.[31,32] As long as he doesn't measure near the edges, we can claim a representative mean coverage of $72.5\,\% \pm 4\,\%$. While we didn't have these numbers at the time, we did know from rough simulations, that the calculated coverage wouldn't be true near the edges, and Daniel Sandbeck was instructed that he should stay away from the edges when measuring. The deposition providing data for table 3.1 and the simulations in figure 3.6 was mapped with XPS by Niklas Secher, Daniel Sandbeck and Florian Speck using the facilities in Erlangen. The result is shown in figure 3.7 which is adapted from the supporting information of paper IV[29]. The left part shows a representative survey spectrum showing the presence of platinum, oxygen and carbon. Using the Pt 4f peaks of the survey scans, the atomic content of platinum relative to carbon and oxygen is shown for different locations on the sample (right side of figure). From this we roughly get a mean atomic concentration of $29 \pm 1\,\%$ Pt which indicates that the raster pattern serves its purpose and produces a largely homogeneous coverage across the surface. Bear in mind, that the uncertainty on the XPS quantification is

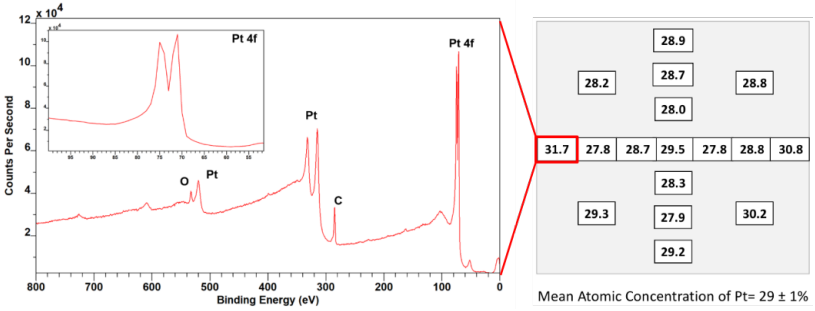

Figure 3.7: Representative XPS spectrum used to map out the Pt content across the 10 mm glassy carbon substrate for 70 % 6 nm Pt nanoparticles. Adapted from Figure S8 and S9 from paper IV.[29]

somewhat larger than usual since only rough survey scans were performed in the interest of time. The Pt atomic concentration relative to target coverage, however, shows a linear trend for samples with low coverage and only starts to deviate around 50 % coverage when the fraction of overlapping nanoparticles begins to dominate.[29] The second raster pattern was developed specifically to ensure a good dispersion of nanoparticles on 5 mm rotating disc electrode stubs (for paper VII and VIII). It therefore employs a much tighter raster pattern than the first one. As is clear from table 3.1 and figure 3.6, this ensures a more homogeneous coverage while requiring a smaller total amount of nanoparticles to finish. The model is only valid inside the centered 5 mm disk area, but will produce high quality results across virtually all possible (realistic) beam profiles. For this pattern, I will onwards be using $d_{ap}^{eff} = 9.535$ mm which for the numbers used in table 3.1 corresponds to a mean coverage of 121.837 % with extreme case uncertainty ±0.3 % coverage with respect to the total mass loading. Local variations are within ±3.0 % coverage (per 121.8 % mean coverage).

3.3.2 Final remarks

I chose to use absolute values in table 3.1 based on the data for the sample used in figure 3.7 in order not to hide any dependencies on assumed beam

profile. It is important to note that for a certain combination of raster pattern and beam profile, the results presented in table 3.1 are intrinsic properties that scale with the total loading. For example, raster pattern 2 when used with effective aperture diameter 9.534 mm according to the off-center beam profile and calculating 5.0 % average coverage from the total amount of deposited nanoparticles, would yield an absolute local variation in coverage equal to

$$2\sigma = \frac{2\sigma_{ref}}{\mu_{ref}} \cdot \mu_{measured} = \frac{3.216}{121.873} \cdot 5.0 = 0.13 \tag{3.9}$$

This is about three times the uncertainty involved in the integration of deposition current under ideal deposition conditions and with parameters visually checked by the user. The uncertainty in total nanoparticle current will usually be dominated by non-ideal circumstances induced by the user during deposition. Creating an ensemble of samples with the same degree of homogeneity is also difficult since the end of the deposition has to be timed with the end of a raster cycle in order for the simulation to be valid. A typical ensemble of samples might be represented by a mean coverage of $5.0\,\% \pm 0.3\,\%$ where not too much effort is put into reaching the target coverage exactly. On a final note, the present version of the simulation has a hardcoded 100 ms step where it waits at the end points every time it changes direction. This was to simulate the communication delay which was significant in the initial version. Recently, I timed the cycles of **Raster 2** versus different motor speeds expecting to see a discrepancy between the expected time to traverse a leg in the raster pattern and the measured time. The results in figure 3.8 surprised me, however. The communication delay is about 25 to 35 ms and is limited by the baud rate of 9600. This delay can fairly easily be reduced by increasing the baud rate. Figure 3.8, however, shows that there is an almost 500 ms discrepancy at normal speeds for the small legs (0.4 mm) of the raster pattern. At these small increments, the elapsed time is dominated by the ramp from 0 mm/s up to X mm/s. This is currently the dominating uncertainty in the simulations as the effect of this is to deposit more nanoparticles along the edges of the pattern. It is somewhat balanced by the hardcoded 100 ms, but the uncertainty in the effective aperture should be estimated by varying this holding step instead

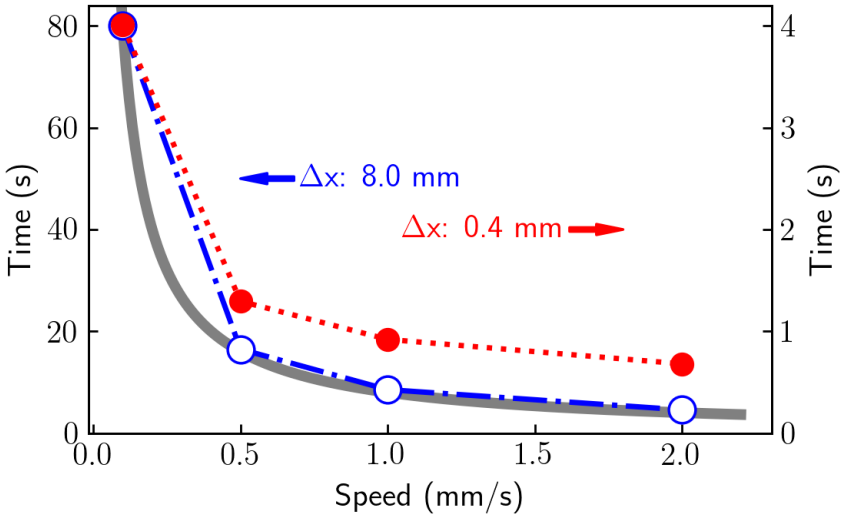

Figure 3.8: Times measured for a motor to travel a long distance (8 mm) and a short distance (0.4 mm) for different speeds. The grey line indicates the expected time if the motors assume steady state motion instantaneously and there are no delays. For short distances, the movement is significantly slower than expected.

of varying the assumed beam profiles. The methodology presented in figure 3.6 and table 3.1 is thereby still valid. The next step would be to increase the baud rate and optimize the velocity ramps and incorporate this motion in the simulation if it still dominates the travel time.

3.4 Summary and outlook

The method of preparing electrodes for supporting mass-selected nanoparticles was improved by introducing rastering of samples during deposition in order to smear out any irregularities of the nanoparticle beam profile across the surface. The implementation was done by attaching two computer controlled stepper motors to the two axes perpendicular to the

particle beam. It is equipped with a simple user interface so as to make the daily handling of samples easier while allowing raster control of samples.

A simulation tool to map the local coverage produced by raster patterns under assumption of various beam profiles was developed. This tool aids in the design of good raster patterns as well as providing a way of quantifying the variations in coverage within the scope of the simulation. It outputs a parameter, d_{ap}^{eff}, which interfaces directly with an existing tool which automatically integrates the deposition current and converts it into an average coverage, thereby allowing users to more easily aim for the desired coverage.

Rastering is shown to be a critical new method if one wants to reduce the worry over the local coverage of mass-selected particles on the substrate surface. The simulation tool proves critical in understanding the validity of a raster pattern and the parameters that can be drawn from it. In order for the simulation to be valid, certain criteria must be met. These include: 1) starting or ending a deposition should only be done in the small space between different raster cycles. This includes changing the intensity of the beam of nanoparticles. 2) one has to know what part of the sample surface is important with regards to a homogeneous coverage and then make sure that the raster pattern gives consistent results in this region regardless of the beam profile fed into the simulation.

The development of this method enabled us to identify a coverage effect of the dissolution of platinum nanoparticles,[29] and by extension, allowed us to find the mass-selected size dependence of the same phenomenon without convoluting the two effects[30]. The method developed here will be an important part of the daily routine at the setup.

Isotope Studies

Chapter 4

The isotope studies covered in this chapter has spawned from my curiosity about LEIS as a technique. When I started my PhD project, LEIS was mostly used for elemental composition of the sampe before and after deposition of nanoparticles as a supplement to XPS. While it is possible to do a lot of cool experiments with LEIS like quantification and angular orientation of adsorbed ligands[33], size sensitivity of nanoparticles[34,35], isotope distinction[36], and sintering effects[37], most of these require extensive calibration or specialized equipment. The ISE 100 ion gun and NanoSAM analyzer is at a fixed angle which sets some limitation on what is possible and I have been curious to see what kind of information can be extracted with this technique. Søren Scott and I discovered a good synergy between his EC-MS setup and LEIS where, in both cases, it is possible to distinguish between the two isotopes of oxygen, ^{16}O and ^{18}O.

In paper II, I took over synthesis and characterization of mass-selected Ni_3Fe nanoparticles when Bela Sebok finished his PhD. My major contribution, though, was designing the isotope experiments with Søren Scott while he did the EC-MS measurements and I prepared samples and oxygen isotope distinction with LEIS characterization before and after electrochemical experiments. In paper V and VI, we took the experiences from paper II and applied them to thin film catalysts of RuO_2 and IrO_2.

My main contributions are experiment design and LEIS characterization.

To me, the projects described in this chapter are characterized by the feeling of drowning in large amounts of data. Each sample investigated has multiple LEIS spectra at each stage in the experiment with each spectrum changing because of sputter effects or varying parameters slightly to optimize one aspect of the data. Keeping track of all these parameters and choosing a representative subset of comparable data has been a real challenge and the results are presented in the following sections. For paper V and VI, we have begun to develop some tools to help us organize and compare the data.

Both isotope studies concern the oxygen evolution reaction under different conditions: in either base or acid.

4.1 Water splitting

The splitting of water into hydrogen and oxygen is known as the oxygen evolution reaction (OER):

$$\mathrm{H_2O\,(liquid)} \underset{\mathrm{ORR}}{\overset{\mathrm{OER}}{\rightleftharpoons}} \mathrm{O_2\,(gas)} + 2\,\mathrm{H_2\,(gas)} \tag{4.1}$$

This reaction is electrocatalytic, i.e. it happens via the transfer of four electrons and protons as shown in figure 4.1 with the competing oxygen reduction reaction (ORR) being the natural (downhill) reaction without applied potential:

$$\mathrm{H_2O} \underset{\mathrm{ORR}}{\longleftarrow} \mathrm{O_2} + 4\,\mathrm{H^+} + 4\,e^- \tag{4.2}$$

$$2\,\mathrm{H^+} + 2\,e^- \underset{\mathrm{HOR}}{\overset{\mathrm{HER}}{\rightleftharpoons}} \mathrm{H_2} \tag{4.3}$$

When the two half-reactions are separated and a potential is applied between the two electrodes, it is possible to drive the electrons in the OER direction. The potential required to put the two end states in thermodynamic equilibrium is 1.23 V, while the potential required to make every step in the OER pathway downhill is calculated to be 1.60 V on

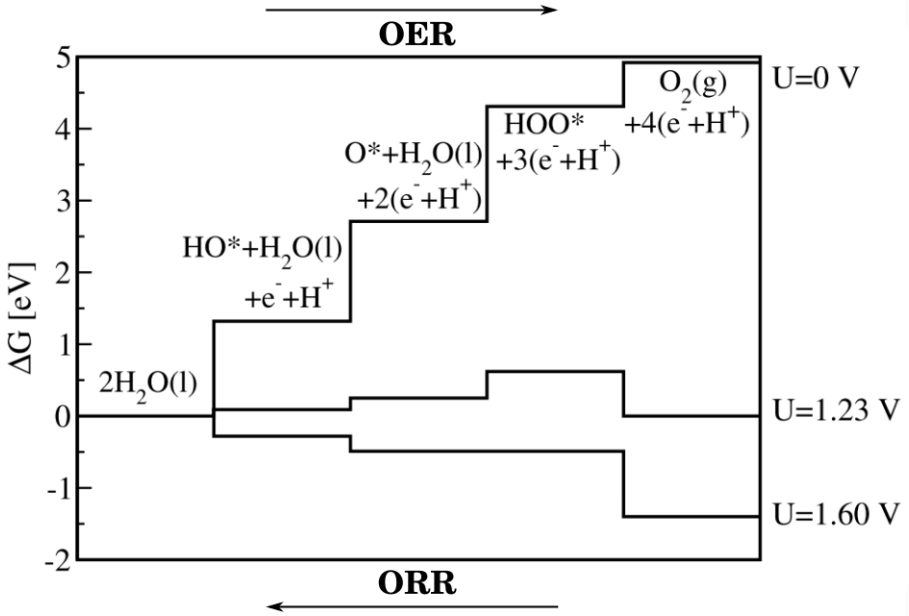

Figure 4.1: Free energy diagram for water splitting on RuO_2 for three different potentials. Adapted from [38]

RuO_2 [38]. The hydrogen evolution reaction (HER) is easily accomplished with Pt at very low overpotentials [39,40] that can meet the Terawatt challenge under realistic conditions [41] and is still active at ultralow Pt loadings [42].

OER and ORR require four electron and proton transfers where the individual steps scale equally with the reactivity of the catalyst towards oxygen. [43] Thus, optimizing the catalyst for one step in the OER pathway deoptimizes another step. To make all steps downhill in energy and thereby make the reaction run at an appreciable rate requires increasing the potential beyond the thermodynamic equilibrium which translates into losing energy. The problem is even worse when tapping into the energy stored in the chemical bonds by running the ORR reaction to combine hydrogen and oxygen into water when you have to pay the extra price again. OER is the main source of the combined cell overpotential. [44] To

make water splitting a more viable solution for energy storage, the overpotential therefore has to be lowered by finding better catalysts.[5] The field is split in two areas: alkaline electrolyzers, and acid polymer electrolyte membrane (PEM) electrolyzers.

4.2 $NiFeO_xH_y$ nanoparticles

$Ni(Fe)O_xH_y$ catalysts are some the most stable and active catalysts for alkaline OER.[45,46] Evidently, it is the intercalation of Fe impurities in NiO_xH_y-based electrodes that is responsible for the high activity.[45,47–50] The exact nature of the active site, however, is still not known. Some believe the nickel atoms to be active[51,52] while others suggest that the iron atoms are the active sites[53–56] or that it is both atoms[57]. But even conservative estimates of turnover frequencies (TOF) are made difficult by studies suggesting that even the bulk atoms in electrodeposited $NiFeO_xH_y$ films might be active[58–60] although this type of site does not extend to arbitrarily high loadings[61].

In this study, we report the activity of well-characterized mass-selected $NiFeO_xH_y$-based catalysts as measured by a rotating disc electrode (RDE) electrochemical setup in 1.0 M KOH, and the reactivity of the nanoparticles' oxygen atoms as measured by EC-MS and LEIS.

4.2.1 Stability and activity

A Ni_3Fe sputter target was used to deposit nanoparticles of mass-charge ratios 120,000 amu, 350,000 amu, 950,000 amu, and 2,000,000 amu at a loading corresponding to 15 % projected coverage on polycrystalline Au stubs that has been mechanically cleaned and annealed prior to deposition. The nanoparticles are deposited in a 4.5 mm circular area giving a mass loading of 50 - 125 ng (or 314 - 785 ng cm^{-2}) depending on the size of the particles. TEM characterization in figure 4.2 shows that the particles are roughly spherical with average characteristic diameters of 3.9 ± 0.5 nm, 5.4 ± 0.6 nm, 6.7 ± 0.5 nm, and 8.4 ± 0.5 nm, respectively. The TEM

analysis method is illustrated in figure C.1a-d and the width reported for the size distributions is the 2σ standard deviation. Based on figure C.1e, I would argue that the consistent standard deviations regardless of mass is an indicator of the resolution or uncertainty of the imaging method, and that the true size distribution is even better.

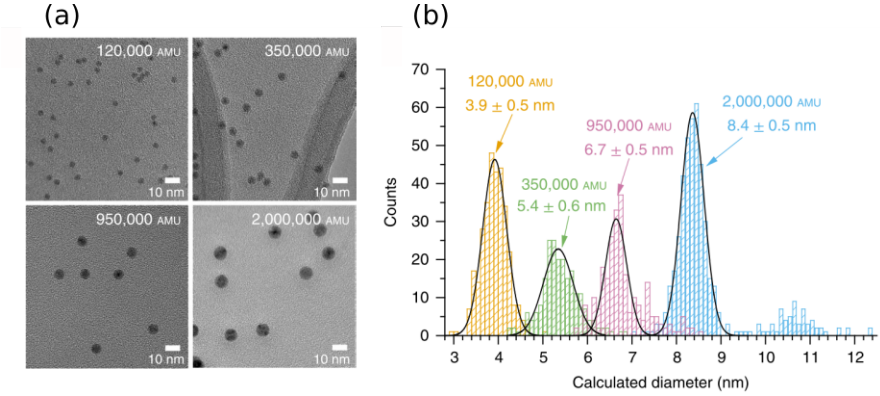

Figure 4.2: TEM characterization of Ni_3Fe nanoparticles mass-selected to 120k amu, 350k amu, 950k amu, and 2M amu. (a) representative TEM images showing spherical shapes regardless of mass, and (b) resulting size distribution from analysis of TEM images with gaussian averages and 2σ peak widths indicated.

XPS shows that the particles are fully metallic as deposited, but are oxidized after the OER treatment with the iron content dropping from 25 % before OER to about 15 % after OER (figure 4.3a-b). Identical-location SEM (figure 4.3c-d) and HRTEM (figure C.2a-b) show that the particles retain their spherical nature after OER and does not sinter, which speaks to the stability of the system. EDX line scan of the particles (figure C.2c-d) furthermore supports that iron leaches out of the particles during OER which was indicated by XPS. This shows, however, that the oxidation that was seen with XPS only penetrates a few nanometers into the surface.

Activity measurements were made in N_2-saturated 1.0 M KOH with RDE at 1600 rpm and is summarized in figure 4.4. The background activity of the gold substrates were measured for three independent samples treated in the same manner as the nanoparticle samples - except for the deposition itself.

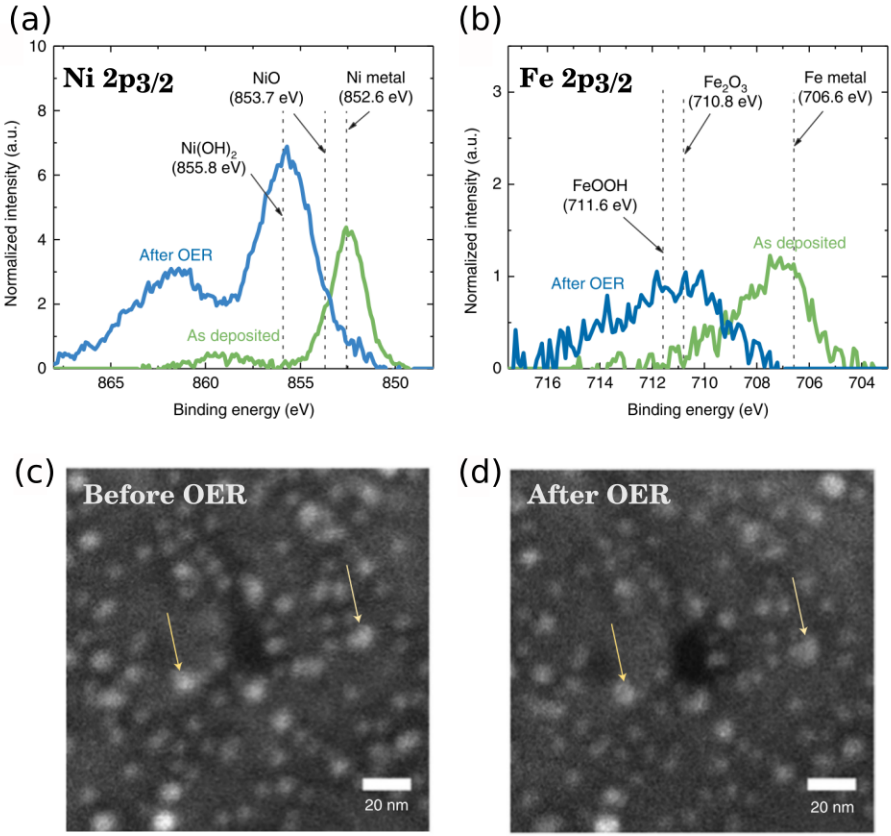

Figure 4.3: XPS Ni $2p_{3/2}$ (a) and Fe $2p_{3/2}$ (b) and identical-location SEM before (c) and after OER (d) of 6.7 nm particles. The arrows are a guide to the eye.

This activity is subtracted from the nanoparticle activity measurements. The measurements were started with five cyclic voltammograms (CVs) at $10\,\mathrm{mV\,s^{-1}}$ followed by 2 hours constant potential at $1.6\,\mathrm{V_{RHE}}$ and finished with a CV to assess the activity. Examples of the mass-normalized activity for each size is shown in figure 4.4a. The average mass-normalized activity of three independent samples per size is shown in figure 4.4b at three different overpotentials $\eta = 270\,\mathrm{mV}$, 300 mV, and 370 mV. The 3.9 nm and

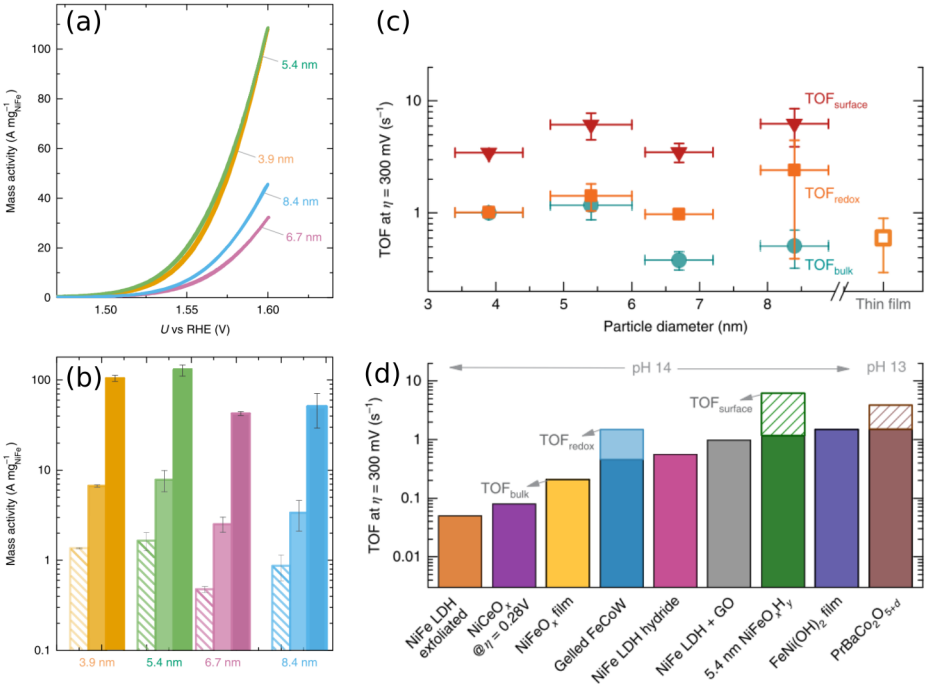

Figure 4.4: Comparison of OER activities. (a) mass-normalized potential sweep at $10\,\mathrm{mV\,s^{-1}}$ after 2 hrs chronoamperometry. (b) same type of data as in (a) represented as a bar plot at three select overpotentials, $\eta = 270\,\mathrm{mV}$ (hatched), $300\,\mathrm{mV}$ (light) and $370\,\mathrm{mV}$ (dark) averaged over three independent samples per size. (c) TOF at $300\,\mathrm{mV}$ overpotential assuming three different models for the active site: all deposited metal atoms are active ($\mathrm{TOF_{bulk}}$), only the outermost layer of metal atoms are active, ($\mathrm{TOF_{surface}}$), or all the $\mathrm{Ni^{2+}/Ni^{3+/4+}}$ redox-active atoms are active, ($\mathrm{TOF_{redox}}$). (d) TOF at $300\,\mathrm{mV}$ overpotential for state-of-the-art non-noble alkaline OER catalysts compared to the 5.4 nm nanoparticles from this study. Where possible, multiple models for the calculation of TOF are included. See paper II for references to the data in (d)[62].

5.4 nm nanoparticles are clearly the more active nanoparticles with respect to utilization of the catalyst. Figure 4.4c shows turnover frequencies at 300 mV overpotential calculated assuming that all the deposited metal atoms are active (TOF_{bulk}) for a worst-case estimate of the intrinsic activity of these particles. Figure 4.4d shows that our worst-case estimate for the 5.4 nm nanoparticles is comparable to or even better than the intrinsic activity of other state-of-the-art catalysts in the field at $1.2 \pm 0.3\,s^{-1}$. If we assume that only the surface metal atoms are active in the reaction, the turnover frequency, $TOF_{surface}$, is a factor five higher at $6.2 \pm 1.6\,s^{-1}$. A third estimate is given by the integral of the Ni reduction peak that is normally attributed to the $Ni^{2+}/Ni^{3+/4+}$ redox couple.[45] This is shown in figure 4.4c as TOF_{redox} and coincides with TOF_{bulk} for the 3.9 nm particles, but seems to follow the trend of $TOF_{surface}$ with increasing particle size.

To further test the stability of the particles beside the SEM analysis, about 100 ng 6.7 nm Ni_3Fe nanoparticles was deposited on a piece of gold foil that was treated similar to the gold stubs. This catalyst was then tested at constant 1.6 V_{RHE} giving a stable current for 1000 hours.[62] Characterization following this test was not done, but the very small amount of initial catalyst attests to the stability of these systems.

4.2.2 Lattice oxygen exchange

Assuming that activity leads to oxygen in the metal lattice exchanging with the reactants, isotope-labeled studies using ^{18}O coupled with operando mass spectrometry is a strong method to distinguish between bulk and surface catalysis.[63] This has been used previously to claim the involvement of lattice-oxygen for OER on Au[64], IrO_2/Ti[65], and Ru-based catalysts[63,66] among others. Some studies that did not indicate the involvement of lattice oxygen includes Pt[67] and oriented rutile RuO_2 thin films[68]. A nice table comparing these various studies has been compiled by Søren Scott.[69]

A study by Shao-Horn and co-workers suggest that lattice oxygen exchange happens on materials that show a pH dependence on the activity.[70] Since $Ni(Fe)O_xH_y$ catalysts shows a higher catalytic activity at higher pH[71], they would be expected to show the involvement of lattice oxygen.

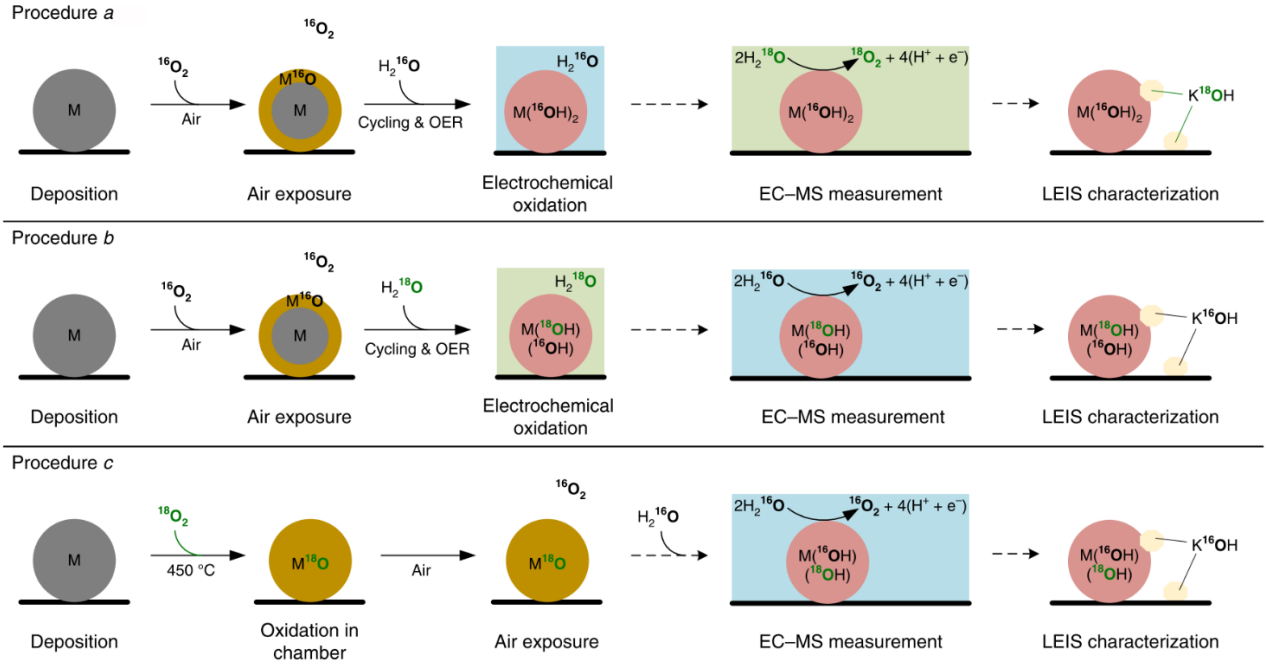

Figure 4.5: Three procedures used for isotope-labeled experiments to probe oxygen exchange during OER. Procedure **a**: Natural labeling of the catalyst followed by OER in isotope-labeled water. Oxygen exchange is seen in EC-MS as excess $^{16}O^{18}O$ and ^{18}O detected afterwards with LEIS must have been incorporated in the catalyst during OER. Procedure **b**: Catalyst is labeled with ^{18}O followed by OER in natural water. Oxygen exchange during OER should result in enrichment of ^{16}O detectable with LEIS. Procedure **c**: Catalyst is labeled in UHV after deposition with ^{18}O with subsequent experiments in natural water. Any excess ^{18}O detected with LEIS after OER comes from the original labeling.

The isotope studies conducted here relies on the extreme sensitivity of EC-MS and the ability to quantify products to be sure that we can detect any lattice oxygen evolved.[28] Three methods are adopted in this study to probe the lattice oxygen exchange: these are depicted in figure 4.5 and are referred to as procedure *a*, *b*, and *c*. They all depend on labeling the catalyst with either ^{16}O or ^{18}O before testing for OER and then testing for OER in an environment rich in the other isotope. Thus, in procedure *a*, the catalyst is prepared fully metallic, and when it is removed from UHV, a thin oxide layer is formed on the surface containing the ^{16}O from air. The catalyst is then oxidized electrochemically in isotopically normal electrolyte so the resulting hydroxide is fully labeled with light oxygen: $M(^{16}OH)_2$ where M represents the Ni and Fe atoms. OER is next performed in electrolyte labeled with ^{18}O, so that any ^{18}O detected with LEIS afterwards should originate from the OER measurement. In procedure *b*, the labeling steps are opposite: the catalyst is electrochemically labeled in ^{18}O-rich electrolyte ($\sim 95\,\%$ ^{18}O) with OER performed in electrolyte containing natural isotope ratios ($99.8\,\%$ ^{16}O). We believe that the oxidation process involves gaseous oxygen and water according to the equation

$$M + 0.5\,{}^{16}O_2 + H_2^{18}O \rightarrow M(^{16}OH)(^{18}OH) \tag{4.4}$$

resulting in an isotope distribution in the catalyst that is roughly $1:1$ between the two isotopes. In procedure *c*, the catalyst is oxidized in $^{18}O_2$ in UHV before the catalyst is exposed to air with subsequent OER performed in ^{16}O.

The three procedures in combination are meant to overcome the difficulties arising from the questions regarding whether or not natural ^{16}O from the air might spontaneously exchange with oxygen on the catalyst surface before and after OER.

Proper LEIS characterization after OER is very difficult because even when rinsed thoroughly in ultrapure water ($18.2\,M\Omega\,cm^{-1}$) the outer layer is completely covered in adventitious carbon (or at least fully terminated by hydrogen) as indicated by the black "as-received after OER" spectrum in figure C.5. Here, only the background signal from Au (at $925\,eV$) is visible along with a huge broad background at low energies characteristic of

adventitious carbon. This layer covers the oxygen region at $\sim 400\,\mathrm{eV}$ and is easily removed by sputtering with helium for a short while. In figure C.5 the sample is sputtered 4 minutes at 10 mA emission current (1x1 raster) with 1 keV He to get rid of this layer and reveal the oxygen peaks.

Following the methods in section 2.1.1, I assume a generic sputter rate for Ni_3Fe of $r_{NiFe} = 0.75 \cdot 0.66 + 0.25 \cdot 0.71 = 0.67\,\mathrm{pm\,s^{-1}}$ and an effective sputter yield of $Y_{NiFe} = 0.75 \cdot 0.145 + 0.25 \cdot 0.150 = 0.146$. If the dose of 1 keV He^+ that was used to clean the adventitious carbon from the surface is applied instead to a clean surface, the estimated sputter damage corresponds to about a monolayer:

$$r\,t = r_{NiFe}\,\frac{i}{\mu\mathrm{A\,cm^{-2}}}\,Y_{NiFe}\cdot t = 0.67\,\frac{\mathrm{pm}}{\mathrm{s}}\cdot\frac{177\cdot 10^{-3}}{0.1^2}\cdot 0.146\cdot 240\,\mathrm{s} = 4\,\text{Å} \quad (4.5)$$

When samples are brought into the UHV chamber from OER, they are sputtered 2-4 minutes with 1 keV He at 10 mA emission current to remove the adventitious carbon. Even if the interesting signal only sits sensitively at the outer surface, only a small part of this should be lost before we are able to see the oxygen region beneath the adventitious carbon in LEIS. After the initial assessment of the surface, the catalyst is sputtered 30 minutes with 1 keV Ar to see if the signal changes deeper down. Again, following section 2.1.1, this corresponds to about 7.2 Å or 2 monolayers. For one of the samples we investigated, I tried to sputter through the nanoparticles in order to verify this estimate. The result for 6.7 nm Ni_3Fe nanoparticles is shown in figure 4.6. Rough relative quantification was made for regions containing oxygen and fluorine peaks, potassium and argon peaks, and the nickel-iron peak, by subtracting a linear background. From the LEIS spectra in the top panel, the signal of the three regions quickly become so small that they drown in the background from the gold substrate peak. After 190 minutes of argon sputtering, the Ni/Fe signal (as measured after OER and after cleaning the adventitious carbon peak) is reduced to about 2-3 % (lower panel figure 4.6). It was also seen with XPS (not shown here) that the Ni and Fe peaks were very small at this point. A rough estimate from this gives a sputter rate per 30 minutes (1 keV Ar): $6.7\,\mathrm{nm} \cdot 30\,\mathrm{min}/190\,\mathrm{min} = 1\,\mathrm{nm}$ or about 3 monolayers. This type of sample is not well suited for such a calibration since uneven or preferential

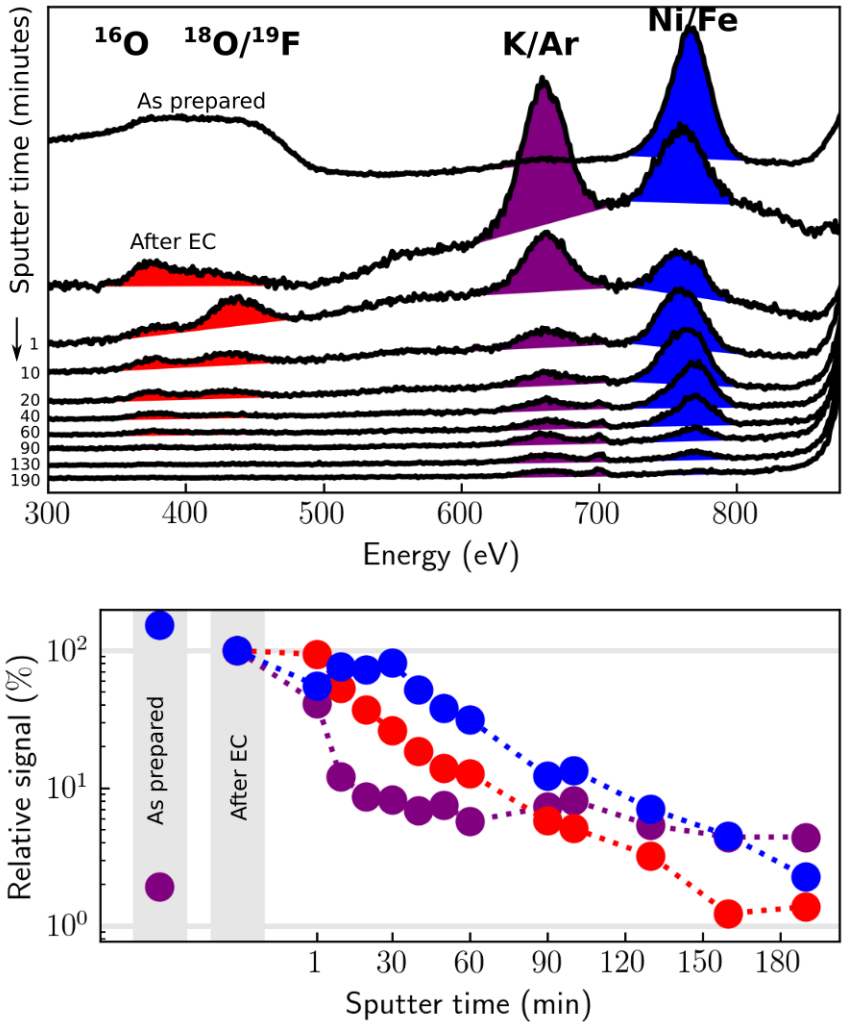

Figure 4.6: Depth profile of 6.7 nm particles to calibrate the sputter rate. Top panel shows a selection of LEIS spectra with the various integrated regions with linear background subtraction: oxygen region in red, potassium in purple, and the nickel-iron peak in blue. Bottom panel shows the integrated signals of each region relative to the measurement after OER. After 190 minutes of 1 keV Ar sputtering, the nickel-iron signal is very small.

sputtering as well as mixing with the substrate will blur the transition where you sputter through the layer of interest. Since the substrate peak is always visible, this will just mean an exponentially decaying tail of the signal of interest. Furthermore, there are both double mass particles and places where nanoparticles land in a group atop one another. However, it does indicate that the estimates made from section 2.1.1 are correct at least within a factor of two. For this, we assume that 30 minutes of 1 keV argon sputtering corresponds roughly to the removal of 1 nm. The samples for the isotope studies were treated a little differently than the samples for activity measurements. The latter were not sputter cleaned in UHV prior to deposition as evidenced by the broad O/F region in the as-prepared spectrum in figure 4.6 that is comparable in intensity to the oxygen signals we are interested in. The reasoning for this was to avoid sputter-induced defects that might make the Au substrate more active towards OER. As we for the isotope study are mainly interested in the oxygen-exchange phenomenon, the Au substrates were here sputter cleaned before deposition and the coverage was not controlled exactly, but in general increased to 20-25 % to increase the signal from the nanoparticles. Furthermore, OER is measured in 0.1 M KOH labeled isotopically according to the procedures in figure 4.5. The calibration of the EC-MS setup for these measurements are explained in figure C.3.

The results from the isotope experiments are collected in figure 4.7. The EC-MS plots show the first CV after isotope labeling that was anodic enough for OER for each procedure. The data is shown by the measured $m/z = 34$ signal ($^{16}O^{18}O$) along with the $m/z = 34$ signal expected given the isotope ratio in the electrolyte. To illustrate the sensitivity of the EC-MS setup, it is simulated how big the signal would be if 1 % of the surface oxygen were to be released as OER products over the course of 5, 15, or 45 seconds. Shown for each procedure is the corresponding LEIS measurements with the as-prepared catalyst (black), after OER and cleaned for adventitious carbon (blue), and after OER and sputtered 1 nm with 1 keV Ar (red). All the LEIS spectra are normalized to the intensity of the Ni/Fe peak.

For procedure *a*, the measured $m/z = 34$ signal coincides exactly with the

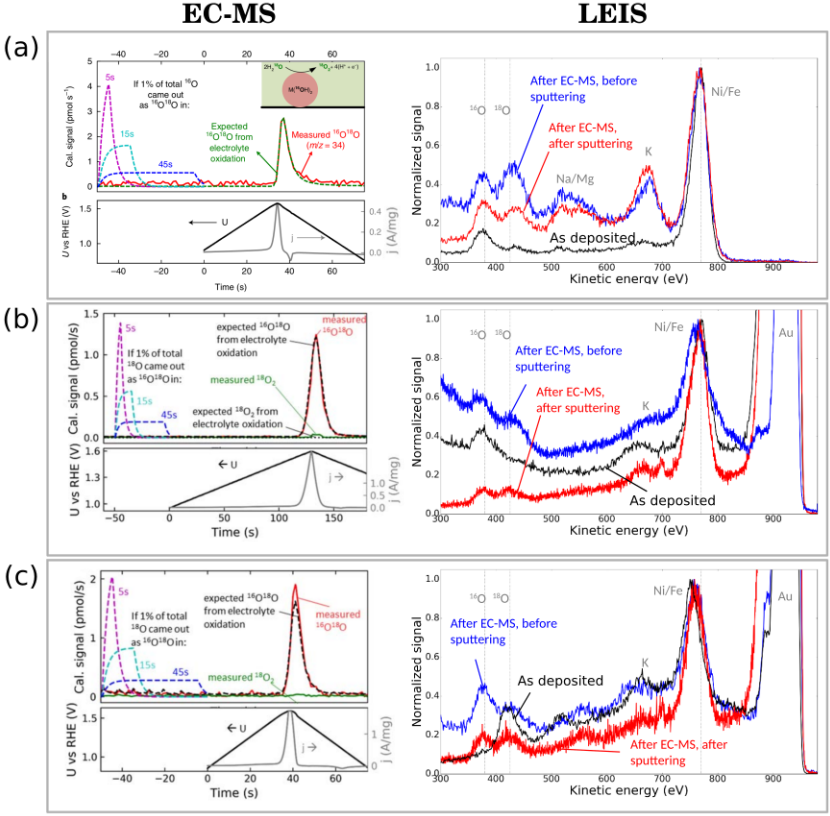

Figure 4.7: EC-MS and LEIS results from isotope-labeled oxygen exchange experiments. (a) Procedure *a*, (b) procedure *b*, and (c) procedure *c*. EC-MS shows the first CV after isotope-labeled oxidation of the catalyst with the O_2 signal scrambled from the presence of the minor isotope, $^{16}O^{18}O$ ($m/z = 34$). The expected signal is calculated as a constant fraction of the major isotope, $^{18}O_2$ ($m/z = 36$) in (a; dashed green) and $^{16}O_2$ ($m/z = 32$) in (b-c; dashed black). The dashed curves in EC-MS for time < 0 is the simulated signal if 1 % of the total surface oxygen were to come out as $^{16}O^{18}O$ over the course of 5 s (magenta), 15 s (cyan), or 45 s (blue). LEIS show spectra for as-deposited (black), after EC-MS sputtered with He (blue) and sputtered 30 minutes with Ar (red).

signal expected from the isotope ratio of the electrolyte indicating that no oxygen exchange is taking place. The LEIS characterization is tricky however. The sample for this procedure was deposited on a glassy carbon stub instead of a gold stub in an effort to improve the sensitivity by getting rid of the large background signal from gold. But it was next to impossible to rinse the sample completely of the isotope labeled electrolyte as evidenced by the potassium peak present in equal amounts after OER and Ar sputtering. This sample shows a peak after the ^{16}O peak that can be attributed to either ^{18}O or ^{19}F. Compared with the pure ^{18}O peak for procedure *c* (black spectrum), this peak is slightly shifted to the right and is likely a combination of fluorine and isotope labeled oxygen bound in the dried electrolyte. The signal is reduced, but still present after sputtering for 30 minutes with 1 keV Ar. The inefficiency of the rinsing after OER is attributed to the microscopically rough glassy carbon surface. The strength of this procedure should have been the sensitivity of LEIS since the catalyst is only exposed to increased amounts of ^{18}O during OER, but this ended up to be countered by the sticking electrolyte. The decreased isotope purity of the electrolyte means EC-MS is less sensitive for this procedure.

In procedure *b*, the catalyst is deposited on a sputter cleaned gold stub and labeled electrochemically with ^{18}O followed by OER in ^{16}O with the expected scrambling resulting from 99.8 % ^{16}O. The measured $m/z = 34$ signal also here coincides with the expected signal, and the isotope ratio measured with LEIS after OER is roughly 1:1 and does not change after 30 minutes 1 keV argon sputtering. This ratio is what was expected due to natural oxidation in air before the sample is introduced in the labeled electrolyte. The small amount of $m/z = 36$ is attributed to the sample not being rinsed between the labeling and OER measurement. Procedure *c* is conducted in the same manner except that the sample was pre-labeled with ^{18}O by preheating the sample to 440°C for 30 minutes and then dosing $^{18}O_2$ for 10 minutes at $1 \cdot 10^{-6}$ mbar. Figure C.4 shows XPS spectra for the synthesis process as well as after OER, LEIS characterization and argon sputtering. A metallic Ni $2p_{3/2}$ peak is still visible after the labeling step although clearly oxidized to a degree. The oxidized peaks could be consistent with the formation of a $NiFe_2O_4$ phase.[15] After OER in ^{16}O, the oxidation states look more like hydroxides consistent with the XPS analysis

for the activity and stability measurements. After sputtering, the oxidation state moves back to the dry oxide state. With EC-MS, we measure slightly more $m/z = 34$ signal than expected (figure 4.7). LEIS shows a pure ^{18}O peak after the partial ^{18}O oxidation in UHV. After OER in ^{16}O, we see an isotopic ratio roughly 2:1 of ^{16}O:^{18}O which after sputtering 30 minutes with argon reduces to the 1:1 ratio that was expected by the electrochemical oxidation. There is no obivous signal from dried electrolyte as in procedure *a*, so the increased ^{16}O signal right after OER could be explained by either ^{16}O during oxidation or air exposure filling out the vacant sites after the partial oxidation in UHV, or by lattice oxygen exchange during OER. Control experiments without doing OER was made to ensure that the labeling of the oxidized catalyst does not spontaneously exchange with contact to air or water.[62] Given the small amount of excess $m/z = 34$ detected, the increased ^{16}O ratio is likely because of the partial oxidation. A strong point here, is that the ^{18}O detected at the surface immediately following OER can only have come from the original UHV labeling regardless of the origin of the increased amount of ^{16}O.

The above results have their own uncertainties, but together indicate that oxygen exchange does not take place on our Ni_3Fe nanoparticles in any notable amount. Given that these nanoparticles are (nearly) metallic at the core and might not be representative for conclusions about $NiFeO_xH_y$ systems in general, a $NiFeO_xH_y$ thin film was electrodeposited according to the method by [47] and tested according to procedure *a*. This did not show any notable oxygen exchange either. To prove that the setup indeed can detect oxygen exchange, the > 1 ML lattice oxygen exchange reported by Fierro et al.[65] on IrO_2/Ti in acid was reproduced following procedure *a*. The result of this is shown in figure 4.8a, while figure 4.8b shows the integrated calibrated signals for quantified comparison of the three samples of nanoparticles and two films. It is clear that the IrO_2 involves lattice oxygen although it only corresponds to about 7 % of the total amount of evolved oxygen from the electrolyte. The $NiFeO_xH_y$ systems, in comparison, shows virtually no oxygen exchange. The small quantified amounts can largely be explained by cross-contamination between labeled electrolytes and background subtraction in the integration process.

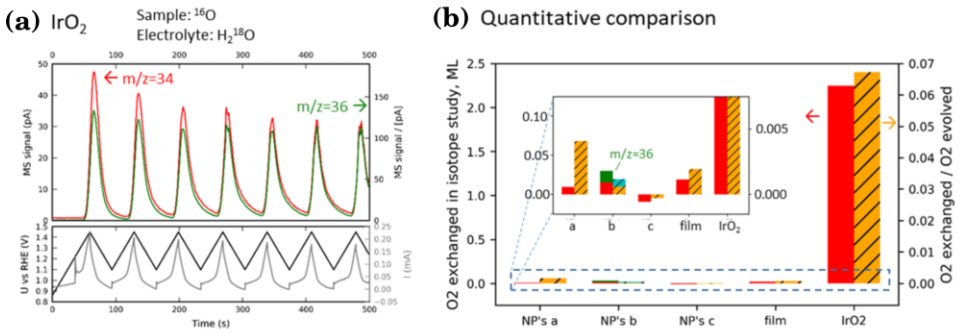

Figure 4.8: Lattice oxygen exchange of IrO_2 compared with our study. (a) EC-MS data showing excessive $m/z = 34$ signal produced during OER in $H_2^{18}O$ electrolyte on $Ir(^{16}O)_2$. (b) Quantitative comparison between the IrO_2 film in (a) and the results in figure 4.7. Red bars (left y-axis) show the measured O_2 exchange in monolayer equivalents. Orange hatched bars (right y-axis) show the ratio of exchanged lattice oxygen relative to the total amount of evolved oxygen. While IrO_2 shows a clear lattice oxygen evolution in a quantified amount corresponding to about 2 ML, the varying results on the nickel-iron nanoparticles and thin film can be considered the baseline resolution of the EC-MS with this technique.

4.2.3 Summary

Mass-selected Ni_3Fe nanoparticles of measured sizes 3.9, 5.4, 6.7, and 8.4 nm was deposited with the cluster source. We find that the as-deposited iron-content of the systems vary around the nominal 25 % of the used sputtering target, but following OER, iron leaches out of the system leaving a more consistent iron concentration of about 15 % near the surface. Identical-location SEM and HRTEM shows that the particles do not coalesce during the 2 hour measurements, and a 1000 hour stable measurement at constant potential for 100 ng 6.7 nm nanoparticles indicate that the systems are very stable. XPS and EDX show that the outer few nanometers of the particles are oxidized during OER measurements to a $NiFeO_xH_y$ system that is more metallic at the core. The highest mass-normalized activity is found for the 5.4 nm particles, which at 300 mV overpotential corresponds to a turnover frequency of $1.2 \pm 0.3\,s^{-1}$ to

$6.2 \pm 1.6\,\mathrm{s}^{-1}$ depending on whether you assume all the metal atoms to be active or only the surface.

To probe the difference between bulk and surface activity, and to investigate whether lattice oxygen plays a role in the oxygen evolution reaction, isotope experiments with isotope-labeled oxygen are conducted using electrochemical-mass spectrometry and low-energy ion scattering. We find no evidence of lattice oxygen being exchanged during oxygen evolution, and low-energy ion scattering experiments indicate that the original isotope concentration of the catalysts remain largely unchanged after oxygen evolution. This means that the original lattice oxygen stay put, at least up to the outer surface, and is not involved in any significant OER mechanism. With this reasoning, we claim that the reaction only takes place at the surface. Hence, $\mathrm{TOF}_{\mathrm{surface}} = 6.2 \pm 1.6\,\mathrm{s}^{-1}$ from figure 4.4 is the best estimate of the intrinsic activity. This sets the record for the number of oxygen atoms produced per second for any alkaline OER catalyst at an overpotential of 300 mV.

4.3 RuO_2 thin films

$NiFeO_xH_y$-based catalysts are the preferred choice for alkaline electrolyzers. In acid, however, only ruthenium and iridium oxides are both stable and active enough to be viable catalysts, although even these catalysts have much need of improvement in these areas.[72–76]

4.3.1 Intrinsic activity

Cyclic voltammograms in 0.1 M $HClO_4$ for RuO_2 (100), (101), and (110) single crystals are compared in figure 4.9 to RuO_2 thin film formed by reactive sputtering with 20 % oxygen and 80 % argon with the substrate kept at room temperature (RT), 200 °C, 300 °C, and 400 °C. The pseudocapacitances of these films are very large and decrease significantly with the annealing temperature. Thus, the 400 °C RuO_2 film has the lowest capacitance which is still more than 10 times larger than the single crystal films. XRD analysis (not shown here) indicates that the room temperature sputter deposited films are amorphous and the films sputter deposited at elevated temperatures show increasing crystallinity. Shown in figure 4.9c is the potential corrected for the ohmic drop as a function of the geometric current density which shows that the films are more active than the single crystals with the more crystalline surfaces being less active. When normalizing the current to the capacitive charge, it seems pretty clear that the films share the same intrinsic activity, but that it is just a matter of available active surface area.

The films were tested in the EC-MS setup in electrolyte labeled with ^{18}O. Since the background signal at $m/z = 36$ is much lower than for $m/z = 32$, this offers much better sensitivity towards low amounts of evolved oxygen. To see how far we could lower the potential and still detect oxygen evolution, a high surface area RuO_2 foam was deposited electrochemically following the procedure by Winiwarter et al.[77] The result is shown in figure 4.10 where evolution of $^{18}O_2$ is detected all the way down to 1.29 V_{RHE}, or 60 mV overpotential. Estimating the turnover frequency for the films and foams[69], and comparing them in figure 4.11, they all seem to share the

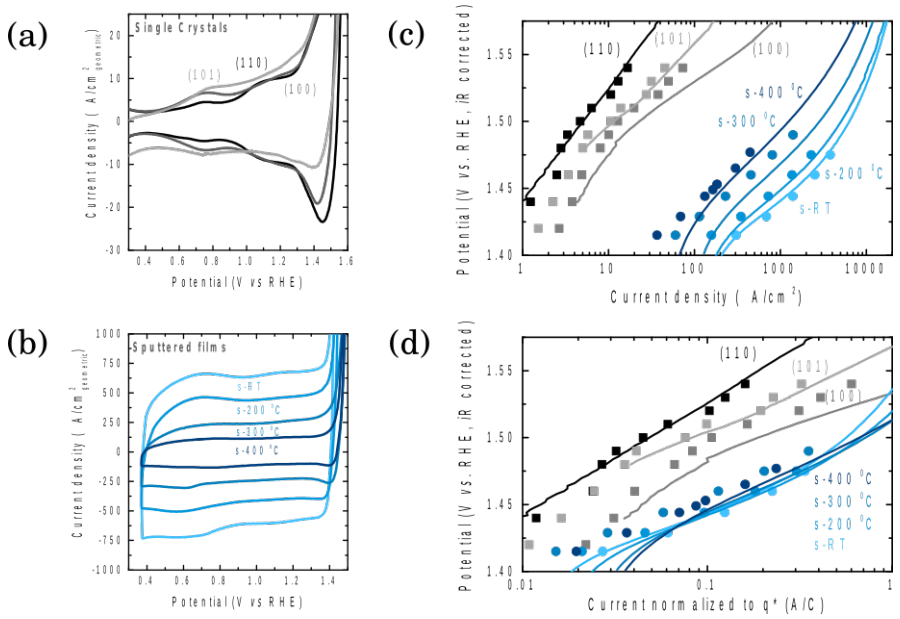

Figure 4.9: RDE activity of RuO_2 single crystals (black) and thin films (blue). CVs of (a) single crystals and (b) thin films sputter deposited at different temperatures. Activities compared as potential versus (c) geometric current density and (d) ECSA normalized current density. Points represent steady-state measurements while curves are from CVs. Data and figure by Reshma Rao.

same intrinsic activity. The evidence of oxygen evolution at lower overpotentials than seen before is therefore not a groundbreaking discovery of a new highly active material, but rather the engineering of high surface area catalyst coupled with a measurement technique more sensitive than previously employed.

4.3.2 The question of lattice oxygen and stability

The thin films were investigated with isotope labeled EC-MS experiments to probe the mechanisms for oxygen evolution at low overpotentials. In the following, I focus on the thin films sputter deposited at room temperature,

amorphous RuO_2, and at 400 °C, rutile RuO_2. Inspired by procedure *a* in figure 4.5, rutile $Ru^{16}O_2$ was cycled in ^{18}O-enriched electrolyte to label it with ^{18}O as a hydrous oxide. Followed by LEIS characterization in figure 4.12 (Treatment 1), we find that the labeling only is about a monolayer thick as evidenced by the large ^{16}O ratio after helium sputtering at a dose corresponding to the one that will be used to clean the surface of adventitious carbon (see the section on Ni_3Fe nanoparticles). Sputtering the surface for 20 minutes with argon completely removes the trace ^{18}O signal. 20 minutes correspond to removal of about 2 monolayers following the assumptions of section 2.1.1. A new calibration sample asserts that this is minimum 1 monolayer and maximum 4 monolayers (see appendix B for details).

The same sample was then cycled more aggressively in labeled electrolyte, which gave a clear 1:1 ratio between ^{16}O and ^{18}O - Treatment 2 in figure 4.12. The sample was then used for ^{16}OER, after which the surface shows an increased concentration of ^{16}O. Removing a few monolayers strongly increases this signal. The presence of ^{18}O after oxygen evolution indicates that the film does not completely exchange its surface oxygen with the electrolyte or reaction products. However, quantifying the amount is difficult since we do not know whether or not the higher concentration of ^{16}O is due to lattice oxygen exchange or because of shallow isotope labeling

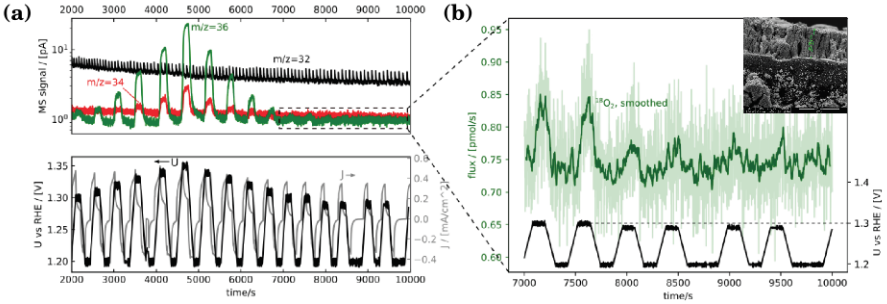

Figure 4.10: Oxygen evolution on RuO_2 foam in ^{18}O-labeled electrolyte. (a) EC-MS at a series of potential holds, and (b) a zoom-in on the low overpotential region where evolution of $^{18}O_2$ is detected down to overpotentials of only 60 mV. Inset shows an SEM image of a cross-section of the foam.

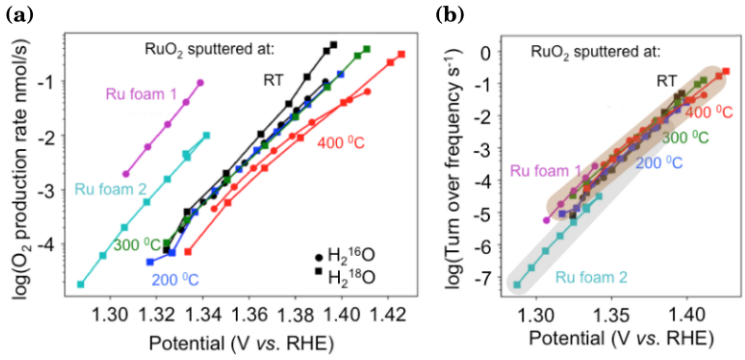

Figure 4.11: Estimated intrinsic activity of the RuO_2 thin films and foam. (a) quantified rate of oxygen evolution, and (b) estimated turnover frequencies.

- especially when considering dissolution processes which are known to be significant for RuO_2.[78]

At this point, we realized that we needed a proper $Ru^{18}O_2$ labeling for these experiments similar to procedure *c* in figure 4.5. The first effort at this was to sputter deposit a metallic ruthenium film, which I then cleaned in UHV by removing most of the native oxide layer by argon sputtering, and then heating in UHV to 300 ∘C while exposed to $^{18}O_2$ for 90 minutes. While this produces a distinct ^{18}O oxide layer as seen in figure 4.13, it is also evident from leaving it in the load lock of the Omicron system exposed to atmosphere for 12 hours that the oxidation is not stable or complete. Rather than search the literature for the correct way to accomplish this in UHV or begin a lengthy trial-and-error based experiment, the best experiments would clearly be obtained by synthesizing the oxide films directly by reactive sputtering as before, but this time labeled with ^{18}O by feeding labeled oxygen into the argon mix instead of normal oxygen. This conclusion coincided with the need to replace the channeltrons of the NanoSAM energy analyzer on Omicron thereby putting both Omicron LEIS and XPS out of commission for 3-4 months. All the following films are therefore synthesized by reactive sputtering with 20 % $^{18}O_2$ and 80 % Ar all LEIS spectra obtained by Søren Scott on the "Thetaprobe" UHV

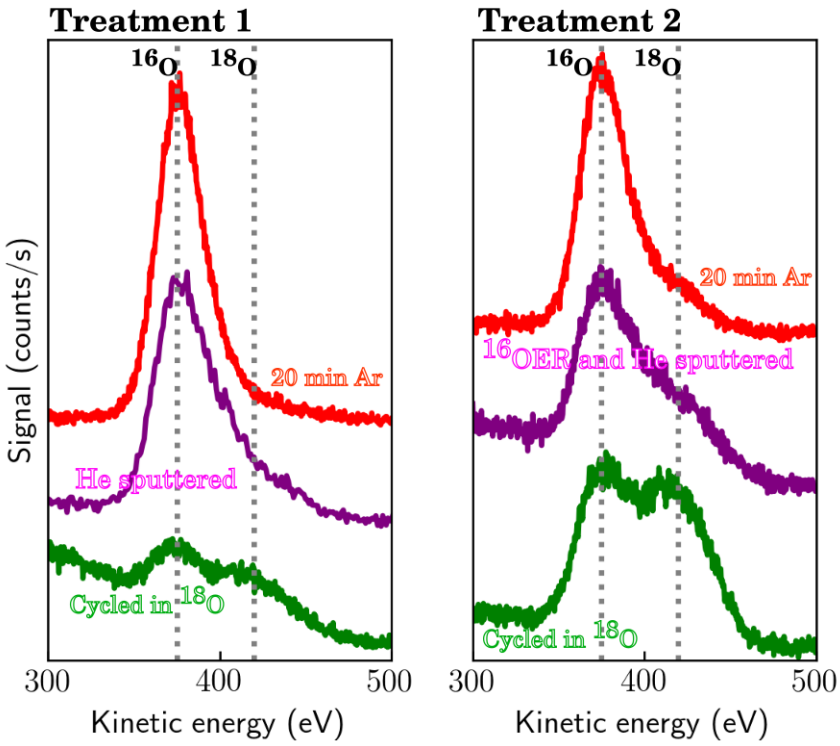

Figure 4.12: $Ru^{16}O_2$ thin film that was electrochemically labeled with ^{18}O by cycling the film in labeled electrolyte. In treatment 1 (left), the film showed a 1:1 isotope ratio after cycling (green), but light helium sputtering (purple) removes most of this. After 20 minutes 1 keV argon sputtering (red) the ^{18}O signal is completely gone. In treatment 2 (right), the film was labeled by cycling more aggresively which show an intense 1:1 isotope ratio (green). After OER, we see an enrichment of ^{16}O (purple). 20 minutes of argon sputtering further reduces the ^{18}O peak (red).

characterization system by ThermoFisher Scientific. Treating the LEIS data is done by me.

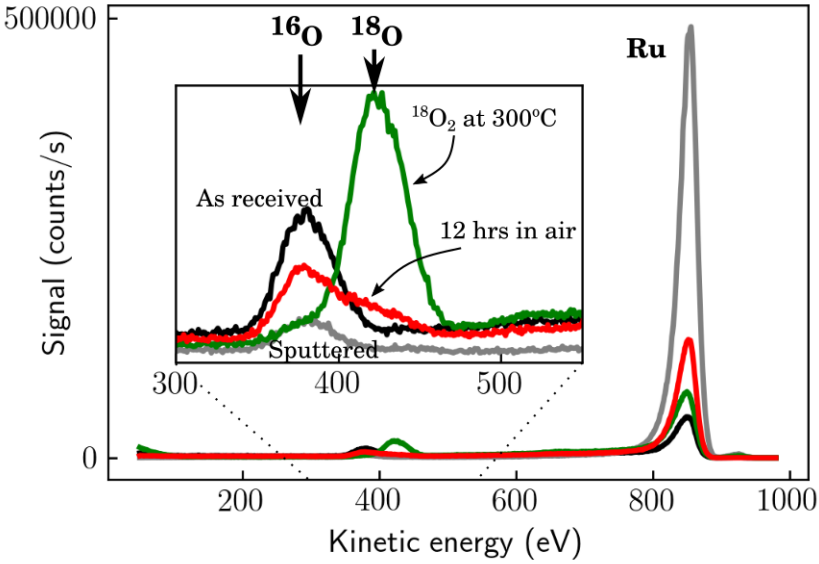

Figure 4.13: LEIS characterization of first effort at labeling a Ru thin film with ^{18}O in UHV. The as-received film (black) was sputtered with argon to reduce the native oxide layer (gray). Annealing to 300 °C in $^{18}O_2$ (green), but exposing it to air for 12 hours (red) clearly reveals a partial oxidation.

In the following part, an effort was made to make a systematic quantifiable study of the dissolution and activity coupled with oxygen exchange for amorphous and rutile ruthenium oxides and compare it to iridium thin films where oxygen exchange has been verified. As mentioned previously, this produced a lot of data that is still being sorted through. One tool in this process is by automatically integrating the oxygen peaks and deconvoluting the two oxygen isotopes. An example of a guiding overview plot is shown in figure C.6 with an inset illustrating the deconvolution of the two oxygen peaks for one data set. This helps in sorting through the data sets and identifying patterns. For example, the points in figure C.6 showing more

than 30 % ^{16}O content tends to be measurements that also contain a lot of titanium signal from the binding layer, and these measurements are likely not a good representative measurement for quantifying the lattice oxygen exchange. Quantification is here done by using reference samples for the two isotope peaks compensated by subtraction of a linear background. The reference peaks are then scaled to fit the experimental spectrum and the ratio of each scaled peak compared to the total signal of the oxygen peaks. I noticed that some spectra were shifted arbitrarily by up to $\pm 10\,\mathrm{eV}$ which is presumably due to the samples charging because of insufficient grounding. To handle automatic fitting of the spectra, each spectrum (including the reference spectra) has been shifted to align the most intense oxygen isotope peak with the expected peak position.

Preliminary conclusions are based on four different samples: amorphous $Ru^{18}O_2$, rutile $Ru^{18}O_2$ at $0.5\,\mathrm{mA\,cm^{-2}}$ and $0.05\,\mathrm{mA\,cm^{-2}}$, and a $Ir^{16}O_2$ thin film that was turned into a hydrous ^{18}O oxide by electrochemical cycling. All the measurements are done at constant current density of $0.5\,\mathrm{mA\,cm^{-2}}$ unless stated otherwise. Samples have been taken of the electrolyte at several intervals for analysis of dissolved metal atoms via inductively coupled plasma mass spectrometry.

Figure 4.14 shows the oxygen exchange experiment on amorphous $Ru^{18}O_2$ with panel (a) showing the ICP-MS/EC-MS plot of the experiment. The top panel shows the average dissolution rate of Ru atoms based on samples taken at intervals marked by the blue dashed lines. The middle panel shows the mass spectrometer data with the quantified $^{16}O^{18}O$ signal in red on the left y-axis and the $^{16}O_2$ signal in black on the right y-axis. The axes are scaled such that the signals overlap if no excess signal of the scrambled isotopes are generated. The bottom panel in (a) shows the electrochemistry data where the potential is ramped to produce a constant $0.5\,\mathrm{mA\,cm^{-2}}$ at a steady state potential $1.40\,V_{RHE}$ for 30 minutes. In the first couple of minutes when the potential is ramped, a total amount of 1280 pmol Ru atoms dissolve compared to 14 pmol of ^{18}O lattice oxygen incorporated in the oxygen evolution products. In the steady state part of the measurement, 5320 pmol Ru atoms dissolved compared to 133 pmol lattice oxygen evolved. Figure 4.14b shows the LEIS data before and after the

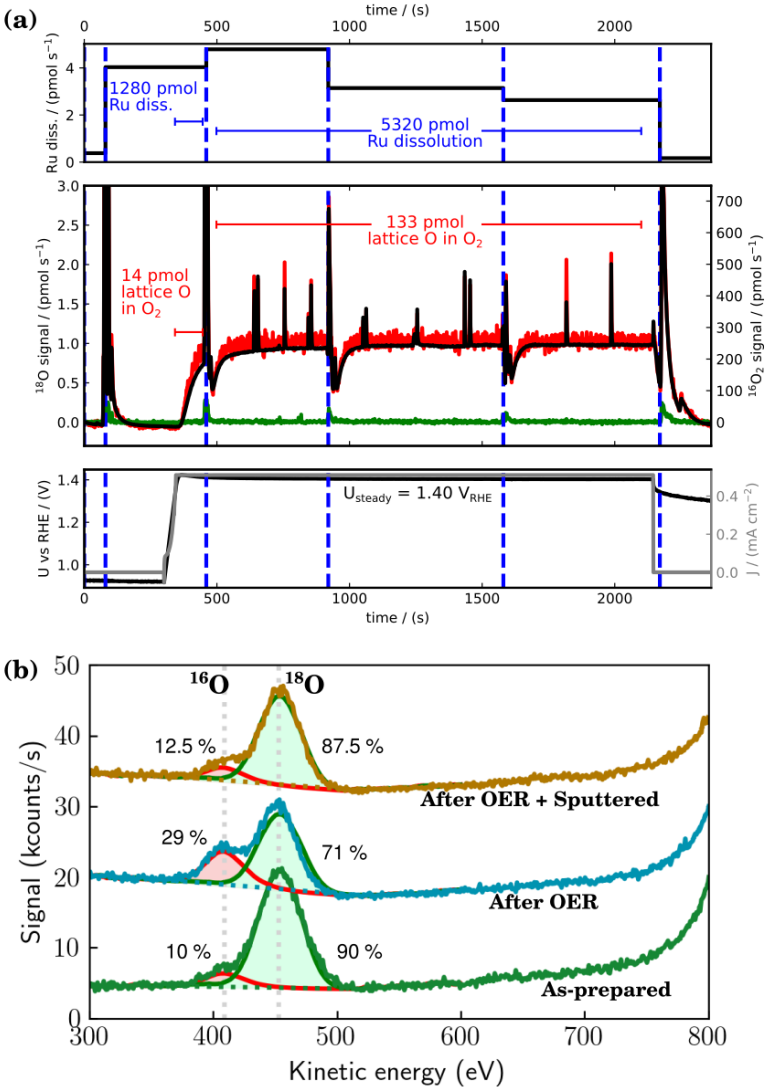

Figure 4.14: Oxygen exchange on amorphous $Ru^{18}O_2$. (a) ICP/EC-MS plot of constant current experiment at 0.5 mA cm^{-2}, and (b) LEIS spectra aligned to oxygen peaks before and after OER with quantification of the oxygen isotopes. After OER experiments ^{16}O content is enriched from 10 to 29 %.

oxygen evolution. The initial isotope distribution from reactive sputter deposition is 10 % ^{16}O and 90 % ^{18}O. After oxygen evolution, the isotope ratio increases to 29 % ^{16}O, but decreases back to 19 % ^{16}O after some sputtering. This is roughly the bulk isotope composition before OER indicating that the exchanged lattice oxygen atoms stay close to the surface.

Comparing this to the rutile $Ru^{18}O_2$ thin film in figure 4.15 measured under the same conditions, we see a slightly higher dissolution rate of Ru at 1700/6020 pmol Ru atoms dissolved during the potential ramp/ constant current measurement. This is an unexpected result, since crystalline RuO_2 is expected to be more stable against dissolution than amorphous RuO_2.[79] The increased instability is likely related to the unwanted presence of bubbles in the EC-MS setup, which is what causes the spikey noise in the middle panel in figure 4.15a. The dissolution is compared to a lower amount of detected lattice oxygen: 0/56 pmol. A steady state potential of 1.43 V_{RHE} was needed to drive 0.5 mA cm^{-2}. The initial bulk isotope ratio is 17 % ^{16}O. After oxygen evolution, the ratio is increased to 27 % ^{16}O which drops back close to bulk concentration after sputtering: 19 % ^{16}O.

Another rutile $Ru^{18}O_2$ sample is measured in figure 4.16 with the measurement performed with a 10x lower constant current (at steady state potential 1.41 V_{RHE}). Here, the dissolution rates are generally much lower, but similar for the two regions: 151/147 pmol. The evolution of lattice oxygen is measured as 0/13 pmol. The isotope ratio changes from 20 % ^{16}O to 25 % ^{16}O after oxygen evolution. No LEIS spectrum available after sputtering.

An amorphous (sputter deposited at room temperature) $Ir^{16}O_2$ was labeled with ^{18}O by cycling it in electrolyte to turn it into a hydrous oxide. This results in an isotope ratio of 25 % ^{16}O (labeling depth unknown) as shown by the "as-prepared" curve in figure 4.17. A foreign peak corresponding to chloride from the electrolyte is also visible. After oxygen evolution in unlabeled electrolyte, the isotope ratio increases to 54 % ^{16}O which drops back to 31 % ^{16}O after sputtering. The oxygen evolution experiment in figure 4.17a shows 171/280 pmol Ir atoms dissolved during the ramp up to and hold at constant current 0.5 mA cm^{-2} (1.47 V_{RHE}) compared to 64/203 pmol lattice oxygen evolved.

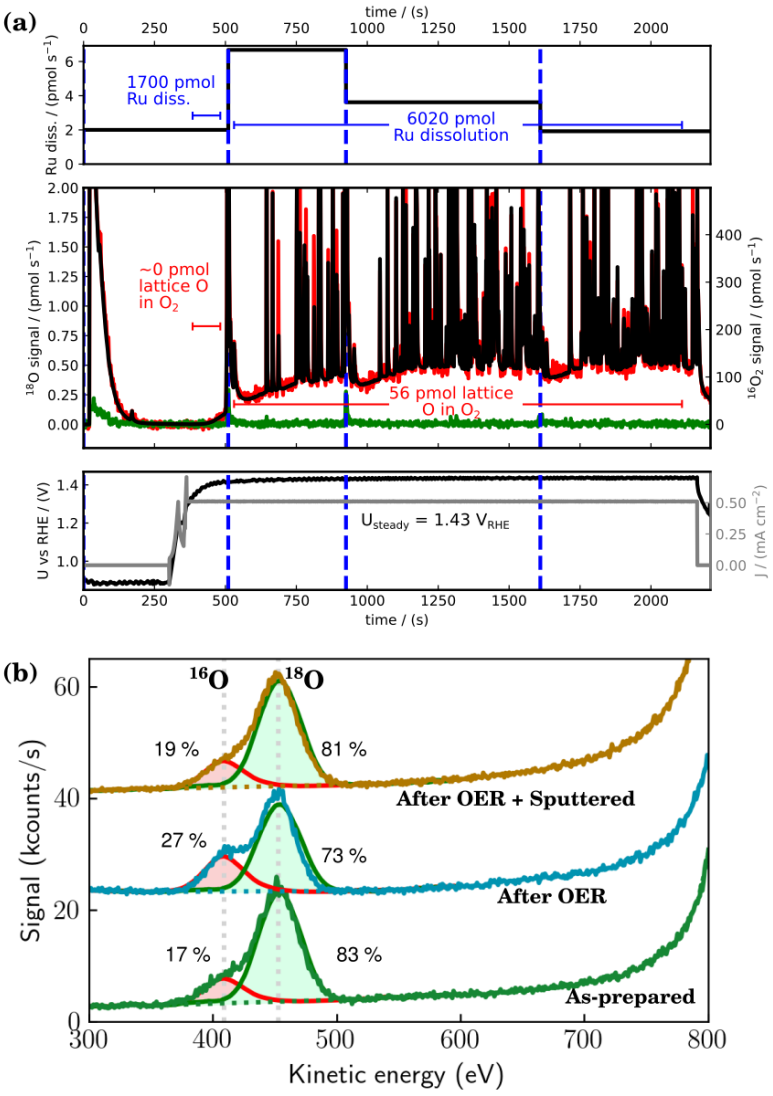

Figure 4.15: Oxygen exchange on rutile $Ru^{18}O_2$. (a) ICP/EC-MS plot of constant current experiment at 0.5 mA cm^{-2}, and (b) LEIS spectra aligned to oxygen peaks before and after OER with quantification of the oxygen isotopes. After OER experiments ^{16}O content is enriched from 17 to 27 %.

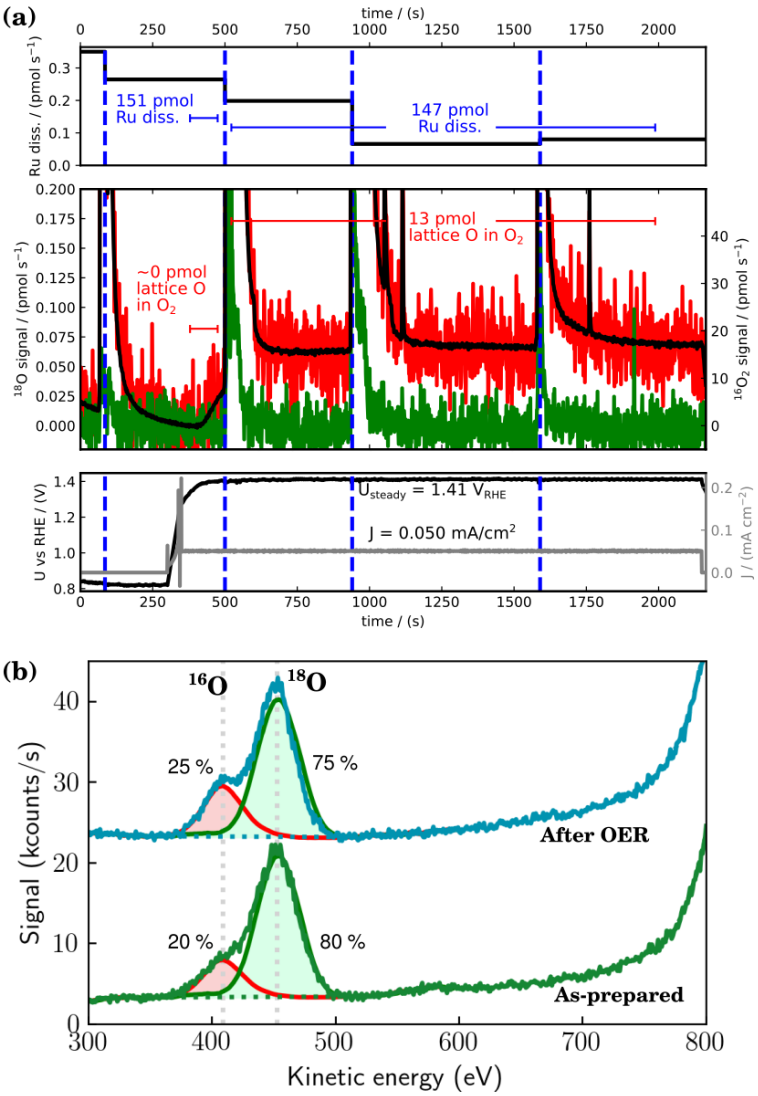

Figure 4.16: Oxygen exchange on rutile $Ru^{18}O_2$. (a) ICP/EC-MS plot of constant current experiment at 0.05 mA cm^{-2}, and (b) LEIS spectra aligned to oxygen peaks before and after OER with quantification of the oxygen isotopes. After OER experiments ^{16}O content is enriched from 20 to 25 %.

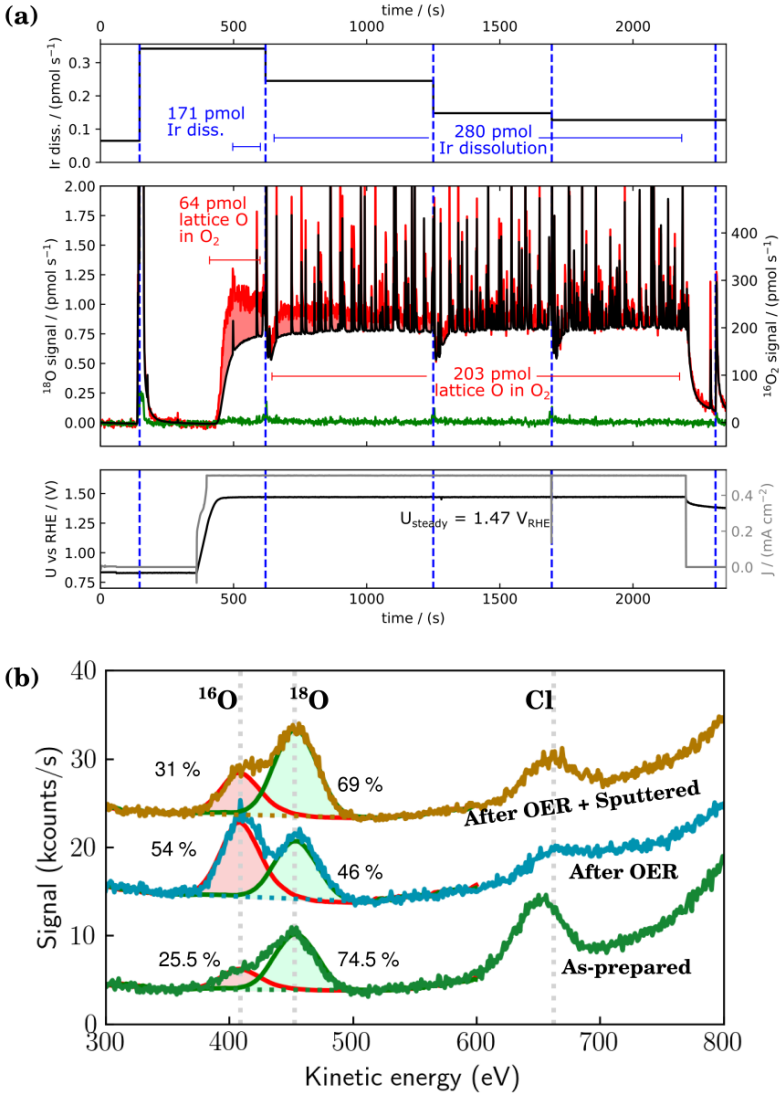

Figure 4.17: Oxygen exchange on amorphous $Ir^{16}O_2$ labeled with ^{18}O by cycling electrochemically. (a) ICP/EC-MS plot of constant current experiment at $0.5\,mA\,cm^{-2}$, and (b) LEIS spectra aligned to oxygen peaks before and after OER with quantification of the oxygen isotopes. After OER experiments ^{16}O content is enriched from 25 to 54 %.

Although we for all types of samples seem to see some degree of lattice oxygen participating in oxygen evolution, it is clear by comparing the axes on figures 4.14 to 4.17 that it is a seemingly insignificant amount of the total evolved oxygen as also evidenced in the last section. The initial bulk ^{16}O content is 10 % for the amorphous RuO_2 film and 17 - 20 % in the two rutile RuO_2 films, which might be due to variations of the isotopic purity of oxygen during sputter deposition - likely because of something desorbing when the sample is heated to 400 °C. After oxygen evolution, the ^{16}O content increases to 25 to 30 % on the RuO_2 thin films. It is interesting that these films seem to reach the same surface concentration of ^{16}O after OER, although this can be an artifact of the difference in initial isotope ratios of the prepared amorphous film versus the two rutile films. The amorphous film does seem to have a higher rate of lattice oxygen evolution which might lead to the relatively higher enrichment of ^{16}O after OER. The dissolution Ru atoms of the three RuO_2 films is much larger than the oxygen exchange, which could either explain why the isotope enrichment does not penetrate very deeply into the surface, or alternately, be the cause of the isotope scrambling. If not all the lattice oxygen per dissolved ruthenium atom follows said atom, it will necessarily have to end up in the electrolyte where it near the surface might cause an enrichment of ^{18}O which then reacts on the catalyst causing an increased $m/z = 34$ signal.

For the iridium hydrous oxide film, however, the measured dissolution of iridium atoms is on the same scale as the evolved lattice oxygen. It would therefore be obvious to consider that the dissolution process is tied to the minor "catalytic" pathway. Of course, if the pathway always require the dissolution of the metal atom, then it is by definition not catalytic.

Lastly it should be stressed that the considerations given here is only based on the reduced data set consisting of four different types of samples. To really assert trends, we have to consider the more complete data set.

4.3.3 Summary

Ruthenium oxides were sputter deposited at different substrate temperatures: room temperature, 200 °C, 300 °C, and 400 °C. The coldest

sputter deposition produced films that was amorphous in nature with the crystallinity increasing with sputter deposition temperature up to a rutile phase at 400 °C. The different films show the same intrinsic activity which is higher than that of RuO_2 (100), (110), and (101) single crystals. To probe the onset potential of oxygen evolution, a high surface area ruthenium oxide foam was electrodeposited on which we were able to detect the evolution of oxygen down to overpotentials of only 60 mV, which is the lowest yet reported in the literature. However, since the intrinsic activity is roughly the same as the thin films, this record-low onset potential is attributed to the unparalleled sensitivity of the measurement setup coupled with the high surface area electrode. This proves that the "onset potential" - while commendable for the description of real catalysts - is a bad metric for describing the intrinsic activity of new (and old) catalysts.

Furthermore, we found preliminary results indicating that there is a small degree of lattice oxygen exchange on the ruthenium oxide thin films that is constrained to the very near-surface region. Since dissolution of ruthenium atoms is larger by at least an order of magnitude than the evolved lattice oxygen, it is likely that the lattice exchange is an effect of the dissolution mechanism. For a hydrous iridium oxide film, lattice oxygen evolution is greater than for the ruthenium films, but is comparable to the dissolution process. Here, the evolution of lattice oxygen could very well be a minor conversion pathway in the OER scheme which in turn induces the dissolution of iridium.

4.4 Remarks on the projects

A thing that has always bothered me with the project on the nickel-iron nanoparticles in the first part of the chapter, is the seemingly non-sensible activity trend in figure 4.4c. If the story was to be continued, I would like to see the addition of particles smaller than 3.9 nm and larger than 8.4 nm to see whether they would support the current interpreted trend or if it is simply the scatter of the data points. For smaller nanoparticles, the TOF_{bulk} and TOF_{redox} should coincide and $TOF_{surface}$ should approach these values. The constant offset between $TOF_{surface}$ and TOF_{redox} indicates

that the thickness of the redox active surface is constant. While the electrodeposited nickel-iron oxyhydroxide thin film was the more relevant comparison to the literature, a more direct link between the two for our study, would be to sputter deposit a metallic Ni_3Fe thin film. Its TOF_{redox} should have roughly the same offset from the $TOF_{surface}$, and it would be interesting to compare its turnover frequency to the electrodeposited electrode and the nanoparticles. Whether or not the oxygen evolution reaction takes place only on the outer surface layer ($TOF_{surface}$) or in the redox active near-surface region (TOF_{redox}) is not entirely unambiguous. We did not however find evidence of any lattice exchange. Given the stability of the Ni_3Fe system compared to the measured corrosion rates of RuO_2 and IrO_2 thin films that do exhibit some degree of lattice oxygen exchange, the apparent lack of this for Ni_3Fe makes sense.

We are currently developing the tools to organize the large amount of data generated in the complex RuO_2 experiments. We go about this by setting the data up in an object-oriented structure that mimics a relational database, which would be the correct way to go about it. It has been quite an effort, but for writing this thesis, I was quite happy with the tools we set up. The overview plot in figure C.6 along with the insets was easily generated with these tools. It is the hope when we finish this project, that these tools will evolve into the planned framework `ixdat` which will help other scientists to organize complex-data projects.[80]

LN_2-cooled CO-TPD

Chapter 5

This last chapter is all about temperature-programmed desorption using carbon monoxide as the probing molecule (CO-TPD). Implementing this method in a version where the sample under investigation is cooled with liquid nitrogen, was a project originally started as part of my master's thesis under supervision of Anders Bodin[20], then carried over into the project description of my PhD and is still ongoing. This chapter is therefore devoted to describing how TPD is presently implemented on *Omicron* along with some of the experiences that went behind it.

The chapter first motivates the implementation of the technique followed by technical details in section 5.2. Some of the general experimental procedures are explained in section 5.3 which will be relevant to users of the setup and for understanding how the results in section 5.4 was acquired. CO-TPD is used for preliminary investigations of mass-selected copper nanoparticles in section 5.4.2 and of palladium-tin alloy thin films in section 5.4.3.

5.1 Motivation

CO-TPD is a common method, but implemented here by a custom design. To motivate this, I will answer the two following questions: 1) Why is

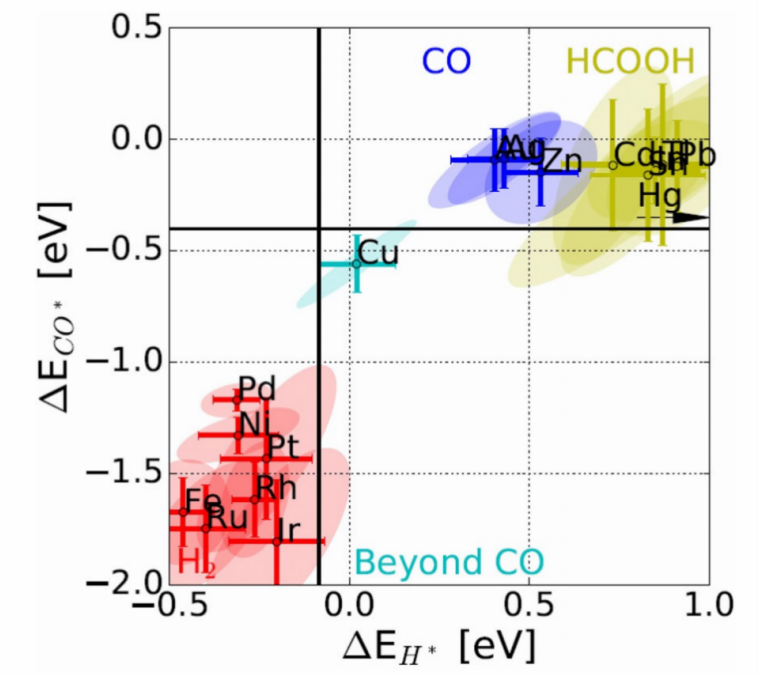

Figure 5.1: Grouping of various metals according to their binding energies of intermediates, ΔE_{CO*} and ΔE_{H*}. The metals are colored by their major CO_2 reduction reaction products: H_2 (red), HCOOH (yellow), CO (blue), and CH_4, C_2H_4 and other products beyond CO (light blue). When shown this way, copper clearly stands out as its own unique group. Figure reprinted from [81].

CO-TPD interesting? and 2) Why does it have to be cooled with liquid nitrogen?

As described in section 2.1.5, TPD allows us to probe the reactivity of a surface towards any gas we choose to expose the surface to. Probing the reactivity by dosing CO, is referred to as CO-TPD. The reactivity is in the form of the desorption energy, which depends on the binding strength between the (CO) molecule and the nature of the specific site (one or several atoms involved in the interaction with the molecule). Remember from figure 4.1 that the intrinsic activity and selectivity of a catalyst can be

described by the binding energies of the reaction intermediates as binding one intermediate too strongly or too weakly will limit the reaction rate or choose one reaction pathway in favor of another.[9,81,82] To answer the first question: CO-TPD experiments provide us with a map describing the reactivity of the various sites which constitute the surface. When this is coupled with other techniques, it can be used to identify the active site of a catalyst, which allows us to design better catalysts that have more of these sites available.[5] Since CO often bind with the carbon atom to the surface[83], this molecule can probe a lot of simple sites and makes an excellent generic test molecule for determining for example the amount of step sites relative to terrace sites. Perez-Alonso et al. used CO-TPD, for example, as evidence for the active site of the oxygen reduction reaction on platinum being on terrace sites.[84] Naturally, the structure of a catalyst depends on the atmosphere and one should be careful when trying to extrapolate UHV results to working conditions under high pressure[85] or immersed in liquids[86]. So while UHV studies gives very useful before-and-after information, it is important to also consider characterization techniques describing the catalyst under operating conditions.

Copper is a unique electrocatalyst when it comes to hydrogenating CO and CO_2. This is conveyed in figure 5.1 where various metals has been plotted versus the binding energy of adsorbed hydrogen and adsorbed carbon monoxide. With the metals colored to indicate their major CO_2 reduction products, the metals are clearly divided in four groups with copper uniquely in the middle of the plot. Copper is the only pure metal catalyst that converts CO and CO_2 into products like, CH_4, C_2H_4, and other hydrogenated carbon products. The problem is that it is not very selective towards a specific product, and so a lot of research has gone into identifying the catalytic properties of copper.[87]

This part of the project was motivated by the stir when oxide-derived copper (OD-Cu) was discovered to favor multicarbon products over the formation of methane or formate.[88,89] Feng et al. correlated the ability of multicarbon product formation of copper nanoparticles on carbon nanotubes with the presence of grain boundaries.[90] Eilert et al. attributed this explanation to the presence of subsurface oxygen[91], while Fields et al.

suggests that such oxygen would likely be either unstable or far enough from the surface to have an effect[92]. Recent evaluation of the results for OD-Cu suggest that the intrinsic activity is not that different from poly-crystalline copper except for the suppression of C1 products due to local pH effects,[92,93] while recent experiments by Lum and Ager indicate at least three distinct sites in OD-Cu with different selectivities which are not present on planar copper surfaces[94]. Copper single crystal studies never show CO desorbing at temperatures higher than 250 K[95–98], but CO-TPD experiments on OD-Cu showed CO desorption extending up to the room temperature region[99]. They tried to explain the higher energy peak by diffusion and readsorption of CO through the porous catalyst. However, a good simulated fit was not achieved until they introduced a new active site with a higher desorption energy than that of copper defect sites. In this project, we wanted to investigate whether this high-temperature feature of oxide-derived copper could be reproduced by creating a system of well-defined mass-selected copper nanoparticles. Specifically, by slowly increasing the projected coverage of particles, more of these will overlap with each other. The sites around these connections might be unique and representative of the grain-boundary type of sites which could explain the reactivity. By using the cluster source for this, we have a means of controlling the amount of overlapping nanoparticles in a well-defined porous system. This can further be coupled with experiments where the porous surface is treated by exposure to different gases such as oxygen to see if this has a lasting effect on the reactivity of the surface.

This brings us to the second question: the full copper CO-TPD spectrum has features starting down below 120 K, so while CO-TPD was already possible on the setup[84], we would have to modify it in order to cool down the samples as much as possible. A cooling extension to the sample manipulator in the preparation chamber was available from Scienta Omicron GmbH[100] in order to cool down samples with liquid nitrogen. This, however, would only be able to cool the samples down to 140-160 K, since it works by copper braids attached to the sampleholder stage at one end being cooled at the other. This way of cooling is too indirect for such low temperatures as radiative heating from the surrounding system is too large. By building a dedicated stage for CO-TPD, we can ensure that the

sample has a good thermal contact to a cooling reservoir to reach the lowest possible temperature.

5.2 Implementation

The method is implemented in the setup in such a way as to enable TPD on samples with freshly prepared mass-selected nanoparticles and utilize the characterization techniques in the setup. This infers certain requirements for the sampleholder design as discussed in [20], and over the course of my PhD project, I have made some adjustments to the initial design to correct some mistakes and improve the functionality.

5.2.1 UHV design

The TPD setup is illustrated in figure 5.2 as a schematic (a) in relation to the UHV chamber and (b) an image through a CF63 viewport. The TPD assembly consists of a cooling block made of a OFHC copper cylinder 4 cm in diameter so it fits through CF40 tubing. The cooling block is hollow inside with two 1/4" tubes providing a connection to the atmospheric side of the setup so liquid nitrogen can be circulated for cooling. In the original design, the cooling block was sitting directly on the flange using the block itself as a copper sealing gasket. By the end of that project, the first cooling test showed that the connection started leaking when the temperature got down to around 220 K.[20] The leak was fixed by submersing the cooling block in liquid nitrogen after the initial tightening of the bolts and nuts, and then carefully tightening them some more when the copper had contracted in the cooled state. This allowed us to reach about 175 K which was only halfway to the goal. By modifying the COMSOL model of the system[20] to fit the data I had acquired from the cooling test, it was very clear that the block absorbed too much heat from the surrounding system, and the effect was immediate when isolating the cooling block from the flange by floating it on the LN_2 tubes. Extending this tubing to around 10 cm would reduce the minimum temperature to about 89 K according to the model. A thermocouple (K) is attached to the inside of the cooling block (figure 5.2b

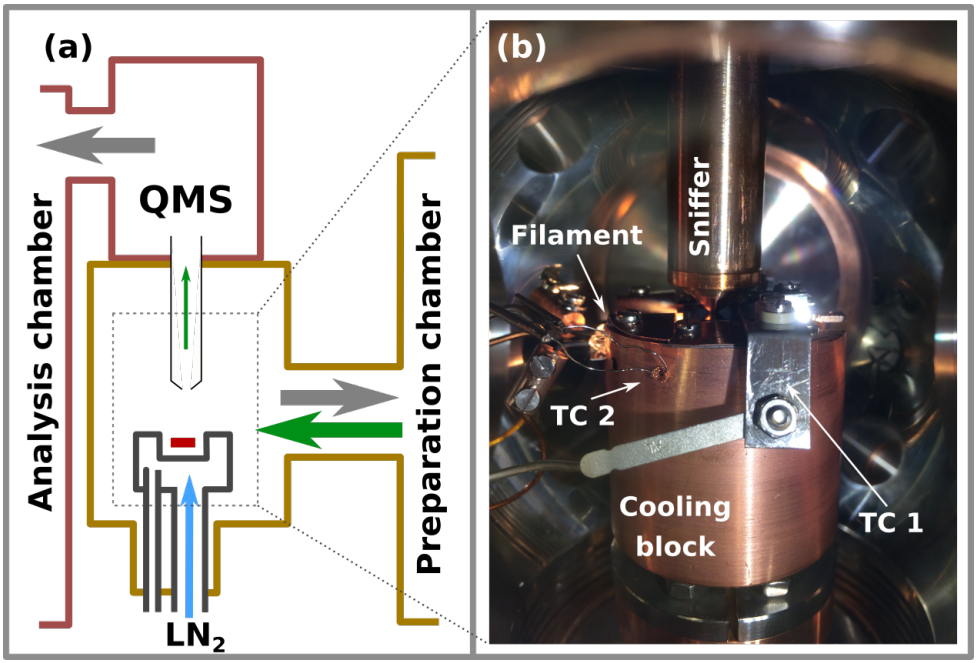

Figure 5.2: TPD setup overview. (a) Schematic. The TPD cube is pumped (gray arrows) via the preparation chamber and connected via a sniffer to the QMS, which is pumped via the analysis chamber. Gases are dosed via the preparation chamber (green arrow). Samples are cooled by contact to a Cu block by flowing liquid nitrogen through it (blue arrow). The cooling block nests a filament for subsequent heating with radiation of heat and electron bombardment (red box). (b) image of the cooling block and sniffer. A thermocouple (TC 2) measures the temperature of the cooling block. The sample thermocouple is contacted to TC 1. In this image, the sniffer is approached to a sample, and the filament is glowing hot.

- TC 2) and now measures a minimum temperature of 84-85 K with the 10 cm tubes implemented. The thermocouple is attached by pushing it into a small hole drilled in the side of the cooling block with a small rolled-up copper mesh. Extending the tubes beyond 10 cm promised very little gain in terms of minimum temperature based on the COMSOL simulations.

The TPD chamber

The cooling block is assembled in a cube with CF63 and CF16 flange connections on each face and corner, respectively. This is called the TPD *chamber* or *cube*. Relative to figure 5.2:

- The cube is attached to the preparation chamber where a small wobblestick can reach the cooling block to insert and remove samples from the right.
- The cooling block is mounted from the bottom.
- Electrical connections are made to the left flange. This contains a double K-type thermocouple feedthrough to measure temperatures of the sample and cooling block simultaneously, and two SHV (10kV/5A) feedthroughs for the filament heater.
- Top connects to the quadrupole mass spectrometer with the sniffer separating the two chambers.
- Front CF63 flange and the two closest top CF16 flanges have viewports connected.
- All remaining flange connections are blind.

Figure 5.2b highlights the alumel contact for the alumel part of the thermocouple mounted on the sample. The corresponding chromel contact is mirrored on the opposite side. They are isolated from the grounded cooling block via PEEK spacers and this, I believe, sets the maximum limit for the bakeout temperature of the TPD module to below $200 - 250\,^{\circ}\mathrm{C}$. As this is above the maximum bakeout temperature of the system ($150\,^{\circ}\mathrm{C}$), this will rarely pose a problem. If using the cooling block assembly for high-temperature purposes, one just have to keep an eye on the cooling block temperature. The peak is in close contact with the cooling block, so the maximum sample temperature should not be affected by this. It is also uncertain whether thermal expansion of the cooling block due to higher temperatures will be a problem given that we had to cold-tighten it to

make it leak-tight at low temperatures. Successful local bakeout of the TPD and QMS chambers has been achieved up to 210 °C where it had a dedicated pumping path via the loadlock. The filament heater is an Osram 150W/15V pin bulb with the protective glass/atmosphere removed to bare the tungsten filament. A heating current is supplied by a NTN 140-6,5 power supply from FuG Elektronik GmbH modified so it can float at ±2 kV. A Glassman PS/EK02R300-220 floats the filament at -2 kV to support electron bombardment assisted heating. Since the bias is negative, electrons are emitted from the filament in all directions. A tantalum foil (0.05 mm thickness) at the same bias as the filament is used to form an electron deflector to direct the majority of energized electrons towards the sample. Sheets of mica are used to ensure that the filament and electron deflector does not short to ground.

Sample temperature control

Readout of the sample temperature is made with a single channel from a DI-2008 Data Acquisition System from DATAQ Instruments data collected at 2000 Hz. Since the data is communicated in minimum packets of 8 points, the effective sampling rate for updated temperature measurements is 2000 Hz/8 = 250 Hz or every 4 ms. To reduce noise, a digital filter is applied that makes a simple linear best fit to the data points within the last 140 ms. This simple method seems to work just fine compared to some FFT-based filters I experimented with. The latter tends to be very inaccurate at the end points of the data sets, which is the most important aspect in this application. Python drivers for serial communication with the filament power supply and sample temperature reader is integrated into a Python program with a simple terminal user interface. The temperature of the sample is controlled by a PID loop calculating the error in the system based on the measured versus desired temperature and modifies the heating current through the filament as a result. With the most recent sampleholder design (figures 5.3 and D.7), linear heating from $100 - 1270$ K was achieved at 0.5 K/s (figure D.4).

QMS and sniffer connection

Pumping of the QMS happens via a CF40 bellow to the analysis chamber. The QMS and sniffer is mounted on a single-axis linear motion drive so the sniffer can be moved close to the surface and back again as necessary. The sniffer aperture is 1 mm in diameter and allows a large pressure difference between the two chambers.

Adsorbent gases are at present dosed by leak valves into the preparation chamber and, by extension, the TPD chamber. When dosing argon to $1.0 \cdot 10^{-6}$ mbar in the preparation chamber with the sniffer fully raised, the analysis chamber pressure increases by only $1.5 \cdot 10^{-10}$ mbar. When the sniffer approaches to within $1 - 2$ mm of a surface, the transmitted amount of gas rapidly decreases with the distance - see figure 5.4.

5.2.2 TPD sampleholder

The original sampleholder design seemingly worked well enough, but it was tedious to use and it took a dedicated Master project by Julius Needham to devote time enough to identify the flaws:[101]

- Despite extensive PID tuning, it was very difficult to achieve a good linear heating ramp.
- The system was so efficient at drawing heat away from the sample that heating above the $100 - 400$ K region was very difficult.

The first solution to this was cutting a window in the bottom of the sampleholder to provide line-of-sight between the filament and sample. I worried that this might increase the minimum sample temperature by some 10 K, but this proved unfounded. The cooling capability of the setup was largely unchanged, while the heating capability was substantially improved. The altered flow of heat in the system revealed that we, at times, suffered from a poor thermal contact between sample and thermocouple.[101]

The sampleholder at this point consisted of a baseplate, a sample, a thin mask, and the thermocouple block. Assembling this usually meant putting

the sample in the indentation in the baseplate meant for this. Then the thermocouple was hooked around the mask, so that it would end up tucked between the mask and sample surface. The sandwiched layers was fastened in the front by a M1.6 screw between the mask and baseplate, while a M2.0 screw in the back fastened all layers at the thermocouple block. Fastening especially the front screw too much could cause the mask to bend away from the sample near the thermocouple probe and the measured temperature would in this case represent the floating thermocouple probe or the mask. The sample would then act as the heating element instead the heated element making it essentially impossible to control the temperature.

New sampleholder design

To ensure a more consistent thermal contact between the sample surface and thermocouple, I came up with the design shown in figure 5.3a, where the different aspects of mounting a sample has been decoupled:

- The sample indentation in the baseplate is still 0.5 mm deep, but the length has been reduced to 14 mm to give more threading for the thermocouple screw.
- The thermocouple block is now attached directly to the baseplate and its only function is now to ensure the thermocouple circuit for the sample.
- A *brace to ceramic block* fits around the thermocouple block and into slits in the baseplate to provide anti-rotation both during mounting and in case the M2 mounting screw loosens inside the vacuum.
- A set of M1.0 threaded holes along the two long edges of the baseplate provide a means to fasten different objects to the baseplate.
- A simple brace has been designed to bridge the sample with a threaded hole for a M1.0 screw to pin the thermocouple tip against the surface, and

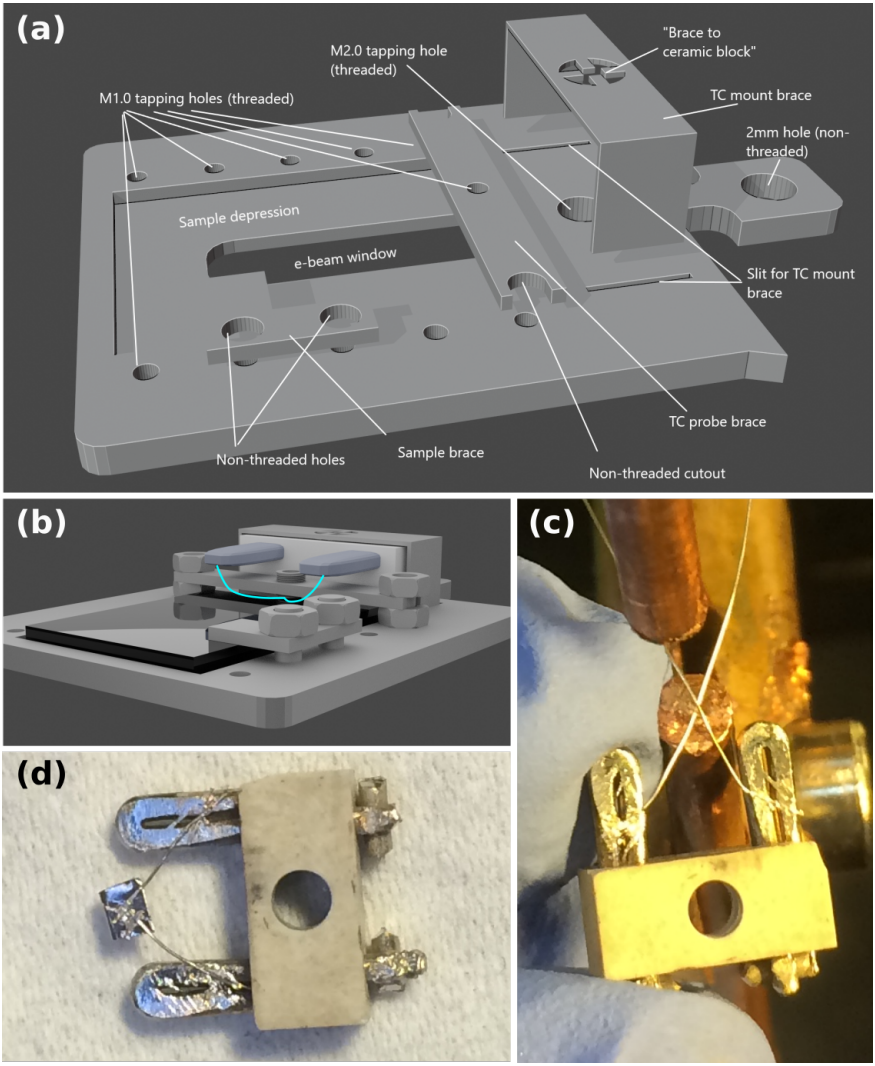

Figure 5.3: New TPD sampleholder design (a) with key features identified and (b) mounted with a glassy carbon sheet (rendered example image) The blue wire indicates the thermocouple probe attached under a fixing screw which is held by the *TC probe brace*. (c) image of my spot welding technique for the 0.125 mm thermocouple, and (d) the finished result including the "pressure cup" of Ta foil.

- a set of braces can be designed to match specific sample geometries for the purpose of clamping the sample to the baseplate and attaching a thermocouple.

The prototype for this was made of a tungsten-copper alloy (60/40 at.%) for its high heat conduction like in the original design[20] and has been used for the preliminary results presented in section 5.4.3.

The thermocouple

The *thermocouple block* consists of an alumel (K-) and a chromel (K+) contact embedded in a Macor ceramic block. For the thermocouple tip, I used 0.125 mm diameter type K wire since this should provide a time response around 0.1 s[102] with a maximum temperature of 590 ℃[103].

Spot-welding these thermocouples was a little tedious, but the following method made the task a lot easier for me. First, weld the individual thermocouple wires to their respective contacts and then flip the contact block so the wires cross between the electrodes of the spot-welder (figure 5.3c). From here, it is rather simple to adjust where the wires cross, weld them and snip the excess wire. Applying a short to medium burst of somewhere between 30 to 40 W s worked for me. Pinning the tip with a screw, however, was difficult. Mostly, the wire would be caught by the threading and wind away from the surface instead of being pinned to it. To circumvent this, a small piece of 0.05 mm tantalum foil was spot-welded to the thermocouple junction and folded into a "cup" to catch the screw and apply pressure on the thermocouple for good surface contact (figure 5.3d).

Once the thermocouple block and braces has been properly fixed to the baseplate, it only takes a few minutes to loosen the thermocouple pinning screw, slide the sample out, insert a new one, and then tighten the pinning screw again.

Dimensions and restrictions

The sample indentation area is 10x14 mm^2. When assembling a sampleholder there is a few restriction that must not be violated. These are gathered in the following list and should be checked before loading the sample into the UHV system.

- Nothing must protrude below the baseplate. Otherwise the sampleholder will not slide in the cooling block or the preparation chamber manipulator.

- The height of attachments put in the two rows of multi-purpose threaded holes must not exceed roughly 3.1 mm. Otherwise the sampleholder will not slide underneath the thermocouple contacts on the cooling block.

- Attachments put in the left row of multi-purpose threaded holes has to leave some space to the edge. The exact clearance is not known, but the M1.0 flat pan screws used in figure D.7a cleared every stage just fine. Fixing a brace with a M1.0 nut instead caused the sampleholder to bump into a contact on the analysis stage. The maximum size is somewhere between that of the flat pan head and the long side of a nut.

- The height between sampleholder bottom and the thermocouple contacts should be measured with a caliper as 3.7 ± 0.1 mm. Otherwise, the contacts on the sample will not connect properly with the contacts on the cooling block.

- From the other restrictions, the maximum height of a sample is about 3.5 mm with the extreme heights requiring extra cutout from the sampleholder bottom and clever braces to hold the sample.

5.3 Experimental procedure

To perform TPD experiments on this system, I suggest the following general guidelines concerning degassing the TPD stage, making sure different experiments can be compared, and managing background signals.

5.3.1 Degassing the stage

TPD is very sensitive to the cleanliness of the surface, so a proper degassing of the stage is recommended before starting experiments. This is especially important if investigating a sensitive surface like mass-selected nanoparticles that you cannot reclean by sputtering with argon if the surface becomes dirty (in the UHV sense).

Before connecting the liquid nitrogen and with the sample hidden safely in the analysis chamber, degas the filament carefully up to 5,A (corresponding to 25,W) without electron bombardment. At high temperatures, tungsten evaporates in vacuum, so sustaining high heating currents ($> 5\,\mathrm{A}$) should be done with care. With a base pressure of $1.2 \cdot 10^{-9}\,\mathrm{mbar}$ in the preparation chamber, I managed after a degassing to sustain 5 A for ten minutes while keeping the pressure below $2.5 \cdot 10^{-9}\,\mathrm{mbar}$. The maximum heating current for the filament during the experiment depends on the type of sample and the temperatures you intend to reach. The filament should at least be degassed in ramps up to beyond these currents until the worst degassing is done. Then with heating current off, switch on the high voltage bias and ramp the heating current up to degas with electron bombardment active.

When degassing is done and the base pressure is back, connect the liquid nitrogen to the cooling block. With a decent flow, the TPD stage will cool down in less than 10 to 20 minutes and will for the duration of the experiments act as a cryopump. One could use a flow of gas at room temperature if LN_2 experiments are not needed.

5.3.2 Approaching the sniffer for a measurement

When the sniffer is within 1 to 2 mm of the surface, the QMS will be highly sensitive towards molecules desorbing from the surface while any signal from random molecules in the background is suppressed. The distance from sample to sniffer also determines how large an area of the sample is probed. So to get comparable measurements across experiments, the approach of

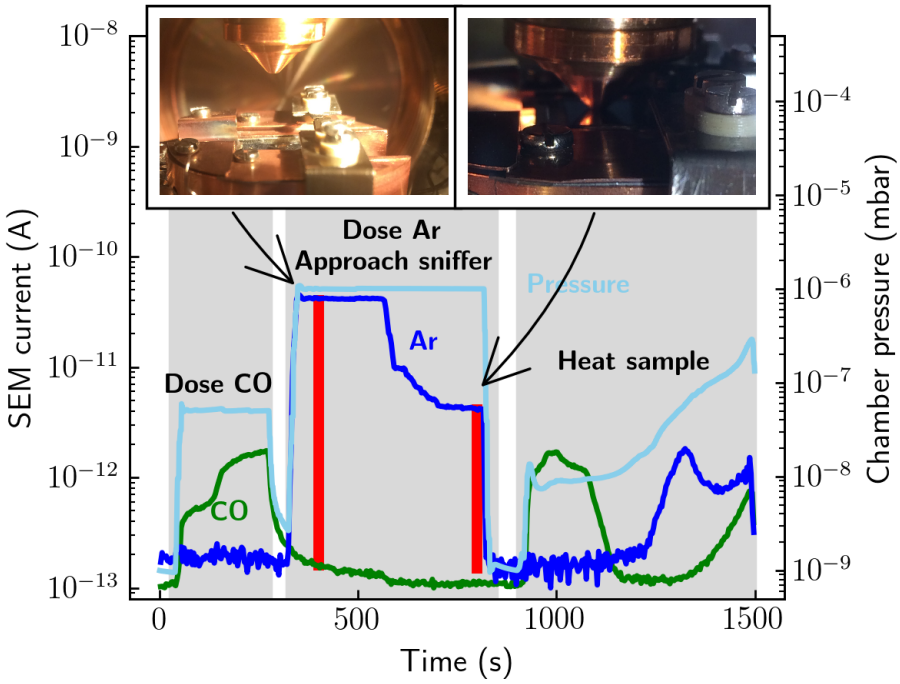

Figure 5.4: Illustration of the sniffer approaching method prior to a TPD experiment. CO (mass 30, green) and Ar (mass 40, blue) on left axis, chamber ion gauge pressure (light blue) on right axis. Magnitude of Ar signal through the sniffer is marked with two red bars: first, with the sniffer raised high to get the maximum background signal (left inset), second, sniffer approached to the sample until Ar signal is reduced by 90 % (right inset). Sample data: Pd_2Sn on silicon.

the sniffer has to be systematic. Figure 5.4 shows a CO-TPD experiment, where the sample is dosed with CO the first 300 seconds while the sniffer is fully retracted. The CO leak valve is then closed and Ar is dosed by leak valve until a preparation chamber pressure of $1.00 \cdot 10^{-6}$ mbar is reached. The argon QMS signal increases by a certain amount (first red bar) depending on the sensitivity of the mass spectrometer and transmission of the sniffer. Approach the sniffer slowly until the signal of argon has been suppressed by a certain amount (second red bar). Remember to take the background signal into account when calculating how much the argon signal is suppressed. Close off the argon and wait a few minutes for the signals to reach the baseline before starting the experiment.

This is the procedure to make sure the sniffer reaches close to the same distance from the surface in every experiment so intensities can be compared across different experiments.

5.3.3 Background signals

It is important to know the shape and size of background signals to avoid getting any false positives of surfaces with none or low signal. A piece of silicon was mounted in the new sampleholder and loaded in the system for a measure of the background signals at low temperatures.

First, the dose of CO was varied between 5 to 37 L with the sniffer at maximum transmission to get a rough uptake curve for the background and a sense of reproducibility (figure 5.5a). The background has a relatively intense peak between $100 - 130$ K and then a broad weak shoulder at $150 - 160$ K consistent with previous observations.[101] Full coverage appears to be reached somewhere between $5 - 20$ L. In figure 5.5b, background signal is plotted as a function of the sniffer-to-surface distance as measured by the reduction in argon ($m/z = 40$) signal. The points of figure 5.5a is projected onto 0 % argon reduction in figure 5.5b since they were recorded at maximum sniffer transmission. The new points were measured with a dose of approximately 20 L as indicated by the color.

Although the shape and intensity of the background varied slightly over the

$4-5$ hours it took to conduct the experiment, it seems safe to draw some conclusions from figure 5.5. Raw background signals at full transmission can have pretty high intensities in the region between $100-130$ K. However, the suppression of background signals is roughly proportional with the measured reduction of argon dosed deliberately in the background. This makes it possible to make a claim for the example in figure 5.4 with 90 % background reduction, that any measured background signal should be on the order of $2.5\ \text{pA} \cdot (100\ \% - 90\ \%) = 0.25$ pA (based on the inset, figure 5.5). The magnitude of the latter will depend on the state of the sniffer and the desorption source (likely the copper cooling block and the filament nest) and the sensitivity of the mass spectrometer. This experiment was made in the beginning of November, 2020, which is after I had replaced a broken

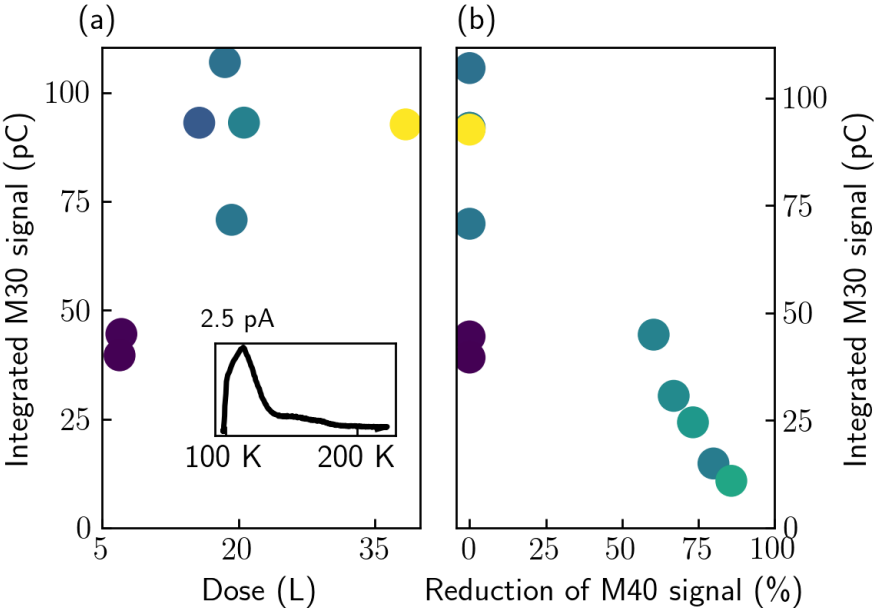

Figure 5.5: Screening of background M30 signals ($C^{18}O$). (a) Uptake curve with the sniffer raised to transmit maximum chamber signal. The inset shows the typical shape of the background signal. (b) Screening ability of the sniffer. 0 % reduction corresponds to the raised sniffer as in (a). Colors represent the dose defined by (a).

filament with a homemade one in August, 2020 (see appendix A), and after the electronics controller had to be re-tuned after lending it to another setup for some troubleshooting. The argument of proportionality should only be invalid if the sniffer is somehow damaged, though.

Furthermore, the intense backgrounds require a full dose of more than 5 L (corresponding roughly to 3 minutes at $5 \cdot 10^8$ mbar), so keeping the dose on the sample below this limit should further suppress the background signal by a factor 2 or more.

5.4 Results

Here is presented some of the preliminary results acquired with the method so far. For all experiments, isotope labeled $C^{18}O$ ($m/z = 30$) has been used as a probe.

5.4.1 Polycrystalline Cu reference foil

To compare results with the literature, we need a reference sample. To this end, a 1 mm thick slab was cut from OFHC copper to use as a reference for polycrystalline copper like Verdaguer-Casadevall et al. did.[99] Figure 5.6 shows an uptake curve for this sample after several cycles of sputtering with 1 keV argon and annealing to 500 K. During the first annealing cycles, silver segregates from the bulk to the surface. The sample was clean when I could no longer detect any signal from Ag in LEIS after annealing and the LEIS copper peak gave more than 300 kcps after sputter cleaning.

Full coverage is practically achieved beyond 3 L as seen in figure 5.6a and consistent with CO uptake on a cleaned Cu(221) crystal.[97] Figure 5.6b shows a high-temperature peak at 208 K at low coverages and 202 ± 2 K at higher coverages. A second peak emerges from 158 K down to 140 K. At very high coverages, a shoulder is seen at 105 K. The general shape resembles the Cu foil of Verdaguer-Casadevall et al.[99] although their high-temperature feature (attributed to defect sites) is measured at roughly 15 K higher temperature. The difference in heating rate can account for

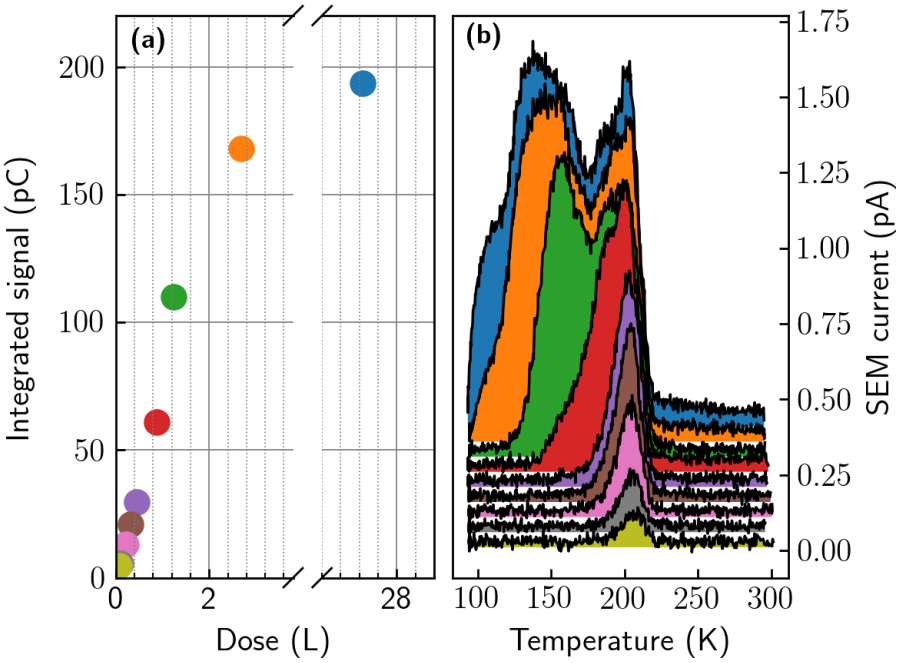

Figure 5.6: (a) Uptake curve calculated for the CO-TPDs in (b) on sputtered polycrystalline copper. Heating rate about 0.5 K/s. For doses larger than 3 L, the surface is close to fully covered. All measurements were done using the old sampleholder.

about 10 K (by simulating equation (2.7)) and the remaining 5 K could be attributed to variations in thermocouple accuracy and thermal contact. This general shape is therefore considered a good copper reference foil.

While I often got reproducible results on this sample, at times, I also got reproducible contradicting results on the exact same sample. I came to think of this as a "bad" copper spectrum. Foil 1 and 2 in figure 5.7 are thus the same sample as in figure 5.6 but at different stages along my project. Regardless of how much argon sputtering I did, a "bad" copper spectrum looks as if the entire defect peak is missing and the second hottest peak has

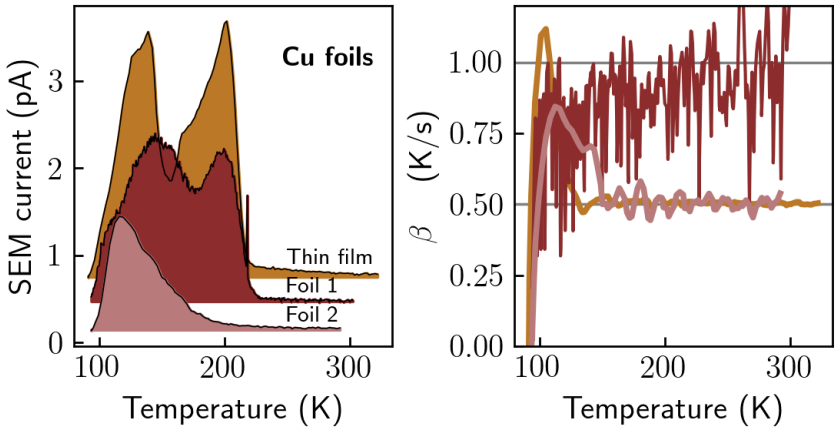

Figure 5.7: Comparison of different Cu CO-TPDs. Desorption of $C^{18}O$ on the left and logged heating rate on the right. **Foil 1** is the very first copper spectrum acquired late 2017 and represents an old "good" measurement. **Foil 2** is the same sample, but acquired early 2020 and represents a "bad" measurement. No apparent differences between the two detected by LEIS. The difference is attributed to variable thermocouple contact in the old sampleholders. A copper thin film mounted in the new sampleholder is shown for comparison.

very low intensity. This was very frustrating since both LEIS and XPS claimed a "bad" copper sample was just as clean as a good one, and around this time we had also struggled to get reproducible EC-MS results on the copper nanoparticles for paper VIII. With my current knowledge, it seems fairly clear that a "bad" copper sample is simply one where the thermocouple has lost its direct contact with the surface. I believe the "good" copper spectrum reappearing correlates with the sample being removed from UHV and remounted.

A 100 nm Cu thin film sputter deposited on silicon by Ezra Clark was mounted in the new sampleholder and is shown in figure 5.7 for comparison with the previous reference foil. The high temperature peak is very intense and matches the position of the other sample. The sharp and intense low-temperature feature is likely an artifact of the heating rate as the PID loop catches up to the setpoint. Less aggressive PID parameters can

mitigate this if needed.

5.4.2 Cu nanoparticles

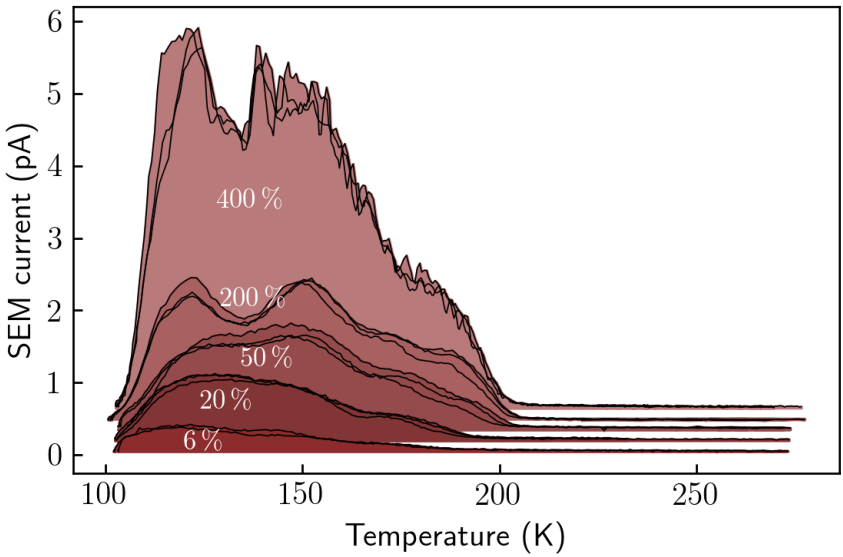

Figure 5.8: CO-TPD of 5 nm Cu nanoparticles at varying projected coverage. From bottom to top (dark to light): 6 %, 20 %, 50 %, 200 %, 400 %. The 400 % is offset 3 K to align with 200 %. Acquired on old sampleholders with a heating rate of 0.5 K/s. Adapted from [101].

Now that we have a decent reference for polycrystalline copper, we can explore the desorption from nanoparticles by varying the projected coverage. Cu nanoparticles of 5 nm sizes were prepared on glassy carbon substrates corresponding to the studies for papers VII and VIII. Projected coverage was varied between 6 % and 400 % coverage as shown in figure 5.8. All sample deposition and subsequent TPD characterization in this subsection was conducted by Julius Needham. [101]

Starting at low coverage, there seem to be two main peaks at 120 K and

150 K, and a tailing shoulder at 170 − 175 K. At 50 % coverage, a fourth shoulder appears at 190 K, which grows in intensity with increasing coverage. At this stage it is not clear whether the fourth shoulder originates from special sites at the overlap of adjacent nanoparticles or just certain under-coordinated sites like corner atoms being present in such small amounts at low coverages that the peak is below the noise level. At this point, we often had problems with getting good heating ramps, and it is entirely possible that some of the apparently distinct peaks are in fact artifacts of the local heating rate. To improve the heating ability, we cut a window in the sampleholder to have a direct line between the filament and sample. This worked wonders for the heating ability, but clearly illustrated the problems we have had with an unreliable thermocouple contact. Further experiments seemed like a waste of time until I had come up with a way of getting reliable temperature measurements (figure 5.3).

When there is better control over the temperature, it would be interesting to redo some of the spectra of figure 5.8 and see if it looks much different. With these spectra, we had a focus on reproducibility with regards to the shape and possible annealing/sintering effects. So every spectrum was acquired three times per sample. In future experiments, adding some uptake curves might help elucidate whether the two high temperature shoulders are two distinct sites from how they fill when increasing the dose. Also for the low coverage samples, a dilute dose might make it possible to increase the heating rate to gain the benefit of higher signal, but without the high temperature peaks being absorbed into the low temperature peaks. If the shoulders at high temperatures are in fact due to distinct sites on the individual nanoparticles, they should also be more sensitive to variations in nanoparticle size selection.

With regards to the original motivation for this project, it seems very clear despite any thermocouple uncertainties, that the sites from these samples have lower desorption energies than that of sputtered copper - not higher. It is therefore doubtful that strong-binding sites like indicated in OD-Cu [99] can be represented with this model system. It may be sites with modified copper that is responsible for the high binding energies seen for OD-Cu. Studies by Abild-Pedersen et al. suggest that atomic carbon present at the

copper surface facilitates a reactive site that dissociates CO.[82,104] It is not at all unreasonable that carbon would have been present in the study by Verdaguer et al. If this effect transmits to the reactivity of copper in ultra-high vacuum, this would make for some nice well-defined UHV experiments, and could very well explain the CO-TPD spectra of OD-Cu. For Pd, though, residual carbon seems to weaken the CO binding energy.[105] It should be simple calculations for theoreticians to estimate whether this is likely. It is also still a possibility that the best efforts at modeling the diffusion through the porous surface of oxide-derived copper was not sufficient, and the explanation for the CO-TPD spectra could simply be diffusion and readsorption.

5.4.3 Binary alloy PdSn thin films

This section contains preliminary results to probe whether CO-TPD could be used to support a project by Ezra Clark where Pd_xSn_y thin films are sputter deposited on flat silicon substrates. In vacuum, Pd and Sn forms a bimetallic film in which intermetallic electron transfer from Pd to Sn modifies the valence band in a way that gives a density of states which resembles Cu at the right Pd/Sn ratio. On exposure to air, Sn segregates at the surface to form a passivating oxide layer which can easily be sputtered away to reveal the bimetallic surface beneath. A similar tactic was employed by Bai et al. by forming carbon-supported PdSn nanoparticles via a "modified wetting chemistry reduction method".[106] They report an almost 100 % faradaic efficiency toward formation of formic acid and attribute this to the special configuration of Pd in the $PdSnO_2$ surface. They also performed CO_2-TPD experiments 300 to 1200 K in which a vague trend is seen depending on the Pd/Sn ratio. Another study showed that forming a thin PdSn bimetallic layer on a Rh(100) crystal exhibits a sharp symmetrical peak at 250 K with 5 K/s consistent with IRAS data that isolated Pd atoms binds CO weaker than monometallic Pd.[107] CO desorption from pure Pd is mainly expected in the region between 300 to 550 K [105,107,108] with Matolin et al. reporting an extra peak between 550 to 800 K attributed to CO dissociation on sputtered palladium[109]. A similar study was done on a mixed Pd/Zn system where the high energy CO-TPD

peak moved down to copper-like temperature.[110]

The following experiments were initiated with roughly one month left of my PhD studies, so I basically had one shot per sample to gather the information to

- test the new sampleholder design using silicon as substrate including heating to higher temperatures, and
- determine if a trend is visible depending on the Pd/Sn ratio.

The results for the individual experiments are presented in chronological order in appendix D where comments regarding the test of the sampleholder is made. Here I present the result of the various thin films.

Comparison

Despite new hints about the uncertainty of the thermocouple measurements, the first CO-TPD spectrum of every thin film is collected for comparison in figure 5.9. They should still depend roughly the same way regarding the temperature error as the substrates are of the same type. A trend is clearly seen where increasing Sn content moves the desorption spectrum towards the copper region which supports the hypothesis of using these intermetallic electron transfers to reduce the reactivity of Pd. The CO-TPD spectra for the different samples shown in figure 5.9 were integrated and is shown in figure 5.10. The measurement for $PdSn_2$ and the second measurement for Pd_2Sn are very close to the background level shown in figure 5.5a. It looks like it a linear fit through zero, will match Pd_2Sn and Pd decently whereas PdSn and $PdSn_2$ deviates more from this with increasing Sn content. This could be explained either by difference in how close the sniffer was approached to the surface after dosing CO, or by the binding energy of the Pd sites becomes close enough to the adsorption temperature that the surface is not fully covered with CO when the experiment is started.

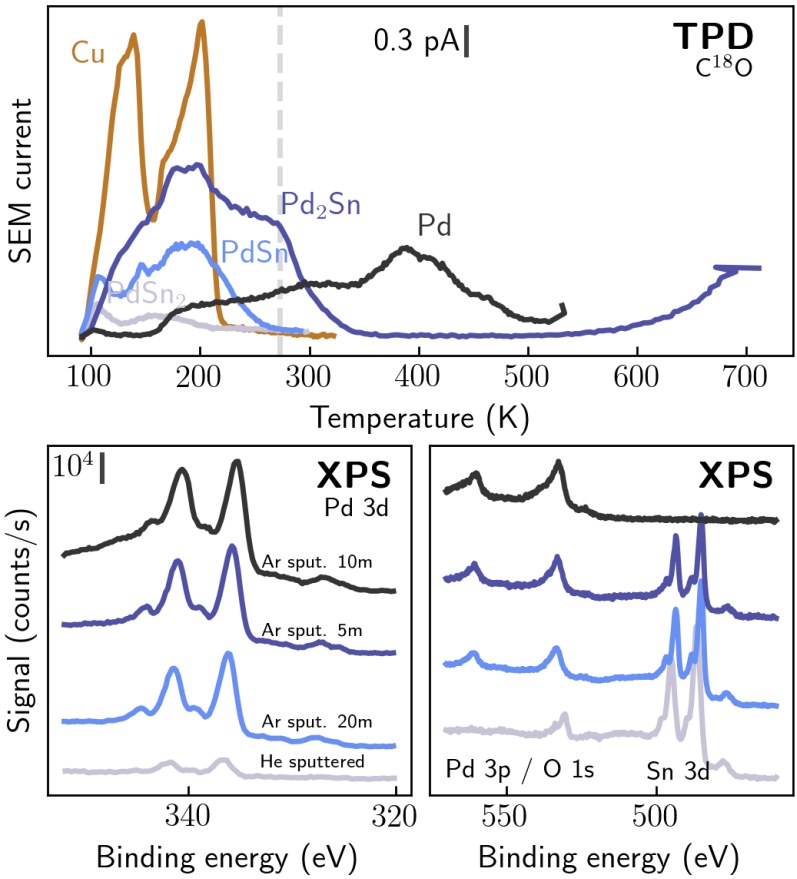

Figure 5.9: Comparison of various thin films on silicon. CO-TPD **top** and XPS **bottom** of the Pd 3d (left) and Sn 3d (right) peaks from survey scans. The Sn 3d region is extended to include Pd 3p and O 1s. Samples: grey - $PdSn_2$, light blue - PdSn, purple - Pd_2Sn, black - Pd, orange - Cu. A trend is seen towards higher CO binding energies for more Pd content in surface. First measurements used with heating rates of 1 K/s for Pd_2Sn and 0.5 K/s for the rest. Note that $PdSn_2$ is only sputtered lightly with 1 keV He and Pd_2Sn is only sputtered 5 minutes with 2 keV Ar.

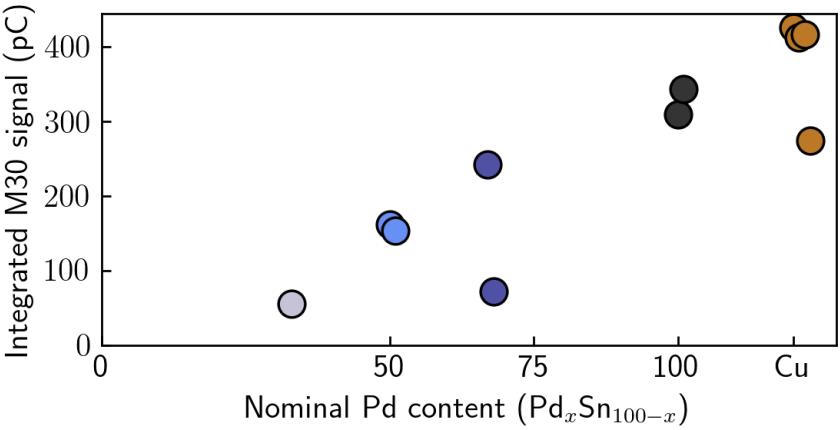

Figure 5.10: Comparison of the total signal from Pd_xSn_{100-x} thin films on silicon as a function of the nominal Pd content and compared with the Cu thin film measurements.

5.5 Summary and outlook

LN_2-cooled CO-TPD has been implemented in the Omicron UHV system by designing a dedicated chamber for the technique. Using a sampleholder that fits into the other analysis stages in the system, it is possible to cool samples down to 95 to 100 K and do CO-TPD - presently using $C^{18}O$ isotope labeled gas which offers a better sensitivity because of the low natural background. A few useful procedures for performing the experiments have been investigated, namely identifying the magnitude of the background signal and ensuring that different experiments can be compared.

The work is only just getting started, though, and some preliminary results were found for a few different systems:

Cu reference foil: It was shown how the setup is able to produce similar results to the literature albeit with strong indications that the

surface temperature might be wrongly estimated by up to 15 K.

5 nm Cu nanoparticles were investigated by varying the coverage from 6 % up to 400 % in order to create a semi-porous system where overlapping nanoparticles might produce unique binding sites. While the reactivity of the nanoparticles in general is found to be lower than for the defects induced in copper foils by argon-sputtering, we do see a higher-energy peak emerging with increasing coverage. At present stage, it is not clear whether this peak is just the natural presence of a low concentration of under-coordinated sites on the individual nanoparticles being scaled up to a signal that is detectable, or if it is an effect of overlapping nanoparticles.

Pd_xSn sputter deposited thin films show a clear trend (despite small issues with every experiment) where the reactivity of the Pd atoms decreased when increasing the relative concentration of Sn atoms in the thin films.

Continuing from here, some further investigation of the temperature measurements have to be made - preferably on single crystals. A Cu thin film on glassy carbon will also clarify if the different substrates have an effect on the temperature measurement or shape of the spectra - which they should not have except for very thin films. Some of the measurements on 5 nm Cu nanoparticles has to be remade with more reliable temperature control for verification. More dedicated experiments can possibly provide more insight in the high-temperature peak of the high-loading nanoparticle samples. On the thin films or single crystals, the cluster source could also be used to put down a well-defined amount of carbon to test whether or not this changes the reactivity of copper.

The list could go on, but let it suffice to say that there are plenty of useful and interesting experiments to continue with as well as some more practical issues to get under control.

Conclusion and Outlook

Chapter 6

My contribution to the projects presented in this thesis has been very focused on methods, and many details are likely only relevant for the people in the laboratory in the future. I have really enjoyed working on the UHV system, and believe that I have left it in a better condition than I "received" it. To conclude my thesis, the projects presented throughout the thesis are summarized.

Chapter 3 covered the implementation of rastering the substrate during deposition of nanoparticles to smooth any variations in the beam of nanoparticles. With this method, it is possible to ensure a very homogeneous coverage of nanoparticles across the sample surface. The downside of this technique is that the coverage is calculated by the total current that neutralizes the nanoparticles, and since these are now no longer only deposited on the substrate, extensive simulation is necessary in order to estimate the correct average coverage. The implementation involved replacing two manual knobs for moving the sample with two stepper motors. Daily manipulation of samples is further simplified via a simple user interface. Depending on which parameters are critical for their study, future users can now make mass-selected nanoparticles following one of two methods:

The original method of keeping the sample stationary during

deposition offers the advantage that the uncertainty on the total mass loading is extremely low as calculated via the deposition current. There can potentially be very large variations of the local coverage, though.

Alternatively, the sample can be rastered, which produces a very homogeneous coverage across the sample, but add some uncertainty to the total mass loading.

Chapter 4 covered isotope studies and includes all the catalytic measurements in this thesis, which comprises two systems for OER catalysts:

Mass-selected Ni_3Fe nanoparticles were shown to be extremely stable and active as oxygen evolution catalysts in alkaline media. Furthermore isotope labeled studies asserted that there was no exchange of lattice oxygen during OER and any reactions are therefore taking place at the surface of the catalyst. With could therefore claim a turnover frequency for our 5.4 nm nanoparticles of $6.2 \pm 1.6\,s^{-1}$ at 300 mV overpotential. This is the highest recorded in the literature, and was possible because of the strengths of the model system comprised of mass-selected nanoparticles on a flat substrate.

RuO_2 and IrO_2 thin films were investigated as catalysts for OER in acid. Coupling the sensitive EC-MS setup with a high surface area RuO_2 foam, we detected oxygen evolution down to as low as 60 mV overpotential, which has never been seen before. Careful calibration and comparison to sputter deposited thin films show that the intrinsic activity is roughly the same as the thin films. Next, through isotope studies, we determine that there is some small amount of lattice exchange on RuO_2, but that it is on a much lower scale than dissolution processes and that the exchanged lattice oxygen is situated near the surface only. On a hydrous IrO_2 thin film, the lattice oxygen exchange is both larger than for the RuO_2 systems and penetrates deeper into the surface. Furthermore dissolution is only slightly larger than the lattice exchange. There is still a lot of data that needs to be assessed for this project to determine trends from outliers, but the end results should provide some valuable knowledge into the

mechanics of dissolution. Furthermore, I intend to use the experiences and tools from this project to contribute to the `ixdat`[80] project, which hopefully will help a lot of people in the future.

Chapter 5 introduced the implementation of another technique: CO-TPD, temperature-programmed desorption with CO. The project is still in early phases with details that need to be sorted out and experimental procedures that need to be perfected. I hope that my inclusion of details and some of my experiences will benefit future users at the setup in getting the most out of the technique. Despite some persisting issues with temperature measurement, I illustrated the technique with preliminary results on three systems:

A reference Cu foil gives a CO-TPD spectrum comparable with reports in the literature.

Varying the coverage of 5 nm Cu nanoparticles to past the 1 monolayer regime reveals an emerging high-temperature peak which indicates stronger-binding sites. At present it is not evident whether this is just the up-concentration of natural under-coordinated sites on the nanoparticles or due to unique sites from overlapping nanoparticles.

The binding energies of CO to Pd in Pd_xSn thin films decreases drastically with increasing relative Sn content, consistent with similar studies in the literature. At slightly more than 50 % Sn content, the binding energies of the surface Pd atoms are similar to those of sputter-induced defects on Cu.

Future studies include revisiting the measurements on Cu nanoparticles when the variation on measured temperatures is better understood, and then variying the size of the nanoparticles. Especially the low-mass regime will be interesting to probe. Lastly, it will be very interesting when the reactivity maps of TPD are coupled with the activity and selectivity of the catalysts in action.

Recurring UHV Problems

Appendix A

Over the cause of my PhD, I have experienced many things breaking - some of which interrupts the work flow until it is fixed. The list of things include things nearing its natural end-of-life like the channeltrons for the NanoSAM detector. Other stuff is electronics related not necessarily old, but suddenly dying, like one of the power supplies for the preparation chamber turbo pump, an ion pump controller, failing high voltage supplies for the TOF-MF, and an X-ray source controller sent for repair several times. Some things die in direct response to a power failure like the ion gauge controller for the cluster source.

Some cases of ultra-high vacuum components being worn are related to the ISE 100 ion gun suddenly acting in an unstable manner giving weird or vanishing signals in LEIS. This turned out to be because the filament had suddenly become crooked and sometimes shorting to ground. Another case was the three screws fixing the final einzel lens in the cluster source to a flange being slightly loosened over time until it drooped enough that it would short to ground when the adjacent gate valve was operated. Similarly, the ball bearings in the magnetically coupled transfer arm between the two Omicron main chambers worn out and had to be fixed, while for the X-ray gun the cooling water connection for the anode had corroded to a point where it had to be replaced while the pump in the

recirculating chiller for the anode cooling water also died and required replacement - presumably due to poor grounding control.

These are all fluke incidents, however, that requires a single fix. Here, I want to let in on some details on the more recurring problems that took a lot of time understanding properly which might help future users. This is:

- Replacing a broken QMS filament with a home-made one
- Fixing the leak current of the deposition stage
- Experiences with the magnetron sputter head shorting to ground

A.1 QMS: making your own filament

Replacing broken filaments is usually pretty straightforward and not a recurring problem as such. I would like, however, to share my experience with making my own filament using some thoriated tungsten wire we had in stock in a cupboard. I heard from Daniel Trimarco in the beginning of my PhD that he fabricated his own filament with success when the EC-MS QMS filament broke without any spare ones in local stock.

I measured the total length of the broken filament to draw a rough reference guide on a piece of paper. The braces from the broken filament was then cleaned and used to support the new filament by spot-welding the thoriated tungsten wire in a straight segment between the two braces as indicated in figure A.1a. The wire was then bent to produce the middle part that emits the electrons (figure A.1b). I misaligned the bend a little so the filament ended up slightly crooked. Not knowing whether or not this would be a problem, I decided to just mount it and try it out. The filament is shown mounted in figure A.1d where it extends a little past the Wehnelt electrode as it should. After a rushed bakeout and degassing step, the filament appeared to be working fine despite some higher carbon signals which decreased over time with further degassing. The mass spectrum in figure 2.3 was acquired some time later with this filament (after retuning the settings due to other circumstances).

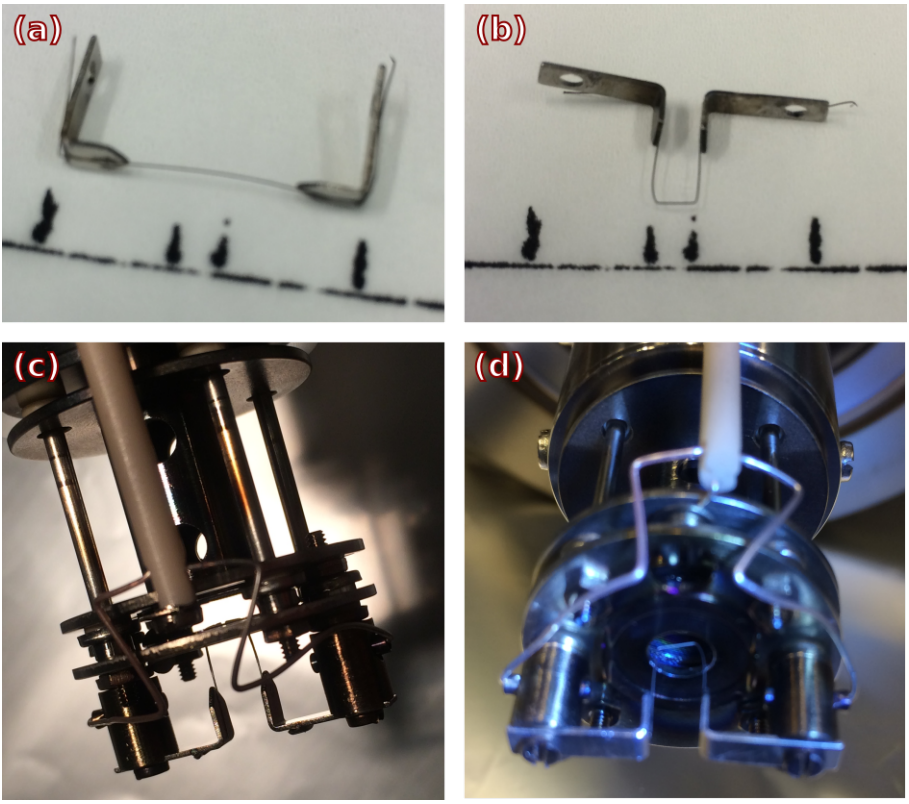

Figure A.1: Replacement of QMS filament by reusing the braces of the broken filament and spot-welding a piece of thoriated tungsten wire to them. (a) The braces with newly attached filament aligned to a roughly drawn reference, and (b) after bending to the final configuration. (c) Image from April 2017 of a broken yttria-coated iridium filament. (d) Image from August 2020 of the newly attached filament from (a) and (b). The mass spectrum shown in figure 2.3 was acquired after bakeout of the filament in (d).

A.2 Depositions: fixing leak current problems

Figure A.2 shows the sample stage that is used during depositions. In the image, it is disconnected from the main manipulator in the preparation

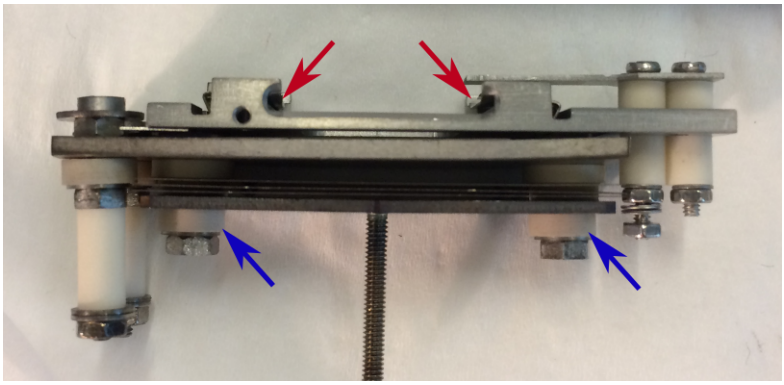

Figure A.2: Image of the deposition stage where the nanoparticles are deposited on a substrate. To measure the deposition neutralization current, the entire part shown in the image is isolated from ground potential by insulating ceramic spacers. The two ceramic pieces marked by blue arrows are usually the main culprits when dealing with high leak currents. The red arrows indicate the position of springs that clamp the sampleholder to the deposition stage.

chamber because the leak current is too high during depositions. Ceramic spacers are responsible for isolating it from ground, but these can get slightly dirty which makes them too conducting. "Too conducting" here means that a leak current of 50 pA is unacceptable at a bias of 45 V. This corresponds to a resistance of $45\,\mathrm{V}/50\,\mathrm{pA} = 0.9 \cdot 10^{12}\,\Omega$. This is a pretty large resistance that can be difficult to measure. In practice, it proved useful to connect one lead of the electrometer to ground and using the other lead to probe the ceramics at a bias of 45 V while the piece in the image is still attached to the main manipulator. In this manner, I identified that one of the two ceramics marked with blue arrows often appeared to be the main cause of the increased leak current. While the conductivity usually decreases when venting the chamber because the contaminants oxidize, I advice to disassemble the stage and clean all the ceramic pieces for the most stable result. This can be done efficiently by beading them on a thick stainless steel wire and blasting them with glass beads.

The source of the increased leak current appears to be contaminants on the ceramics from when the deposition stage has been used for sample

annealing (which is why the sample in figure 4.13 was only heated to 300 °C). I believe that this only poses a problem when heating is done at high enough temperatures for extended times so the temperature of the main part of the manipulator crosses some threshold and starts desorbing a lot of contaminants.

A second problem related to the deposition stage in figure A.2, is the springs marked with red arrows that clamp the sample holder to the stage. These get loose over time after which the samples will slide out of the stage when rotating it for sputter cleaning or depositions.

A.3 Depositions: shorting magnetron sputter head

Having to fix the leak current is time-consuming but straightforward to do. The most frustrating and recurring problem I have encountered during my work with Omicron and the cluster source, is after changing target when the magnetron head sometimes shorts to ground. The elements comprising the magnetron sputter head assembly is illustrated in figure A.3. The high voltage for the plasma control is applied to the magnetron sputter head on which the target is attached. The magnetron head is attached to the flange via the cooling water feedthroughs (arrows #4 in figure A.3c) which isolates it electrically from ground. The magnetron sputter head is surrounded by a chimney which is grounded through the attaching flange.

There are three possible ways for the magnetron sputter head to short. Two of them is caused by the very narrow gap between the magnetron sputter head and the chimney, which has to be small in order to ignite the plasma, I believe. The gap is indicated by arrow #2 in figure A.3b, where the head of the chimney is removed. Small particles can sometimes get in there and bridge the gap. This type of short can often be circumvented without breaking the vacuum by connecting the leads of an external power supply to ground and the magnetron lead. If a high enough power can be applied, it is possible to burn through the particle. The alternative short is caused by the chimney not being properly fastened so it moves slightly during deposition conditions and shorts the magnetron sputter head by

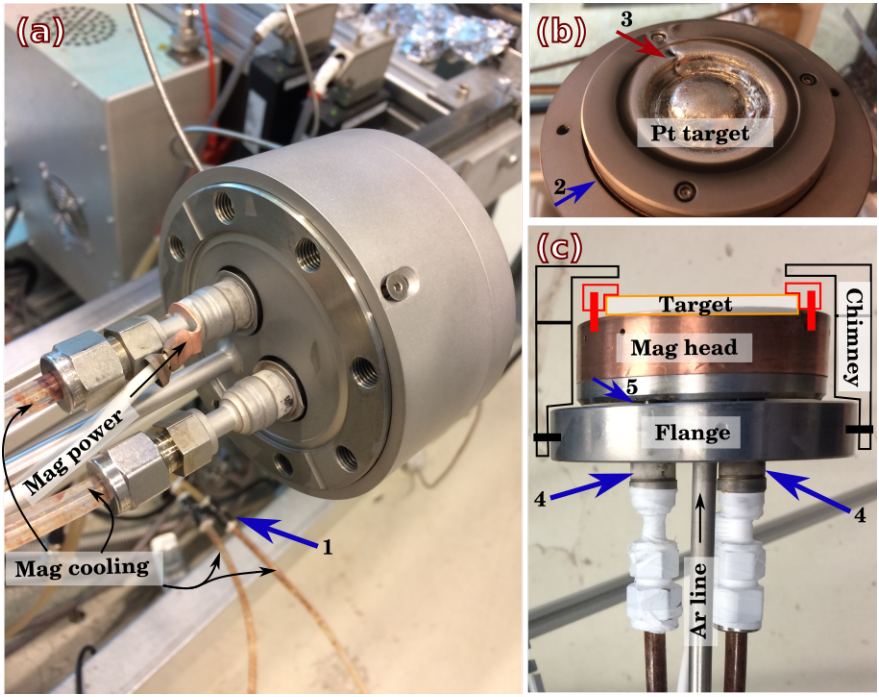

Figure A.3: Images of the magnetron sputter head at various stages to highlight the areas that can cause a short circuit in the magnetron. (a) backside of the fully assembled magnetron head, (b) the front of the magnetron with the head of the chimney removed. The blue arrow (2) shows the narrow gap between chimney at ground potential and magnetron sputter head at high voltage. (c) the fully disassembled sputter head with schematics drawn to indicate how the sputter head is assembled.

direct contact. This problem is difficult to against while the vacuum is broken, since everything can seem fine, from atmosphere to UHV and across the bakeout and cooling the aggregation zone down to 77 K. Then 10 minutes into tuning for deposition conditions, the magnetron shorts. When the aggregation zone later heats up again, the short circuit is gone. I believe this has to do with the chimney being able to twist slightly when some components are cooled while others get heated. The narrow gap is slightly asymmetric, which makes it difficult to align properly. The last

time I changed target during my PhD, I jammed a small piece of insulating Mica in between the gap on one side in an effort to prevent any risk of twisting while in vacuum. With the fixing screws barely tightened, I was not able to twist the chimney. With this setting, I experienced that I had to go to a higher sputter power (25 to 30 W) in order to ignite the plasma. Once it was started, however, the sputter power could be tuned down again. Aside from this detail, the solution seemed to work just fine.

If in doubt whether the short is caused by the chimney, remove it completely and measure the resistance between the magnetron sputter head and the flange in figure A.3c. The resistance should be on the order of 1 MΩ or more, but is sometimes as low as 100 kΩ which is dominated by the conductivity of the magnetron cooling water. This can be easily disconnected at the quickfittings at arrow #1 in figure A.3a to measure a resistance that is purely across the ceramic feedthroughs. Typical working conditions of the magnetron sputter head would be about 200 V to sustain a plasma current about 100 mA. At a resistance of 100 kΩ, the leak current would be on the order of 2 mA. This should not pose problem unless the leaking current induces a higher conductivity along its path. If the ceramics are dirty, then they have to be cleaned, e.g. by blasting them with glass beads (just be careful not to damage knife edge on the flange or the feedthroughs). This type of problem could arise when the valves on the argon line has been closed for one reason or another, and the magnetron is started without the user remembering to open the valve first. When the stream of argon dies, the magnetron plasma controller will ramp the voltage up to 1000 V in an effort to sustain the plasma. Since the ceramic parts of the feedthroughs are in air, sparking could be induced across the ceramics which leaves them more conducting. Especially if the humidity is high in the lab at the time. I have seen that the ceramics can go from a resistance too high to measure with a digital multimeter to 100 Ω or less when deliberately wetting the ceramic with water or ethanol. Once sparking across the ceramics happens once, the magnetron sputter head is much more likely to short through this mechanism.

I have also seen an object in one of the feedthroughs between the magnetron sputter head and the flange that is movable when the ring of

magnets is removed (arrow #5 in figure A.3c). I believe this is some broken part of the feedthrough or an insulating spacer. While its position did influence the resistance measurements, I do not believe it can be the source of a short circuit.

Lastly, not related to shorting the magnetron sputter head: red arrow #3 in figure A.3b shows the effect of not assembling the ring of magnets correctly after removal so the plasma is not contained on the target. The magnets should all have their field lines pointing in the same direction. This means that the last slot of magnets is difficult to fill, since you have to push the magnets against the field lines of the almost complete ring. Thus when doing it right, it *feels* like you are inserting the magnets facing the wrong way.

Sputter Rate Calibration on RuO_2 Thin Films

Appendix B

A reference sample was dedicated to a depth profile in order to calibrate the sputter rate for the RuO_2 thin films in chapter 4 and verify the assumptions of section 2.1.1. The sample was a thin layer of RuO_2 on TiO_2 on Si. Compared to the calibration sample in figure 4.6, a system such as this should enable us to more clearly identify the transition regions of the various layers. Unfortunately, the exact (nominal) thicknesses of these layers are unknown as things were quite hectic around that time and the records concerning the synthesis has been lost. A record around the time of synthesis details a sample of 10 nm IrO_2 on 5 nm Ti on Si, but this reference sample clearly consists of a ruthenium layer. The layers should have been thin for the depth profile and it probably was intended as 5 or 10 nm RuO_2 on 5 nm Ti. I recall mention of some uncertainty during the synthesis conditions that maybe the ruthenium layer was twice as thick as intended. In hindsight, the sample should just have been discarded and a new one prepared, but at the time we were pressed for time and tunnel visioned on the planned experiments. The depth profile was completed as shown in figure B.1 with integration of peaks done similarly to the experiment in figure 4.6. Since thin films gives more consistent signals, the intensities in figure B.1 are the absolute values of the integrated peaks and not relative. It took around 450 minutes of 1 keV argon sputtering to reach the titanium layer and 600 minutes more to reach the silicon layer. With the assumptions

from section 2.1.1, this corresponds to 12.8 nm $Ru(O_2)$ and 9.9 nm $Ti(O_2)$. Despite the uncertainties of thickness mentioned before, I am quite certain that the ruthenium layer is minimum 5 nm thick and at most 25 nm thick with the titanium layer probably 5 to 10 nm thick. The only conclusion that can be drawn from this is that the assumptions from section 2.1.1 seem to be correct within a factor 2 as was also claimed in the previous section. 20 minutes 1 keV argon sputtering should therefore still be minimum a monolayer and may be as much as four monolayers. For better accuracy, another well-defined reference sample is needed and/or a more thorough investigation of sputter rates of oxides relative to pure metals.[14]

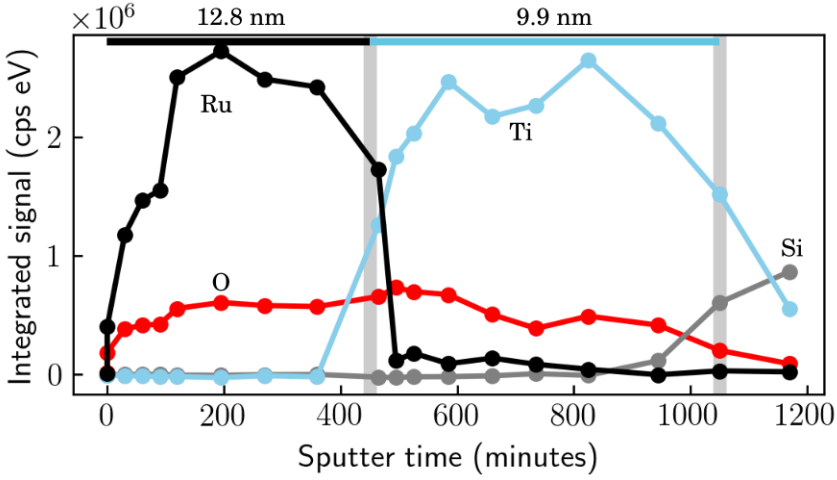

Figure B.1: Sputter depth profile using 1 keV Ar tracking the integrated region signals corresponding to oxygen (red), silicon (gray), titanium (blue), and ruthenium (black) versus sputter time. The crossover between layers are indicated with bars at time $t = 450$ minutes and $t = 1050$ minutes. The depth indicated at the top is calculated from the sputtering time following the (metallic) assumptions from section 2.1.1. Note: the channeltrons in the detector were replaced between the 5th and 6th data points explaining the sudden change in intensity.

Supplemental Information - Chapter 4

Appendix C

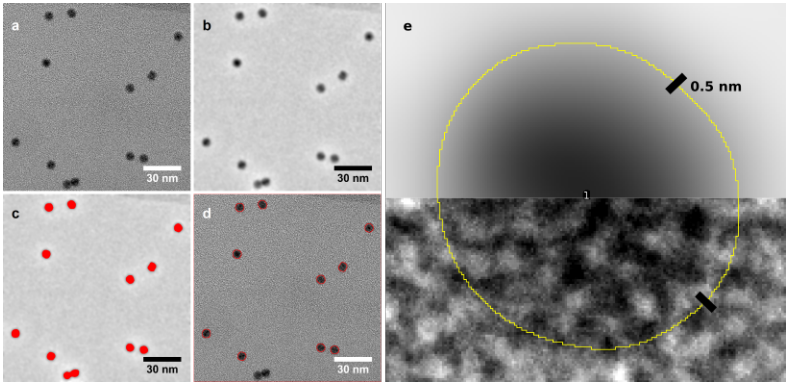

Figure C.1: Ni_3Fe nanoparticle TEM analysis procedure in ImageJ software. Raw image (a), bandpass filter (b) to remove background noise, Otsu thresholding algorithm (c) to detect the edge of nanoparticles, and the final outline of nanoparticles overlaid on the raw image (d). (e) shows such an outline overlaid on the filtered image (top half) and raw image (bottom half). The 2σ deviation of the fitted distributions are marked with a black bar in (e) for reference.

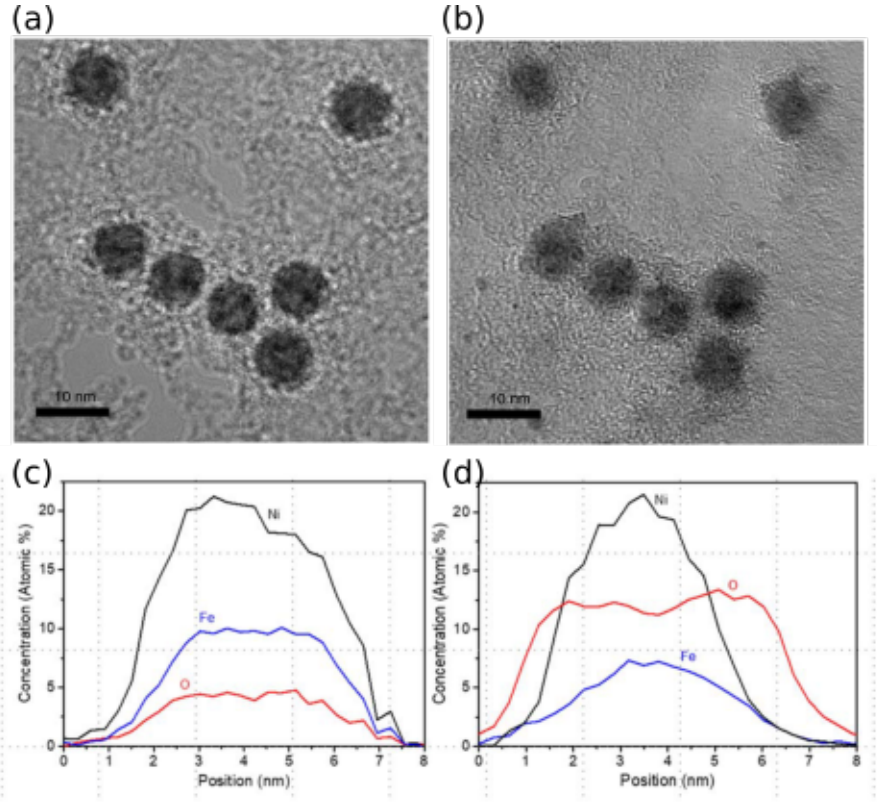

Figure C.2: Identical location HRTEM before (a) and after OER (b), and representative EDX line scan of a particle before (c) and after OER (d).

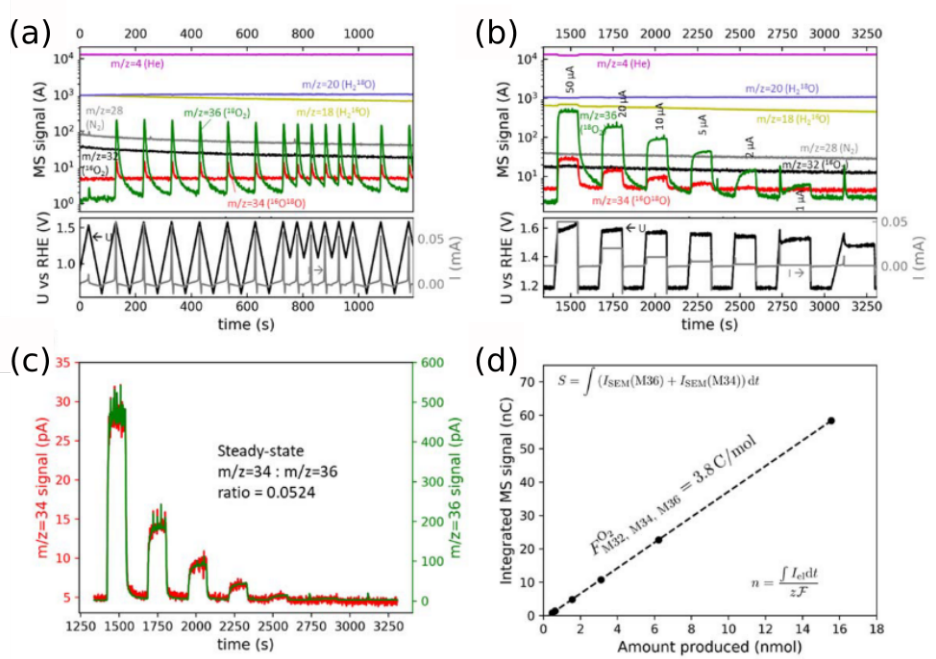

Figure C.3: EC-MS calibration for oxygen isotope experiments corresponding to Procedure *a* in figure 4.5. (a) Raw EC-MS CVs of OER on 6.7 nm particles in $H_2^{18}O$. (b) The second half of the experiment in (a) where oxygen is evolved in constant current steps for calibration of the ratio between the oxygen isotopes. (c) $^{18}O_2$ (green) and $^{16}O^{18}O$ (red) from (b) rescaled to show the linearity between them, and (d) the integrated OER current vs. the integrated MS signal showing a linear response.

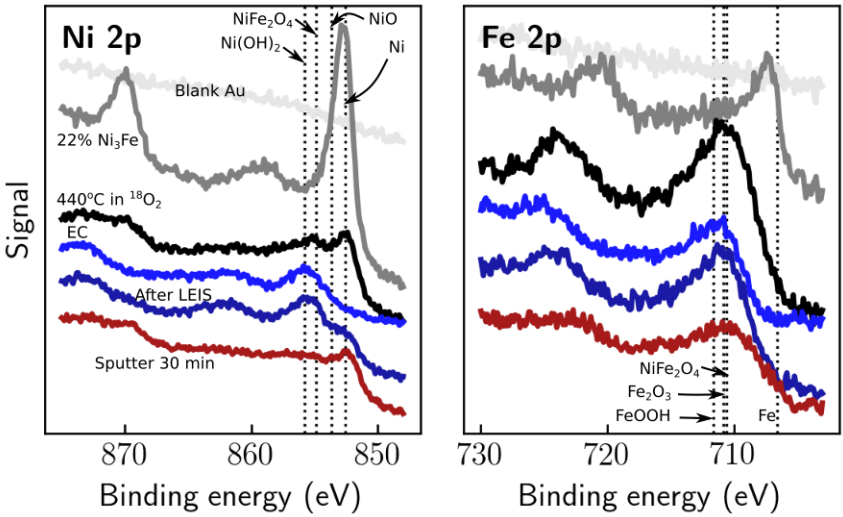

Figure C.4: XPS Ni 2p (left) and Fe 2p regions (right) of ^{18}O labeling of nickel-iron particles for Procedure *c* in figure 4.5. 22 % Ni_3Fe deposited on a sputtered Au stub and then annealed in $^{18}O_2$ in UHV without being exposed to air. Metallic nickel is still visible after UHV oxidation. Reference lines from [15]

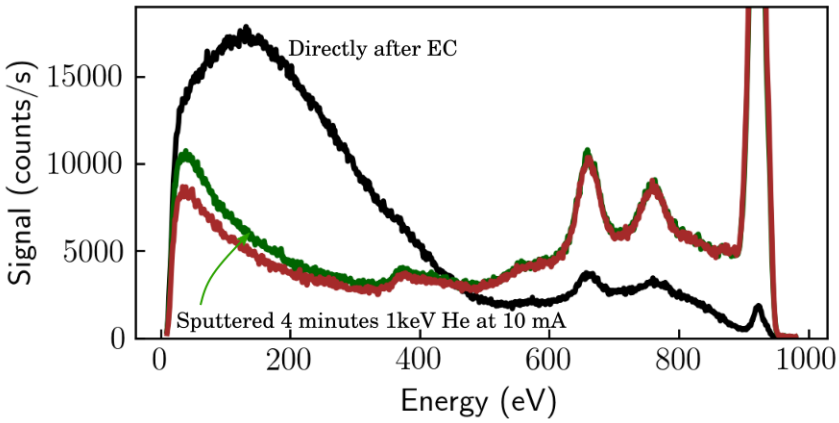

Figure C.5: LEIS of a Ni_3Fe sample after OER - 1 keV He^+ at 1 mA emission current. First scan in black, then two consecutive scans after 4 minutes of sputtering at 10 mA emission current to clean the sample of adventitious carbon.

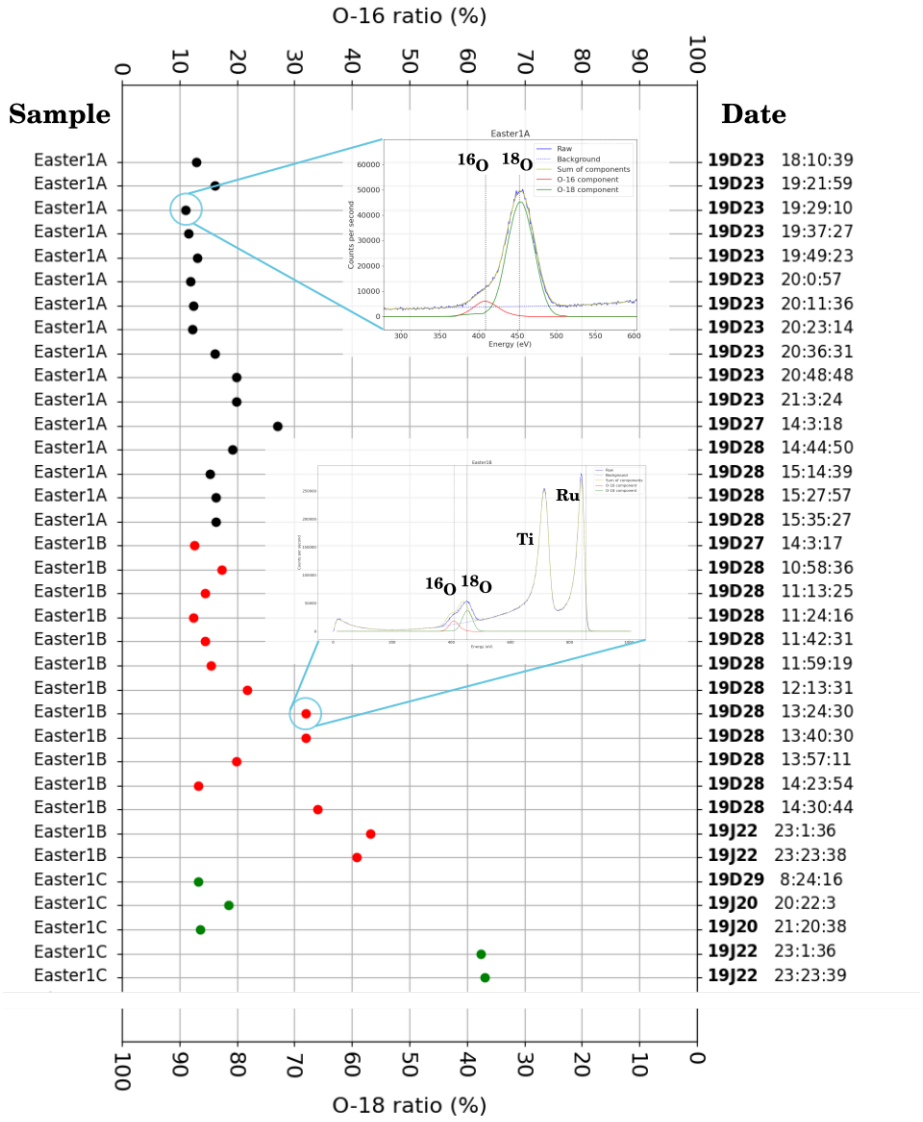

Figure C.6: Example of overview of samples/data by plotting the $^{16}O/^{18}O$ content for each sample. Shown here is all the data sets for the sample series "Easter". Insets shows the corresponding deconvolution of peaks for selected data points.

Supplemental Information - Chapter 5

Appendix D

D.1 TPD experiments on thin films

Included here is a presentation and discussion of the individual samples investigated for the PdSn study presented in chronological order. I want to include this as a basis of details for figure 5.9 and 5.10 since the experiments were conducted in a series within 1 - 2 weeks as my very last experiments to test the new sampleholder design. These experiments illustrate some of my experiences during TPD measurements and indicates that there are still issues. This way of presenting it, however, broke the flow in the main chapter and so I give it here instead.

All the thin films are prepared by Ezra Clark with a film thickness of 100 nm. A 10 nm Ti binding layer is between the main metal and the silicon substrate.

D.1.1 Cu thin film

Before testing the PdSn films, a copper thin film was sputter deposited on silicon to verify that we could produce a representative copper spectrum on this substrate. The sample was sputter cleaned with 2 keV argon for 15

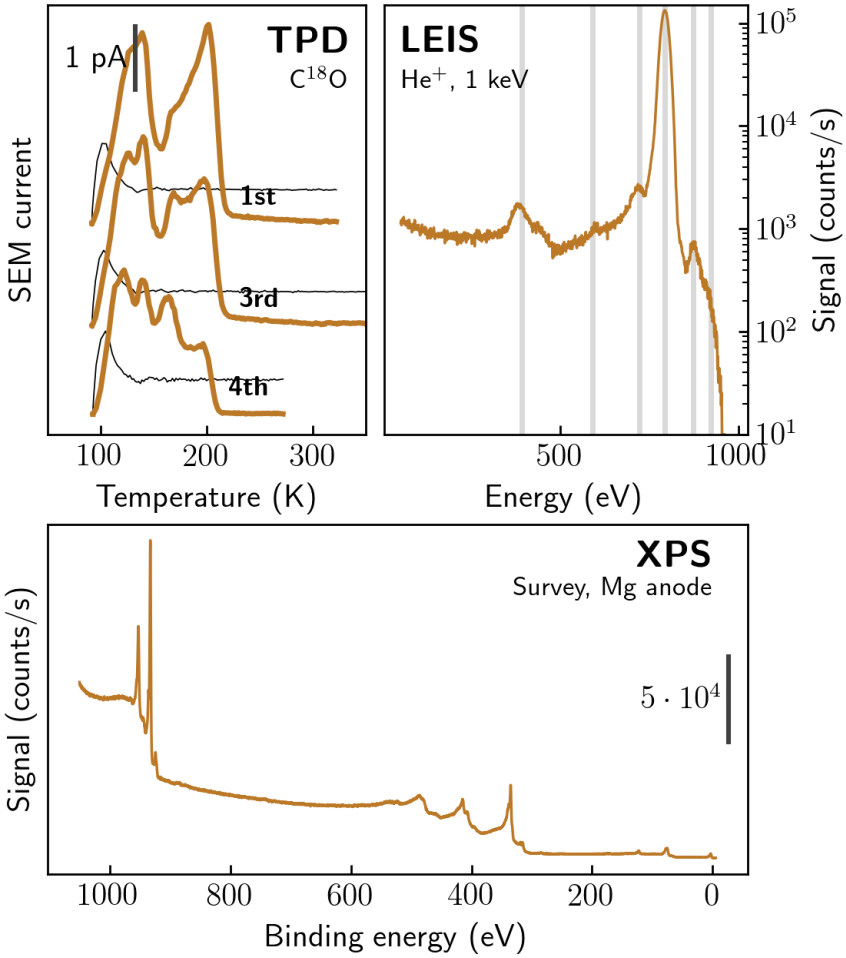

Figure D.1: TPD spectrum (**upper left**) of $>5\,\mathrm{L}$ $^{12}C^{18}O$. Heating rate is 0.5 K/s. The ramps, in chronological order, were heated to 320 K, 320 K, 770 K, and 270 K. The measured heating rate is indicated by the black lines - steady-state rate: 0.5 K/s. The second ramp looked identical to the third ramp. LEIS spectrum (**upper right**) and XPS survey (**bottom**) show the copper surface after the 4th TPD experiment. Small amounts of carbon visible with XPS. LEIS reveals surface impurities below the detection limit of XPS. The grey lines indicate the calculated masses from left to right: 16, 28, 45, 63.5, 108, 184.

minutes (4 to 5 μA sample current) prior to dosing CO for the first TPD. Based on previous investigations of this sample type, the only surface contaminant I need to remove, would be adventitious carbon and a thin layer of native oxide. The mentioned treatment should remove most of this. For the desorption spectra shown in figure D.1, the sample was dosed with more than 5 L at 94 K. The sniffer was approached for a 75 % background reduction.

The first ramp has a very intense sharp peak at 200 K. The sharpness of the low temperature feature and the shoulder on the following peak could in principle be artifacts of non-uniform heating rate. The measured heating rate is plotted in black for each spectrum. While variations in the heating rate from 100 K to about 160 K are visible, the measured variations do not align with the changing signal. An explanation for this could be that the thermocouple tip does not have sufficient contact to the surface or has too much thermal contact with the pinning cup and screw. This would also help explain why our peaks seem to consistently lie at lower temperatures than the literature.[97]

The spectrum changed shape after the first desorption spectrum heating to 320 K and after the third desorption spectrum heating to 770 K. The second scan heating to 320 K looked identical to the third scan. After annealing at 770 K, the peak corresponding to defects is much smaller and shifted left by about 5 K.

For this specific sample, a LEIS and XPS spectrum was only recorded after the TPD experiments as shown in figure D.1. XPS only indicates a small amount of carbon contamination, while LEIS further indicates the presence of oxygen, and some heavier elements that might be silver and tungsten (silver as a common bulk contaminant, and tungsten from the sampleholder during sputter cleaning). LEIS with helium ions do not provide enough resolution to identify these trace contaminants as other than 4d and 5d transition metals. Marked with grey lines, is also what could be a small silicon peak and titanium, which are both present beneath the thin film.

Besides characterization at more stages, I would have liked to resputter the film after the fourth run to see that the foil returns to the shape of the first

or second desorption spectrum.

D.1.2 PdSn

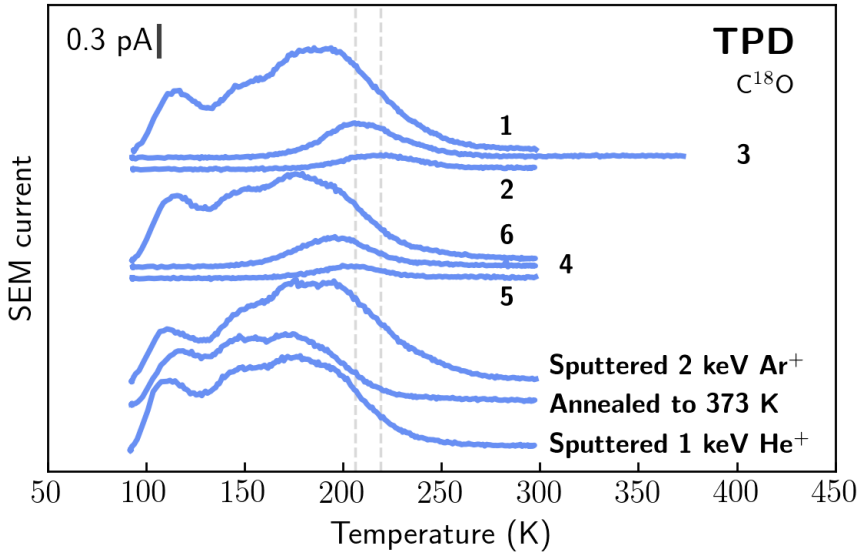

Figure D.2: CO-TPD on PdSn thin film on Si. Numbers indicate which order the spectra were recorded in. After ramping to 373 K, the high-temperature peak moves down. Ar-sputtering and annealing afterwards reproduces the spectra. Heating rate 0.5 K/s.

Figure D.3 shows the results of a PdSn film that was prepared by 20 minutes sputtering with 2 keV argon ions. The sample was dosed about 30 L CO and the sniffer was approached to 75 % background reduction. The first two scans look largely identical with the annealing temperature being 300 K. The high temperature peak position is just below 200 K (the same as our polycrystalline copper reference), but has a slowly decaying tail that only dies down shortly before room temperature. Annealing to 373 K during the second ramp causes this high temperature tail to shift down.

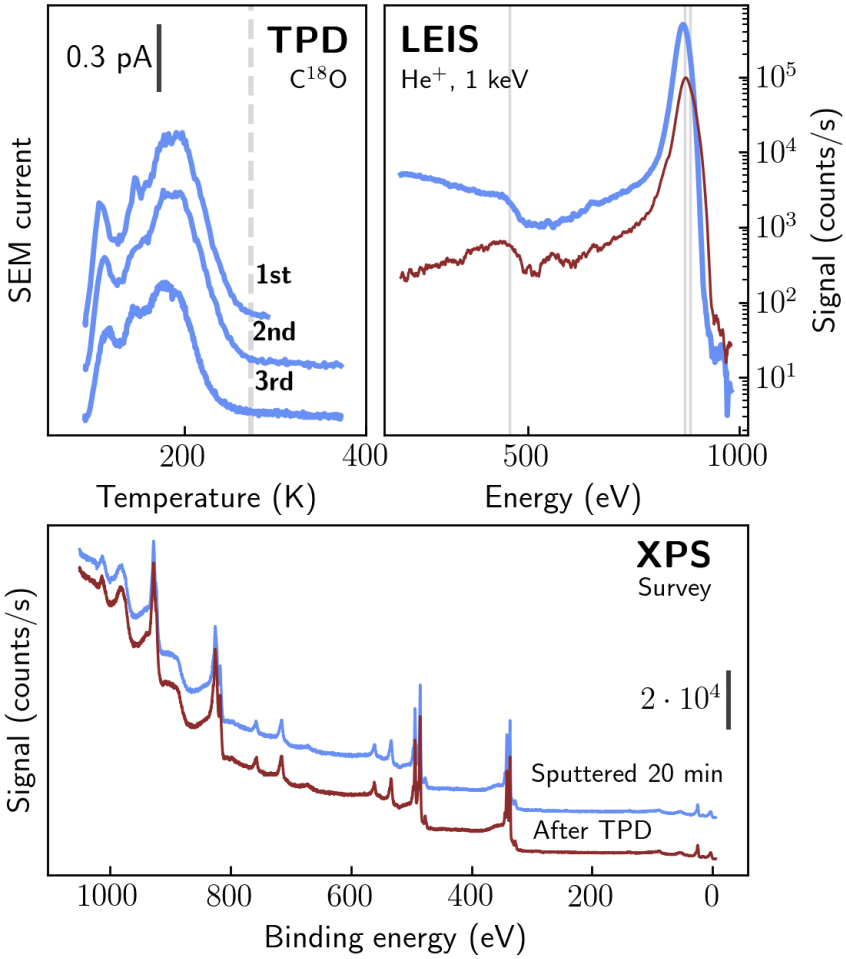

Figure D.3: First CO-TPDs (upper left) on PdSn. After annealing to 373 K (3rd), the high-temperature peak moves down. Dashed line indicates 273 K. Heating rates 0.5 K/s. LEIS (upper right) and XPS (bottom) shows the sample sputter cleaned 20 minutes with 2 keV Ar before TPD experiments (blue) and before removing from the UHV chamber (brown). No significant differences.

This effect was explored more closely the following day and is shown in figure D.2. For this, the sample was recleaned by sputtering extensively with 1 keV He ions, dosed by 7 L CO, and the sniffer approached to block 75 % of the background to verify I got the same signal as the previous day. I then did two scans where I dosed first 0.2 L and then 0.7 L to probe the high temperature peak in the dilute phase. This peak behavior could be indicative of dissociative desorption or a strong coverage-dependence for the heat of desorption. It should be possible to distinguish between the two with equation (2.7) since dissociative desorption should depend on the coverage squared. Annealing to 373 K shows that the high energy peak shifts down from 220 K to 205 K - based on the lowest coverage peak. By resputtering/annealing, I get a completely reversible process. I ended the experiment by sputtering with 1 keV He ions to see whether they induced the same defects in the sample. While the desorption peak does shift to a higher temperature, it does not shift as much as for argon sputtering. One would need to sputter it for longer to see if that would increase the shift. If no further shifting occurs, then it would hint at some weaker defects than produced by 2 keV argon ions. The first desorption peak showing the "strong" defect sites, had not been annealed since the experiments of the previous day, so it is possible that these will have survived.

XPS and LEIS in figure D.3 show no contaminants on the surface after these experiments except for a small persistent oxygen shoulder in LEIS.

D.1.3 $PdSn_2$

This sample showed such a weak signal at temperatures below PdSn that I decided to do a thorough background test on clean silicon, the results of which was used for figure 5.5. As the spectra are mostly background, they are not included in the comparison in the main chapter. Another reason for not including it is that I did some high temperature experiments after which the sample was clearly discolored (see figure D.7b) and both ISS and XPS showed large amounts of silicon present at the surface and only small amounts of Pd and Sn. In order to track desorption of argon (mass 40), I ended up ramping the sample up to 1273 K at which point the temperature

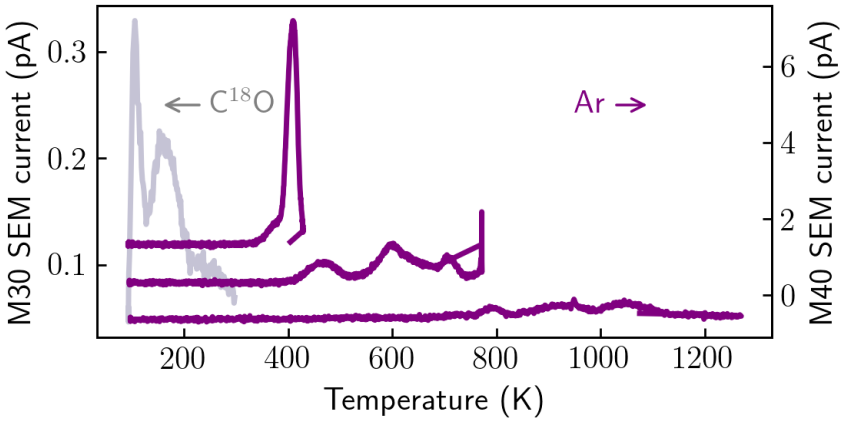

Figure D.4: CO-TPD on $PdSn_2$ thin film. CO signal on left axis, and Ar signal at higher temperatures on right axis. The stop temperature was progressively increased to probe the argon signal. The sample likely broke under the thermocouple around 1270 K.

control seemed unstable. I think this point is where the sample broke under the thermocouple contact point. The argon ramps are shown in figure D.4 along with the best CO-TPD spectrum of $PdSn_2$.

D.1.4 Pd

Figure D.5 shows a Pd thin film that was sputtered 10 minutes with 2 keV Ar ions. The film was given doses of CO larger than 5 L for full coverage. At this point, I had realized the correct way to determine the approach of the sniffer via figure 5.4, so the sniffer was approached to 90 % background reduction for the following experiments (as compared to 75 % previously). The first ramp runs at 0.5 K/s, but breaks shortly after 500 K due to induced oscillations in the temperature ramp. Not sure why it became unstable before, I changed the second ramp to use 1.0 K/s which reached the target 720 K smoothly (see figure D.8 for an example of the data resolved in time). Both desorption spectra show a high temperature peak at

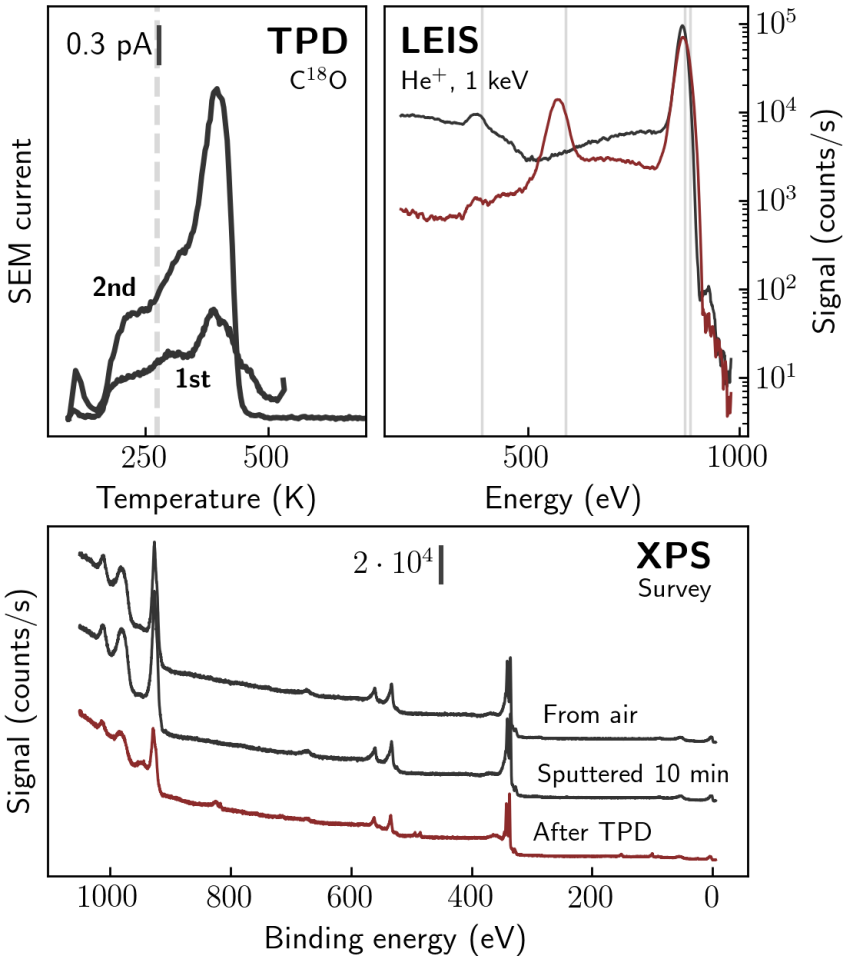

Figure D.5: CO-TPDs (upper left) on Pd at 0.5 and 1.0 K/s for the first and second run, respectively. LEIS (upper right) and XPS (bottom) shows the sample before (black) and after TPD (brown). The black line in LEIS is before sputtering. Si is clearly visible afterwards in both XPS and LEIS, while a small amount of Sn is also visible in XPS. Masses for oxygen, silicon, palladium and tin marked with grey lines in LEIS.

390 K, which is about 100 K less than expected.[105,109]

XPS and ISS afterwards show signal from silicon and tin - both of which are diminished after sputtering with argon ions. The Sn should not be there and is probably a cross-contamination from the previous high-temperature ramps, which likely evaporated some of the Sn in the thin film.

D.1.5 Pd_2Sn

Figure D.6 shows the Pd_2Sn film sputtered 5 minutes with 2 keV Ar ions after which it still shows some oxygen being present (LEIS)c. The sample was covered fully with CO (> 5 L) and the sniffer was approached to 90 % background reduction. Heating rates are 1.0 K/s.

The first desorption spectrum shows a large peak at 190 K with a prominent shoulder continuing well into the room temperature region. After 600 K, there is some serious degassing in the background causing most signals to increase, and just before 700 K the temperature oscillates out of control. The subsequent scan is about a third of the intensity of the first, and the shape of the spectrum looks very much like the first one except for being squashed to lower masses. Again, this could indicate a bad thermocouple contact. Sometime during the two TPD runs, the sample broke in a line where the thermocouple tip touched the surface. There is a high probability that this happened towards the end of the first ramp, since I did have problems then, and a broken sample would explain the bad thermocouple contact of the second ramp. An image of the sample after the TPD spectra were acquired is seen in figure D.7a. LEIS after the second ramp, however, shows a less intense Pd/Sn peak, and XPS shows a slightly higher Sn concentration. So Sn enriching the surface coupled with contaminants from degassing covering part of the surface could also explain the intensity and position of the second scan. In this case, the high temperature feature of the second scan might be due to a mono-metallic phase of Pd. The high temperature feature in the first scan is attributed to general degassing in the TPD chamber.

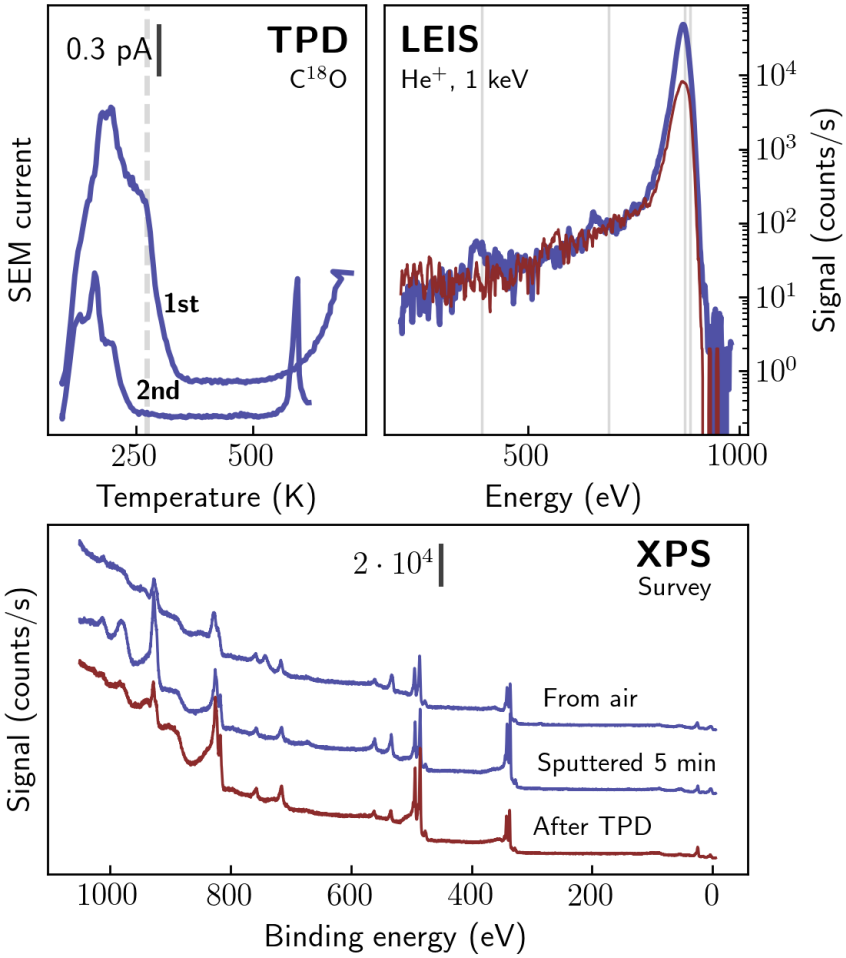

Figure D.6: CO-TPDs (upper left) on Pd_2Sn at 1.0 K/s heating rate. Desorption extends above room temperature. For the first scan, the increasing signal towards the end of the run is due to heavy desorption in the background. This may also be why the second run has so low intensity. LEIS (upper right) and XPS (bottom) before (purple) and after (brown) CO-TPDs. The Sn/Pd ratio is significantly larger after the two TPD spectra. No contaminants detected measured after the experiments despite the visual change in figure D.7. Masses for oxygen, argon, palladium and tin are marked in LEIS with grey lines.

D.2 Additional figures

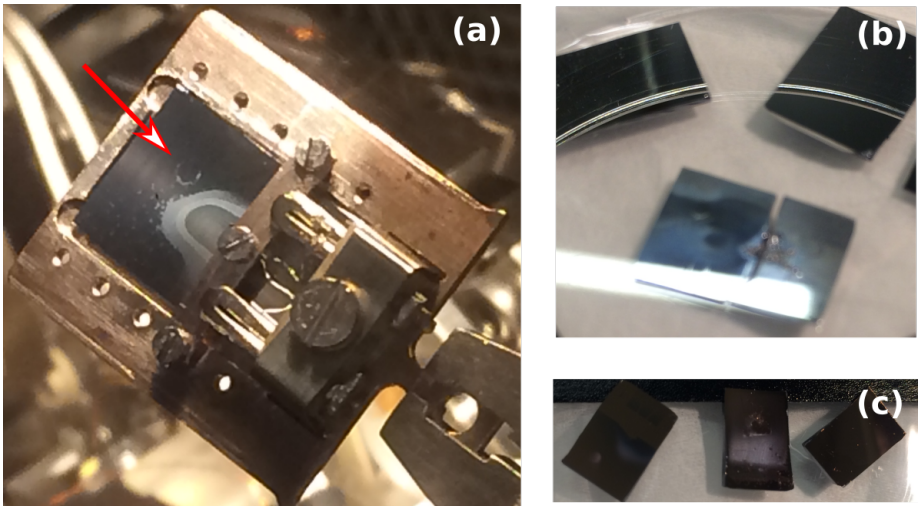

Figure D.7: Visual inspection of samples after CO-TPDs. Pd_2Sn (a), $PdSn_2$ (b), and two Cu (c) thin films on silicon are all miscolored to varying degrees after TPD experiments. The arrow in (a) indicates a 1 mm diameter imprint left by the sniffer.

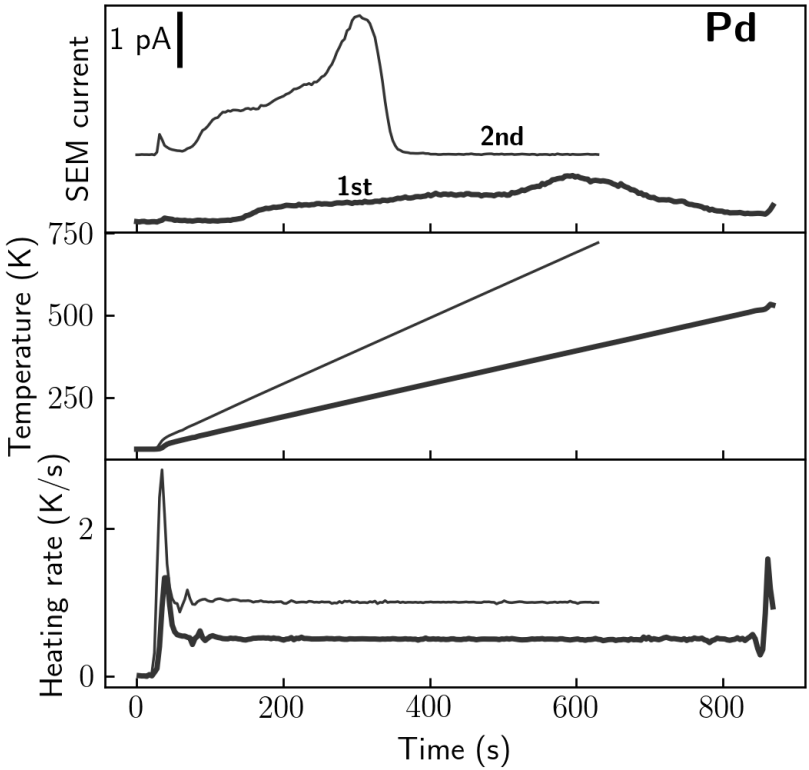

Figure D.8: Example of TPD heating rates on Pd. As function of time: CO (mass 30, top), temperature (middle), and back-calculated heating rate (bottom). Set heating rate: 0.5 K/s for 1st run and 1.0 K/s for 2nd run.

Appended papers

Appendix E

Papers II, III, IV, V, VI are appended here. Papers V and VI are presently being drafted and are only included as abstracts.

Paper II

https://doi.org/10.1038/s41929-018-0162-x

Impact of nanoparticle size and lattice oxygen on water oxidation on $NiFeO_xH_y$

Claudie Roy, Bela Sebok, Søren B. Scott, Elisabetta M. Fiordaliso, Jakob E. Sørensen, Anders Bodin, Daniel B. Trimarco, Christian D. Damsgaard, Peter C.K. Vesborg, Ole Hansen, Ifan E.L. Stephens, Jakob Kibsgaard, and Ib Chorkendorff

Nat Catal **1**, 820-829 (2018)

ARTICLES
https://doi.org/10.1038/s41929-018-0162-x
nature catalysis

Impact of nanoparticle size and lattice oxygen on water oxidation on $NiFeO_xH_y$

C. Roy[1,5], B. Sebok[1,5], S. B. Scott[1,5], E. M. Fiordaliso[2], J. E. Sørensen[1], A. Bodin[1], D. B. Trimarco[1], C. D. Damsgaard[2], P. C. K. Vesborg[1], O. Hansen[3], I. E. L. Stephens[1,4], J. Kibsgaard[1] and I. Chorkendorff[1*]

$NiFeO_xH_y$ are the most active catalysts for oxygen evolution in a base. For this reason, they are used widely in alkaline electrolysers. Several open questions remain as to the reason for their exceptionally high catalytic activity. Here we use a model system of mass-selected NiFe nanoparticles and isotope labelling experiments to show that oxygen evolution in 1 M KOH does not proceed via lattice exchange. We complement our activity measurements with electrochemistry–mass spectrometry, taken under operando conditions, and transmission electron microscopy and low-energy ion-scattering spectroscopy, taken ex situ. Together with the trends in particle size, the isotope results indicate that oxygen evolution is limited to the near-surface region. Using the surface area of the particles, we determined that the turnover frequency was $6.2 \pm 1.6\ s^{-1}$ at an overpotential of 0.3 V, which is, to the best of our knowledge, the highest reported for oxygen evolution in alkaline solution.

Renewable energy technologies, such as wind turbines and solar panels, hold the potential to satisfy both rising global energy demand and mitigate CO_2 emissions[1,2]. The intermittent nature of wind and solar energy means that energy storage is one of the most critical challenges as it limits their widespread implementation. One possibility is to store the energy in chemical bonds[3]. Thus far, one of the most promising means to convert electricity into fuels is water electrolysis, in which H_2 and O_2 gases are formed[4]. Their recombination to provide electrical energy only has water as a by-product, which makes it a clean process.

The hydrogen evolution reaction, which takes place on the cathode side during water electrolysis, is possible at minimal energy losses[5,6]. However, the slow reaction kinetics of the anodic reaction, the oxygen evolution reaction (OER), involves the transfer of four electrons and four protons and so limits the efficiency of electrolysers[7]. No electrode material approaches the equilibrium potential of 1.23 V on the reversible hydrogen electrode scale (V_{RHE})[8–10], which corresponds to the minimum energy needed for the reaction. Consequently, the widespread use of electrolysers is contingent on improvements to the OER kinetics.

Although $Ni(Fe)O_xH_y$ mixed electrodes were used even in the nineteenth century in alkaline electrolysers[11], the science is still under intense debate[12,13]. Pure NiO_xH_y is an inactive catalyst, but the activity drastically increases when Fe is intercalated into the structure[12–16], with the optimal activity for compositions between 10% and 50% Fe (ref. [13]). There are two main hypotheses as to the role of Fe: (1) Ni is the active site and Fe affects its valency, which makes it more active[17,18] or (2) Fe itself is the active site[19–22], as first evidenced by X-ray adsorption spectroscopy and density functional theory calculations[19], and subsequently by electrochemical scanning microscopy[22]. Conversely, more recently, it was suggested that both Ni and Fe sites are directly involved[23].

Some studies indicated that the bulk, and not just the outer surface, of the catalyst is active. For example, Batchellor and Boettcher reported a linear increase of the OER current as a function of catalyst loading up to ~450 monolayer equivalents[24]. The notion of bulk activity was supported by a recent theoretical study[25] that found similar thermodynamics for the OER intermediates in the bulk of the material as for the (001) surface. However, Hu and co-workers showed that the apparent turnover frequency (TOF) of $NiFeO_x$ decreases at high loading[26], which suggests either that thick samples are not as active or that the OER becomes readily transport limited.

Previous studies probed $Ni^{3+,4+}/Ni^{2+}$ redox chemistry on $NiFeO_xH_y$ electrodes at ~1.3–1.4 V_{RHE} using cyclic voltammetry (CV) and gravimetric analysis, and concluded that each nickel atom in the film contributes on average approximately one electron[24,27]. This observation indicates that the entire film is electrochemically accessible, which motivates the hypothesis that oxygen evolution occurs between the nanosheets of the layered double hydroxide structure of the catalyst, and so blurs the distinction between surface and bulk[14]. Moreover, $NiFeO_xH_y$ films, which are typically electrodeposited, are highly porous[13]. These various studies point to three possibilities: (1) the activity is confined to an outer surface, which may be large for porous materials, (2) the activity is confined to a near surface region in which there is ionic conductivity and electrolyte intercalated between the nanosheets and (3) bulk activity in which the entire material is active. This complicates the determination of the intrinsic activity, a critical step towards the design of more-efficient OER catalysts, and motivates the use of a model system with a known and well-defined surface area[14].

Isotope labelling studies using ^{18}O and operando mass spectrometry are a powerful tool to distinguish surface from bulk catalysis[28]. Most of the catalysts probed using this method have revealed at least some degree of lattice-oxygen involvement, including Au (ref. [29]), IrO_2/Ti (ref. [30]), Co_3O_4 spinel[31], molecular cobaltate nanoclusters[32], Ru-based catalysts[28,33] and perovskite materials with a high metal–oxygen bond covalency[34]. Others, which include Pt (ref. [35]), oriented thin films of rutile RuO_2 (ref. [36]) and perovskites with low

[1]SurfCat, Department of Physics, Technical University of Denmark, Kgs. Lyngby, Denmark. [2]Center for Electron Nanoscopy, Technical University of Denmark, Kgs. Lyngby, Denmark. [3]Department of Micro- and Nanotechnology, Technical University of Denmark, Kgs. Lyngby, Denmark. [4]Department of Materials, Imperial College London, Royal School of Mines, London, UK. [5]These authors contributed equally: C. Roy, B. Sebok, S. B. Scott. *e-mail: ibchork@fysik.dtu.dk

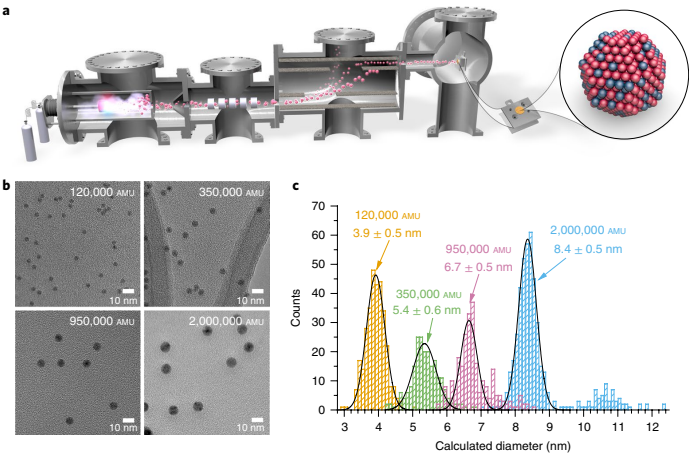

Fig. 1 | Deposition of mass-selected nanoparticles. a, A d.c. magnetron sputtering, gas-aggregation mass-selected nanoparticle source with lateral time-of-flight mass filter. Mass selected NiFe nanoparticles were deposited on polycrystalline gold disks for the activity measurements. **b**, TEM images of four different masses of NiFe nanoparticles. **c**, Size distributions, determined using the diameter measured on the TEM images in **b**, show the average size and 2σ for each mass deposited.

metal–oxygen bond covalency[34], have not. Shao-Horn and co-workers observed that lattice exchange occurs with materials that have a catalytic activity that is pH dependent, which indicates decoupled proton and electron transfers in the OER mechanism[34]. Based on that argument, $Ni(Fe)O_xH_y$, which shows a higher catalytic activity in a stronger alkaline electrolyte, should also show participation of lattice oxygen[37]. However, to the best of our knowledge, no studies have probed $Ni(Fe)O_xH_y$ using isotopically labelled water, even though it is the catalyst of choice for industrial water electrolysis.

Such isotope studies consist of preparing the $NiFeO_xH_y$ catalyst with one oxygen isotope (^{16}O or ^{18}O) or isotopic ratio, and then monitoring the O_2 products during oxygen evolution in an electrolyte that has a different isotopic ratio using a mass spectrometer ($^{16}O_2$ at $m/z=32$, $^{16}O^{18}O$ at $m/z=34$ and/or $^{18}O_2$ at $m/z=36$). Should the O_2 that is evolved differ in isotopic composition from the electrolyte, then it is probably derived from the lattice oxygen or from water molecules intercalated between the layered nanosheets.

To draw a conclusion on the participation of lattice oxygen requires high sensitivity and thorough characterization: (1) to ensure that the isotopic oxygen is included in the $NiFeO_xH_y$ catalyst, (2) to correctly identify whether it is evolved during the OER and, if so, (3) to quantify accurately the amount. To satisfy these requirements, we used a microchip-based electrochemistry–mass spectrometry (EC–MS) technology that has a high sensitivity. For example, it can detect 0.05 monolayer equivalents of H_2 desorbing from a flat Pt surface with a signal-to-noise ratio of ~20 (ref. [38]). We complement the operando mass spectrometry experiments with postcharacterization by low-energy ion scattering (LEIS) spectroscopy, a surface sensitive technique that enables the differentiation of ^{16}O and ^{18}O.

In this study, we prepared size-selected NiFe particles using a magnetron sputtering nanoparticle source (Fig. 1a). This physical synthesis method yields homogeneous, monodisperse and chemically pure metallic particles, with a well-defined size and loading, ideal for fundamental studies[39,40]. We compared the nanoparticles to $NiFeO_xH_y$ electrodeposited thin films. We tested the catalytic activity using a rotating disk electrode assembly in 1.0 M KOH, in which the particles oxidize under operando conditions. We complemented these experiments with X-ray photoelectron spectroscopy (XPS), high-resolution transmission electron microscopy (HRTEM) and scanning electron microscopy (SEM), and performed isotope studies as described above. The nanoparticle samples function as a model system with a well-defined and tunable surface area.

Together, the nanoparticle model system, extensive characterization and isotope studies enabled us to answer two fundamental questions: (1) What is the intrinsic activity of the active sites on a well-defined surface of $NiFeO_xH_y$; (2) Does lattice oxygen participate in the reaction?

Results

NiFe model system. Figure 1b shows TEM images of the as-prepared nanoparticles. Figure 1c shows the size distribution of the as-prepared nanoparticles. The size distribution was determined from the TEM images as described in Supplementary Note 1. As presented in Fig. 1b, all the nanoparticles have a regular and spherical shape regardless of their mass. The average particle diameters were 3.9 ± 0.5 nm, 5.4 ± 0.5 nm, 6.7 ± 0.6 nm and 8.4 ± 0.5 nm, respectively, for the four selected masses (Fig. 1b,c). There was a small population of larger particles with double the intended mass, which resulted from doubly charged nanoparticles, especially in the case of the 8.4 nm particles.

Stability and effects of OER operating conditions. The 6.7 nm nanoparticles were characterized with LEIS and XPS, as shown in Fig. 2a,b, respectively. The LEIS spectra of the as-deposited nanoparticles (green curve) showed clear Ni and Fe peaks, which cannot be differentiated due to the small difference between their atomic masses. After electrochemical testing (blue curve), the LEIS spectra showed additional features identified as K, O and C, most probably from residual KOH electrolyte, nanoparticle oxidation and air exposure. XPS spectra (Fig. 2b) of the as-deposited nanoparticles revealed metallic Ni and Fe. XPS analysis after

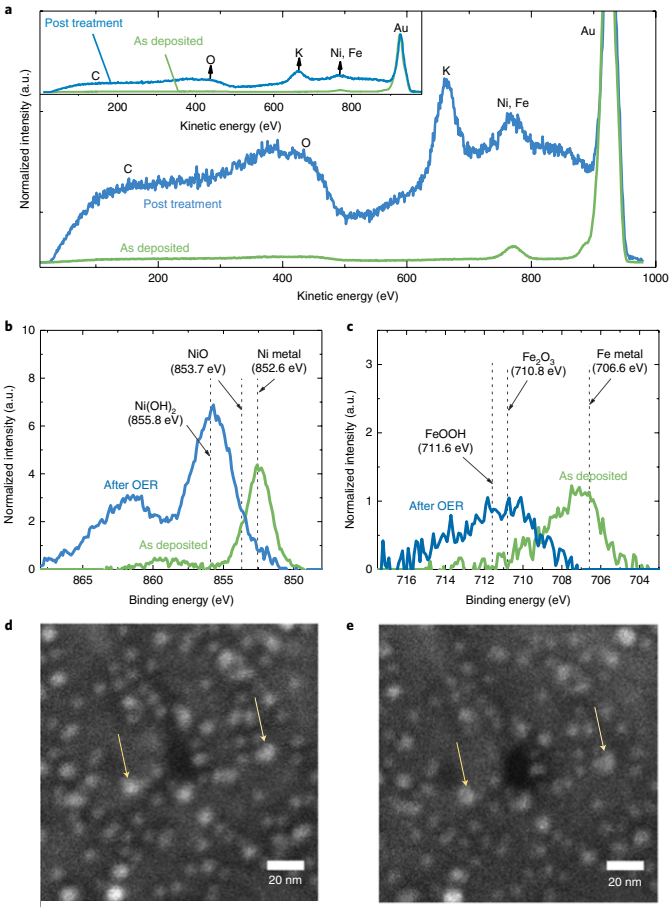

Fig. 2 | Ex situ characterization of the deposited 6.7 nm NiFe particles. a, LEIS spectra, **b**–**e**, XPS spectra (**b**,**c**) and SEM (**d**,**e**) of nanoparticles as deposited (**b**,**d**) and after electrochemical testing (**c**,**e**). The LEIS spectra are normalized to the height of the Au peak. The XPS spectra, shown for the Ni $2p_{3/2}$ (**b**) and Fe $2p_{3/2}$ (**c**) regions, are charge corrected and normalized with the Au *4f* peak area after the subtraction of a Shirley background. The reference XPS binding energies are taken from refs [59–61]. The SEM images are taken at identical locations to evaluate the resistance against sintering and corrosion.

electrochemical treatment showed that oxide and hydroxide states are formed for both Ni and Fe. More precisely, NiO and $Ni(OH)_2$, and FeOOH and Fe_2O_3, were identified from the Ni and Fe 2*p* peaks, respectively. The composition determined based on the XPS spectra shows a similar Fe content before the electrochemical testing to the target for the deposition, namely 25%, and an Fe content of ~15% after electrochemical testing for all the nanoparticle sizes (Supplementary Note 3).

One challenge with nanoparticle catalysts is that they often coalesce under reaction conditions[41–43]. In addition, the conditions under which the OER electrodes operate can cause metal dissolution[44,45]. As a first step to evaluate the stability and resistance towards corrosion and sintering, SEM images were acquired before and after the OER at identical locations to visualize directly any change in particle size or positions[46]. From the example images shown in Fig. 2d,e taken before and after testing the activity, it can be seen that the 5.4 nm NiFe particles do not coalesce or dissolve during the two hour potentiostatic measurement at 1.6 V_{RHE}. Most of the nanoparticles can be found directly in both images. To probe the stability further, a chronoamperometric measurement was performed at 1.6 V_{RHE}. As presented in Fig. 3, the OER current was stable over 41 days (~1,000 hours). This result further confirms the stability of the NiFe catalyst previously reported by a stable chronoamperometric measurement at 10 mA cm^{-2} over 24 hours[47,48].

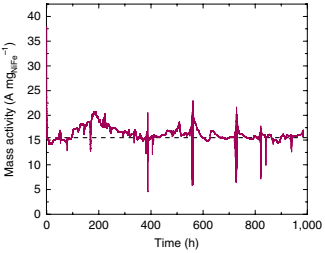

Fig. 3 | Stability of NiFe nanoparticles at 1.6 V_{RHE} in 1 M KOH. The mass activity of ~100 ng of 6.7 nm NiFe nanoparticles at 1.6 V_{RHE}, with current interrupt (*iR*) correction, in 1 M KOH. The dashed line is a guide to the eye.

To gain insight into the morphology and composition at the atomic level, we acquired identical-location HRTEM images of particles deposited on graphene-covered Au TEM grids both before and after two CV cycles at 10 mV s^{-1} up to 1.5 V_{RHE}. The electrochemical treatment was mild to avoid the corrosion of the carbon grid at more anodic potentials. Before OER, the NiFe nanoparticles showed a polycrystalline structure. The typical image in Fig. 4a shows a single particle in which the Ni_3Fe phase can be identified[49]. Figure 4b,c shows HRTEM images of the same nanoparticles before and after being electrochemically tested. We found that after electrochemical testing, the nanoparticles maintained their shape and their polycrystalline nature, as indicated by the non-uniform orientation of the lattice fringes, and by the contrast difference caused by diffraction. We used energy-dispersive spectroscopy (EDX) along with a focused electron beam to map the dispersion of Ni and Fe in the particles using cross-sectional line scans (Supplementary Note 4). A comparison of the Ni and Fe concentrations before and after electrochemical testing showed that some of the Fe leaches out after OER. This decrease in Fe concentration could be associated with the dissolution of FeOOH, known to be highly unstable under these experimental conditions[50].

Activity. The representative CVs of samples from each of the four nanoparticle-size groups, taken after 2 hours at 1.6 V_{RHE}, plotted in Fig. 5a show a clear difference in activity for the different particle sizes. The smallest particles, that is, 3.9 and 5.4 nm, provide the highest current normalized to the deposited metal mass. A significant OER current is observed that starts from $U = \sim 1.5\ V_{RHE}$ (overpotential of $\eta = 270$ mV). Using what is typically attributed to the Ni^{2+} to $Ni^{3+/4+}$ redox couple[13], we showed that the integral of the Ni reduction peak scales better with the calculated surface area than the total loading (Supplementary Fig. 4). Less than one electron is transferred per Ni atom in the larger nanoparticles. Figure 5b shows the average mass activity on a deposited metal basis at $\eta = 270$, 300 and 370 mV as a function of particle size. The activity was taken from the current recorded at a scan rate of 10 mV s^{-1}. No obvious difference in trend was observed when comparing the mass activities as a function of the size for different overpotentials.

To show the intrinsic activity, for Fig. 6a we converted the activity into TOF, that is, the number of O_2 molecules produced per active site per unit time, using three estimates for the number of active sites. TOF_{bulk} assumes that all the deposited Ni and Fe atoms are active, TOF_{redox} assumes one active site per electron is transferred in the Ni reduction peak of the CV and $TOF_{surface}$ assumes that only the surface metal atoms of the nanoparticles are active sites (Methods and equations (1)–(6)). We also included the

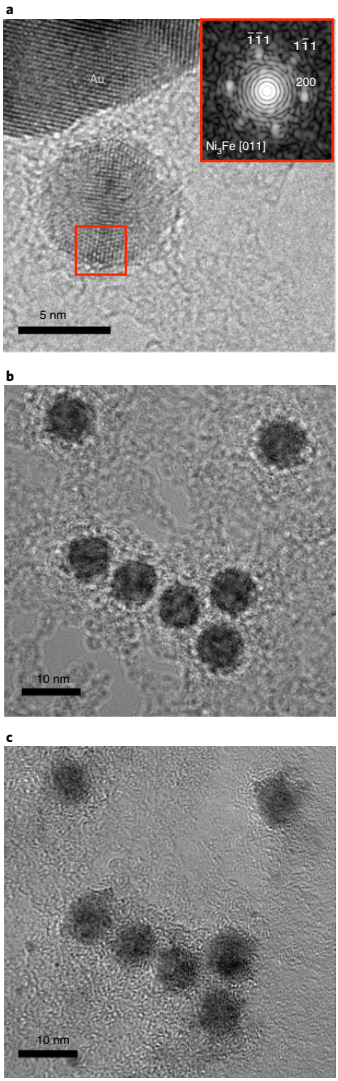

Fig. 4 | HRTEM investigation of the particles. HRTEM images of 6.7 nm (950×10^3 AMU) NiFe nanoparticles deposited on Au TEM grids. **a**, HRTEM image of a nanoparticle. Inset: The Fourier transform of the highlighted area shows the Ni_3Fe phase. **b**,**c**, Identical-location HRTEM images of nanoparticles before (**b**) and after (**c**) electrochemical oxidation.

TOF_{redox} calculated for $NiFeO_xH_y$ thin films, for which the activity was measured by the same procedure as for the nanoparticles (Supplementary Fig. 5).

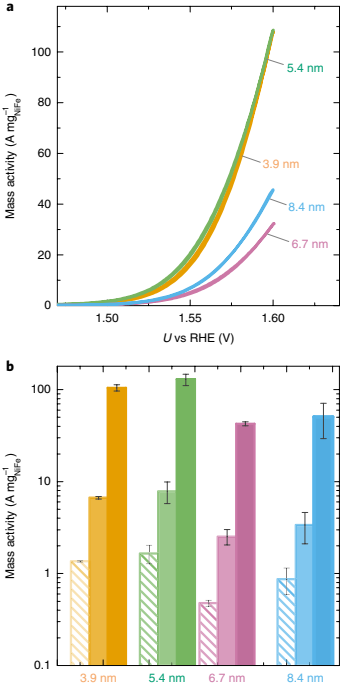

Fig. 5 | Catalytic activity of the NiFe nanoparticles. a CV at 10 mV s^{-1} of representative $NiFeO_xH_y$ nanoparticle samples for each nanoparticle size. The current is normalized to the total metal mass loading. **b**, Mass-normalized activities at $\eta = 270$ (hatched), 300 (lighter shade) and 370 mV (darker shade). The average mass activity and s.d. are from three independent samples. All the activity measurements were done on Au substrates in N_2-saturated 1 M KOH at 1,600 revolutions per minute. The metal mass was determined from the nanoparticle deposition current.

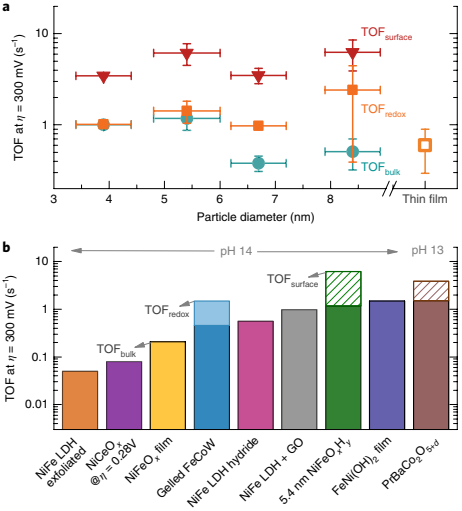

Fig. 6 | TOF as a function of size, and comparison to state-of-the-art non-noble metal catalysts. a, TOF calculated from the total metal mass (TOF_{bulk}), the Ni redox peak (TOF_{redox}) and the estimated surface atoms ($TOF_{surface}$) of the NiFe nanoparticles at $\eta = 300$ mV measured in N_2-saturated 1.0 M KOH at 10 mV s^{-1} as a function of particle size. The Ni redox peak was used to measure the TOF of the NiFe thin film. The y-axis error bars come from three independent samples and were calculated using $\sqrt{\frac{\Sigma(x-\bar{x})^2}{(n-1)}}$, where x is the activity value and $\bar{x}$ the average activity from the three samples (n). **b**, TOF of state-of-the-art non-noble OER catalysts in alkaline. Sources: NiFe layered double hydroxide (LDH) exfoliated[53], $NiCeO_x$@$\eta = 0.2$ V (ref. [47]), $NiFeO_x$ film[27], gelled FeCoW (ref. [51]), NiFe LDH hydride[52], NiFe-LDH + GO (ref. [54]), 5.4 nm $NiFeO_xH_y$ (this work) $FeNi(OH)_2$ film[16] and $PrBaCo_2O_{5+d}$ (ref. [4]). When possible, both the minimum (bulk, darker solid colours) and maximum (surface, striped colour, or redox, lighter shade of the solid colour) TOFs were estimated. The TOF_{redox} of gelled FeCoW was calculated using the Co redox peak, and the $TOF_{surface}$ for $PrBaCo_2O_{5+d}$ was calculated based on the surface area from N_2 physisorption (Brunauer–Emmett–Teller).

The TOFs thus calculated show different trends with particle size. TOF_{bulk} is higher for the smaller particles, that is, 5.4 and 3.9 nm, and lower for the larger particles. TOF_{redox} and $TOF_{surface}$ do not show any obvious particle-size dependence, though TOF_{redox} has a larger scatter.

The $TOF_{surface}$ and TOF_{bulk} of the 5.4 nm NiFe nanoparticles were compared to state-of-the-art non-noble metal catalysts for the OER in alkaline media (Fig. 6b). The reaction rates of $6.2 \pm 1.6\,s^{-1}$ ($TOF_{surface}$) and $1.2 \pm 0.3\,s^{-1}$ (TOF_{bulk}) for 5.4 nm NiFe particles at 1.53 V_{RHE} ($\eta = 300$ mV) are among the highest reported for non-noble metal catalysts in an alkaline electrolyte[4,16,27,47,51–54].

Isotope labelling experiments. To provide further insight as to which TOF represents the true intrinsic activity, we used three complimentary isotope labelling procedures, all on samples with 6.7 nm particles, referred to below as procedures *a*, *b* and *c*, and illustrated schematically in Fig. 7. The natural oxidation of NiFe particles when exposed to air meant we had to oxidize the catalyst in $H_2{}^{16}O$ and then perform OER in an ^{18}O-based electrolyte (procedure *a*). We also oxidized the NiFe particles in $H_2{}^{18}O$ (procedure *b*) and $^{18}O_2$ (procedure *c*) atmosphere to study the possible differences between hydroxide and oxide compounds.

In procedure *a*, ^{16}O is incorporated into the NiFe nanoparticles through cycling in 0.1 M KOH made from ultrapure water, and the oxygen evolution process takes place in 0.1 M KOH made from ^{18}O water (~97% ^{18}O). Due to the natural abundance of ^{16}O, this has the advantage that the nanoparticles can easily be prepared with 99.8% ^{16}O. However, the lower isotopic purity of ^{18}O-labelled water limits the sensitivity towards isotope exchange of the subsequent EC–MS measurement. In procedures *b* and *c*, ^{18}O is incorporated in the NiFe structure either by cycling in an ^{18}O-labelled 0.1 M KOH electrolyte (procedure *b*) or by heating at 450 °C in the vacuum chamber in the presence of $^{18}O_2$ gas (procedure *c*). This allows for a greater sensitivity towards lattice exchange, but adds some uncertainty to the initial isotopic composition of the catalyst.

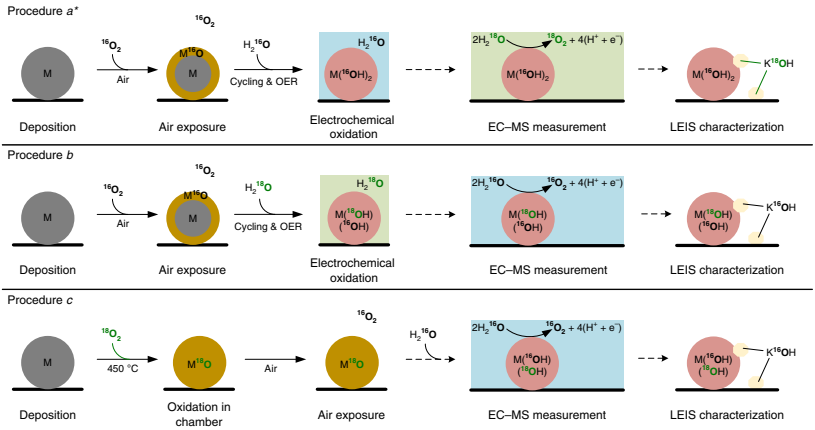

Fig. 7 | Isotope labelling experimental procedures. Schematic representation of the isotopic labelling experiments. Procedure *a* uses $H_2{}^{16}O$ to oxidize the nanoparticles and $H_2{}^{18}O$ for the oxygen evolution, and the opposite is done for Procedure *b*. Procedure *c* uses $^{18}O_2$ gas to oxidize NiFe and the oxygen evolution is performed in ^{16}O water. In the representation, M refers to Ni and Fe metal atoms. *The main text focuses on procedure *a*.

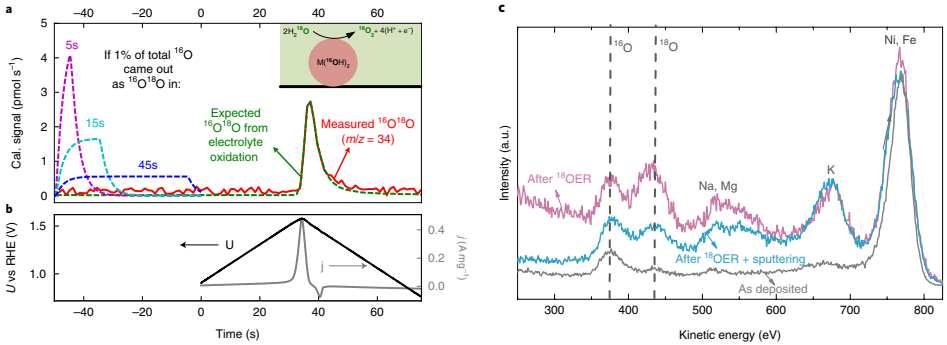

Fig. 8 | EC–MS and LEIS results from the isotope labelling experiment using procedure *a*. a, First linear sweep voltammetry in the $H_2{}^{18}O$ electrolyte after the sample preparation with ^{16}O. Calibrated mass spectrometer signal of $^{16}O^{18}O$ ($m/z = 34$) (red line) detected during oxygen evolution in 0.1 M KOH made with $H_2{}^{18}O$ during the first electrochemical potential cycle after the sample preparation with ^{16}O. The $^{16}O^{18}O$ signal expected without lattice exchange due to the composition of the electrolyte, which is a constant fraction of the $^{18}O_2$ ($m/z = 36$) signal, is co-plotted (green line). Also included are simulations of the $m/z = 34$ signal if 1% of the total ^{16}O contained by the oxidized catalyst came out as $^{18}O^{16}O$ in 5 s (magenta), 15 s (cyan) or 45 s (blue). The inset is a schematic of the oxygen evolution reaction in a ^{18}O-electrolyte on a $NiFeO_xH_y$ nanoparticle. **b**, The potential (black) and current (grey) from the same experiment. **c**, The LEIS spectra of the sample as deposited (grey), after the EC–MS experiment (purple) and after sputtering (blue).

In procedure *a*, the sample of deposited particles was cycled in 0.1 M KOH made from ultrapure water until a stable CV was obtained, that is, 20 cycles 0.5–1.5 V_{RHE}. At this point we assumed that the catalyst was in the fully oxygenated form, nominally $M(^{16}OH)_2$ where $M = Ni_xFe_{1-x}$. The electrode was then transferred at an open-circuit voltage to a stagnant thin-layer cell filled with ^{18}O-labelled 0.1 M KOH for measurement by EC–MS. The first cycle up to 1.55 V_{RHE} and back to 0.5 V_{RHE} is shown in Fig. 8a,b. In Fig. 8a, the calibrated $m/z = 34$ ($^{16}O^{18}O$) mass spectrometer signal is plotted as a function of time, and in Fig. 8b the potential and current are plotted on the same time axis. Co-plotted with the measured $^{16}O^{18}O$ signal in Fig. 8a is the expected $^{16}O^{18}O$ signal due to oxidation of the electrolyte, which contains only ~97% ^{18}O. The expected $^{16}O^{18}O$ signal is the measured $^{18}O_2$ ($m/z = 36$) signal multiplied by the steady-state $^{16}O^{18}O/^{18}O_2$ ratio. This ratio, as well as the calibration, were determined under operando conditions by steady-state oxygen evolution (Supplementary Note 5). The measured and expected $^{16}O^{18}O$ coincided, which indicates that all of the signal at $m/z = 34$

can be explained by the oxidation of the electrolyte alone. The onset of the oxygen signal is delayed with respect to the onset of the OER current by about ~3 s, as predicted by the mass-transport model described in Trimarco et al.[38], which indicates that the current at low overpotential does, indeed, go to OER and not another process.

To illustrate the sensitivity, we included in Fig. 8a the expected excess $m/z=34$ signal if 1% of the total ^{16}O contained by the catalyst, equivalent to approximately 10% of a monolayer, were released as $^{16}O^{18}O$. The release of 1% of the total ^{16}O in 45 seconds (dashed blue line in Fig. 8a), which corresponds to approximately 0.2% of a monolayer per second, is significantly above the detection limit. In comparison, the peak oxygen signal (at $m/z=36$) in this scan corresponds to 19% of a monolayer per second, or about 100 times greater. This proves that if even 1% of the OER activity were due to lattice oxygen evolution, it would be detectable.

The results of procedures *b* and *c* (Supplementary Fig. 7a–d) are similar, but because of low natural abundance of ^{18}O (0.02%), the sensitivity towards isotope exchange at $m/z=34$ and 36 is even higher. To determine whether the result is general, we also performed the isotope experiment (following procedure *a*) on a $NiFeO_xH_y$ thin film, and again observed no lattice exchange (Supplementary Fig. 7e). Additionally, to prove that our set-up is, indeed, sensitive enough to detect a lattice exchange when it does take place, we performed the same experiment on IrO_2/Ti in acid, as described in Fierro et al.[30], and reproduced their result of an isotope exchange greater than one monolayer. In Supplementary Fig. 8, this result is directly compared with that from $NiFeO_xH_y$.

In procedure *a*, after the EC–MS, the sample was rinsed in $H_2{}^{18}O$ before being transferred back to a vacuum for LEIS. The LEIS spectrum after OER, that is, the purple line in Fig. 8c, shows additional peaks when compared to the initial LEIS spectrum (black line), which we attribute to ^{16}O, ^{18}O, impurity Na and Mg salt deposits from the $H_2{}^{18}O$ rinsing, and to residual K from the electrolyte. The sample was then Ar-sputtered for 30 minutes before another LEIS spectrum was taken. This spectrum (blue line) shows an increased $^{16}O/^{18}O$ ratio, compared to the initial one. We therefore attribute the ^{18}O peak to residual $K^{18}OH$ and/or other hydroxide salts on the surface of the sample and the ^{16}O peak to ^{16}O that remained in the catalyst. After both procedures *b* and *c*, the $^{18}O/^{16}O$ ratio in LEIS after OER, rinsing with ultrapure water and sputtering, was approximately 1:1, with little to no K or other impurities, as shown in Supplementary Fig. 7. In both cases, there is a clear ^{18}O signal even before sputtering, which indicates that this isotope is present at the surface of the catalyst. The postsputtering 1:1 ratio presumably reflects the nominal $M(^{18}OH)(^{16}OH)$ formula that results from the experimental procedures, as illustrated in Fig. 7b,c. As the natural abundance of ^{18}O is so low (0.2%), the presence of ^{18}O on the LEIS spectra in procedures *b* and *c* implies that it was incorporated during the catalyst preparation before OER, and not during transfer through air from EC–MS to LEIS.

Discussion

The results obtained from the identical-location SEM (Fig. 2c), in addition to the stable current over 1,000 hours (Fig. 3), prove that the $NiFeO_xH_y$ particles are remarkably stable against corrosion.

The activity dependence on particle size is similar at 270, 300 and 370 mV overpotential (Fig. 5b). This is consistent with a lack of subsurface activity, which would involve the diffusion of water and oxygen through the nanoparticles, and could therefore introduce greater mass transport limitations for larger particles at high overpotentials, if the diffusion is sufficiently slow. Furthermore, the activity of the particles normalized to surface area, that is, $TOF_{surface}$, does not change with particle size (Fig. 6a). In contrast, the activity of the particles normalized to the total mass, which is proportional to the TOF_{bulk}, decreases with increasing particle size. Different Fe content cannot explain the observed trends (Supplementary Fig. 2b). TOF_{redox} of the electrodeposited $NiFeO_xH_y$ film shows a similar activity to that reported by Trotochaud et al.[27]. This is slightly lower than the TOF_{redox} for the nanoparticles, also consistent with a lack of subsurface activity and the observation that the Ni redox peak probes more than the Ni surface atoms.

Mass spectrometry and LEIS measurements for isotope experiments on $NiFeO_xH_y$ particles using three different approaches all indicate that oxygen is retained in the catalyst during OER, both in the bulk and, to at least some degree, also on the surface of the catalyst. Isotope experiments on a $NiFeO_xH_y$ thin film agree. The significance of this result is twofold. First, it provides additional evidence against activity below the outer surface or a near-surface region in which water is highly mobile, as this would involve lattice oxidation and/or the oxidation of low-mobility intercalated water. Second, the oxygen evolution mechanism does not proceed via lattice oxygen.

Based on the arguments above, we conclude that active sites are limited to a near-surface region, and that TOF_{redox} is a lower bound to the intrinsic activity of the active sites. Previous studies that show a linear correlation between loading and activity used porous electrodes without a well-defined outer surface[24]. Given the evidence presented here against bulk activity, we explain this observation on the basis that the surface area scales linearly with loading for these porous materials.

However, to determine if activity is limited to the outer surface atomic layer ($TOF_{surface}$) is more difficult. Although the charge passed in the Ni redox feature during cyclic voltammetry corresponds to ~3 atomic layers, this does not necessarily mean that this entire region also participates in OER. The nature of the transport involved in the Ni redox feature in alkaline is an unsolved problem[13], and models based on the transport of protons, hydroxide or cations have been proposed[55]. Whereas the Ni redox feature may only require the shuttling of a proton, OER necessarily requires the net transport of oxygen species. Our isotope result indicates that transport below the outer surface is either so slow as to inhibit OER or fast enough that any water or hydroxide in this region exchanges with the electrolyte before the onset of OER. We must admit that we cannot yet conclusively distinguish between the two possibilities.

As mentioned previously, lattice exchange is material dependent. The phenomenon is observed with Co_3O_4 (ref. [31]), iridium-based catalysts[30] and a few perovskites[34]. Besides being sensitive to the composition of the material, the lattice oxygen exchange also seems to be dependent on the structure. Indeed, lattice exchange was observed with amorphous and nanocrystalline RuO_2 phases with undercoordinated edge sites[28,33], but not with crystalline rutile RuO_2 (ref. [36]). Although we did not observe lattice exchange during OER in the case of $NiFeO_xH_y$ nanoparticles or an electrodeposited $NiFeO_xH_y$ thin film, the results may not be generalizable to all synthesis methods. Furthermore, we cannot rule out that such phenomena could, in principle, occur at much higher potentials which, unfortunately, cannot yet be studied in our EC–MS set-up, due to bubble formation.

The absence of the participation of lattice oxygen in $NiFeO_xH_y$ is in disagreement with the hypothesis that lattice exchange should occur with materials that have a catalytic activity that is pH dependent on the hydrogen scale[34], which is the case for $NiFeO_xH_y$ (ref. [56]). In contrast, it provides evidence for an associative mechanism, such as that proposed by Bell and co-workers[19].

In summary, we used well-characterized mass-selected nanoparticles of Ni and Fe as a model system to investigate their fundamental properties under oxygen-evolution conditions. We provided fundamental insight into the reaction and the origin of the high performance using LEIS spectroscopy and the microchip-based EC–MS set-up. The particles showed an exceptionally high activity and stability over 1,000 hours at 1.6 V_{RHE}. Isotope-labelling experiments performed after three distinct approaches showed that there was no participation of lattice oxygen or intercalated water in the oxygen

evolution. This allows us to conclude that the active sites responsible for such exceptional activity are only located in the ~3 atomic layer redox-active near-surface region of the nanoparticles, but to determine if the activity is limited to the outer surface requires a better knowledge of the ionic transport mechanisms within this region. Normalizing the activity to the outer surface results in a TOF of $6.2 \pm 1.6\,s^{-1}$ at $\eta = 0.3$ V, the highest reported to date. Further enhancements to the catalytic activity should focus on tailoring the atoms at the near-surface region, as opposed to the bulk.

Methods

Preparation of mass-selected NiFe nanoparticles. NiFe nanoparticles were prepared using a noble-gas aggregation magnetron sputtering nanoparticle source combined with a lateral time-of-flight mass filter (Fig. 1a) capable of mass selection of the nanoparticles before deposition[57] (Nano-Beam 2011, Birmingham Instruments Ltd) similar to that described by Pratontep et al.[58]. A 75 at% Ni/25 at% Fe sputtering target (99.95%, Kurt J. Lesker Ltd) was used and the particles were deposited onto clean and smooth Au disks. The nanoparticle source was fully UHV compatible and the mass filter had a base pressure in the low 10^{-10} mbar region. The mass filter was set to be used with negatively charged particles, and to have a mass resolution of $\sim m/\Delta m = 20$ to maximize the current of the particles. The vast majority of the particles that exited the nanoparticle source carried a single charge, and thus the current measured on the sample during the deposition together with the deposition time can be translated into the number of deposited particles. If not otherwise stated, the loading of the electrodes was a 15% projected surface area coverage, which corresponds to a total metal mass loading of 50–125 ng, which means a 315–785 ng cm^{-2} loading in circular spots of 4.5 mm in diameter, depending on the particle size.

Determination of particle-size distributions. NiFe nanoparticles with masses of 120,000, 350,000, 950,000 and 2,000,000 AMU were deposited onto Cu TEM grids covered with lacey carbon (300 mesh, Agar Scientific Ltd). After deposition and transfer under atmospheric conditions, the particles were imaged in the bright-field TEM mode in an FEI Tecnai T20 G^2 equipped with a thermionic electron source and using a 200 keV acceleration voltage. The images were analysed with ImageJ software to extract the average area of the particle projections, and a diameter was calculated assuming a circular shape (Supplementary Note 1).

Electrochemical measurements. Electrochemical measurements were performed using a rotating disk electrode in a PTFE (Teflon) cell at 1,600 revolutions per minute in N_2-saturated 1.0 M KOH. A carbon rod was used as the counter electrode with a Hg/HgO electrode as the reference electrode, which was calibrated to the RHE in the same electrolyte saturated with 1 bar H_2 over a clean Pt mesh before each experiment. The Ohmic drop was measured by using electrochemical impedance spectroscopy over a range of 10–200,000 Hz at an a.c. amplitude of 10 mV. The high-frequency intercept was fitted to an equivalent circuit to obtain the Ohmic losses, which typically ranged from 4 to 18 Ω. The Ohmic drop compensation was done by online Ohmic drop correction in which an 85% correction was applied. Ultrapure water (Milli-Q, 18.2 MΩ cm) with KOH (semiconductor grade, pellets, 99.9%) were used to prepare 1.0 M KOH. The initial catalytic activity was measured by recording five cyclic voltammograms at 10 mV s^{-1} up to 1.6 V_{RHE} followed by a 2 h potentiostatic measurement at 1.6 V_{RHE}. Finally, the activity was again assessed using CV. The activity of the different samples for the OER presented in this work was taken from the final CV. For each experiment, three independent samples were tested and the activity was averaged (Supplementary Figs. 9–11). The longer stability measurement was a static measurement at 1.6 V_{RHE}, for which the NiFe particles were deposited onto a gold sheet. The duration of this experiment meant only two samples were tested. The mass activity was obtained by normalizing the current with the total mass of Ni and Fe determined from the deposition current and time.

To compare the differences between lattice oxygen participation in $NiFeO_xH_y$ nanoparticles and thin film, thin films of $NiFeO_xH_y$ were electrodeposited. Using a three-electrode set-up, a current of −0.2 mA cm^{-2} for 5 min in an electrolyte of 0.1 M $Ni(NO_3)_2{\cdot}6H_2O$ and 5 mM $FeCl_2$. The composition determine by XPS indicates a mixture of approximately 32% Fe and 68% Ni at the surface.

Turnover frequency. To calculate the TOF, we used the formula:

$$\mathrm{TOF}(s^{-1}) = \frac{r_{O_2}}{\text{of active sites}} \quad (1)$$

The rate of O_2 turnovers (r_{O_2} s^{-1}) was calculated from the raw current:

$$r_{O_2} = i \times \left(\frac{N_A}{zF}\right) \quad (2)$$

Where i (A) is the current, N_A is the Avogadro number (6.022×10^{23} O_2 molecules per mol O_2), z is the number of electrons involved in the evolution of 1 O_2 molecule and F the Faraday constant (96,485 C mol^{-1}).

We determined a minimum (TOF_{bulk}) and a maximum ($TOF_{surface}$) TOF based on two different assumptions on the number of active sites.

For the calculation of TOF_{bulk}, we assumed that all the metal atoms deposited are active for OER. To calculate the total number of Ni and Fe metal atoms deposited on the surface ($N^{total}_{metal\ atom}$), the number of deposited particles ($N_{particles}$) were multiplied by the average number of atoms in each particle ($N^{particle}_{metal}$):

$$N^{total}_{metal\ atom} = N_{particles} \times N^{particle}_{metal\ atom} \quad (3)$$

$N_{particles}$ can be calculated from the deposition current (I_{depo} (A)), time of deposition (t_{depo} (s)) and the electric charge C (6.242×10^{-18} electrons C^{-1}) using equation (4):

$$N_{particles} = I_{depo} \times t_{depo} \times C \quad (4)$$

Finally, to calculate the number of metal atoms in a particle, we used the deposited particle mass set by the mass filter ($m_{particle}$ (kg)), N_A (mol^{-1})) and the average molar mass ($\overline{M}_{Ni_xFe_{1-x}}$ [kgmol^{-1}]) using the composition determined from the XPS after electrochemical treatment for each sample:

$$N^{particle}_{metal\ atom} = \frac{N_A \times m_{particle}}{\overline{M}_{Ni_xFe_{1-x}}} \quad (5)$$

To calculate the $TOF_{surface}$, the number of surface Ni and Fe atoms had to be calculated. The diameter of the nanoparticles was determined by TEM images and used to calculate the surface area per particle ($A_{particle}$) assuming a spherical shape. This is a conservative approach as part of the nanoparticle's surface will interface with the substrate and therefore will not contribute to the OER. Finally, this area was multiplied by $N_{particles}$ and the density of surface metal atoms to get the total number of surface Ni and Fe atoms. The assumed density of the surface metal atoms (ρ_{atoms}) of 12.5 metal atoms nm^{-2} is based on the metal–metal distance of 2.83 Å for $NiFeO_xH_y$ measured in situ under OER conditions[59]:

$$N^{total}_{surface\ atom} = N_{particles} \times \rho_{atoms} \times A_{particle} \quad (6)$$

XPS and LEIS characterization. LEIS (Supplementary Figs. 12 and 13) and XPS spectra (Supplementary Figs. 14–16) were recorded for each sample after deposition (without breaking the vacuum) and after activity testing. To remove the remaining electrolyte on the surface after the activity test, the samples were thoroughly rinsed with ultrapure water (18.2 MΩ cm) before loading into the ultrahigh vacuum chamber to prevent the formation of a potassium layer hindering the detection of other elements.

For LEIS measurements, 1 keV He^+ ions from an Omicron ISE100 ion gun were used and the energy of the scattered ions was recorded with the same 7-channel analyser used for XPS measurements operated in constant retard ratio mode (with a retard ratio of 5). The LEIS spectra presented are normalized based on the intensity of the gold peak at ~ 925 eV.

For the XPS measurements, unmonochromatized Mg Kα radiation from a SPECS XR50 dual filament X-ray gun was used. The electron energies were measured with an Omicron NanoSAM 7-channel energy analyser operated in the constant pass energy mode. A pass energy of 50 eV was chosen to increase the signal from the low loadings of nanoparticles. For each sample, a survey scan and detailed scans of Au 4f, O 1s, Ni 2$p_{3/2}$ and Fe 2$p_{3/2}$ were recorded. All the spectra were charge corrected based on the Au 4$f_{7/2}$ peak, which we assumed to correspond to metallic Au at 84 eV binding energy. A Shirley background was subtracted from the detailed spectra presented and the intensities were normalized with the Au 4f peak area.

Identical-location SEM imaging. Identical-location SEM imaging was performed on a sample that contained 5.4 nm NiFe particles on the Au electrode after deposition and transfer under atmospheric conditions and after electrochemical testing. SEM images were acquired at 5 kV using an FEI Helios EBS3 microscope equipped with a field emission gun and a through-the-lens detector for high-resolution imaging.

Identical-location TEM imaging and EDX line scans. Identical-location HRTEM images were recorded at 80 kV electron energy, using a FEI Titan E-Cell 80–300 ST TEM with a monochromated electron source and postobjective aberration correction. For the identical-location TEM studies, particles were deposited on Au-coated Cu TEM grids with suspended monolayer graphene layers (Quantifoil). After imaging, the grids were mounted to a rotating disk electrode set-up and subjected to two CVs at 10 mV s^{-1} between 1 and 1.5 V_{RHE} in 1 M KOH. After the electrochemical oxidation, the particles were transferred back to the TEM and imaged a second time. EDX line scans were recorded using a silicon drift detector from Oxford Instruments on random particles before and after electrochemical oxidation.

EC–MS experiments. To investigate oxygen exchange between the NiFe particles and the electrolyte, isotopically labelled electrolyte (with ^{18}O) and EC–MS were used. The EC–MS set-up was based on a microfabricated membrane coated with

a fluorinated polymer and a well-defined capillary. Below the membrane, a small cavity was pressurized with He carrier gas and, together with the capillary forces, the electrolyte is kept out of the chip. The cavity was connected to a vacuum chamber equipped with a quadrupole mass spectrometer (Pfeiffer Vacuum QMA 125) through a well-defined microfabricated capillary that limited the flow of molecules to a level that can be handled by a single turbomolecular pump. For the experiments, a self-designed stagnant layer electrochemical cell was used in which the electrolyte thickness was 100 µm, which, together with the design of the vacuum chamber and microchip, gave a time response below 1 s. The area under the modelled curves in Fig. 8 (blue, magenta and cyan lines) corresponds to the nominal number labelled oxygen atom in the nanoparticle samples, and the shapes of these curves were calculated by a mass transport model that accounted for diffusion of O_2 through the 100 µm electrolyte layer. Details of the set-up, experimental method and mass-transport model are described elsewhere[58]. All the experiments were performed using a 0.1 M KOH electrolyte made with either ultrapure water (natural isotope distribution) or ^{18}O enriched water (97.2% $H_2{}^{18}O$, 1.3% $H_2{}^{17}O$ and 1.5% $H_2{}^{16}O$, Medical Isotopes). The mass spectrometer signals were calibrated internally for each experiment, as was the steady-state ratio of $m/z = 34$ to $m/z = 36$ for procedure *a*. The raw data for these calibrations are shown (for procedure *a*) in Supplementary Fig. 6.

Data availability

The data that support the plots within this paper and other findings of this study are available from the corresponding author upon reasonable request.

Received: 28 February 2018; Accepted: 14 September 2018;
Published online: 5 November 2018

References

1. Lewis, N. S. & Nocera, D. G. Powering the planet: chemical challenges in solar energy utilization. *Proc. Natl Acad. Sci. USA* **103**, 15729–15735 (2006).
2. Debe, M. K. Electrocatalyst approaches and challenges for automotive fuel cells. *Nature* **486**, 43–51 (2012).
3. Montoya, J. H. et al. Materials for solar fuels and chemicals. *Nat. Mater.* **16**, 70–81 (2017).
4. Hong, W. T. et al. Toward the rational design of non-precious transition metal oxides for oxygen electrocatalysis. *Energy Environ. Sci.* **8**, 1404–1427 (2015).
5. Durst, J. et al. New insights into the electrochemical hydrogen oxidation and evolution reaction mechanism. *Energy Environ. Sci.* **7**, 2255–2260 (2014).
6. Stamenkovic, V. R., Strmcnik, D., Lopes, P. P. & Markovic, N. M. Energy and fuels from electrochemical interfaces. *Nat. Mater.* **16**, 57–69 (2017).
7. Greeley, J. & Markovic, N. M. The road from animal electricity to green energy: combining experiment and theory in electrocatalysis. *Energy Environ. Sci.* **5**, 9246 (2012).
8. Cifrain, M. & Kordesch, K. in *Handbook of Fuel Cells—Fundamentals, Technology and Applications* Vol. 1 (eds Vielstich, W.A., Gasteiger, H.A. & Lamm, A.) 267–280 (Wiley, Hoboken, 2010).
9. Pagliaro, M., Konstandopoulos, A. G., Ciriminna, R. & Palmisano, G. Solar hydrogen: fuel of the near future. *Energy Environ. Sci.* **3**, 279 (2010).
10. Seh, Z. W. et al. Combining theory and experiment in electrocatalysis: insights into materials design. *Science* **355**, eaad4998 (2017).
11. The production of hydrogen and oxygen through the electrolysis of water. *Scientific American Supplement No. 819* Vol. XXXII, article II (1891).
12. Trotochaud, L., Young, S. L., Ranney, J. K. & Boettcher, S. W. Nickel–iron oxyhydroxide oxygen-evolution electrocatalysts: the role of intentional and incidental iron incorporation. *J. Am. Chem. Soc.* **136**, 6744–6753 (2014).
13. Dionigi, F. & Strasser, P. NiFe-based (oxy)hydroxide catalysts for oxygen evolution reaction in non-acidic electrolytes. *Adv. Energy Mater.* **6**, 1600621 (2016).
14. Burke, M. S., Enman, L. J., Batchellor, A. S., Zou, S. & Boettcher, S. W. Oxygen evolution reaction electrocatalysis on transition metal oxides and (oxy)hydroxides: activity trends and design principles. *Chem. Mater.* **27**, 7549–7558 (2015).
15. Enman, L. J., Burke, M. S., Batchellor, A. S. & Boettcher, S. W. Effects of intentionally incorporated metal cations on the oxygen evolution electrocatalytic activity of nickel (oxy)hydroxide in alkaline media. *ACS Catal.* **6**, 2416–2423 (2016).
16. Klaus, S., Cai, Y., Louie, M. W., Trotochaud, L. & Bell, A. T. Effects of Fe electrolyte impurities on $Ni(OH)_2$ /NiOOH structure and oxygen evolution activity. *J. Phys. Chem. C* **119**, 7243–7254 (2015).
17. Li, N. et al. Influence of iron doping on tetravalent nickel content in catalytic oxygen evolving films. *Proc. Natl Acad. Sci. USA* **114**, 1486–1491 (2017).
18. Görlin, M. et al. Oxygen evolution reaction dynamics, Faradaic charge efficiency, and the active metal redox states of Ni–Fe oxide water splitting electrocatalysts. *J. Am. Chem. Soc.* **138**, 5603–5614 (2016).
19. Friebel, D. et al. Identification of highly active Fe sites in (Ni,Fe)OOH for electrocatalytic water splitting. *J. Am. Chem. Soc.* **137**, 1305–1313 (2015).
20. Stevens, M. B., Trang, C. D. M., Enman, L. J., Deng, J. & Boettcher, S. W. Reactive Fe-Sites in Ni/Fe (oxy)hydroxide are responsible for exceptional oxygen electrocatalysis activity. *J. Am. Chem. Soc.* **139**, 11361–11364 (2017).
21. Hunter, B., Winkler, J. & Gray, H. Iron is the active site in nickel/iron water oxidation electrocatalysts. *Molecules* **23**, 903 (2018).
22. Ahn, H. S. & Bard, A. J. Surface interrogation scanning electrochemical microscopy of $Ni_{1-x}Fe_xOOH$ ($0 < x < 0.27$) oxygen evolving catalyst: kinetics of the 'fast' iron sites. *J. Am. Chem. Soc.* **138**, 313–318 (2016).
23. Xiao, H., Shin, H. & Goddard, W. A. Synergy between Fe and Ni in the optimal performance of (Ni,Fe)OOH catalysts for the oxygen evolution reaction. *Proc. Natl Acad. Sci. USA* **115**, 5872–5877 (2018).
24. Batchellor, A. S. & Boettcher, S. W. Pulse-electrodeposited Ni–Fe (oxy) hydroxide oxygen evolution electrocatalysts with high geometric and intrinsic activities at large mass loadings. *ACS Catal.* **5**, 6680–6689 (2015).
25. Doyle, A. D., Bajdich, M. & Vojvodic, A. Theoretical insights to bulk activity towards oxygen evolution in oxyhydroxides. *Catal. Lett.* **147**, 1533–1539 (2017).
26. Morales-Guio, C. G., Liardet, L. & Hu, X. Oxidatively electrodeposited thin-film transition metal (oxy)hydroxides as oxygen evolution catalysts. *J. Am. Chem. Soc.* **138**, 8946–8957 (2016).
27. Trotochaud, L., Ranney, J. K., Williams, K. N. & Boettcher, S. W. Solution-cast metal oxide thin film electrocatalysts for oxygen evolution. *J. Am. Chem. Soc.* **134**, 17253–17261 (2012).
28. Wohlfahrt-Mehrens, M. & Heitbaum, J. Oxygen evolution on Ru and RuO_2 electrodes studied using isotope labelling and on-line mass spectrometry. *J. Electroanal. Chem. Interfacial Electrochem.* **237**, 251–260 (1987).
29. Diaz-Morales, O., Calle-Vallejo, F., de Munck, C. & Koper, M. T. M. Electrochemical water splitting by gold: evidence for an oxide decomposition mechanism. *Chem. Sci.* **4**, 2334 (2013).
30. Fierro, S., Nagel, T., Baltruschat, H. & Comninellis, C. Investigation of the oxygen evolution reaction on Ti/IrO_2 electrodes using isotope labelling and on-line mass spectrometry. *Electrochem. Commun.* **9**, 1969–1974 (2007).
31. Amin, H. M. A. & Baltruschat, H. How many surface atoms in Co_3O_4 take part in oxygen evolution? Isotope labeling together with differential electrochemical mass spectrometry. *Phys. Chem. Chem. Phys.* **19**, 25527–25536 (2017).
32. Surendranath, Y., Kanan, M. W. & Nocera, D. G. Mechanistic studies of the oxygen evolution reaction by a cobalt–phosphate catalyst at neutral pH. *J. Am. Chem. Soc.* **132**, 16501–16509 (2010).
33. Macounova, K., Makarova, M. & Krtil, P. Oxygen evolution on nanocrystalline RuO_2 and $Ru_{0.9}Ni_{0.1}O_{2-\delta}$ electrodes—DEMS approach to reaction mechanism determination. *Electrochem. Commun.* **11**, 1865–1868 (2009).
34. Grimaud, A. et al. Activating lattice oxygen redox reactions in metal oxides to catalyse oxygen evolution. *Nat. Chem.* **9**, 457–465 (2017).
35. Willsau, J., Wolter, O. & Heitbaum, J. In the oxygen evolution reaction on platinum? *J. Electroanal. Chem.* **195**, 299–306 (1985).
36. Stoerzinger, K. A. et al. Orientation-dependent oxygen evolution on RuO_2 without lattice exchange. *ACS Energy Lett.* **2**, 876–881 (2017).
37. Lu, X. & Zhao, C. Electrodeposition of hierarchically structured three-dimensional nickel–iron electrodes for efficient oxygen evolution at high current densities. *Nat. Commun.* **6**, 6616 (2015).
38. Trimarco, D. B. et al. Enabling real-time detection of electrochemical desorption phenomena with sub-monolayer sensitivity. *Electrochim. Acta* **268**, 520–530 (2018).
39. Paoli, E. A. et al. Oxygen evolution on well-characterized mass-selected Ru and RuO_2 nanoparticles. *Chem. Sci.* **6**, 190–196 (2015).
40. Li, Z. Y. et al. Three-dimensional atomic-scale structure of size-selected gold nanoclusters. *Nature* **451**, 46–48 (2008).
41. Ferreira, P. J. et al. Instability of Pt/C electrocatalysts in proton exchange membrane fuel cells. *J. Electrochem. Soc.* **152**, A2256 (2005).
42. Meier, J. C. et al. Design criteria for stable Pt/C fuel cell catalysts. *Beilstein J. Nanotechnol.* **5**, 44–67 (2014).
43. Fiordaliso, E. M., Dahl, S. & Chorkendorff, I. Strong metal support interaction of Pt and Ru nanoparticles deposited on HOPG probed by the H–D exchange reaction. *J. Phys. Chem. C* **116**, 5773–5780 (2012).
44. Binninger, T. et al. Thermodynamic explanation of the universal correlation between oxygen evolution activity and corrosion of oxide catalysts. *Sci. Rep.* **5**, 12167 (2015).
45. Spöri, C., Kwan, J. T. H., Bonakdarpour, A., Wilkinson, D. P. & Strasser, P. The stability challenges of oxygen evolving catalysts: towards a common fundamental understanding and mitigation of catalyst degradation. *Angew. Chem. Int. Ed.* **56**, 5994–6021 (2017).
46. Hartl, K., Hanzlik, M. & Arenz, M. IL-TEM investigations on the degradation mechanism of Pt/C electrocatalysts with different carbon supports. *Energy Environ. Sci.* **4**, 234–238 (2011).
47. Ng, J. W. D. et al. Gold-supported cerium-doped NiO_x catalysts for water oxidation. *Nat. Energy* **1**, 16053 (2016).
48. Xu, X., Song, F. & Hu, X. A nickel iron diselenide-derived efficient oxygen-evolution catalyst. *Nat. Commun.* **7**, 12324 (2016).

49. Silva, H. et al. Synthesis and characterization of Fe-Ni/χ-Al_2O_3 egg-shell catalyst for H_2 generation by ammonia decomposition. *Appl. Catal. A* **505**, 548–556 (2015).
50. Burke, M. S. et al. Revised oxygen evolution reaction activity trends for first-row transition-metal (oxy)hydroxides in alkaline media. *J. Phys. Chem. Lett.* **6**, 3737–3742 (2015).
51. Zhang, B. et al. Homogeneously dispersed multimetal oxygen-evolving catalysts. *Science* **352**, 333–337 (2016).
52. Gong, M. et al. An advanced Ni–Fe layered double hydroxide electrocatalyst for water oxidation. *J. Am. Chem. Soc.* **135**, 8452–8455 (2013).
53. Song, F. & Hu, X. Exfoliation of layered double hydroxides for enhanced oxygen evolution catalysis. *Nat. Commun.* **5**, 4477 (2014).
54. Long, X. et al. A strongly coupled graphene and FeNi double hydroxide hybrid as an excellent electrocatalyst for the oxygen evolution reaction. *Angew. Chem. Int. Ed.* **53**, 7584–7588 (2014).
55. Wehrens-Dijksma, M. & Notten, P. H. L. Electrochemical quartz microbalance characterization of $Ni(OH)_2$-based thin film electrodes. *Electrochim. Acta* **51**, 3609–3621 (2006).
56. Lu, X. & Zhao, C. Electrodeposition of hierarchically structured densities. *Nat. Commun.* **6**, 1–7 (2015).
57. von Issendorff, B. & Palmer, R. E. A new high transmission infinite range mass selector for cluster and nanoparticle beams. *Rev. Sci. Instrum.* **70**, 4497–4501 (1999).
58. Pratontep, S., Carroll, S. J., Xirouchaki, C., Streun, M. & Palmer, R. E. Size-selected cluster beam source based on radio frequency magnetron plasma sputtering and gas condensation. *Rev. Sci. Instrum.* **76**, 045103 (2005).
59. Biesinger, M. C., Lau, L. W. M., Gerson, A. R. & Smart, R. S. C. The role of the Auger parameter in XPS studies of nickel metal, halides and oxides. *Phys. Chem. Chem. Phys.* **14**, 2434 (2012).
60. Biesinger, M. C. et al. Resolving surface chemical states in XPS analysis of first row transition metals, oxides and hydroxides: Cr, Mn, Fe, Co and Ni. *Appl. Surf. Sci.* **257**, 2717–2730 (2011).
61. Grosvenor, A. P., Biesinger, M. C., Smart, R. S. C. & McIntyre, N. S. New interpretations of XPS spectra of nickel metal and oxides. *Surf. Sci.* **600**, 1771–1779 (2006).

Acknowledgements

This work was supported by a research grant (9455) from VILLUM FONDEN. We also acknowledge UPCAT under project no. 2015-1-12315.

Author contributions

I.E.L.S., J.K. and I.C. conceived the experiments. C.R. participated in the conception of the experiments and performed the electrochemical measurements. B.S. participated in the conception of the experiments, prepared the nanoparticles and performed the UHV experiments. S.B.S. performed and helped in the design of the EC–MS experiments. D.B.T., P.C.K.V. and O.H. designed and helped with the interpretation of the EC–MS experiments. E.M.F. and C.D.D. performed the microscopy characterization. J.E.S. and A.B. contributed to the LEIS measurements. C.R., B.S. and S.B.S. co-wrote the manuscript. All the authors discussed the results and commented on the manuscript.

Competing interests

The authors declare no competing interests.

Additional information

Supplementary information is available for this paper at https://doi.org/10.1038/s41929-018-0162-x.

Reprints and permissions information is available at www.nature.com/reprints.

Correspondence and requests for materials should be addressed to I.C.

Publisher's note: Springer Nature remains neutral with regard to jurisdictional claims in published maps and institutional affiliations.

Paper III

https://dx.doi.org/10.1021/acscatal.0c00779

Particle Size Effects on Platinum Dissolution: Considerations for Accelerated Stability Testing of Fuel Cell Catalysts

Daniel J.S. Sandbeck, Niklas M. Secher, Florian D. Speck, Jakob E. Sørensen, Jakob Kibsgaard, Ib Chorkendorff, and Serhiy Cherevko

ACS Catal. 2020, 10, 6281-6290

ACS Catalysis

pubs.acs.org/acscatalysis Research Article

Particle Size Effect on Platinum Dissolution: Considerations for Accelerated Stability Testing of Fuel Cell Catalysts

Daniel J. S. Sandbeck,*[,⊥] Niklas Mørch Secher,[⊥] Florian D. Speck, Jakob Ejler Sørensen, Jakob Kibsgaard, Ib Chorkendorff, and Serhiy Cherevko*

Cite This: ACS Catal. 2020, 10, 6281−6290 Read Online

ACCESS | Metrics & More | Article Recommendations | Supporting Information

ABSTRACT: Polymer electrolyte membrane fuel cells (PEMFCs) are highly attractive for use in electric vehicles. In PEMFCs, small particle sizes of the Pt catalyst are required to increase Pt utilization, which lower costs and also increase Pt dispersion, which itself minimizes O_2 mass transport losses. Reducing the particle size improves both the utilization and dispersion; however, stability of small particle sizes is an issue. Pt dissolution, as one of the major degradation mechanisms of PEMFC catalyst layers, is predicted to depend on the particle size. The particle size cannot be independently varied from loading in commercial Pt/C materials that have been used in numerous studies employing accelerated stability tests (ASTs). Therefore, in the study presented here, the Pt particle diameter was varied from 2 to 10 nm by depositing mass-selected nanoparticles on a flat glassy carbon substrate using magnetron sputtering. This allows exclusive control over particle density (interparticle distance) and particle size, which becomes difficult even with advanced synthetic techniques for applied Pt/C materials. Additionally, effects of the 3D porous support are eliminated. These model systems were subjected to an aggressive AST in order to cause significant Pt dissolution, which was monitored online using the scanning flow cell coupled to an inductively coupled plasma mass spectrometer. The results uncover a previously overlooked phenomenon: two competing trends in dissolution from (1) particle passivation caused by particle size-dependent shifts on oxophilicity and (2) electrochemically active surface area. Therefore, crucial impacts of the particle size on degradation may be overlooked in a variety of electrochemical studies, which compare catalytic materials. Finally, suggestions are given for improved ASTs for dissolution, which provide insights into the intrinsic stability of Pt nanoparticles toward dissolution.

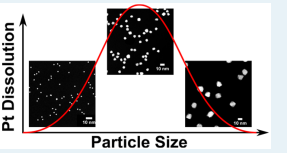

KEYWORDS: *Pt dissolution, particle size effect, stability, degradation, AST, ADT, PEMFC*

1. INTRODUCTION

Because of increasing interest in alternative transportation technologies, electric vehicles have gained considerable attention in recent years. Battery electric vehicles have been prominently covered in media with the advent of Tesla Inc. and other manufacturers. If electricity is generated from renewable sources, battery electric vehicles present a promising green technology to help reduce CO_2 and other toxic emissions, alleviating air pollution and climate change concerns. However, there is still room for improvement of such electrochemical technologies as they are to some extent limited in driving range, charging time, and there exist concerns regarding lithium resources.[1−5] Regardless, developing a singular economy dependent on a narrow range of technology and resources is a precarious endeavor and increased economic stability will benefit from complimentary industries.[4,5]

Polymer electrolyte membrane fuel cell (PEMFC) electric vehicles alleviate several shortcomings of battery electric vehicles, such as driving range and charging time,[6,7] and have already entered consumer production by several automakers.[8−10] However, this technology also comes with its own set of challenges such as high costs and limited lifetime, which remain as key challenges on the road to widespread market penetration. A majority of the cost comes from the use of Pt as an electrocatalyst for the sluggish oxygen reduction reaction (ORR) in the catalyst layer.[11,12] In order to minimize the required quantities, Pt is dispersed in the form of nanoparticles on a carbon support (Pt/C) to maximize the available surface area relative to mass, that is, Pt utilization. Furthermore, small particle sizes, yielding high Pt utilization and dispersion, are required to minimize local O_2 mass transport loses necessary for high power performance.[13−16] Therefore, considerable research efforts have focused on developing highly active and highly dispersed nanoparticulate catalysts,[17−24] with the end goal of reducing the required quantities of Pt via decreased metal loading.[13,25] By minimizing the Pt particle size and maximizing dispersion, (ideally) higher

Received: February 14, 2020
Revised: April 18, 2020
Published: May 6, 2020

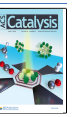

https://dx.doi.org/10.1021/acscatal.0c00779
ACS Catal. 2020, 10, 6281−6290

ORR currents relative to Pt mass (i.e., mass-specific activity) can be achieved, reducing the required Pt quantities.

Unfortunately, elucidation of the particle size on activity has been met with discrepancies. Several studies have shown a maximum in mass-specific activity (i.e., $mA \cdot mg_{Pt}^{-1}$) in the range 2−5 nm, which has been attributed to the adsorption strength of oxygenated species on terraces reaching a minimum at a particular particle size.[26−29] However, some studies have reported a continuous decrease in mass activity with increasing particle size.[21,30−32] It is possible that the lack of observed maxima was hindered by experimental error, limited variation of particle sizes within the studied materials, and wide particle size distributions within single samples.

Additionally, disparities exist between studies on area-specific activity (i.e., $mA \cdot cm_{Pt}^{-2}$). By normalizing to the real, that is electrochemically active surface area (ECSA), the intrinsic activity of catalytic surfaces may be understood. Many studies converge on the conclusion of increasing area-specific activity with increasing particle size approaching that of bulk Pt,[21,26,28,31,33] although some reports have not seen a change within experimental error, depending on the conditions.[32,34] The observed trend has been attributed to the decreasing oxophilicity of Pt nanoparticles with size, which diminishes the adsorption of poisoning oxygenated species for the ORR.[33] Although the area-specific activity appears to be diminished as particle sizes are reduced, mass activity remains to be the critical parameter dictated by costs. Furthermore, small particle sizes and high dispersion are required to meet high power performance targets.[13−16] However, stability may become an issue in implementing very small particle sizes.

Recently, in addition to activity, a surge in publications which includes catalyst stability reflects the recognition of this vital issue.[35] Platinum dissolution and carbon corrosion have been recognized as the primary degradation mechanisms of the catalyst layer, which are closely related to the secondary degradation mechanisms of Ostwald ripening, agglomeration, and particle detachment.[36] To study degradation, experiments typically measure ORR activity before and after an accelerated stability/stress test (AST), otherwise known as accelerated degradation test (ADT) or accelerated degradation protocol. Various tests/protocols have been adapted; however, in general, most studies use potential ranges from 0.6 to 1.0 (or 0.6 to 0.95) and 1.0 to 1.5 V_{RHE}, in an effort to exclusively study Pt dissolution and carbon corrosion, respectively (these ranges are intended to represent the load and start/stop conditions of a PEMFC, respectively).[13,21,22,24,28,32,34,37−43]

In recent years, our research group and others have uncovered fundamental aspects of transient electrochemical Pt dissolution and a very brief summary should be given here, whereas interested readers may be referred to comprehensive reviews.[44,45] During relatively slow scan rates during a cyclic voltammogram (CV), a so-called anodic dissolution peak is seen at an onset of ca. 1.0 V_{RHE} during the positive-going, anodic potential scan.[44−49] This dissolution coincides with the place-exchange mechanism during Pt oxidation, and as an oxide layer forms the dissolution rate decreases as the Pt surface becomes passivated. In the negative-going, cathodic potential scan, a much larger so-called cathodic dissolution peak is seen as the formed oxide is reduced. The extent and onset of cathodic dissolution depends on the amount of oxide which was formed; however, significant dissolution does not take place without reaching potentials below ca. 1.0 V_{RHE}.

From this it is clear that minimal dissolution will take place during typically used ASTs which do not transverse 1.0 V_{RHE}, and furthermore, realistic spikes in potential during start/stop of a PEMFC will go from potentials <1.0 V_{RHE} to even higher than 1.5 V_{RHE}. Hence, Pizzutilo et al. exclusively investigated the impact of AST potential limits using in situ Pt dissolution and carbon corrosion (CO_2) experiments.[50] The central outcome of the study was the suggested use of a "combined cycle" AST spanning 0.6−1.5 V_{RHE}, as the results showed this to cause substantial Pt dissolution with relatively minimal carbon corrosion. Therefore, this AST could aid in understanding the degradation behavior of PEMFC catalysts.

Stability investigations focused on particle size effects remain to establish firm conclusions, as ambiguities exist in analogy to the discussed activity studies. Many studies have indeed shown a decreasing stability with decreasing particle size via losses in ECSA and area-specific activity.[21,28,32] On the contrary, some studies have reported no particle size dependence by studying materials of varying size but with narrow particle size distributions within each material, and rather suggest that large particle size distributions promote degradation via Ostwald ripening.[34,37] However, in the studies which found small sizes to be the least stable, the smallest particle sizes had the narrowest particle size distributions, a consequence of the commonly used procedures of annealing heat treatments to increase in the particle size of Pt/C materials. Furthermore, Ahluwalia et al. observed that the particle size effect on Pt dissolution can depend on the applied potential protocol with ex situ ICP−MS dissolution experiments.[38]

These uncertainties in particle size effects described above highlight the need for well-defined systems in fundamental investigations. To vary particle size via typically used impregnation and precipitation synthetic techniques of commercial materials, a subsequent annealing procedure is used, which results in wide size distributions, increased interparticle distances, and can alter the carbon support.[26,34,37,38,51−55] Some chemical approaches yield exclusive control over particle size and loading, with much narrower size distributions; however, the surfactants used in synthesis can be difficult to remove from the products. Furthermore, the type of support used will influence the interparticle distance and diffusional paths of dissolved Pt species.

Therefore, there is an immediate need for well-defined systems to reach firm conclusions on particle size effects. The use of a magnetron gas aggregation source allows precise control over particle size and coverage (interparticle distance) by depositing mass-selected nanoparticles on a relatively flat substrate.[56,57] Also, alloy clusters have been investigated using this method, but they show optimal mass activity at much larger sizes than pure Pt.[58,59] This method eliminates the possibility of organic contaminations, impacts of a 3D porous support on Pt dissolution,[60] and also results in a narrow size distribution. Furthermore, precise control over interparticle distance excludes possible effects which have recently shown to drastically alter dissolution/degradation,[61,62] and will be addressed further in a parallel investigation.

Here, in this study, magnetron-sputtered mass-selected materials were synthesized with varying particle sizes (i.e., masses) of 2, 3, 4, 6, 7, 8, and 10 nm diameters (identical diameter within a given sample) with similar interparticle distances of around 6 nm (1−9% coverages). Using a large sample set reduces the possibility of missing trends and the reasonably large interparticle distance should minimize

https://dx.doi.org/10.1021/acscatal.0c00779
ACS Catal. 2020, 10, 6281−6290

possible interparticle distance effects (addressed in a parallel study).[62] To investigate degradation, online electrochemical dissolution of Pt was monitored using the scanning flow cell coupled to an inductively coupled plasma mass spectrometer (SFC−ICP−MS). An AST was chosen that was previously suggested to cause minimal carbon corrosion with enhanced transient Pt dissolution. Trends in Pt dissolution rates and dissolved quantities are observed, which depend on the applied potential protocol, and a maximum in Pt dissolution emerges at intermediate particle sizes as a consequence of two competing phenomena. These critical conclusions highlight overlooked mechanisms which should be given careful consideration by researchers when designing stability studies.

2. EXPERIMENTAL SECTION

2.1. Mass-Selected Sample Preparation. The Pt nanoparticles were prepared using magnetron sputtering of a Pt target (99.99%, AJA International Inc., USA) and subsequent noble-gas aggregation in a liquid nitrogen cooled aggregation zone. This was followed by a time-of-flight mass filtering, which allows for fine control of particle sizes as previously described.[57] The nanoparticle source (Birmingham Instruments Ltd. 2011) was operated at a mass filter resolution of $m/\Delta m$ = 20 for high deposition rates, which for 6 nm particles results in an uncertainty in size of 0.1 nm. Following the filtering, the charged particles were soft-landed (0.001−0.15 eV/atom) on a planar glassy carbon substrate (10 × 10 × 3 mm, SIGRADUR G, HTW GmbH) under ultrahigh vacuum conditions. The glassy carbon substrate was sputtered for 10 min with 1 keV Ar^+ to clean the surface of adventitious carbon and increase the stability of the nanoparticles against sintering. As most particles exiting the mass filter are singly charged, the coverage of nanoparticles on the sample was controlled by monitoring the neutralization current on the sample (which also ensures electrical contact of the Pt particles). Coverage was calculated by comparing the total projected area of the nanoparticles to the deposition area and is reported in % of a monolayer of particles. To ensure a homogeneous coverage across the entire sample area, the supports were rastered in front of the beam during deposition. Particles of seven different sizes were prepared with similar interparticle distances, resulting in different coverages determined by simulation of interparticle distances.[63] The mean interparticle distance was kept constant to eliminate the recently reported effects of interparticle distance on Pt and also Pd degradation,[61,62] and is exclusively addressed in a parallel investigation on platinum dissolution under AST protocols. Because of the random nature of particle depositions, there is an inherent normal distribution in the interparticle distances for all the particles in a sample (see interparticle distance distributions in Figure S1). The mean interparticle distance is therefore a variable that represents these distributions and can be used to distinguish between different distributions. The samples were deposited with mean interparticle distances between 6.1 and 6.5 nm with the standard deviation of the distributions ranging from 4.4 to 6.8 nm. As the particles are filtered based on mass and not size, equivalent particle diameters were calculated using the density of Pt and assuming spherical particles. The different sample parameters are summarized in Table S1.

2.2. Scanning Transmission Electron Microscopy. Scanning Transmission electron microscopy (STEM) images were acquired on a FEI Titan Analytical 80-300ST TEM with a preobjective lens spherical aberration corrector (CESCOR form CEOS Company) operated at 300 kV in STEM mode using a high-angle annular dark field detector with a maximum resolution of 0.08 nm. For STEM imaging, the mass-selected particles were deposited on Cu TEM grids with a lacey carbon film (SPI Supplies) at suitable coverages for image analysis, ensuring a low number of overlapping particles (see Figure S3). All images used for image analysis were acquired with a pixel size of approx. 0.1 nm and more than 100 particles were measured for each sample. Size analysis was performed with ImageJ (1.51j8) by using the Threshold and Analyze Particles functions to find the projected area of each individual particle. The particle diameters were calculated from the projected particle areas assuming circular particle projections because of the number of different particle shapes. Any overlapping particles were ignored in the analysis.

2.3. X-ray Photoelectron Spectroscopy. X-ray photoelectron spectra were measured on a PHI Quantera II scanning X-ray microprobe using Al Kα irradiation ($h\nu$ = 1486.6 eV) of a 100 μm diameter area at 25 W and 15 kV. Survey scans at a step size of 1 and 280 eV pass energy were collected for 200 ms dwell time per step. Data were analyzed in CasaXPS (2.3.18PR1.0), using instrument-specific relative sensitivity factors, Shirley type backgrounds, and a binding energy scale calibrated to the graphitic carbon peak at 284.5 eV.

2.4. Online Electrochemical Dissolution (SFC−ICP−MS). Potential control was supplied by a Gamry Reference 600 potentiostat/galvanostat. The working electrode (WE) was created by making contact with the mass-selected nanoparticles on the glassy carbon substrate. The contact area inside the SFC silicon ring was 0.011 cm^2 and contact was maintained with a force sensor (KD45, ME-Meßsysteme) at 400 mN. A graphite rod (Pentel Hi-polymer HB) in the SFC electrolyte inlet was used as a counter electrode with a double junction Ag/AgCl (3 M, Metrohm) reference electrode.

Dissolution of Pt was measured online with the scanning flow cell coupled to an inductively coupled plasma mass spectrometer (SFC−ICP−MS) (NexION 300X, PerkinElmer), with detection of ^{195}Pt, as described previously.[64,65] For an internal standard, ^{187}Re was used with a concentration of 10 $\mu g \cdot L^{-1}$. The internal standard in all cases was constantly fed into the ICP−MS, and connected to the SFC outlet via a Y-connector. The ICP−MS dwell time per AMU was set to 50 ms, with 5 sweeps/reading. The Pt ICP−MS signal was calibrated daily from solutions of 0.5, 1, and 5 $\mu g \cdot L^{-1}$ in 0.1 M $HClO_4$ prepared from 70% $HClO_4$ (Suprapur, Merck), ultrapure water (18.2 MΩ·cm, Milli-Q, Merck), and ICP−MS calibration standards (Certipur, Merck). The dissolution rate was calculated from regularly measured flow rates of ca. 200 $\mu L \cdot min^{-1}$, and the dissolution rate profiles were correlated to potential considering the delay time between the SFC and the ICP−MS of 25 s. The total quantities of dissolution were obtained by integration of the ^{195}Pt dissolution signal with the flow rate. The 0.1 M $HClO_4$ electrolyte was continuously purged with Ar immediately before introduction into the cell. No IR drop correction was used, as this becomes negligible because of the low currents produced within the SFC (ca. maximum 5 mV shift).[66]

3. RESULTS

Initial XPS characterization showed that there were no contaminants present on the surface with only Pt, O, Ar, and C peaks detected in the spectra, as seen in the representative spectra in Figure S2. The STEM imaging and subsequent

https://dx.doi.org/10.1021/acscatal.0c00779
ACS Catal. 2020, 10, 6281−6290

particle size analysis showed narrow particle size distributions with two distributions for each size, the single-charged and double-charged double mass particles (Figure 1). Because of

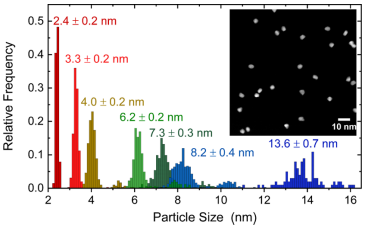

Figure 1. Size distribution of different particle sizes labeled with the average size and standard deviation. The inset shows a representative image of the 4 nm particles.

the low number of double-charged particles, these are negligible and only the mean and standard deviation for the single-charged particles are shown. These particles have sizes similar to the equivalent particle diameter calculated in Table S1. The discrepancy between the equivalent particle diameter and measured particle sizes comes from the nonspherical structure of the particles, which are instead a variety of shapes (Figure 1 inset). The standard deviation is limited by the STEM pixel size for the 2, 3, 4, and 6 nm samples, but increases with particle size because of the variation in the projected area for different particle shapes. This is a consequence of the 2D projection generated from a 3D structure in STEM. It should be noted that the particles with an equivalent particle diameter of 10 nm appear to be significantly larger because of their shapes, which are noticeably different from the smaller particles; however, it does not appear to lead to significant differences in dissolution rates (Figures 2 and S3).

An AST protocol that was previously shown to cause extensive Pt dissolution with minimal carbon corrosion was chosen for this study ("traditional" start/stop and load potential ranges have been shown to cause insignificant Pt dissolution on the timescale of online experiments, to be discussed later).[50] The electrochemical conditions of the AST are shown in Figure 2a, which is also preceded and followed by relatively slower CVs, which allow the deconvolution of the separate anodic and cathodic dissolution processes (to be discussed later).[45−48,60,65] The resulting mass-specific (normalized to total Pt mass on the WE) smoothed dissolution rate profiles are displayed in Figure 2b (Figures S4 and S5 alternatively show raw data and rates normalized to geometrical surface area, respectively). Normalization to the initial Pt mass was chosen as it takes into account the different loadings of the samples (which keep interparticle distance constant). Estimation of ECSA from the hydrogen region is not possible for such model electrodes, because of low current signals. Slightly higher noise in the signal for smaller particles results from the mass normalization as smaller particle sizes result in lower loadings in order to maintain a similar interparticle distance (1.2 vs 8.6% coverage for 2 and 10 nm particles, respectively), Table S1. No particle detachment is observed in the dissolution profiles, which should result in large signal spikes.[62] For the smallest (2 nm) particles, the

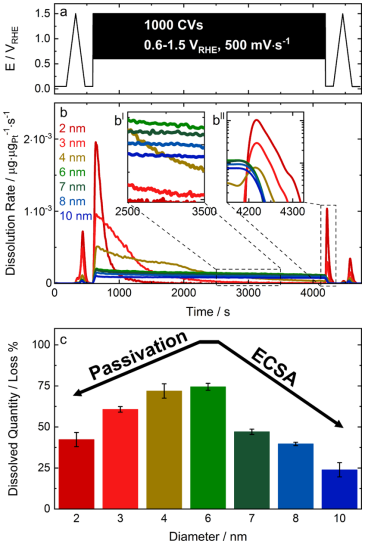

Figure 2. (a) Applied AST of CVs from 0.6 to 1.5 V_{RHE} at 500 $mV \cdot s^{-1}$ for 1000 cycles preceded and followed by a CV from 0.05 to 1.5 V_{RHE} at 10 $mV \cdot s^{-1}$. (b) Corresponding mass-normalized dissolution rate of the samples of varied particle size with b^{I} and b^{II} insets showing midway dissolution and cathodic peak during reductive hold following the AST. (c) Quantified dissolution during the AST total Pt loss % (mass-normalized).

dissolution rate in the initial stages of the AST drastically peaks because of a higher surface area relative to mass (ECSA), followed by a very sharp deceleration of the rate to baseline values. A smaller initial peak is seen for the 3 nm material, and the deceleration of rate also becomes less drastic. Moving to the 4 nm particle size, the peak is even less pronounced and even slower deceleration in rate is observed. The larger particle sizes ≥6 nm behave similarly to one another, where no initial peak in the dissolution rate is seen and the dissolution rates only gradually decrease (from loss of Pt material) and remain far above the baseline until the end of the AST. For these larger particles (≥6 nm), the mass-specific dissolution rate very clearly decreases with increasing particle size (Figure 2b^{I} inset).

After the AST, a reductive potential of 0.05 V_{RHE} is immediately applied. Subsequently, an additional cathodic dissolution peak caused by reduction of formed PtO_x is seen for the three smallest particle sizes of 2, 3, and 4 nm (Figure 2b^{II}). The peak height during this reductive hold decreases with increasing particle size.

The mass-specific dissolution rate profiles appear highly distinct for the different particle sizes, and a plausible explanation is given in the following. It appears from the dissolution profiles that the lower potential limit (LPL) of 0.6 V_{RHE} is too positive to fully reduce the formed PtO_x on the timescale of the AST for small particle sizes. This is further demonstrated by evolution of the CVs during the AST, shown in Figure S6, in which it is clear that the small particle sizes

https://dx.doi.org/10.1021/acscatal.0c00779
ACS Catal. 2020, 10, 6281−6290

have minimal reductive currents. This causes a dissolution inhibiting passivation of the Pt nanoparticles that increases with decreasing particle size, and in turn causes the drastic deceleration of initial dissolution rate, that is, a stable layer of PtO_x prevents further dissolution. This may be expected because of the known increase in oxophilicity with decreasing particle size.[33] Furthermore, this is evidenced in the additional cathodic peak during the reductive hold at 0.05 V_{RHE} following the ADT, which indicates increasing oxidation/passivation going from 4, 3, to 2 nm particle sizes.

The particle size effect on passivation becomes clearly evident in Figure 2c, where the total quantity of Pt dissolved during the AST is shown as a percentage of Pt mass lost. A maximum in Pt dissolution appears, where there is a tradeoff between decreased dissolution because of passivation of smaller particles and decreased dissolution because of increasing particle size. By estimating ECSA from the particle size and loading (assuming fully accessible spherical Pt particles), the dissolved quantities are also shown in Figure S7, where this trend persists. As the particle size increases, less mass-specific dissolution is inherently expected because of decreasing ECSA (i.e., less surface area relative to total Pt mass).[21,26,28,31,32,34,37] Based on the total quantities dissolved (Figure 2c) and the dissolution rate profiles (Figure 2b), it appears that the 2 nm size is highly oxophilic and quickly passivating, whereas for the 3 and 4 nm particle sizes the passivation and ECSA effects are mixed, and for ≥6 nm sizes there is negligible passivation during the AST. It should be made clear that this dissolution maximum is highly dependent on the applied AST: potential limits, scan rate, and number of cycles. For instance, slower scan rates and LPLs may allow further reduction of formed passivating PtO_x, whereas a sufficient number of cycles may negate the initial transient effects (Figure 2b,b^{l}).

To further corroborate the attribution of the dissolution trends to Pt passivation, Figure 3 shows the electrical charges

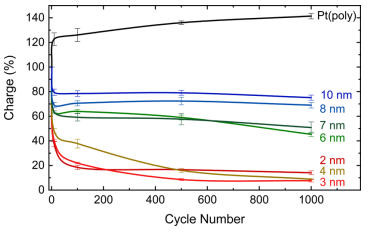

Figure 3. Total charge during a CV normalized to the first CV cycle for the 1st, 10th, 100th, 500th, and 1000th cycle for the ADT from 0.6 to 1.5 V_{RHE}, at 500 mV·s^{-1} for 1000 cycles.

during the course of the AST, which comes from oxidation and reduction of the Pt nanoparticles. It is important to note that dissolution currents contribute negligibly (e.g., 0.1−0.5%) to the measured electrical currents, and by cycling from 0.6 to 1.5 V_{RHE} the majority of measured charge should originate from oxidation and reduction of Pt (carbon quickly passivates at such cycling conditions).[50] By normalizing to the measured charge from the first cycle, the trends appear to closely mirror those of the dissolution rate profile. In the first 10 cycles, there is a drastic drop in charge, possibly due to the oxidation of minor contaminants that were initially present on the surfaces. With decreasing particle size, increased passivation is visible by a loss in oxidation and reduction charges (indicating that the particles are not being fully oxidized and reduced in the later cycles). For the 2 nm particles, the charges drop drastically and remain constant after 100 cycles, indicating that a large degree of passivation quickly takes place. The charges drop more gradually for the 3 and 4 nm particles but eventually reach a level similar to the 2 nm particles, in analogy to the dissolution rate profile. It is possible that as significant dissolution takes place (ca. 75% loss for 3 and 4 nm, Figure 2c), some particle sizes are shrinking with a lowering of their oxidation potential. The 6 and 7 nm particles retain a much higher charge, which only slightly decreases during the AST. For particle sizes of 8 and 10 nm, the charge remains approximately constant between 10 and 1000 cycles. With such large particles sizes and relatively less dissolution (ca. 50−25% loss, Figure 2c), the large particles are not passivated and minimal shrinking from dissolution should be expected.

It is clear that particle size has a severe impact on the oxidation and reduction of Pt, which causes transient platinum dissolution. This is typically seen in the shift of the oxidation and reduction peaks of CVs to more positive potentials for large particles,[21,29,32,33,67] whereas unfortunately the low loadings and low currents from the flat (2D) model systems inhibit such detection.[63,68] Increased loadings become possible with the use of 3D, porous Pt support on carbon, which has been addressed in a parallel study.[69]

The relatively slower CVs preceding and following the AST span a much larger potential window (Figure 4a), with a much more negative LPL of 0.05 V_{RHE} and a slower scan rate of 10 mV·s^{-1}, which will fully reduce the formed oxides in the cathodic scan. The mass-normalized dissolution rates and total dissolved quantities shown in Figure 4b,c (normalized to geometrical WE surface area in Figure S8) show a clear decrease with increasing particle size, which may be attributed to decreasing ECSA, as mentioned above.[21,26,28,31,32,34,37] Unfortunately, estimating ECSA through the conventional hydrogen underpotential deposition area of the CV becomes difficult because of the low loadings used in an effort to eliminate possible interparticle distance effects,[30,51−53,55,62,63,70,71] which will be addressed on applied Pt/C materials. However, Figure S9 presents the dissolved quantities normalized to ECSA, calculated assuming fully accessible spherical Pt particles. The trend from mass-normalization indeed persists, although not as smooth, possibly an artifact of such an estimation.

4. DISCUSSION

Using well-defined 2D model systems with particle diameters from 2 to 10 nm and similar interparticle distance distributions, the particle size has been shown to have a severe impact on the oxidation, reduction, and subsequent dissolution of Pt nanoparticles. Considering recent developments on the impact of interparticle distance on stability,[61,62] this has been recognized as the critical parameter rather than loading, and is further investigated in an upcoming dedicated publication. In recent years, it has become well-established that significant Pt dissolution is caused by the oxidation and reduction of Pt, governed by the place-exchange mechanism.[45,48,72−76] When applying CVs in a large potential range causing significant Pt oxidation and reduction (Figure 4), a clear trend of decreasing mass-specific dissolution with

https://dx.doi.org/10.1021/acscatal.0c00779
ACS Catal. 2020, 10, 6281−6290

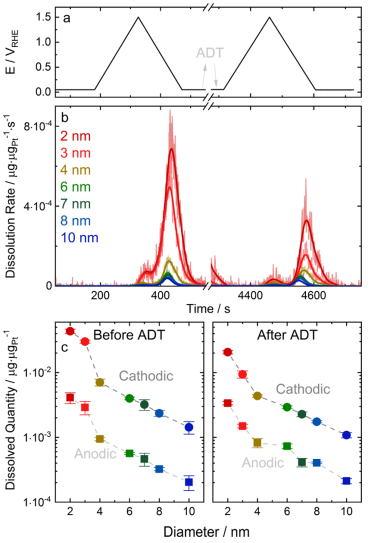

Figure 4. (a) CVs preceding and following the AST from 0.05 to 1.5 V_{RHE}. (b) Corresponding mass-normalized dissolution rate of the samples of varied particle size. (c) Total mass-normalized dissolved quantities from the anodic (solid box) and cathodic (solid circle) dissolution peaks.

increasing particle size was observed. This was simply rationalized by decreasing the surface area relative to total Pt mass, that is, ECSA.[21,26,28,31,32,34,37] Therefore, from an engineering standpoint, larger Pt particles are more stable toward dissolution, in agreement with many activity-based studies.[21,28,32,42]

Intriguingly, a rather unexpected maximum in dissolved Pt quantities was observed, which depends on particle size in the potential range of the applied AST (Figure 2). Decreasing particle sizes cause a negative potential shift, causing particle passivation and quickly inhibiting dissolution rates in the initial stages of the AST (further exemplified by loss of charge in Figure 3). As particle sizes increase from 2 to 6 nm, this effect is diminished and dissolved quantities of Pt increase. At larger particle sizes (≥6 nm), dissolved quantities of Pt again decrease; however, this is due to the abovementioned decreasing ECSA with increasing particle size. At these larger particle sizes, a positive shift in oxidation potential prevents significant passivation.

This situation becomes more complex when moving to more commonly employed AST experiments. In 2011, the Fuel Cell Commercialization Conference of Japan (FCCJ) proposed two types of ASTs with different potential windows in order to simulate the operational load and the start/stop conditions of PEMFCs.[77] Square wave cycling from 0.6 to 1.0 V_{RHE} for the load and triangular wave cycling from 1.0 to 1.5 V_{RHE} for the start/stop was suggested. A triangular wave form from 0.6 to 1.0 V_{RHE} had also been adopted by the US DOE by as early as 2010, whereas in 2013 their suggested protocols also included a 1.0−1.5 V_{RHE} test for start/stop conditions (identical to the above FCCJ).[43,78−82] The load cycle ASTs are thought to largely induce Pt dissolution/degradation, whereas the start/stop ASTs induce carbon corrosion, that is, these two types of tests should ideally separate the two primary degradation mechanisms of PEMFC catalyst layers.[36] Furthermore, without any type of standardized testing, comparisons across different laboratories would be infeasible, and to a large extent many scientific groups have adopted the use of ASTs within these potential limits (although with small variations in potential limits and scan rates).[13,21,22,24,28,32,34,37−43] However, it is known that the potential profile (square wave vs triangular wave) impacts degradation and Pt dissolution,[42,48,83,84] whereas even slight variations to potential limits which transverse 1.0 V_{RHE} will drastically impact Pt dissolution.[46,48]

In recent years, it has been shown that significant transient electrochemical dissolution of Pt coincides with Pt oxidation and reduction when crossing a threshold of ca. 1.0 V_{RHE}.[46,48] When cycling below 1.0 V_{RHE}, Pt will not be significantly oxidized, and when cycling above 1.0 V_{RHE} Pt will not be significantly reduced. Therefore, it is clear that neither type of potential window suggested above will cause substantial Pt dissolution. However, many AST studies span a much larger timescale than presented here, easily possible in typical bulk-cell experiments, and over many thousands of cycles of low rates of Pt dissolution may amount to a significant degradation, which depends on particle size because of shifts in oxidation, reduction, and dissolution potentials. Several degradation studies on particle size effects have been conducted within a load cycle potential range similar to those described above (although with slight variations in potential limits and scan rates).[21,28,32,34,37,42] Most results have shown a trend of increased degradation with decreasing particle size based on losses in ECSA and activity,[21,28,32,42] whereas some have shown no dependence.[34,37] Additionally, Ahluwalia et el. used ex situ dissolution (ICP−MS) experiments and demonstrated a reversal in this trend to larger particles dissolving more (mass-specific dissolution) when changing their AST protocol from 0.6−1.0 V_{RHE} at 50 mV·s^{-1} to 0.5−1.15 V_{RHE} at 10 mV·s^{-1}.[38] This surprising result was attributed to size-dependent kinetic/thermodynamic control of oxide formation.

The abovementioned studies reporting decreased stability with decreasing particle size have nearly exclusively attributed these results to enhanced Ostwald ripening.[21,28,32,42] However, this was only directly observed by Li et al. via post-mortem TEM.[21] The degradation of a fuel cell catalyst layer is highly complex with many interconnected mechanisms. For instance, when observing post-mortem particle growth, it is difficult to attribute the degree of this result to the mechanisms of migration/coalescence and Ostwald ripening. Furthermore, performance and ECSA deterioration may result from other mechanisms such as Pt loss because of dissolution, carbon corrosion, and particle detachment. Therefore, the goal of this study was to exclusively trigger Pt dissolution and minimize other effects by synthesizing a well-defined system.

On the 2D surface with constant interparticle distances, Ostwald ripening should be minimized relative to the porous 3D carbon network in applied systems: such drastically increased pathways to the bulk electrolyte of dissolved Pt^{n+} ions in a support network will significantly enhance the probability of redeposition and Ostwald ripening,[60] although identical AST experiments on Pt/C systems show minimal particle growth.[62] Shrinking of particle size can be expected

https://dx.doi.org/10.1021/acscatal.0c00779
ACS Catal. 2020, 10, 6281−6290

considering the massive mass loses of Pt (ca. 25−75%) during the AST. Additionally, in the SFC system, the constant flow of electrolyte sweeps away dissolved species, hindering redeposition. Wide particle size distributions have also been reported to promote Ostwald ripening,[21,34,37,85] and here narrow distributions were obtained by optimizing a specialized synthesis method. Furthermore, the previous reports utilized load cycle ASTs from 0.6 V_{RHE} to UPLs of 1.0, 1.1, and 1.2 V_{RHE},[21,28,32,34,37,42] which are in a more negative range than the AST used here, and will also promote redeposition.

The previous reports on Pt particle size effects and degradation all use similar load cycle ASTs.[21,28,32,34,37,42] In such a potential window, particularly when using the suggested square-wave potential protocol,[43,77−82] passivation effects as discussed in this study should be minimized. The dissolution results here in Figures 4 and S9 show that in the absence of passivation, smaller particles dissolve at faster rates and in higher quantities. These results support the previously proposed enhancement of particle growth via Ostwald ripening (rather than migration/coalescence),[21,28,32,42] although Pt losses and redeposition in the membrane will take place.[42]

In future studies employing start/stop ASTs, constant particle size (and interparticle distance) will be critical.[62] In this relatively more positive potential range with fast scan rates,[43,77−82] the results of this study show that particle size will dictate the degree of Pt passivation and thus impact the Pt dissolution. Such an effect would be undetectable in typical bulk cell degradation and even dissolution experiments. However, as discussed above, such a potential window will produce negligible Pt dissolution on the timescale of online/in situ experiments, prompting the use the optimized AST protocol proposed by Pizzutilo et al.[50]

Considering the limited dissolution of such typically used load and start/stop ASTs, Pizzutilo et al. investigated the impact of a variety of potential windows on Pt/C degradation in an online SFC−ICP−MS dissolution study.[50] As expected,[46−48,86] no significant Pt dissolution was observed when cycling from 0.6 to 1.0 or 1.0 to 1.5 V_{RHE}. The Pt dissolution rate signal then jumped over 2 orders of magnitude when cycling in a "combined cycle" from 0.6 to 1.5 V_{RHE} and 1 order of magnitude for 0.05 to 1.5 V_{RHE}. The lower rate for the latter (large potential window) can be explained by increased redeposition caused by the more negative potentials. From online SFC-OLEMS (scanning flow cell coupled to online electrochemical mass spectrometry) CO_2 measurements, the larger potential window induced a much higher corrosion rate of the carbon support, attributed to reduction of oxygenated surface functional groups by reaching potentials below the thermodynamic potential for carbon oxidation (0.2 V_{RHE}). Therefore, the combined cycle, which caused significant Pt dissolution with rather minimal carbon corrosion, was suggested for use in degradation studies and adapted in this work.

Considering the significant dissolution observed during the combined cycle AST by Pizzutilo et al., it was assumed that the LPL of 0.6 V_{RHE} was sufficient to reduce their commercial (TKK) 3 nm Pt nanoparticles.[50] However, here it was shown that this size is in the range of particle passivation, that is, 0.6 V_{RHE} is too positive to fully reduce this particle size. Therefore, a similar experiment on an identical sample of annealed TKK Pt/C with a larger particle size of ca. 5 nm should yield increased mass-specific dissolution (assuming identical Pt density/interpaticle distance) and could be misinterpreted as an intrinsic particle size-dependent property rather than the competition of two effects.

As the results here have shown, particle size drastically impacts degradation through Pt dissolution in ASTs depending on the potential limits. Therefore, the authors suggest caution in studies comparing different materials of varying particle size. For instance, if studying 2 and 8 nm particle sizes, the former may be protected by a passivating oxide layer, whereas the latter has a lower ECSA when applying a start/stop AST. In samples containing large size distributions, different populations could degrade completely differently, skewing firm conclusions on the parameters of interest. Comparisons between samples with varied loading via catalyst layer thickness or particle density (i.e., interparticle distance) could also become compromised without exclusive control of particle size. Commercial catalysts synthesized using impregnation or precipitation methods typically increase the particle size via heat/annealing treatments which change interparticle distance, alter the carbon support, and also result in increased size distributions with the extent of the treatment (i.e., larger distributions for larger sizes).[26,34,37,38,51−55] These important insights demonstrate the importance of studying well-defined model systems on the road to improved experimental techniques in PEMFC electrocatalytic research.

With the new data that have shed light on this critical issue of competing particle size effects of passivation and dissolution, we suggest an AST protocol in addition to the commonly used load and start/stop cycle potential ranges. Indeed, a more aggressive AST can aid in the understanding of the degradation of promising electrocatalytic materials, by causing significant Pt dissolution in a short time frame.[23] Applying a UPL of 1.5 V_{RHE} will cause significant Pt oxidation without extending into the oxygen evolution reaction (OER) range, which causes Pt dissolution at ca. 1.7 V_{RHE}.[45,47] By using a LPL of 0.3 V_{RHE}, the formed oxides should be fully reduced while avoiding extensive Pt redeposition and carbon corrosion through reduction at low potentials.[50] Therefore, a Pt "dissolution AST" from 0.3 to 1.5 V_{RHE} at 500 $mV \cdot s^{-1}$ is suggested for a protocol to cause extensive Pt dissolution on a short time scale while also circumventing the particle size-dependent passivation effect, providing a clear picture of the intrinsic stability. This Pt passivation will depend on particle size; therefore, slower scan rates or square waveforms of applied potential can alternatively provide increased time lengths at oxidative and reductive potentials, which may narrow the necessary potential window. However, such recommendations will require dedicated investigations.

5. CONCLUSIONS

Using magnetron sputtering, Pt particle size and particle density were exclusively controlled on a planar glassy carbon substrate with narrow size distributions and constant interparticle distance distributions. Using this precise synthetic method, Pt dissolution may be studied while minimizing other complex degradation mechanisms. In the range studied with diameters from 2 to 10 nm, applying a wide potential window resulted in increased dissolution rates and quantities with decreasing particle size. Such a dissolution trend demonstrates that particle size-dependent degradation via particle growth may be largely attributed to Ostwald ripening. Applying an AST caused a maximum in dissolution detected online, induced by competing effects: particle size-dependent shifts in oxophilicity and ECSA. As the particle size decreases, the

https://dx.doi.org/10.1021/acscatal.0c00779
ACS Catal. 2020, 10, 6281−6290

particles become more oxophilic, causing the formation of a dissolution inhibiting passivation layer of PtO_x. As the particle size increases, ECSA decreases, similarly decreasing the amount of Pt dissolution. These effects must be considered in future investigations on the particle size effect on Pt stability. Furthermore, minimizing the particle size is a critical issue in decreasing PEMFC costs by maximizing Pt utilization, and alleviating mass transport issues with high dispersion. Therefore, the implantation of suitable experimental designs and ASTs is paramount and the subsequent suggestions for AST protocols should be helpful for researchers designing future studies on particle size effects and degradation.

■ ASSOCIATED CONTENT

Supporting Information

The Supporting Information is available free of charge at https://pubs.acs.org/doi/10.1021/acscatal.0c00779.

Parameters of synthesized materials; simulated interparticle distances; Pt nanoparticles' XPS spectra; representative STEM images; dissolution profiles and quantities normalized to geometrical electrode surface area and also ECSA; and evolution of CVs during the AST for all materials (PDF)

■ AUTHOR INFORMATION

Corresponding Authors

Daniel J. S. Sandbeck − *Helmholtz-Institute Erlangen-Nürnberg for Renewable Energy (IEK-11), Forschungszentrum Jülich GmbH, 91058 Erlangen, Germany; Department of Chemical and Biological Engineering, Friedrich-Alexander-Universität Erlangen-Nürnberg, 91058 Erlangen, Germany;* orcid.org/0000-0002-7618-3574; Email: d.sandbeck@fz-juelich.de

Serhiy Cherevko − *Helmholtz-Institute Erlangen-Nürnberg for Renewable Energy (IEK-11), Forschungszentrum Jülich GmbH, 91058 Erlangen, Germany;* orcid.org/0000-0002-7188-4857; Email: s.cherevko@fz-juelich.de

Authors

Niklas Mørch Secher − *Department of Physics, Technical University of Denmark, 2800 Lyngby, Denmark*

Florian D. Speck − *Helmholtz-Institute Erlangen-Nürnberg for Renewable Energy (IEK-11), Forschungszentrum Jülich GmbH, 91058 Erlangen, Germany; Department of Chemical and Biological Engineering, Friedrich-Alexander-Universität Erlangen-Nürnberg, 91058 Erlangen, Germany;* orcid.org/0000-0002-7649-9261

Jakob Ejler Sørensen − *Department of Physics, Technical University of Denmark, 2800 Lyngby, Denmark*

Jakob Kibsgaard − *Department of Physics, Technical University of Denmark, 2800 Lyngby, Denmark;* orcid.org/0000-0002-9219-816X

Ib Chorkendorff − *Department of Physics, Technical University of Denmark, 2800 Lyngby, Denmark;* orcid.org/0000-0003-2738-0325

Complete contact information is available at: https://pubs.acs.org/10.1021/acscatal.0c00779

Author Contributions

[⊥]D.J.S.S. and N.M.S. contributed equally to this work.

Notes

The authors declare no competing financial interest.

■ REFERENCES

(1) Gruber, P. W.; Medina, P. A.; Keoleian, G. A.; Kesler, S. E.; Everson, M. P.; Wallington, T. J. Global Lithium Availability. *J. Ind. Ecol.* **2011**, *15*, 760−775.

(2) Kesler, S. E.; Gruber, P. W.; Medina, P. A.; Keoleian, G. A.; Everson, M. P.; Wallington, T. J. Global lithium resources: Relative importance of pegmatite, brine and other deposits. *Ore Geol. Rev.* **2012**, *48*, 55−69.

(3) Kavanagh, L.; Keohane, J.; Garcia Cabellos, G.; Lloyd, A.; Cleary, J. Global Lithium Sources—Industrial Use and Future in the Electric Vehicle Industry: A Review. *Resources* **2018**, *7*, 57.

(4) Harvey, L. D. D. Resource implications of alternative strategies for achieving zero greenhouse gas emissions from light-duty vehicles by 2060. *Appl. Energy* **2018**, *212*, 663−679.

(5) Jasiński, D.; Meredith, J.; Kirwan, K. The life cycle impact for platinum group metals and lithium to 2070 via surplus cost potential. *Int. J. Life Cycle Assess.* **2017**, *23*, 773−786.

(6) Wang, J.; Wang, H.; Fan, Y. Techno-Economic Challenges of Fuel Cell Commercialization. *Engineering* **2018**, *4*, 352−360.

(7) Gröger, O.; Gasteiger, H. A.; Suchsland, J.-P. Review—Electromobility: Batteries or Fuel Cells? *J. Electrochem. Soc.* **2015**, *162*, A2605−A2622.

(8) Wang, G.; Yu, Y.; Liu, H.; Gong, C.; Wen, S.; Wang, X.; Tu, Z. Progress on design and development of polymer electrolyte membrane fuel cell systems for vehicle applications: A review. *Fuel Process. Technol.* **2018**, *179*, 203−228.

(9) Curtin, S.; Gangi, J. *Fuel Cell Technologies Market Report 2016*; U.S. Department of Energy, Office of Energy Efficiency & Renewable Energy, 2016.

(10) Yoshida, T.; Kojima, K. Toyota MIRAI Fuel Cell Vehicle and Progress Toward a Future Hydrogen Society. *Interface* **2015**, *24*, 45−49.

(11) Yang, Y. *PEM Fuel Cell System Manufacturing Cost Analysis for Automotive Applications*; Austin Power Engineering LLC, 2015.

(12) de Frank Bruijn, A.; Janssen, G. J. M. PEM Fuel Cell Materials: Costs, Performance and Durability. In *Fuel Cells*; Springer, 2013; pp 249−303.

(13) Kongkanand, A.; Mathias, M. F. The Priority and Challenge of High-Power Performance of Low-Platinum Proton-Exchange Membrane Fuel Cells. *J. Phys. Chem. Lett.* **2016**, *7*, 1127−1137.

(14) Kongkanand, A.; Subramanian, N. P.; Yu, Y.; Liu, Z.; Igarashi, H.; Muller, D. A. Achieving High-Power PEM Fuel Cell Performance with an Ultralow-Pt-Content Core−Shell Catalyst. *ACS Catal.* **2016**, *6*, 1578−1583.

(15) Owejan, J. P.; Owejan, J. E.; Gu, W. Impact of Platinum Loading and Catalyst Layer Structure on PEMFC Performance. *J. Electrochem. Soc.* **2013**, *160*, F824−F833.

(16) Harzer, G. S.; Orfanidi, A.; El-Sayed, H.; Madkikar, P.; Gasteiger, H. A. Tailoring Catalyst Morphology towards High Performance for Low Pt Loaded PEMFC Cathodes. *J. Electrochem. Soc.* **2018**, *165*, F770−F779.

(17) Li, M.; Zhao, Z.; Cheng, T.; Fortunelli, A.; Chen, C.-Y.; Yu, R.; Zhang, Q.; Gu, L.; Merinov, B. V.; Lin, Z.; Zhu, E.; Yu, T.; Jia, Q.; Guo, J.; Zhang, L.; Goddard, W. A., 3rd; Huang, Y.; Duan, X. Ultrafine jagged platinum nanowires enable ultrahigh mass activity for the oxygen reduction reaction. *Science* **2016**, *354*, 1414−1419.

(18) Bu, L.; Zhang, N.; Guo, S.; Zhang, X.; Li, J.; Yao, J.; Wu, T.; Lu, G.; Ma, J.-Y.; Su, D.; Huang, X. Biaxially strained PtPb/Pt core/shell nanoplate boosts oxygen reduction catalysis. *Science* **2016**, *354*, 1410−1414.

(19) Stephens, I. E. L.; Rossmeisl, J.; Chorkendorff, I. Toward sustainable fuel cells. *Science* **2016**, *354*, 1378−1379.

(20) Chen, C.; Kang, Y.; Huo, Z.; Zhu, Z.; Huang, W.; Xin, H. L.; Snyder, J. D.; Li, D.; Herron, J. A.; Mavrikakis, M.; Chi, M.; More, K. L.; Li, Y.; Markovic, N. M.; Somorjai, G. A.; Yang, P.; Stamenkovic, V. R. Highly crystalline multimetallic nanoframes with three-dimensional electrocatalytic surfaces. *Science* **2014**, *343*, 1339−1343.

(21) Li, D.; Wang, C.; Strmcnik, D. S.; Tripkovic, D. V.; Sun, X.; Kang, Y.; Chi, M.; Snyder, J. D.; van der Vliet, D.; Tsai, Y.;

Stamenkovic, V. R.; Sun, S.; Markovic, N. M. Functional links between Pt single crystal morphology and nanoparticles with different size and shape: the oxygen reduction reaction case. *Energy Environ. Sci.* **2014**, *7*, 4061−4069.
(22) George, M.; Zhang, G.-R.; Schmitt, N.; Brunnengräber, K.; Sandbeck, D. J. S.; Mayrhofer, K. J. J.; Cherevko, S.; Etzold, B. J. M. Effect of Ionic Liquid Modification on the ORR Performance and Degradation Mechanism of Trimetallic PtNiMo/C Catalysts. *ACS Catal.* **2019**, *9*, 8682−8692.
(23) Zhang, G.-R.; Wolker, T.; Sandbeck, D. J. S.; Munoz, M.; Mayrhofer, K. J. J.; Cherevko, S.; Etzold, B. J. M. Tuning the Electrocatalytic Performance of Ionic Liquid Modified Pt Catalysts for the Oxygen Reduction Reaction via Cationic Chain Engineering. *ACS Catal.* **2018**, *8*, 8244−8254.
(24) Lindahl, N.; Zamburlini, E.; Feng, L.; Grönbeck, H.; Escudero-Escribano, M.; Stephens, I. E. L.; Chorkendorff, I.; Langhammer, C.; Wickman, B. High Specific and Mass Activity for the Oxygen Reduction Reaction for Thin Film Catalysts of Sputtered Pt3Y. *Adv. Mater. Interfaces* **2017**, *4*, 1700311.
(25) Gazdzicki, P.; Mitzel, J.; Dreizler, A. M.; Schulze, M.; Friedrich, K. A. Impact of Platinum Loading on Performance and Degradation of Polymer Electrolyte Fuel Cell Electrodes Studied in a Rainbow Stack. *Fuel Cells* **2018**, *18*, 270−278.
(26) Shao, M.; Peles, A.; Shoemaker, K. Electrocatalysis on platinum nanoparticles: particle size effect on oxygen reduction reaction activity. *Nano Lett.* **2011**, *11*, 3714−3719.
(27) Perez-Alonso, F. J.; McCarthy, D. N.; Nierhoff, A.; Hernandez-Fernandez, P.; Strebel, C.; Stephens, I. E. L.; Nielsen, J. H.; Chorkendorff, I. The effect of size on the oxygen electroreduction activity of mass-selected platinum nanoparticles. *Angew. Chem., Int. Ed.* **2012**, *51*, 4641−4643.
(28) Xu, Z.; Zhang, H.; Zhong, H.; Lu, Q.; Wang, Y.; Su, D. Effect of particle size on the activity and durability of the Pt/C electrocatalyst for proton exchange membrane fuel cells. *Appl. Catal., B* **2012**, *111*−*112*, 264−270.
(29) Gasteiger, H. A.; Kocha, S. S.; Sompalli, B.; Wagner, F. T. Activity benchmarks and requirements for Pt, Pt-alloy, and non-Pt oxygen reduction catalysts for PEMFCs. *Appl. Catal., B* **2005**, *56*, 9−35.
(30) Quinson, J.; Inaba, M.; Neumann, S.; Swane, A. A.; Bucher, J.; Simonsen, S. B.; Theil Kuhn, L.; Kirkensgaard, J. J. K.; Jensen, K. M. Ø.; Oezaslan, M.; Kunz, S.; Arenz, M. Investigating Particle Size Effects in Catalysis by Applying a Size-Controlled and Surfactant-Free Synthesis of Colloidal Nanoparticles in Alkaline Ethylene Glycol: Case Study of the Oxygen Reduction Reaction on Pt. *ACS Catal.* **2018**, *8*, 6627−6635.
(31) Nesselberger, M.; Ashton, S.; Meier, J. C.; Katsounaros, I.; Mayrhofer, K. J. J.; Arenz, M. The particle size effect on the oxygen reduction reaction activity of Pt catalysts: influence of electrolyte and relation to single crystal models. *J. Am. Chem. Soc.* **2011**, *133*, 17428−17433.
(32) Sheng, W.; Chen, S.; Vescovo, E.; Shao-Horn, Y. Size Influence on the Oxygen Reduction Reaction Activity and Instability of Supported Pt Nanoparticles. *J. Electrochem. Soc.* **2011**, *159*, B96−B103.
(33) Mayrhofer, K. J. J.; Blizanac, B. B.; Arenz, M.; Stamenkovic, V. R.; Ross, P. N.; Markovic, N. M. The impact of geometric and surface electronic properties of pt-catalysts on the particle size effect in electrocatalysis. *J. Phys. Chem. B* **2005**, *109*, 14433−14440.
(34) Yano, H.; Watanabe, M.; Iiyama, A.; Uchida, H. Particle-size effect of Pt cathode catalysts on durability in fuel cells. *Nano Energy* **2016**, *29*, 323−333.
(35) Cherevko, S. Stability and dissolution of electrocatalysts: Building the bridge between model and "real world" systems. *Curr. Opin. Electrochem.* **2018**, *8*, 118−125.
(36) Meier, J. C.; Galeano, C.; Katsounaros, I.; Witte, J.; Bongard, H. J.; Topalov, A. A.; Baldizzone, C.; Mezzavilla, S.; Schüth, F.; Mayrhofer, K. J. J. Design criteria for stable Pt/C fuel cell catalysts. *Beilstein J. Nanotechnol.* **2014**, *5*, 44−67.
(37) Watanabe, M.; Yano, H.; Uchida, H.; Tryk, D. A. Achievement of distinctively high durability at nanosized Pt catalysts supported on carbon black for fuel cell cathodes. *J. Electroanal. Chem.* **2018**, *819*, 359−364.
(38) Ahluwalia, R. K.; Arisetty, S.; Wang, X.; Wang, X.; Subbaraman, R.; Ball, S. C.; DeCrane, S.; Myers, D. J. Thermodynamics and Kinetics of Platinum Dissolution from Carbon-Supported Electrocatalysts in Aqueous Media under Potentiostatic and Potentiodynamic Conditions. *J. Electrochem. Soc.* **2013**, *160*, F447−F455.
(39) Schmies, H.; Bergmann, A.; Drnec, J.; Wang, G.; Teschner, D.; Kühl, S.; Sandbeck, D. J. S.; Cherevko, S.; Gocyla, M.; Shviro, M.; Heggen, M.; Ramani, V.; Dunin-Borkowski, R. E.; Mayrhofer, K. J. J.; Strasser, P. Unravelling Degradation Pathways of Oxide-Supported Pt Fuel Cell Nanocatalysts under In Situ Operating Conditions. *Adv. Energy Mater.* **2018**, *8*, 1701663.
(40) Spanos, I.; Dideriksen, K.; Kirkensgaard, J. J. K.; Jelavic, S.; Arenz, M. Structural disordering of de-alloyed Pt bimetallic nanocatalysts: the effect on oxygen reduction reaction activity and stability. *Phys. Chem. Chem. Phys.* **2015**, *17*, 28044−28053.
(41) Fichtner, J.; Garlyyev, B.; Watzele, S.; El-Sayed, H. A.; Schwämmlein, J. N.; Li, W.-J.; Maillard, F. M.; Dubau, L.; Michalička, J.; Macak, J. M.; Holleitner, A.; Bandarenka, A. S. Top-Down Synthesis of Nanostructured Platinum-Lanthanide Alloy Oxygen Reduction Reaction Catalysts: Pt xPr/C as an Example. *ACS Appl. Mater. Interfaces* **2019**, *11*, 5129−5135.
(42) Yang, Z.; Ball, S.; Condit, D.; Gummalla, M. Systematic Study on the Impact of Pt Particle Size and Operating Conditions on PEMFC Cathode Catalyst Durability. *J. Electrochem. Soc.* **2011**, *158*, B1439.
(43) Yu, H.; Baricci, A.; Bisello, A.; Casalegno, A.; Guetaz, L.; Bonville, L.; Maric, R. Strategies to mitigate Pt dissolution in low Pt loading proton exchange membrane fuel cell: I. A gradient Pt particle size design. *Electrochim. Acta* **2017**, *247*, 1155−1168.
(44) Myers, D. J.; Wang, X.; Smith, M. C.; More, K. L. Potentiostatic and Potential Cycling Dissolution of Polycrystalline Platinum and Platinum Nano-Particle Fuel Cell Catalysts. *J. Electrochem. Soc.* **2018**, *165*, F3178−F3190.
(45) Cherevko, S.; Kulyk, N.; Mayrhofer, K. J. J. Durability of platinum-based fuel cell electrocatalysts: Dissolution of bulk and nanoscale platinum. *Nano Energy* **2016**, *29*, 275−298.
(46) Topalov, A. A.; Katsounaros, I.; Auinger, M.; Cherevko, S.; Meier, J. C.; Klemm, S. O.; Mayrhofer, K. J. J. Dissolution of Platinum: Limits for the Deployment of Electrochemical Energy Conversion? *Angew. Chem., Int. Ed. Engl.* **2012**, *51*, 12613−12615.
(47) Cherevko, S.; Zeradjanin, A. R.; Keeley, G. P.; Mayrhofer, K. J. J. A Comparative Study on Gold and Platinum Dissolution in Acidic and Alkaline Media. *J. Electrochem. Soc.* **2014**, *161*, H822−H830.
(48) Topalov, A. A.; Cherevko, S.; Zeradjanin, A. R.; Meier, J. C.; Katsounaros, I.; Mayrhofer, K. J. J. Towards a comprehensive understanding of platinum dissolution in acidic media. *Chem. Sci.* **2014**, *5*, 631−638.
(49) Cherevko, S. Electrochemical Dissolution of Noble Metals. In *Encyclopedia of Interfacial Chemistry*; Elsevier, 2018; pp 68−75.
(50) Pizzutilo, E.; Geiger, S.; Grote, J.-P.; Mingers, A.; Mayrhofer, K. J. J.; Arenz, M.; Cherevko, S. On the Need of Improved Accelerated Degradation Protocols (ADPs): Examination of Platinum Dissolution and Carbon Corrosion in Half-Cell Tests. *J. Electrochem. Soc.* **2016**, *163*, F1510−F1514.
(51) Speder, J.; Altmann, L.; Bäumer, M.; Kirkensgaard, J. J. K.; Mortensen, K.; Arenz, M. The particle proximity effect: from model to high surface area fuel cell catalysts. *RSC Adv.* **2014**, *4*, 14971−14978.
(52) Speder, J.; Zana, A.; Spanos, I.; Kirkensgaard, J. J. K.; Mortensen, K.; Hanzlik, M.; Arenz, M. Comparative degradation study of carbon supported proton exchange membrane fuel cell electrocatalysts − The influence of the platinum to carbon ratio on the degradation rate. *J. Power Sources* **2014**, *261*, 14−22.
(53) Speder, J.; Spanos, I.; Zana, A.; Kirkensgaard, J. J. K.; Mortensen, K.; Altmann, L.; Bäumer, M.; Arenz, M. From single

https://dx.doi.org/10.1021/acscatal.0c00779
ACS Catal. 2020, 10, 6281−6290

crystal model catalysts to systematic studies of supported nanoparticles. *Surf. Sci.* **2015**, *631*, 278−284.
(54) Quinson, J.; Inaba, M.; Neumann, S.; Swane, A. A.; Bucher, J.; Simonsen, S. B.; Theil Kuhn, L.; Kirkensgaard, J. J. K.; Jensen, K. M. Ø.; Oezaslan, M.; Kunz, S.; Arenz, M. Investigating Particle Size Effects in Catalysis by Applying a Size-Controlled and Surfactant-Free Synthesis of Colloidal Nanoparticles in Alkaline Ethylene Glycol: Case Study of the Oxygen Reduction Reaction on Pt. *ACS Catal.* **2018**, *8*, 6627−6635.
(55) Proch, S.; Kodama, K.; Inaba, M.; Oishi, K.; Takahashi, N.; Morimoto, Y. The "Particle Proximity Effect" in Three Dimensions: a Case Study on Vulcan XC 72R. *Electrocatalysis* **2016**, *7*, 249−261.
(56) Kemppainen, E.; Bodin, A.; Sebok, B.; Pedersen, T.; Seger, B.; Mei, B.; Bae, D.; Vesborg, P. C. K.; Halme, J.; Hansen, O.; Lund, P. D.; Chorkendorff, I. Scalability and feasibility of photoelectrochemical H2evolution: the ultimate limit of Pt nanoparticle as an HER catalyst. *Energy Environ. Sci.* **2015**, *8*, 2991−2999.
(57) Roy, C.; Sebok, B.; Scott, S. B.; Fiordaliso, E. M.; Sørensen, J. E.; Bodin, A.; Trimarco, D. B.; Damsgaard, C. D.; Vesborg, P. C. K.; Hansen, O.; Stephens, I. E. L.; Kibsgaard, J.; Chorkendorff, I. Impact of nanoparticle size and lattice oxygen on water oxidation on NiFeOxHy. *Nat. Catal.* **2018**, *1*, 820−829.
(58) Hernandez-Fernandez, P.; Masini, F.; McCarthy, D. N.; Strebel, C. E.; Friebel, D.; Deiana, D.; Malacrida, P.; Nierhoff, A.; Bodin, A.; Wise, A. M.; Nielsen, J. H.; Hansen, T. W.; Nilsson, A.; Stephens, I. E. L.; Chorkendorff, I. Mass-selected nanoparticles of PtxY as model catalysts for oxygen electroreduction. *Nat. Chem.* **2014**, *6*, 732−738.
(59) Velázquez-Palenzuela, A.; Masini, F.; Pedersen, A. F.; Escudero-Escribano, M.; Deiana, D.; Malacrida, P.; Hansen, T. W.; Friebel, D.; Nilsson, A.; Stephens, I. E. L.; Chorkendorff, I. The enhanced activity of mass-selected Pt Gd nanoparticles for oxygen electroreduction. *J. Catal.* **2015**, *328*, 297−307.
(60) Keeley, G. P.; Cherevko, S.; Mayrhofer, K. J. J. The Stability Challenge on the Pathway to Low and Ultra-Low Platinum Loading for Oxygen Reduction in Fuel Cells. *ChemElectroChem* **2016**, *3*, 51−54.
(61) Goodman, E. D.; Johnston-Peck, A. C.; Dietze, E. M.; Wrasman, C. J.; Hoffman, A. S.; Abild-Pedersen, F.; Bare, S. R.; Plessow, P. N.; Cargnello, M. Catalyst deactivation via decomposition into single atoms and the role of metal loading. *Nat. Catal.* **2019**, *2*, 748−755.
(62) Sandbeck, D. J. S. On the Dissolution of Platinum: From Fundamental to Advanced Catalytic Materials. Ph.D. Thesis, Friedrich-Alexander-Universität Erlangen-Nürnberg, Erlangen, Germany, 2019.
(63) Nesselberger, M.; Roefzaad, M.; Fayçal Hamou, R.; Ulrich Biedermann, P.; Schweinberger, F. F.; Kunz, S.; Schloegl, K.; Wiberg, G. K. H.; Ashton, S.; Heiz, U.; Mayrhofer, K. J. J.; Arenz, M. The effect of particle proximity on the oxygen reduction rate of size-selected platinum clusters. *Nat. Mater.* **2013**, *12*, 919−924.
(64) Schuppert, A. K.; Topalov, A. A.; Katsounaros, I.; Klemm, S. O.; Mayrhofer, K. J. J. A Scanning Flow Cell System for Fully Automated Screening of Electrocatalyst Materials. *J. Electrochem. Soc.* **2012**, *159*, F670−F675.
(65) Cherevko, S.; Topalov, A. A.; Zeradjanin, A. R.; Keeley, G. P.; Mayrhofer, K. J. J. Temperature-Dependent Dissolution of Polycrystalline Platinum in Sulfuric Acid Electrolyte. *Electrocatalysis* **2014**, *5*, 235−240.
(66) Geiger, S. Stability investigations of iridium-based catalysts towards acidic water splitting. Ph.D. Thesis, Ruhr-University Bochum, 2017.
(67) Fabbri, E.; Taylor, S.; Rabis, A.; Levecque, P.; Conrad, O.; Kötz, R.; Schmidt, T. J. The Effect of Platinum Nanoparticle Distribution on Oxygen Electroreduction Activity and Selectivity. *ChemCatChem* **2014**, *6*, 1410−1418.
(68) Quinson, J.; Röefzaad, M.; Deiana, D.; Hansen, T. W.; Wagner, J. B.; Nesselberger, M.; Crampton, A. S.; Ridge, C. J.; Schweinberger, F. F.; Heiz, U.; Arenz, M. Electrochemical stability of subnanometer Pt clusters. *Electrochim. Acta* **2018**, *277*, 211−217.
(69) Sandbeck, D.; Inaba, M.; Quinson, J.; Bucher, J.; Zana, A.; Arenz, M.; Cherevko, S. The Particle Size Effect on Platinum Dissolution: Practical Considerations for Fuel Cells. *ACS Appl. Mater. Interfaces* **2020**, DOI: 10.1021/acsami.0c02801.
(70) Speder, J.; Altmann, L.; Roefzaad, M.; Bäumer, M.; Kirkensgaard, J. J. K.; Mortensen, K.; Arenz, M. Pt based PEMFC catalysts prepared from colloidal particle suspensions - a toolbox for model studies. *Phys. Chem. Chem. Phys.* **2013**, *15*, 3602−3608.
(71) Speder, J.; Zana, A.; Spanos, I.; Kirkensgaard, J. J. K.; Mortensen, K.; Arenz, M. On the influence of the Pt to carbon ratio on the degradation of high surface area carbon supported PEM fuel cell electrocatalysts. *Electrochem. Commun.* **2013**, *34*, 153−156.
(72) Eslamibidgoli, M. J.; Eikerling, M. H. Atomistic Mechanism of Pt Extraction at Oxidized Surfaces: Insights from DFT. *Electrocatalysis* **2016**, *7*, 345−354.
(73) Fantauzzi, D.; Mueller, J. E.; Sabo, L.; van Duin, A. C. T.; Jacob, T. Surface Buckling and Subsurface Oxygen: Atomistic Insights into the Surface Oxidation of Pt(111). *ChemPhysChem* **2015**, *16*, 2797−2802.
(74) Conway, B. E.; Jerkiewicz, G. Surface Orientation Dependence of Oxide Film Growth at Platinum Single-Crystals. *J. Electroanal. Chem.* **1992**, *339*, 123−146.
(75) Drnec, J.; Ruge, M.; Reikowski, F.; Rahn, B.; Carlà, F.; Felici, R.; Stettner, J.; Magnussen, O. M.; Harrington, D. A. Initial stages of Pt(111) electrooxidation: dynamic and structural studies by surface X-ray diffraction. *Electrochim. Acta* **2017**, *224*, 220−227.
(76) Conway, B. E. Electrochemical Oxide Film Formation at Noble-Metals as a Surface-Chemical Process. *Prog. Surf. Sci.* **1995**, *49*, 331−452.
(77) Ohma, A.; Shinohara, K.; Iiyama, A.; Yoshida, T.; Daimaru, A. Membrane and catalyst performance targets for automotive fuel cells by FCCJ membrane, catalyst, MEA WG. *ECS Trans.* **2011**, *41*, 775−784.
(78) DOE. *U.S. DRIVE Fuel Cell Tech Team Cell Component Accelerated Stress Test and Polarization Curve Protocols for PEM Fuel Cells*, 2013. https://www.energy.gov/eere/fuelcells/downloads/fuel-cell-tech-team-accelerated-stress-test-and-polarization-curve.
(79) DOE. *USCAR Fuel Cell Tech Team Cell Component Accelerated Stress Test Protocols for PEM Fuel Cells*, 2010.
(80) DOE. *DOE Cell Component Accelerated Stress Test Protocols for PEM Fuel Cells*, 2007.
(81) Myers, D. J. *2010 Annual Progress Report-Polymer Electrolyte Fuel Cell Lifetime Limitations: The Role of Electrocatalysts Degradation*; US DOE, 2010. https://www.hydrogen.energy.gov/annual_progress10_fuelcells.html#h.
(82) Borup, R.; Meyers, J.; Pivovar, B.; Kim, Y. S.; Mukundan, R.; Garland, N.; Myers, D.; Wilson, M.; Garzon, F.; Wood, D.; Zelenay, P.; More, K.; Stroh, K.; Zawodzinski, T.; Boncella, J.; McGrath, J. E.; Inaba, M.; Miyatake, K.; Hori, M.; Ota, K.; Ogumi, Z.; Miyata, S.; Nishikata, A.; Siroma, Z.; Uchimoto, Y.; Yasuda, K.; Kimijima, K.-i.; Iwashita, N. Scientific Aspects of Polymer Electrolyte Fuel Cell Durability and Degradation. *Chem. Rev.* **2007**, *107*, 3904−3951.
(83) Gilbert, J. A.; Kariuki, N. N.; Wang, X.; Kropf, A. J.; Yu, K.; Groom, D. J.; Ferreira, P. J.; Morgan, D.; Myers, D. J. Pt Catalyst Degradation in Aqueous and Fuel Cell Environments studied via In-Operando Anomalous Small-Angle X-ray Scattering. *Electrochim. Acta* **2015**, *173*, 223−234.
(84) Uchimura, M.; Sugawara, S.; Suzuki, Y.; Zhang, J.; Kocha, S. S. Electrocatalyst Durability under Simulated Automotive Drive Cycles. *ECS Trans.* **2008**, *16*, 225.
(85) Wettergren, K.; Schweinberger, F. F.; Deiana, D.; Ridge, C. J.; Crampton, A. S.; Rötzer, M. D.; Hansen, T. W.; Zhdanov, V. P.; Heiz, U.; Langhammer, C. High sintering resistance of size-selected platinum cluster catalysts by suppressed Ostwald ripening. *Nano Lett.* **2014**, *14*, 5803−5809.
(86) Cherevko, S.; Keeley, G. P.; Geiger, S.; Zeradjanin, A. R.; Hodnik, N.; Kulyk, N.; Mayrhofer, K. J. J. Dissolution of Platinum in the Operational Range of Fuel Cells. *ChemElectroChem* **2015**, *2*, 1471−1478.

https://dx.doi.org/10.1021/acscatal.0c00779
ACS Catal. 2020, 10, 6281−6290

Paper IV

https://dx.doi.org/10.1149/1945-7111/abc767

The Dissolution Dilemma for low Pt Loading Polymer Electrolyte Membrane Fuel Cell Catalysts

Daniel J.S. Sandbeck, Niklas M. Secher, Masanori Inaba, Jonathan Quinson, Jakob E. Sørensen, Jakob Kibsgaard, Alessandro Zana, Francesco Bizzotto, Florian D. Speck, Michael T.Y. Paul, Alexandra Dworzak, Carsten Dosche, Mehtap Oezaslan, Ib Chorkendorff, Matthias Arenz, and Serhiy Cherevko

Journal of The Electrochemical Society, 2020, **167** 164501

Journal of The Electrochemical Society, 2020 **167** 164501

The Dissolution Dilemma for Low Pt Loading Polymer Electrolyte Membrane Fuel Cell Catalysts

Daniel J. S. Sandbeck,[1,2,=,z] Niklas Mørch Secher,[3,=] Masanori Inaba,[4,5] Jonathan Quinson,[4] Jakob Ejler Sørensen,[3] Jakob Kibsgaard,[3] Alessandro Zana,[6] Francesco Bizzotto,[6] Florian D. Speck,[1,2] Michael T. Y. Paul,[1] Alexandra Dworzak,[7,8] Carsten Dosche,[7,8] Mehtap Oezaslan,[7,8,*] Ib Chorkendorff,[3] Matthias Arenz,[4,6,z] and Serhiy Cherevko[1,z]

[1]*Helmholtz-Institute Erlangen-Nürnberg for Renewable Energy (IEK-11), Forschungszentrum Jülich GmbH, 91058 Erlangen, Germany*
[2]*Department of Chemical and Biological Engineering, Friedrich-Alexander-Universität Erlangen-Nürnberg, 91058 Erlangen, Germany*
[3]*Department of Physics, Technical University of Denmark, 2800 Lyngby, Denmark*
[4]*Department of Chemistry, University of Copenhagen, DK-2100 Copenhagen Ø, Denmark*
[5]*Toyota Central R&D Labs, Inc., Nagakute, Aichi 480-1192, Japan*
[6]*Department of Chemistry and Biochemistry, University of Bern, CH-3012 Bern, Switzerland*
[7]*Department of Chemistry, Carl von Ossietzky University of Oldenburg, 26111 Oldenburg, Germany*
[8]*Institute of Technical Chemistry, Technical University of Braunschweig, 38106 Braunschweig, Germany*

Cost and lifetime currently hinder widespread commercialization of polymer electrolyte membrane fuel cells (PEMFCs). Reduced electrode Pt loadings lower costs; however, the impact of metal loading (on the support) and its relation to degradation (lifetime) remain unclear. The limited research on these parameters stems from synthetic difficulties and lack of in situ analytics. This study addresses these challenges by synthesizing 2D and 3D Pt/C model catalyst systems via two precise routes and systematically varying the loading. Pt dissolution was monitored using on-line inductively coupled plasma mass spectrometry (on-line-ICP-MS), while X-ray spectroscopy techniques were applied to establish the oxidation states of Pt in correlation with metal loading. Dissolution trends emerge which can be explained by three particle proximity dependent mechanisms: (1) shifts in the Nernst dissolution potential, (2) redeposition, and (3) alteration of Pt oxidation states. These results identify engineering limitations, which should be considered by researchers in fuel cell development and related fields.
 [DOI: 10.1149/1945-7111/abc767]

Manuscript submitted September 2, 2020; revised manuscript received October 23, 2020. Published November 20, 2020. *This paper is part of the JES Focus Issue on Proton Exchange Membrane Fuel Cell and Proton Exchange Membrane Water Electrolyzer Durability.*

Supplementary material for this article is available online

For years' polymer electrolyte membrane fuel cell (PEMFC) electrocatalysis research has been aimed at increasing catalyst activity towards the sluggish oxygen reduction reaction (ORR), in an effort to decrease the total Pt loading necessary in the cathode catalyst layer. By decreasing Pt loading the total cost[1] and amount of Pt in circulation can be reduced, thereby increasing manufacturing production volumes of fuel cell electric vehicles.[2]

Several strategies have been suggested to increase catalyst activity, with major research efforts focused on Pt alloys and shape-controlled Pt nanoparticles.[3–10] Although such advanced materials show promising ORR activity, less can be said regarding their stability. Furthermore, on the pathway to lower Pt loadings, it is of immediate interest to understand the degradation behavior of current state-of-the-art materials.[11]

Decreased Pt loading achieved via thin catalyst layers is known to severely compromise performance at high current densities in membrane electrode assemblies (MEAs).[1,2] Such loading dependent performance has been attributed to flooding and a local O_2 resistance related to changing Pt substrate-ionomer interactions when going from thick to thin ionomer films. In contrast, the mechanisms behind the observed increase in irreversible degradation can only be speculated without dedicated investigations.

Under well-defined half-cell conditions, which become necessary for elucidating fundamental phenomena undetectable in complex systems, studying the impact of catalyst layer thickness on the primary degradation mechanism of Pt dissolution revealed crucial phenomena.[12,13] On-line dissolution measurements with a scanning flow cell coupled to an inductively coupled plasma mass spectrometer (SFC-ICP-MS) showed that electrochemical specific dissolution normalized by electrochemically active surface area (ECSA) increased with decreasing catalyst layer thickness. While the exact mechanism remains unknown, this observed dissolution trend was tentatively attributed to a shift in the Nernst potential for dissolution, which was greater for the increased diffusional path lengths of thicker catalyst layers. Due to these unambiguous performance and degradation issues, lower Pt content via catalyst layer thickness will be limited to a yet to be defined length without further materials improvements.

Considering the perceived limitations of thin catalyst layers, a new contrasting approach to lower Pt loading must be investigated. By lowering the Pt density within the catalyst layer, i.e. the wt.% Pt, the Pt content can be varied independent of thickness. Similar to the low Pt content of thin catalyst layers, low Pt density has been reported to decrease ORR activity.[14–17] However, in comparison to catalyst layer thickness, the dependence of Pt density on degradation remains largely unexplored.[15,16,18,19] Therefore, in this work the SFC-ICP-MS technique was employed to elucidate the effect of loading on dissolution with constant catalyst layer thickness. Three-dimensional (3D) Pt/Vulcan materials and two-dimensional (2D) model magnetron-sputtered mass-selected systems of varied loadings were investigated. For the 3D Pt/C materials, exclusive control of material properties such as particle size and loading was achieved

[=]These authors contributed equally to this work.
*Electrochemical Society Member.
[z]E-mail: d.sandbeck@fz-juelich.de; matthias.arenz@dcb.unibe.ch; s.cherevko@fz-juelich.de

Journal of The Electrochemical Society, 2020 **167** 164501

with a two-step surfactant-free polyol synthetic technique, termed the "toolbox" approach.[14,15,20–24] Moving to the 2D model systems, particle size and distribution were precisely tuned using a magnetron-based cluster source where Pt clusters were deposited on a planar glassy carbon substrate.[17] By studying model 2D systems, further analytical confirmation becomes possible which ensures firm conclusions on the complex, applied 3D systems. For direct comparison, the common parameter of the edge-to-edge interparticle distance (ipd) is used, which was recently shown to be crucial in the degradation of Pd heterogeneous catalysts[25] and now also to electrocatalyst degradation via Pt dissolution.

Results

By studying well-defined model 2D (mass-selected, magnetron sputtered) in parallel to the applied 3D (Pt/Vulcan) materials, the combined simplicity of the former and complexity of the latter reaffirm the conclusions to be discussed. The model 2D materials eliminate possible support effects, contaminations from wet-chemical syntheses and allow precise calculation of interparticle distance,[13,20,21,26] while the 3D Pt/Vulcan materials provide a realistic applied material. The critical parameters of particle size and interparticle distance for both the 2D and 3D materials were analyzed and are shown in Fig. 1. SEM images of the 1, 2 and 5% coverages for the 2D materials are displayed in the top row of Figs. 1a–1c. At higher coverages, the interparticle distances become difficult to estimate from the SEM images due to poor resolution and increasing probability of particle overlap; therefore, the three lowest coverages are used to estimate values of interparticle distance from the SEM images and are plotted in Fig. 1d. To obtain interparticle distances at higher coverages, it is possible to use calculations assuming a homogenous (evenly spaced) distribution. However, it is seen in Fig. 1d (magnified in Fig. S1 is available online at stacks.iop.org/JES/167/164501/mmedia) that this would overestimate the interparticle distances at low coverages. Therefore, the interparticle distances were simulated by generating random particle positions with the number of particles in a given area determined by coverage (detailed in supplementary information), which fit well with the measured SEM values and are used in the following discussion. To ensure a narrow size distribution as a result from the synthesis, Pt particles were deposited on a Cu TEM grid and analyzed via STEM. The resulting particle size distribution is displayed in Fig. 1e (full image sets are found in Fig. S4). Two narrow distributions were obtained, the single mass and the double mass particles. Due to the low number of double mass particles these can be neglected. A mean diameter of 6.5 ± 0.4 nm was obtained. The deviation from 6 to 6.5 nm is due to the error of the assumption of spherical particles when calculating particle size from mass. The particles are not perfect spheres as is evident from Fig. S4b. A narrow distribution with mean diameter of 6.8 ± 0.7 nm was obtained, with a small fraction of larger particles which unavoidably result from doubly charged particles passing through the mass filter. The use of rather large particle sizes here enabled the estimation of interparticle distances at low coverages confirming the accuracy of the simulation and enabling it predict values at higher coverages, which becomes nearly impossible for smaller particle sizes due to the limited resolution of SEM analysis.

Analysis of the 3D Pt/Vulcan materials was carried out using TEM, and is analogously displayed with increasing loading in the bottom row of Figs. 1f–1h (a full set of images is found in Fig. S5). Highly homogeneous particle distributions and increasing loading of NPs are clearly observed. In contrast to the 2D materials, estimation of the interparticle distance becomes difficult from a 2D image of a 3D material,[15,22] highlighting the increased complexity of moving from model to applied catalyst systems. Therefore, for the 3D systems, the interparticle distance was calculated using Eq. S1 which assumes homogeneously spaced particles and is shown in Fig. 1i (magnified in Fig. S3) for all Pt/Vulcan materials. However, it should be noted that for the 2D materials this treatment overestimates the distances at low coverages, as similarly reported for Pt/Vulcan previously.[22] The particle size distribution of each material was measured and a representative histogram is displayed in Fig. 1j (a full set of data is found in Fig. S6). The particle sizes were found to be identical within error (1.9 ± 0.5 nm average), as to be expected with the two-step synthetic approach which yields high control over particle size and loading. Further analysis on the crystalline nature of such synthesized Pt nanoparticles was carried out previously by Quinson et al.[20]

Aside from the physical properties on the nanoscale of the material, macroscopic properties are critical in fundamental electrochemical studies. The 2D materials are sputtered in a raster pattern (Fig. S7) over a large area of glassy carbon, relative to the contact area of the SFC comprising the working electrode. Therefore, the Pt coverage must be highly homogeneous to ensure that any area can be contacted and measured electrochemically. By measuring an array of XPS spectra and quantifying the atomic content of Pt across each sample (Figs. S8 and S9) the homogeneity of each sample was

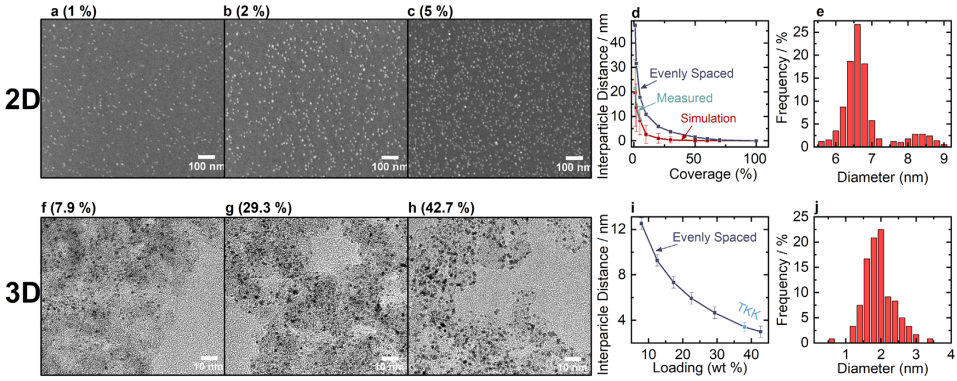

Figure 1. Physical characterization of 2D (sputtered) and (3D Pt/Vulcan) materials. (a)–(c) Selected SEM images of the 2D mass-selected materials of 1, 2 and 5% coverage. (d) Interparticle distances measured from the SEM images, calculated assuming homogeneous spacing and from simulations. (e) Particle size distribution obtained from STEM. (f)–(h) TEM images of the 3D Pt/Vulcan materials of 7.9, 29.3 and 42.7 wt.% Pt. (i) Interparticle distance calculated assuming a homogenous distribution. (j) Particle size distribution measured for the 29.3 wt.% Pt/Vulcan. Note that the percent values in the top and bottom rows represent Pt coverage and Pt to carbon mass ratio, respectively.

Journal of The Electrochemical Society, 2020 **167** 164501

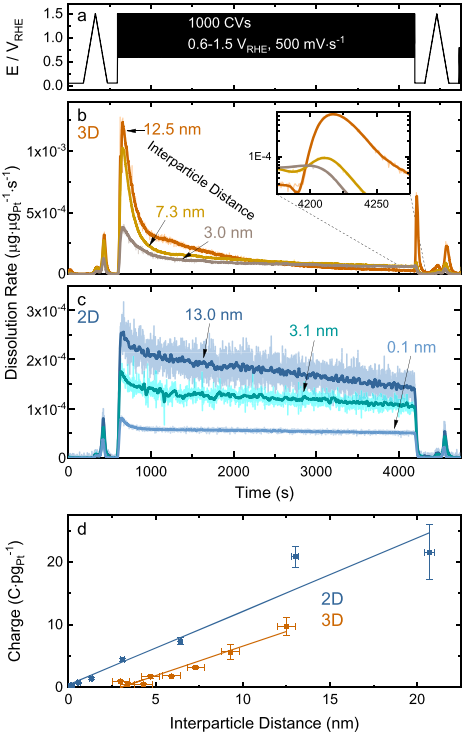

Figure 2. Pt dissolution during the ADT. (a) Full ADT protocol of CVs from 0.6–1.5 V_{RHE}, 500 $mV \cdot s^{-1}$ for 1000 cycles. (b) Resultant dissolution rate profiles for the 3D Pt/Vulcan and (c) 2D magnetron-sputtered systems for three interparticle distances. (d) The mass-normalized charge during the 0.05 V_{RHE} reductive hold immediately following the ADT cycling ($n \geqslant 3$).

assured after synthesis. For the 70% coverage sample, a relative standard deviation of only 3.4% was obtained, demonstrating the effectiveness of the raster technique. In addition to ensuring coverage homogeneity, the XPS spectra (Fig. S8) indicate a clean surface with no contaminations while the atomic content of Pt shows a linear increase with coverage (Fig. S10), indicating that significant particle overlap is only taking place at coverages $> 50\%$.

In contrast to the 2D materials sputtered over a large piece of glassy carbon, the 3D Pt/Vulcan materials are dropcast as spots onto glassy carbon, and completely enclosed by the SFC contact area. The amount of Pt on the working electrode will be determined simply by the volume of ink dropcast; however, constant and uniform catalyst layer thickness becomes a prerequisite to separate the previously reported effects of varying thickness from Pt density (i.e. wt.% loading). Therefore, profilometry was employed as a screening tool. A constant average thickness/height of 0.4 μm was found for all samples as shown in Fig. S11. Microscopy and profilometry (Figs. S12 and S13) show homogenous catalyst layer surfaces with no "coffee ring"[22,27–33] effect and only slight agglomeration in the middle of the spots. However, the commercial Pt/Vulcan (TKK) catalyst has a significant amount of agglomeration and some degree of the coffee ring effect, causing a bumpy surface. The differing dropcasting results could possibly be due to varying properties of the Vulcan support, such as surface area and/or functionalization degree. It is well known that small variations of parameters can yield vastly different dropcasting results.[22,27,29–32,34]

To measure the electrochemical dissolution of the 2D and 3D systems the samples were subjected to a cyclic voltammogram (CV, 0.05–1.5 V_{RHE}) with a slow scan rate (10 $mV \cdot s^{-1}$) followed by aggressive accelerated degradation test (ADT) protocol (1000 cycles of 0.6–1.5 V_{RHE}, 500 $mV \cdot s^{-1}$) and finally another "slow" CV, as seen in Fig. 2a. By employing these two specific scan rates and potential windows, different aspects of dissolution are elucidated. The potential window used here has been demonstrated to cause significant Pt dissolution with rather minimal carbon corrosion.[35] In comparison, the typically used potential windows in accelerated degradation tests in the range of 0.6–1.0 V_{RHE} and 1.0–1.5 V_{RHE} (used to simulate load and start/stop conditions, respectively), will not cause significant Pt dissolution in such a half-cell experiment designed for online detection. The impact of potential window will additionally be addressed in an upcoming manuscript.

The mass-normalized dissolution rate profiles for the 3D and 2D systems during the ADT are shown in Figs. 2b and 2c, which caused extensive Pt dissolution from 15%–65% loss for the 2D and 3D systems (Fig. S14). No particle detachment is observed in the ICP-MS signal (which would cause excessively large spikes), even in the absence of ionomer, indicating strong binding of the nanoparticles to oxygenated support sites, as observed previously for the Pt/Vulcan toolbox synthesis method.[21] Dissolution clearly decreases with decreasing interparticle distance (increasing loading), but here the distinct shapes of the profiles are strikingly different. For the 3D systems, the rate drastically decreases in the initial stages of the ADT, which is far more pronounced for large interparticle distances. At the end of the ADT, an additional cathodic dissolution peak is observed only at large interparticle distances when a reductive potential of 0.05 V_{RHE} was applied (Fig. 2b, inset). This is most pronounced for the 12.5 nm interparticle distance and is only observed for the three largest interparticle distances of the 3D systems. Such behavior is absent from the rather linear decline in dissolution rate of the 2D system, which has larger 6.8 nm particles in comparison to 1.9 nm for Pt/Vulcan.

It appears that for large interparticle distances, the Pt nanoparticles become (partially) passivated by formed PtO_x, i.e. the lower potential limit (LPL) of 0.6 V_{RHE} is too positive to fully reduce this formed layer on the time scale of the ADT cycling. This is further illustrated in the mass-normalized charge during the reductive hold following the ADT in Fig. 2d (error from $n \geqslant 3$ where raw data treatment is shown in Figs. S15 and S16). The mass-normalized charge is used to take into account variations of Pt mass on the glassy carbon substrate. The larger interparticle distances contain more PtO_x at the end of the ADT and thus more charge is passed to the nanoparticles, which leads to a higher accumulated charge measured during the reductive hold. This is further pronounced by the Gibbs-Thomson effect[36–39] for the 3D system of smaller particle size, causing the additional cathodic peak at the end of the ADT.

The intercept of the mass-specific reduction charge (Fig. 2d) is shifted for the 3D materials, which theoretically must go through the origin (as interparticle distance approaches zero the relative Pt mass approaches infinite values). Calculation of interparticle distances for the 3D materials assumed homogeneously distributed, evenly spaced particles, due to lack of accurate experimental techniques. For the 2D materials this was shown by SEM and simulations to overestimate interparticle distances (Fig. 1d), while for Pt/Vulcan it has been suggested that inaccessible pores cause an overestimation of surface area (and thus interparticle distance), which explains the observed shift of the intercept away from the origin. This result highlights the importance of comparing well-defined model systems to applied materials on the quest to understand electrocatalytic materials and their degradation.

To further explore the phenomena of particle passivation, which may be compounded by particle size shrinking during the ADT (due to dissolution), an "extended" ADT to 2500 cycles was applied to the 20.7 nm interparticle distance (1% coverage) 2D sample. As

Journal of The Electrochemical Society, 2020 **167** 164501

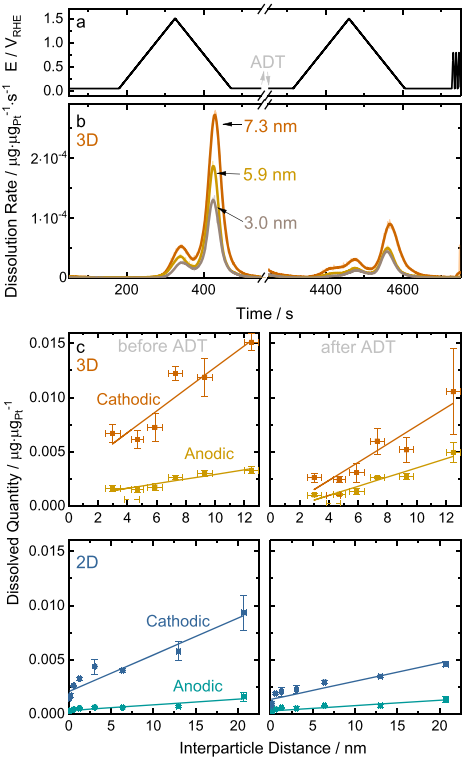

Figure 3. Pt dissolution preceding and following the ADT. (a) Two CVs from 0.05–1.5 V_{RHE} at 10 $mV \cdot s^{-1}$ prior and following a harsh ADT protocol from 0.6–1.5 V_{RHE}, 500 $mV \cdot s^{-1}$ for 1000 cycles. (b) Resultant dissolution rate profiles normalized to total Pt mass on the glassy carbon substrate for varying interparticle distance. (c) Quantified anodic and cathodic dissolution before and after the ADT normalized to mass for the 3D Pt/Vulcan (top) and 2D magnetron-sputtered (bottom) materials (n ⩾ 3).

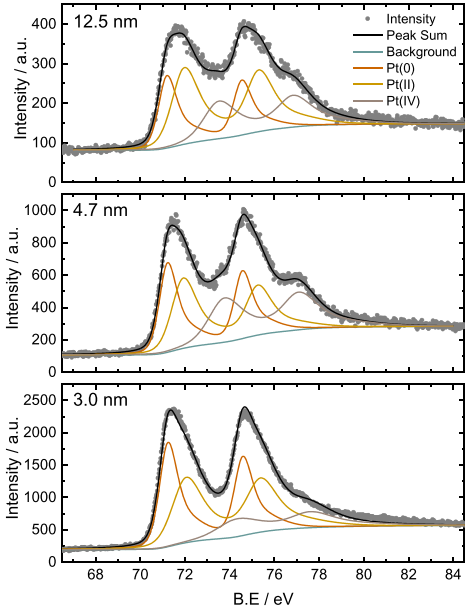

Figure 4. Ex-situ Pt 4f XPS spectra of the 12.5, 4.7 and 3.0 nm interparticle distance samples, showing the measured intensity and fitted spectra.

shown in Fig. S17, ∼80% of the initial material was lost as the dissolution rate decreases to near baseline values, indicating highly passivated Pt particles. In comparison ∼60% Pt loss was observed in Fig. S14 for 1000 cycles for the same material. After 2500 cycles the potential was held again at 0.05 V_{RHE} and a large spike in the dissolution rate was observed, due to the reduction of oxide-passivated Pt particles. The reduction charge after 2500 cycles of ADT was found to be identical to after 1000 cycles, which follows that the dissolution rate is approaching low values and the particles are approaching full passivation by this point of the experiment.

The slower CVs preceding and following the ADT have a larger potential window with a more negative lower potential limit (LPL) of 0.05 V_{RHE}, in comparison to 0.6 V_{RHE} during the ADT. Therefore, the formed oxide layers should be fully reduced during the cathodic scan down to 0.05 V_{RHE} and eliminate formed passivating layers skewing results, thus the intrinsic interparticle distance effect on Pt dissolution can be observed. Figure 3b shows the electrochemical mass-normalized Pt dissolution rate profiles for the 3D systems during the two slow CVs before and after the ADT. The separate anodic and cathodic dissolution processes are visible at this relatively slow scan rate (unobservable during the fast ADT scans) and dissolution is clearly diminished after the ADT (expected after significant Pt loss). Some degree of tailing is seen, as compared to slower 2 $mV \cdot s^{-1}$ scans.[13] Most importantly, a trend is observed for both 2D and 3D systems in which dissolution decreases with decreasing interparticle distance, exemplified in the dissolved quantities for the anodic and cathodic peaks in Fig. 3c. A similar observation for varying catalyst layer thickness and constant interparticle distance was earlier attributed to a diffusional effect causing a shift in the Nernst potential for dissolution.[13] An additional observation is seen in the anodic dissolution peak after the ADT (only for Pt/Vulcan materials), where a shoulder appears with an onset ⩽ 0.5 V_{RHE}. Dissolution during the ADT will cause the shrinking of some particles to sub-nanometer sizes which may be susceptible to dissolution at such lower potentials.[13,40,41] Further IL-TEM experiments before and after the ADT on the 3D Pt/Vulcan material indeed show particle shrinking caused by dissolution (Fig. S18), and that dissolution rather than agglomeration appears to the primary degradation mechanism during this ADT experiment.

Ex-situ XPS, XANES and EXAFS characterization techniques were used to further corroborate the above observations of increasing nanoparticle oxidation at larger interparticle distances for the as-prepared 3D Pt/Vulcan materials. Considering that the 2D mass-selected materials are limited to flat surfaces for accurate control of interparticle distance and that the 3D Pt/Vulcan materials with smaller particle sizes showed a much more drastic passivation effect on the Pt dissolution above, only the 3D applied systems were characterized further. By analyzing the Pt 4f XPS peak positions and areas it is possible to ascertain the relative amount of Pt surface oxidation. The fitted XPS spectra of 3.0, 4.7 and 12.5 nm interparticle distance Pt/Vulcan materials are shown in Fig. 4 and as interparticle distance increases, the relative amounts of Pt(0) decreases and the Pt 4f peak shifts to higher binding energies (Table SII), indicating increased oxidation state of the Pt species.

Journal of The Electrochemical Society, 2020 **167** 164501

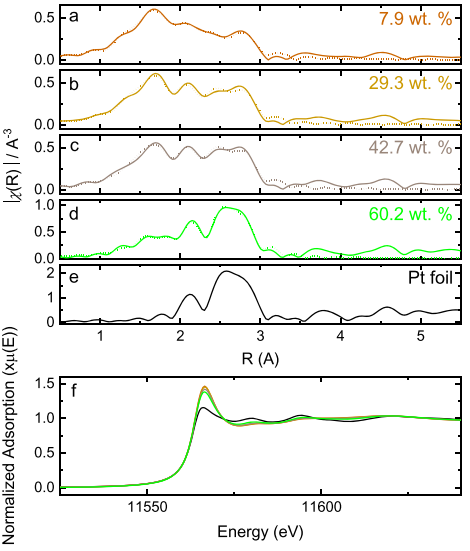

Figure 5. FT-transformed magnitudes of the k^2-weighted EXAFS spectra and fits (dotted) for interparticle distances of (a) 7.9 wt.%, (b) 29.3 wt.%, (c) 42.7 wt.%, (d) 60.2 wt.% and (e) Pt foil as reference. (f) Corresponding L_{III} XANES spectra.

With EXAFS and XANES characterization, inferences regarding the nearest neighbor coordination and the density of unoccupied states may be made, providing further information on the oxidation of the Pt NPs. The FT-transformed magnitudes of the k^2-weighted EXAFS data and the corresponding fits for Pt/Vulcan materials with different loadings (decreasing interparticle distance with increasing loading) are shown in Fig. 5a. For analysis, the nearest neighbor Pt-O and Pt-Pt contributions to the EXAFS data were determined and summarized in Table SIII. The total coordination number of Pt (sum of the partial coordination numbers of N(Pt-Pt) and N(Pt-O) are similar irrespective of the loading, indicating that the particle size of the Pt NPs are in the same range. More interestingly, the contribution of Pt-O increases with decreasing loading. Despite similar total coordination numbers, the partial coordination number of Pt-O increases from 1.6 ± 0.3 to 2.8 ± 0.8 for 60.2 and 7.9 wt.% loadings, respectively. Evidently, the oxophilic properties of these Pt NPs are enhanced with increasing interparticle distance. The changes in the oxidation state of Pt NPs coincide with changes in the white line intensity from the Pt L_{III} edge XANES data (Fig. 5b), which corresponds closely to the density of unoccupied states and thus affinity to PtOH formation.

Discussion

The trends of decreasing dissolution rate and quantities with decreasing interparticle distance may be explained by three fundamental mechanisms, visually illustrated in Fig. 6 for two (mass-selected) materials, where smaller interparticle distances are shown in the foreground. Here the red arrows indicate hinder dissolution of Pt atoms as opposed to the unhindered white arrows. These three mechanisms are further described:

1) As interparticle distance decreases, local Pt^{n+} ion concentrations will more quickly build up in the vicinity of the Pt nanoparticles, causing a shift in the Nernst equilibrium potential for electrochemical dissolution.[13]
2) As interparticle distance decreases, the probability for Pt^{n+} ion redeposition on adjacent Pt particles or particles within the diffusion path from inside the electrode pores to the bulk electrolyte during cathodic potentials will increase.
3) As interparticle distance decreases, the Pt NPs begin to impact each other's oxophilicity. In acidic electrolyte there is increasing overlap between the Pt nanoparticles' electrochemical double layer (EDL), which shifts the oxidation potential of the particles to more positive potentials. Therefore, the Pt nanoparticles become less oxidized during the electrochemical protocol,[14–17,42] which results in decreased dissolution. Such an overlap in the EDL was predicted for interparticle distances smaller than the Debey length,[17] i.e. for interparticle distances smaller than 2 nm for chosen conditions. As evidenced by ex situ XPS and XANES/EXAFS, there is also an impact on the electronic configuration of the NPs, which move from one of isolated NPs towards one of NP ensembles with screened coulomb interaction and more metallic film like properties.[43–46] According to the shift in the oxygen reduction potential from CVs (Fig. S19)[14–17,42] and the diminished d-band vacancy from XANES at low interparticle distances, there are changes in the affinity of Pt nanoparticles for oxidation. Consequently, and similar to the impact of double layer overlap, the Pt nanoparticles with lower interparticle distance will become less oxidized during the electrochemical protocol which results in decreased dissolution.

Although all suggested mechanisms (1–3) must contribute to the trends in mass-specific dissolution shown in Figs. 2 and 3, they cannot be the only factors at play. If the dissolution trend were entirely a consequence of diffusion controlled mechanisms (1) and (2) a directly proportional change in dissolution with coverage or loading should be expected. Mechanism (3) would also contribute to a more drastic decrease in specific dissolution when combined with (1) and (2); however, the dissolution decreases more gradually than can be accounted for by these mechanisms alone. In other words, the total dissolution rates and quantities should more than double if the interparticle distance doubles. The dissolution of Pt is one of many complex interconnected degradation mechanisms, but one possible explanation here is that dissolution is also being controlled kinetically due to low-coordinated defect sites (i.e. edges, corners, adislands and adatoms) present on the nanoparticles surface.[47]

While mechanisms (1–2) are arguably intuitive and have shown to play a role in dissolution on varied diffusion path lengths (catalyst layer thicknesses) at constant interparticle distance, mechanism (3) has a very interesting effect on electrochemical dissolution. During the 0.6–1.5 V_{RHE} ADT (Fig. 2), for both the 2D and 3D systems the Pt particles become (partially) passivated by PtO_x, which clearly depends on the interparticle distance. From the shape of the 3D dissolution rate profile, the sharp initial decrease indicates such passivation is pronounced at large interparticle distances, further evidenced by the cathodic dissolution peak during the subsequent reductive hold. Small interparticle distances diminish this effect and the particles are more easily reduced (become less passivated during the ADT). Similarly, mechanism (3) has previously been attributed to observed increases in ORR activity with decreasing interparticle distance for 2D and 3D systems, as poisoning oxygenated species can block active catalytic sites.[14–17] Inhibited oxide formation also explains the observed shift in the Pt CV reduction peak (Fig. S19).[14–17,42]

The XPS and XANES data demonstrate that the shift in the Pt CV reduction peak is at least partially due to mechanism (3), i.e. a change in electronic configuration of Pt with decreasing interparticle distance. As interparticle distance increases, the relative amounts of Pt(0) decrease and Pt(II) and Pt(IV) increase, and consequently the Pt 4f peak shifts to higher binding energies in the XPS spectra. From the EXAFS experiments an increase in Pt-O coordination is seen, while XANES results clearly show a decreased d-band vacancy at small interparticle distances, resulting in less affinity to PtOH formation. This suggests that the interface between the particles is influenced by coupling/dipole-dipole interactions between the

Journal of The Electrochemical Society, 2020 **167** 164501

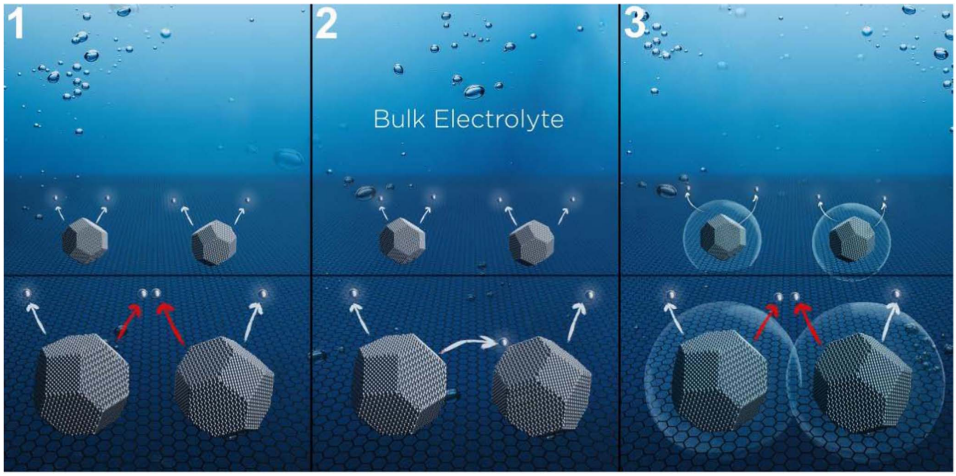

Figure 6. Schematic representation of mechanisms (1–3) on a planar carbon surfaces below a liquid electrolyte for (foreground) small interparticle distance and (background) large interparticle distance. White arrows show dissolved Pt atoms while red arrows indicate inhibited dissolution.

particles. Similar effects have been observed previously in the electronic structure of ensembles of metallic and semiconducting NPs,[43–45] but so far dipole-dipole interactions have not been related to catalytic reactions. At interparticle distances between 0.5 and 10 nm, dipole-dipole interactions can lead to energy transfer between neighboring nanoparticles.[43] The length scale is well within the range of interparticle distances reported here.

Such coupling in closely-spaced NP systems has been shown to modify electronic structures and transport properties. In isolated sub-10 nm NPs the electronic structure can be described by isolated wavefunctions, but when brought in close proximity the wave functions can couple, forming bands transition from insulator to conductor with decreasing interparticle distance.[43–46] Although the individual contributions of the double layer and electronic structure of mechanism (3) on observed dissolution trends may only be speculated at this time, it is highly evident that smaller interparticle distances cause profound interactions which significantly impact oxidation, reduction and dissolution.

With larger particles size of 6.8 nm compared to 1.9 nm, the Gibbs-Thomson equation dictates a more positive oxidation potential for larger particles,[36–38] and this system is less easily passivated than the 3D system.[48,49] This explains the distinctly different shapes of the dissolution rate profiles during the ADT: the 2D systems fit a more linear trend. However, the recorded mass-specific reduction charge at 0.05 V_{RHE} after the ADT follows a similar slope to the 3D system of smaller particle size. As particles shrink during the ADT, they will become more easily passivated due to mechanism (3). This is further corroborated by the extended ADT to 2500 cycles (Fig. S17), where the dissolution rate ceases as shrinking particles become heavily passivated, and the reduction charge after 1000 or 2500 cycles becomes identical.

The study presented here investigated fundamental aspects of PEMFC catalyst degradation, while some important aspects of applied systems should be considered. In real PEMFC devices, the effect of ionomer and interaction with Pt influences performance and degradation.[1,2] However, in situ/online dissolution studies as conducted here are currently infeasible on a full cell level, and a bottom-up approach gives us valuable insights that can predict PEMFC degradation. For instance, Pt dissolution in full cell MEAs is known to be most pronounced close to the membrane, resulting in a Pt "depletion band," where a significant portion of the Pt is redeposited within the membrane itself.[50] This is not unexpected, as dissolved Pt^{n+} atoms require a conductive medium (ionomer/membrane), and effectively increased degrees of freedom close to the membrane allow increased Pt^{n+} diffusion. Therefore, decreasing Pt interparticle distance (Pt density) near the membrane should alleviate the depletion band effect, as was found by Yu et al.[50]

'An interesting study of Lopes et al. has demonstrated the effective use of Pt-Au core–shell/adlayer structures to improve catalyst stability towards degradation,[51] a technique known to hinder Pt dissolution.[52,53] As is common place in rotating disk electrode activity studies, the Pt loading, i.e. the mass of Pt on the electrode, was kept constant. Therefore, although experiments of this work suggest that increasing interparticle distance decreases area-specific Pt dissolution, the thickness of the catalyst layer was drastically changed between electrodes, possibly up to a factor of four, skewing firm conclusions on the impact of interparticle distance. The large impact of catalyst thickness was previously studied by Keeley et al.,[13] which can account for this seemingly contradictory observation. Such a comparison highlights the need for investigations which independently vary parameters such as interparticle distance and particle size, which was not the focus of Lopes et al.

Current applied PEMFC electocatalysts take advantage of the high activity of Pt-transition metal alloys in vehicles such as the Toyota Mirai.[54] The dissolution of the alloying metal will also contribute to degradation, via loss of activity enhancement.[55–57] Dissolution of the alloying metal can cause an increased particle surface area and enhance dissolution of Pt, while Pt dissolution itself can expose additional alloy towards further dissolution.[58–61] Therefore, increased Pt dissolution remains detrimental to alloyed systems. However, the composition, nature of the alloying metal, initial leaching procedure and applied potential protocol (i.e. accelerated durability test) all drastically impact the dissolution of both metals. Furthermore, inhomogenieties in the support material have been shown to impact Pt dissolution, emphasizing possible influences of the carbon structure.[62] Here, the single, fundamental parameter of interparticle distance for pure Pt nanoparticles was varied independently of others, while additional studies will be

required to definitively determine the impacts of additional variables in increasingly complex catalytic systems.

In addition to the complexity of alloyed systems, the complete degradation of PEMFC catalysts is convoluted. The additional degradation mechanisms of carbon corrosion, Ostwald ripening, coalescence and particle detachment are all intricately intertwined with Pt dissolution.[36] Following the discoveries presented here on the impact of interparticle distance on Pt dissolution, future studies should investigate the impact on the other detrimental degradation mechanisms.

Nevertheless, the observations on both 2D model systems and 3D porous Pt/Vulcan materials clearly demonstrate a dissolution dependence on interparticle distance, governed by three different mechanisms. Mechanism (3) contributes to this dependence by altering the redox behavior of the nanoparticles, which can be further compounded by the Gibbs-Thomson (particle-size) effect as nanoparticles shrink from electrochemical dissolution. Therefore, in conventional half-cell ADT experiments, potential limits should be chosen carefully with regards to the large variety of loadings and particle sizes in experimental and commercially available electrocatalytic materials.

It is also important for future engineers to take such considerations into account when designing PEMFC stacks in order to optimize performance and lifetime. Very high loadings can lead to nanoparticle agglomeration and lower Pt utilization, while very low loadings may cause increased mass transport, both lowering performance. As Pt dissolution decreases with increased loading, the clear goal would be to synthesize Pt/C materials with as high loadings as possible without substantial agglomeration effects. In the quest for increasingly active ORR electrocatalysts to reduce required Pt quantities in PEMFCs, from this perspective lower loadings should come in the form of thin catalyst layers made from high wt.% Pt/C materials. However, thin catalyst layers may present their own performance and degradation issues.[1,2,63–70] Furthermore, the effect of interparticle distance on Pt dissolution and catalyst layer degradation in full cell MEAs still remains to be explored.

Conclusions

A clear coverage/loading effect on transient Pt electrochemical dissolution has been observed for model 2D mass-selected systems and applied 3D Pt/Vulcan materials. With increased coverage/loading mass-specific electrochemical dissolution significantly decreases and stability increases. These observations may be attributed to three possible mechanisms: (1) increased local Pt^{n+} ion concentrations causing a shift in the Nernst equilibrium potential for dissolution, (2) increased probability for Pt^{n+} ion redeposition, (3) increasing overlap between the nanoparticles electric double layer and coupling/with pronounced dipole-dipole interactions between neighboring nanoparticles. Further ex situ characterization has provided evidence of (3) where Pt oxidation decreases in XPS spectra, and EXAFS data unveils decreasing Pt coordination to oxygen with increasing loading. The consequential passivation effect during accelerated degradation testing is seen to be pronounced for large interparticle distances due to (3), which is diminished for larger particle sizes, emphasizing the importance of potential limits in accelerated degradation test experiments with varied loading or particle size.

Acknowledgments

This work was funded by the Villum Foundation V-SUSTAIN grant 9455 to the Villum Center for the Science of Sustainable Fuels and Chemicals and the Swiss National Science Foundation (SNSF) via the project No. 200021_184742. The Escalab 250 Xi XPS facility has been co-funded by the Deutsche Forschungsgemeinschaft (INST 184/144-1 FUGG). Bundesministerium für Bildung und Forschung (BMBF, FKZ 03SF0539) are gratefully acknowledged. The SLS is acknowledged for the provision of beamtime at the SuperXAS beamline (project ID 20161303). Diamond Light Source, Hartwell, UK is thanked—in particular Dr. Giannantonio Cibin and Ann-Kathrin Geiger—for access to synchrotron beamline B18 (proposal SP12746). We thank Dr. L. Theil Kuhn and Dr. S. B. Simonsen, Technical University of Denmark for access to TEM facilities. The access to the microscope for IL-TEM imaging was made possible through the School for Micro- and Nanostructure & Center for Nanoanalysis and Electron Microscopy (CENEM) at the Friedrich-Alexander-University Erlangen-Nürnberg.

Experimental

Full experimental procedures can be found in the first section of the associated supporting information.

ORCID

Daniel J. S. Sandbeck https://orcid.org/0000-0002-7618-3574
Niklas Mørch Secher https://orcid.org/0000-0003-1027-5027
Masanori Inaba https://orcid.org/0000-0002-2292-7961
Jonathan Quinson https://orcid.org/0000-0002-9374-9330
Jakob Ejler Sørensen https://orcid.org/0000-0001-5465-3769
Jakob Kibsgaard https://orcid.org/0000-0002-9219-816X
Alessandro Zana https://orcid.org/0000-0003-0588-3116
Francesco Bizzotto https://orcid.org/0000-0002-5624-6697
Florian D. Speck https://orcid.org/0000-0002-7649-9261
Michael T. Y. Paul https://orcid.org/0000-0003-2206-0592
Alexandra Dworzak https://orcid.org/0000-0002-8689-9517
Carsten Dosche https://orcid.org/0000-0003-3837-5169
Mehtap Oezaslan https://orcid.org/0000-0001-8545-7576
Ib Chorkendorff https://orcid.org/0000-0003-2738-0325
Matthias Arenz https://orcid.org/0000-0001-9765-4315
Serhiy Cherevko https://orcid.org/0000-0002-7188-4857

References

1. A. Kongkanand and M. F. Mathias, *J. Phys. Chem. Lett.*, **7**, 1127 (2016).
2. P. Gazdzicki, J. Mitzel, A. M. Dreizler, M. Schulze, and K. A. Friedrich, *Fuel Cells*, **18**, 270 (2018).
3. V. R. Stamenkovic, B. Fowler, B. S. Mun, G. Wang, P. N. Ross, C. A. Lucas, and N. M. Marković, *Science*, **315**, 493 (2007).
4. P. Hernandez-Fernandez et al., *Nat. Chem.*, **6**, 732 (2014).
5. M. Escudero-Escribano, P. Malacrida, M. H. Hansen, U. G. Vej-Hansen, A. Velázquez-Palenzuela, V. Tripkovic, J. Schiøtz, J. Rossmeisl, I. E. L. Stephens, and I. Chorkendorff, *Science*, **352**, 73 (2016).
6. D. Li et al., *Energy Environ. Sci.*, **7**, 4061 (2014).
7. M. Oezaslan, F. Hasché, and P. Strasser, *J. Phys. Chem. Lett.*, **4**, 3273 (2013).
8. I. A. Safo, C. Dosche, and M. Oezaslan, *ChemPhysChem*, **20**, 15 (2019).
9. S. Chen, H. A. Gasteiger, K. Hayakawa, T. Tada, and Y. Shao-Horn, *J. Electrochem. Soc.*, **157**, A82 (2010).
10. C. E. Carlton, S. Chen, P. J. Ferreira, L. F. Allard, and Y. Shao-Horn, *J. Phys. Chem. Lett.*, **3**, 161 (2012).
11. S. Cherevko, *Curr. Opin. Electrochem.*, **8**, 118 (2018).
12. S. Cherevko, N. Kulyk, and K. J. J. Mayrhofer, *Nano Energy*, **29**, 275 (2016).
13. G. P. Keeley, S. Cherevko, and K. J. Mayrhofer, *ChemElectroChem*, **3**, 51 (2016).
14. J. Speder, I. Spanos, A. Zana, J. J. K. Kirkensgaard, K. Mortensen, L. Altmann, M. Bäumer, and M. Arenz, *Surf. Sci.*, **631**, 278 (2015).
15. J. Speder, L. Altmann, M. Bäumer, J. J. K. Kirkensgaard, K. Mortensen, and M. Arenz, *RSC Adv.*, **4**, 14971 (2014).
16. E. Fabbri, S. Taylor, A. Rabis, P. Levecque, O. Conrad, R. Kötz, and T. J. Schmidt, *ChemCatChem*, **6**, 1410 (2014).
17. M. Nesselberger et al., *Nat. Mater.*, **12**, 919 (2013).
18. M. Inaba, "Systematic study of Pt/C catalysts for polymer electrolyte membrane fuel cells." *Department of Chemistry* (Unversity of Copenhagen, Copenhagen, Denmark) (2018).
19. S. Taylor, E. Fabbri, P. Levecque, T. J. Schmidt, and O. Conrad, *Electrocatalysis*, **7**, 287 (2016).
20. J. Quinson et al., *ACS Catal.*, **8**, 6627 (2018).
21. J. Speder, L. Altmann, M. Roefzaad, M. Baumer, J. J. Kirkensgaard, K. Mortensen, and M. Arenz, *Phys. Chem. Chem. Phys.*, **15**, 3602 (2013).
22. S. Proch, K. Kodama, M. Inaba, K. Oishi, N. Takahashi, and Y. Morimoto, *Electrocatalysis*, **7**, 249 (2016).
23. J. Speder, A. Zana, I. Spanos, J. J. K. Kirkensgaard, K. Mortensen, and M. Arenz, *Electrochem. Commun.*, **34**, 153 (2013).
24. J. Speder, A. Zana, I. Spanos, J. J. K. Kirkensgaard, K. Mortensen, M. Hanzlik, and M. Arenz, *J. Power Sources*, **261**, 14 (2014).
25. E. D. Goodman, A. C. Johnston-Peck, E. M. Dietze, C. J. Wrasman, A. S. Hoffman, F. Abild-Pedersen, S. R. Bare, P. N. Plessow, and M. Cargnello, *Nat. Catal.*, **2**, 748 (2019).

Journal of The Electrochemical Society, 2020 **167** 164501

26. G. S. Harzer, A. Orfanidi, H. El-Sayed, P. Madkikar, and H. A. Gasteiger, *J. Electrochem. Soc.*, **165**, F770 (2018).
27. Y. Garsany, O. A. Baturina, K. E. Swider-Lyons, and S. S. Kocha, *Anal. Chem.*, **82**, 6321 (2010).
28. Y. Garsany, I. L. Singer, and K. E. Swider-Lyons, *J. Electroanal. Chem.*, **662**, 396 (2011).
29. Y. Garsany, J. Ge, J. St-Pierre, R. Rocheleau, and K. E. Swider-Lyons, *J. Electrochem. Soc.*, **161**, F628 (2014).
30. K. Shinozaki, J. W. Zack, S. Pylypenko, B. S. Pivovar, and S. S. Kocha, *J. Electrochem. Soc.*, **162**, F1384 (2015).
31. M. Inaba, J. Quinson, and M. Arenz, *J. Power Sources*, **353**, 19 (2017).
32. M. Inaba, J. Quinson, J. R. Bucher, and M. Arenz, *J. Vis. Exp.*, **133**, 10 (2018).
33. K. Ke, K. Hiroshima, Y. Kamitaka, T. Hatanaka, and Y. Morimoto, *Electrochim. Acta*, **72**, 120 (2012).
34. R. Sharma and S. M. Andersen, *ACS Appl. Mater. Interfaces*, **10**, 38125 (2018).
35. E. Pizzutilo, S. Geiger, J. P. Grote, A. Mingers, K. J. J. Mayrhofer, M. Arenz, and S. Cherevko, *J. Electrochem. Soc.*, **163**, F1510 (2016).
36. J. C. Meier, C. Galeano, I. Katsounaros, J. Witte, H. J. Bongard, A. A. Topalov, C. Baldizzone, S. Mezzavilla, F. Schuth, and K. J. J. Mayrhofer, *Beilstein J. Nanotechnol.*, **5**, 44 (2014).
37. W. J. Plieth, *J. Phys. Chem.*, **86**, 3166 (1982).
38. K. J. Mayrhofer, B. B. Blizanac, M. Arenz, V. R. Stamenkovic, P. N. Ross, and N. M. Markovic, *J. Phys. Chem. B*, **109**, 14433 (2005).
39. K. Yu, D. J. Groom, X. Wang, Z. Yang, M. Gummalla, S. C. Ball, D. J. Myers, and P. J. Ferreira, *Chem. Mater.*, **26**, 5540 (2014).
40. L. Tang, B. Han, K. Persson, C. Friesen, T. He, K. Sieradzki, and G. Ceder, *J. Am. Chem. Soc.*, **132**, 596 (2010).
41. L. Tang, X. Li, R. C. Cammarata, C. Friesen, and K. Sieradzki, *J. Am. Chem. Soc.*, **132**, 11722 (2010).
42. J. Huang, J. Zhang, and M. H. Eikerling, *J. Phys. Chem. C*, **121**, 4806 (2017).
43. C. B. Murray, C. R. Kagan, and M. G. Bawendi, *Annu. Rev. Mater. Sci.*, **30**, 545 (2000).
44. H. Liu, B. S. Mun, G. Thornton, S. R. Isaacs, Y.-S. Shon, D. F. Ogletree, and M. Salmeron, *Phys. Rev. B*, **72**, 155430 (2005).
45. J. Liao, S. Blok, S. J. van der Molen, S. Diefenbach, A. W. Holleitner, C. Schonenberger, A. Vladyka, and M. Calame, *Chem. Soc. Rev.*, **44**, 999 (2015).
46. D. V. Talapin, J. S. Lee, M. V. Kovalenko, and E. V. Shevchenko, *Chem. Rev.*, **110**, 389 (2010).
47. J. Ustarroz, I. M. Ornelas, G. Zhang, D. Perry, M. Kang, C. L. Bentley, M. Walker, and P. R. Unwin, *ACS Catal.*, **8**, 6775 (2018).
48. D. J. S. Sandbeck, N. M. Secher, F. D. Speck, J. E. Sørensen, J. Kibsgaard, I. Chorkendorff, and S. Cherevko, *ACS Catal.*, **10**, 6281 (2020).
49. D. J. S. Sandbeck, M. Inaba, J. Quinson, J. Bucher, A. Zana, M. Arenz, and S. Cherevko, *ACS Appl. Mater. Interfaces*, **12**, 25718 (2020).
50. H. Yu, A. Baricci, A. Casalegno, L. Guetaz, L. Bonville, and R. Maric, *Electrochim. Acta*, **247**, 1169 (2017).
51. P. P. Lopes et al., *Nat. Mater.*, **19**, 1207 (2020).
52. S. Cherevko, G. P. Keeley, N. Kulyk, and K. J. J. Mayrhofer, *J. Electrochem. Soc.*, **163**, I1228 (2016).
53. J. Zhang, K. Sasaki, E. Sutter, and R. R. Adzic, *Science*, **315**, 220 (2007).
54. R. L. Borup, R. Mukundan, K. More, K. C. Neyerlin, A. Z. Weber, D. Myers, and R. Ahluwalia, *233rd Meeting of the Electrochemical Society, r. M. o. t. E. Society Editor*, Seatle, Washington, USA (2018).
55. I. Spanos, K. Divideriksen, J. J. Kirkensgaard, S. Jelavic, and M. Arenz, *Phys. Chem. Chem. Phys.*, **17**, 28044 (2015).
56. V. Beermann, M. E. Holtz, E. Padgett, J. F. de Araujo, D. A. Muller, and P. Strasser, *Energy Environ. Sci.*, **12**, 2476 (2019).
57. Q. Jia et al., *Nano Lett.*, **18**, 798 (2018).
58. P. Jovanovič et al., *J. Power Sources*, **327**, 675 (2016).
59. M. Gatalo, P. Jovanovič, U. Petek, M. Šala, V. S. Šelih, F. Ruiz-Zepeda, M. Bele, N. Hodnik, and M. Gaberšček, *ACS Appl. Energy Mater.*, **2**, 3131 (2019).
60. R. K. Ahluwalia, D. D. Papadias, N. N. Kariuki, J.-K. Peng, X. Wang, Y. Tsai, D. G. Graczyk, and D. J. Myers, *J. Electrochem. Soc.*, **165**, F3024 (2018).
61. C. Baldizzone, L. Gan, N. Hodnik, G. P. Keeley, A. Kostka, M. Heggen, P. Strasser, and K. J. J. Mayrhofer, *ACS Catal.*, **5**, 5000 (2015).
62. P. Jovanovic, U. Petek, N. Hodnik, F. Ruiz-Zepeda, M. Gatalo, M. Sala, V. S. Selih, T. P. Fellinger, and M. Gaberscek, *Phys. Chem. Chem. Phys.*, **19**, 21446 (2017).
63. M. K. Debe, A. K. Schmoeckel, S. M. Hendricks, G. D. Vernstrom, G. M. Haugen, and R. T. Atanasoki, *ECS Trans.*, **1**, 51 (2006).
64. A. J. Steinbach, K. Noda, and M. K. Debe, *ECS Trans.*, **1**, 835 (2006).
65. M. K. Debe, A. K. Schmoeckel, G. D. Vernstrom, and R. Atanasoski, *J. Power Sources*, **161**, 1002 (2006).
66. A. Bonakdarpour, K. Stevens, G. D. Vernstrom, R. Atanasoski, A. K. Schmoeckel, M. K. Debe, and J. R. Dahn, *Electrochim. Acta*, **53**, 688 (2007).
67. P. K. Sinha, W. Gu, A. Kongkanand, and E. Thompson, *J. Electrochem. Soc.*, **158**, B831 (2011).
68. A. Kongkanand, M. Dioguardi, C. Ji, and E. L. Thompson, *J. Electrochem. Soc.*, **159**, F405 (2012).
69. A. Kongkanand, J. Zhang, Z. Liu, Y.-H. Lai, P. Sinha, E. L. Thompson, and R. Makharia, *J. Electrochem. Soc.*, **161**, F744 (2014).
70. A. J. Steinbach et al., *ECS Trans.*, **80**, 659 (2017).

Paper V

Kinetics of oxygen evolution in acid on RuO2 down to 60 mV overpotential

Reshma Rao, Søren B. Scott, Choongman Moon, Jakob E. Sørensen, Jakob Kibsgaard, Yang Shao-Horn, and Ib Chorkendorff

In preparation

Abstract

Ruthenium and ruthenium dioxide are the most active catalysts for water oxidation in acidic electrolyte, but the exact activity at low overpotential can be difficult to measure accurately due to the high pseudocapacitance. Herein, we apply electrochemistry - mass spectrometry (EC-MS) to measure the oxygen produced by the oxygen evolution reaction (OER) on sputter-deposited RuO2 and electrodeposited Ru foam. Both of these materials show higher normalized activity than single crystals, implying an undercoordinated active site. Due to the unprecedented sensitivity of our EC-MS method, we are able to extend the activity trends of ruthenium-based electrodes to extremely low current densities, down to a turn-over frequency (TOF) of 5e-4 s-1 at 60 mV overpotential. We show that the potential-dependence of the TOF, i.e the Tafel slope, goes through three regimes. The OER activity at low overpotential (U¡1.35 V vs-RHE) shows the steepest potential dependence of 20 mV/decade, which had not been seen before. We explain as the result of a potential-dependent coverage of the surface motifs that participate in the rate-determining step.

Paper VI

Comparison of lattice oxygen evolution and metal dissolution in RuO2 and IrO2 films at low overpotential

Reshma Rao, Søren B. Scott, Choongman Moon, Jakob E. Sørensen, Jakob Kibsgaard, Yang Shao-Horn, and Ib Chorkendorff

In preparation

Abstract

Improved understanding of catalytic and degradation mechanisms can help to optimize oxides of ruthenium and iridium for water oxidation in acidic electrolyte. Here we prope degradation and catalytic mechanism by dissolved metal detection with inductively coupled plasma mass spectrometry (ICP-MS) and by isotope labelling studies coupled with electrochemistry - mass spectrometry (EC-MS). Fully quantitative experiments using these two techniques allow us to compare the absolute number of metal atoms dissolved to the number of lattice oxygen atoms incorporated in the O2 evolved on a number of sputter-deposited RuO2 and IrO2 films, as well as electrochemically oxidized Ru and Ir films. Lattice oxygen was comparable to or slighly greater than metal dissolution for a number of iridium-based samples, though they were more stable than ruthenium-based samples on both measures. Ruthenium-based samples always showed much higher metal dissolution than lattice oxygen evolution, but the lattice oxygen evolution signal has a potential dependence matching that of OER activity rather than that of metal dissolution, implying the two phenomena occur by distinct mechanisms. Importantly, lattice oxygen was in all cases a tiny portion of the total oxygen evolved and thus at most a minor contribution to the electrocatalytic mechanism.

Bibliography

[1] R. E. Smalley. Future global energy prosperity: The terawatt challenge. In *MRS Bulletin*, volume 30, pages 412–417. Materials Research Society, 2005. doi:10.1557/mrs2005.124.

[2] N. S. Lewis and D. G. Nocera. Powering the planet: Chemical challenges in solar energy utilization. *Proceedings of the National Academy of Sciences*, 103(43):15729–15735, 2006. doi:10.1073/pnas.0710683104.

[3] N. Armaroli and V. Balzani. The future of energy supply: Challenges and opportunities. *Angewandte Chemie-international Edition*, 46 (1-2):52–66, 2007. doi:10.1002/anie.200602373.

[4] P. C. K. Vesborg and T. F. Jaramillo. Addressing the terawatt challenge: scalability in the supply of chemical elements for renewable energy. *RSC Adv.*, 2(21):7933–7947, 2012. doi:10.1039/C2RA20839C.

[5] Z. W. Seh, J. Kibsgaard, C. F. Dickens, I. Chorkendorff, J. K. Nørskov, and T. F. Jaramillo. Combining theory and experiment in electrocatalysis: Insights into materials design. *Science*, 355(6321), 2017. doi:10.1126/science.aad4998.

[6] I. Chorkendorff and J. W. Niemantsverdriet. *Concepts of Modern Catalysis and Kinetics*. John Wiley & Sons, Ltd, 2007.

[7] B. Hammer and J. K. Nørskov. Electronic factors determining the reactivity of metal surfaces. *Surface Science*, 343(3):211–220, dec 1995. doi:10.1016/0039-6028(96)80007-0.

[8] B. Hammer and J. K. Norskov. Why gold is the noblest of all the metals. *Nature*, 376(6537):238–240, 1995. doi:10.1038/376238a0.

[9] P. Sabatier. Hydrogénations et déshydrogénations par catalyse. *Berichte der deutschen chemischen Gesellschaft*, 44(3):1984–2001, jul 1911. doi:10.1002/cber.19110440303.

[10] J. K. Nørskov, T. Bligaard, J. Rossmeisl, and C. H. Christensen. Towards the computational design of solid catalysts. *Nature Chemistry*, 1(1):37–46, apr 2009. doi:10.1038/nchem.121.

[11] IAP/TU Wien. A Simple Sputter Yield Calculator. URL `https://www.iap.tuwien.ac.at/www/surface/sputteryield`.

[12] N. Matsunami, Y. Yamamura, Y. Itikawa, N. Itoh, and Y. Kazumata. Energy dependence of sputtering yields of monatomic solids (IPPJ-AM–14), 1980. URL `http://inis.iaea.org/Search/search.aspx?orig{_}q=RN:12628118`.

[13] Periodic Table - Ptable. URL `https://ptable.com/{#}Properties`.

[14] M. P. Seah and T. S. Nunney. Sputtering yields of compounds using argon ions. *Journal of Physics D: Applied Physics*, 43(25), 2010. doi:10.1088/0022-3727/43/25/253001.

[15] C. Wagner, W. Riggs, L. Davis, and J. Moulder. *Handbook of X-ray photoelectro spectroscopy*. Perkin-Elmer Corporation, 1978.

[16] D. A. Shirley. High-resolution x-ray photoemission spectrum of the valence bands of gold. *Physical Review B*, 5(12):4709–4714, 1972. doi:10.1103/PhysRevB.5.4709.

[17] M. Seah and W. Dench. Quantitative Electron Spectroscopy of Surface. *Surface and Interface Analysis*, 1(1):2–11, 1979.

[18] G. C. Nelson. Summary Abstract: Semiempirical modeling of the background in low energy ion scattering spectra. *Journal of Vacuum Science & Technology A*, 4(3):1567–1569, 1986. doi:10.1116/1.573508.

[19] H. H. Brongersma, M. Draxler, M. de Ridder, and P. Bauer. Surface composition analysis by low-energy ion scattering. *Surface Science Reports*, 62(3):63–109, 2007. doi:10.1016/j.surfrep.2006.12.002.

[20] J. E. Sørensen. *Mass-selected copper nanoparticles for CO2 electroreduction*. Master thesis, DTU, 2017.

[21] Y. Huttel, editor. *Gas-Phase Synthesis of Nanoparticles*. Wiley-VCH Verlag GmbH & Co. KGaA, Weinheim, Germany, jul 2017. ISBN 9783527698417. doi:10.1002/9783527698417.

[22] H. Haberland, M. Karrais, M. Mall, and Y. Thurner. Thin films from energetic cluster impact: A feasibility study. *Journal of Vacuum Science & Technology A: Vacuum, Surfaces, and Films*, 10(5): 3266–3271, 1992. doi:10.1116/1.577853.

[23] B. Von Issendorff and R. E. Palmer. A new high transmission infinite range mass selector for cluster and nanoparticle beams. *Review of Scientific Instruments*, 70(12):4497–4501, 1999. doi:10.1063/1.1150102.

[24] U. Heiz and U. Landman, editors. *Nanocatalysis*. Nanoscience and Technology. Springer Berlin Heidelberg, Berlin, Heidelberg, 2007. ISBN 978-3-540-74551-8. doi:10.1007/978-3-540-32646-5.

[25] K. Bromann, C. Félix, H. Brune, W. Harbich, R. Monot, J. Buttet, and K. Kern. Controlled deposition of size-selected silver nanoclusters. *Science*, 274(5289):956–958, nov 1996. doi:10.1126/science.274.5289.956.

[26] K. Bromann, H. Brune, C. Félix, W. Harbich, R. Monot, J. Buttet, and K. Kern. Hard and soft landing of mass selected Ag clusters on

Pt (111). *Surface Science*, 377-379:1051–1055, apr 1997. doi:10.1016/S0039-6028(96)01544-0.

[27] D. B. Trimarco, T. Pedersen, O. Hansen, I. Chorkendorff, and P. C. K. Vesborg. Fast and sensitive method for detecting volatile species in liquids. *Review of Scientific Instruments*, 86(7):75006, 2015. doi:10.1063/1.4923453.

[28] D. B. Trimarco, S. B. Scott, A. H. Thilsted, J. Y. Pan, T. Pedersen, O. Hansen, I. Chorkendorff, and P. C. Vesborg. Enabling real-time detection of electrochemical desorption phenomena with sub-monolayer sensitivity. *Electrochimica Acta*, 268:520–530, apr 2018. doi:10.1016/j.electacta.2018.02.060.

[29] D. J. S. Sandbeck, N. M. Secher, M. Inaba, J. Quinson, J. E. Sørensen, J. Kibsgaard, A. Zana, F. Bizzotto, F. Speck, M. T. Y. Paul, A. Dworzak, C. Dosche, M. Oezaslan, I. Chorkendorff, M. Arenz, and S. Cherevko. The Dissolution Dilemma for low Pt Loading Polymer Electrolyte Membrane Fuel Cell Catalysts. *Journal of the Electrochemical Society*, 2020. doi:10.1149/1945-7111/abc767.

[30] D. J. S. Sandbeck, N. M. Secher, F. D. Speck, J. E. Sørensen, J. Kibsgaard, I. Chorkendorff, and S. Cherevko. Particle Size Effect on Platinum Dissolution: Considerations for Accelerated Stability Testing of Fuel Cell Catalysts. *ACS Catalysis*, 10(11):6281–6290, jun 2020. doi:10.1021/acscatal.0c00779.

[31] A. K. Schuppert, A. A. Topalov, I. Katsounaros, S. O. Klemm, and K. J. J. Mayrhofer. A Scanning Flow Cell System for Fully Automated Screening of Electrocatalyst Materials. *Journal of The Electrochemical Society*, 159(11):F670–F675, aug 2012. doi:10.1149/2.009211jes.

[32] S. Cherevko, A. A. Topalov, A. R. Zeradjanin, G. P. Keeley, and K. J. Mayrhofer. Temperature-Dependent Dissolution of Polycrystalline Platinum in Sulfuric Acid Electrolyte. *Electrocatalysis*, 5(3):235–240, feb 2014. doi:10.1007/s12678-014-0187-0.

[33] R. D. Van de Grampel, W. Ming, A. Gildenpfennig, J. Laven, H. H. Brongersma, G. De With, and R. Van der Linde. Quantification of Fluorine Density in the Outermost Atomic Layer. *Langmuir*, 20(1): 145–149, 2004. doi:10.1021/la0353071.

[34] W. P. Jansen, J. M. Harmsen, A. W. V. Gon, J. H. Hoebink, J. C. Schouten, and H. H. Brongersma. Noble metal segregation and cluster size of Pt/Rh/Ceo2/γ-Al2O3 automotive three-way catalysts studied with low-energy ion scattering. *Journal of Catalysis*, 204(2): 420–427, 2001. doi:10.1006/jcat.2001.3391.

[35] C. T. Campbell and T. E. James. Ion scattering spectroscopy intensities for supported nanoparticles: The hemispherical cap model. *Surface Science*, 641:166–169, 2015. doi:10.1016/j.susc.2015.06.013.

[36] H. H. Brongersma, T. Grehl, E. R. Schofield, R. A. Smith, and H. R. Ter Veen. Analysis of the outer surface of platinum-gold catalysts by low-energy ion scattering. *Platinum Metals Review*, 54(2):81–87, 2010. doi:10.1595/147106710X494358.

[37] W. E. Kaden, W. A. Kunkel, and S. L. Anderson. Cluster size effects on sintering, CO adsorption, and implantation in Ir/SiO2. *The Journal of Chemical Physics*, 131(11):114701, sep 2009. doi:10.1063/1.3224119.

[38] J. Rossmeisl, Z. W. Qu, H. Zhu, G. J. Kroes, and J. K. Nørskov. Electrolysis of water on oxide surfaces. *Journal of Electroanalytical Chemistry*, 607(1-2):83–89, 2007. doi:10.1016/j.jelechem.2006.11.008.

[39] J. Durst, A. Siebel, C. Simon, F. Hasché, J. Herranz, and H. A. Gasteiger. New insights into the electrochemical hydrogen oxidation and evolution reaction mechanism. *Energy and Environmental Science*, 7(7):2255–2260, jun 2014. doi:10.1039/c4ee00440j.

[40] V. R. Stamenkovic, D. Strmcnik, P. P. Lopes, and N. M. Markovic. Energy and fuels from electrochemical interfaces. *Nature Materials*, 16(1):57–69, jan 2017. doi:10.1038/nmat4738.

[41] E. Kemppainen, A. Bodin, B. Sebok, T. Pedersen, B. Seger, B. Mei, D. Bae, P. C. Vesborg, J. Halme, O. Hansen, P. D. Lund, and I. Chorkendorff. Scalability and feasibility of photoelectrochemical H2 evolution: the ultimate limit of Pt nanoparticle as an HER catalyst. *Energy and Environmental Science*, 8(10):2991–2999, oct 2015. doi:10.1039/c5ee02188j.

[42] J. N. Tiwari, S. Sultan, C. W. Myung, T. Yoon, N. Li, M. Ha, A. M. Harzandi, H. J. Park, D. Y. Kim, S. S. Chandrasekaran, W. G. Lee, V. Vij, H. Kang, T. J. Shin, H. S. Shin, G. Lee, Z. Lee, and K. S. Kim. Multicomponent electrocatalyst with ultralow Pt loading and high hydrogen evolution activity. *Nature Energy*, 3(9):773–782, sep 2018. doi:10.1038/s41560-018-0209-x.

[43] J. K. Nørskov, J. Rossmeisl, A. Logadottir, L. Lindqvist, J. R. Kitchin, T. Bligaard, and H. Jónsson. Origin of the overpotential for oxygen reduction at a fuel-cell cathode. *Journal of Physical Chemistry B*, 108(46):17886–17892, nov 2004. doi:10.1021/jp047349j.

[44] E. T. Ojong, J. T. H. Kwan, A. Nouri-Khorasani, A. Bonakdarpour, D. P. Wilkinson, and T. Smolinka. Development of an experimentally validated semi-empirical fully-coupled performance model of a PEM electrolysis cell with a 3-D structured porous transport layer. *International Journal of Hydrogen Energy*, 42(41):25831–25847, oct 2017. doi:10.1016/j.ijhydene.2017.08.183.

[45] F. Dionigi and P. Strasser. NiFe-Based (Oxy)hydroxide Catalysts for Oxygen Evolution Reaction in Non-Acidic Electrolytes. *Advanced Energy Materials*, 6(23):1600621, dec 2016. doi:10.1002/aenm.201600621.

[46] J. Kibsgaard and I. Chorkendorff. Considerations for the scaling-up of water splitting catalysts. *Nature Energy*, 4(6):430–433, jun 2019. doi:10.1038/s41560-019-0407-1.

[47] L. Trotochaud, S. L. Young, J. K. Ranney, and S. W. Boettcher. Nickel-Iron oxyhydroxide oxygen-evolution electrocatalysts: The role

of intentional and incidental iron incorporation. *Journal of the American Chemical Society*, 136(18):6744–6753, may 2014. doi:10.1021/ja502379c.

[48] M. S. Burke, L. J. Enman, A. S. Batchellor, S. Zou, and S. W. Boettcher. Oxygen Evolution Reaction Electrocatalysis on Transition Metal Oxides and (Oxy)hydroxides: Activity Trends and Design Principles, oct 2015. ISSN 15205002. URL https://pubs.acs.org/sharingguidelines.

[49] L. J. Enman, M. S. Burke, A. S. Batchellor, and S. W. Boettcher. Effects of Intentionally Incorporated Metal Cations on the Oxygen Evolution Electrocatalytic Activity of Nickel (Oxy)hydroxide in Alkaline Media. *ACS Catalysis*, 6(4):2416–2423, apr 2016. doi:10.1021/acscatal.5b02924.

[50] S. Klaus, Y. Cai, M. W. Louie, L. Trotochaud, and A. T. Bell. Effects of Fe electrolyte impurities on Ni(OH)2/NiOOH structure and oxygen evolution activity. *Journal of Physical Chemistry C*, 119(13): 7243–7254, apr 2015. doi:10.1021/acs.jpcc.5b00105.

[51] N. Li, D. K. Bediako, R. G. Hadt, D. Hayes, T. J. Kempa, F. Von Cube, D. C. Bell, L. X. Chen, and D. G. Nocera. Influence of iron doping on tetravalent nickel content in catalytic oxygen evolving films. *Proceedings of the National Academy of Sciences of the United States of America*, 114(7):1486–1491, feb 2017. doi:10.1073/pnas.1620787114.

[52] M. Görlin, P. Chernev, J. F. De Araújo, T. Reier, S. Dresp, B. Paul, R. Krähnert, H. Dau, and P. Strasser. Oxygen evolution reaction dynamics, faradaic charge efficiency, and the active metal redox states of Ni-Fe oxide water splitting electrocatalysts. *Journal of the American Chemical Society*, 138(17):5603–5614, may 2016. doi:10.1021/jacs.6b00332.

[53] D. Friebel, M. W. Louie, M. Bajdich, K. E. Sanwald, Y. Cai, A. M. Wise, M. J. Cheng, D. Sokaras, T. C. Weng, R. Alonso-Mori, R. C.

Davis, J. R. Bargar, J. K. Nørskov, A. Nilsson, and A. T. Bell. Identification of highly active Fe sites in (Ni,Fe)OOH for electrocatalytic water splitting. *Journal of the American Chemical Society*, 137(3):1305–1313, jan 2015. doi:10.1021/ja511559d.

[54] M. B. Stevens, C. D. Trang, L. J. Enman, J. Deng, and S. W. Boettcher. Reactive Fe-Sites in Ni/Fe (Oxy)hydroxide Are Responsible for Exceptional Oxygen Electrocatalysis Activity. *Journal of the American Chemical Society*, 139(33):11361–11364, aug 2017. doi:10.1021/jacs.7b07117.

[55] B. Hunter, J. Winkler, and H. Gray. Iron Is the Active Site in Nickel/Iron Water Oxidation Electrocatalysts. *Molecules*, 23(4):903, apr 2018. doi:10.3390/molecules23040903.

[56] H. S. Ahn and A. J. Bard. Surface Interrogation Scanning Electrochemical Microscopy of Ni1-xFexOOH ($0 < x < 0.27$) Oxygen Evolving Catalyst: Kinetics of the "fast" Iron Sites. *Journal of the American Chemical Society*, 138(1):313–318, jan 2016. doi:10.1021/jacs.5b10977.

[57] H. Xiao, H. Shin, and W. A. Goddard. Synergy between Fe and Ni in the optimal performance of (Ni,Fe)OOH catalysts for the oxygen evolution reaction. *Proceedings of the National Academy of Sciences of the United States of America*, 115(23):5872–5877, jun 2018. doi:10.1073/pnas.1722034115.

[58] A. S. Batchellor and S. W. Boettcher. Pulse-Electrodeposited Ni-Fe (Oxy)hydroxide Oxygen Evolution Electrocatalysts with High Geometric and Intrinsic Activities at Large Mass Loadings. *ACS Catalysis*, 5(11):6680–6689, nov 2015. doi:10.1021/acscatal.5b01551.

[59] L. Trotochaud, J. K. Ranney, K. N. Williams, and S. W. Boettcher. Solution-cast metal oxide thin film electrocatalysts for oxygen evolution. *Journal of the American Chemical Society*, 134(41): 17253–17261, oct 2012. doi:10.1021/ja307507a.

[60] A. D. Doyle, M. Bajdich, and A. Vojvodic. Theoretical Insights to Bulk Activity Towards Oxygen Evolution in Oxyhydroxides. *Catalysis Letters*, 147(6):1533–1539, jun 2017. doi:10.1007/s10562-017-2010-z.

[61] C. G. Morales-Guio, L. Liardet, and X. Hu. Oxidatively Electrodeposited Thin-Film Transition Metal (Oxy)hydroxides as Oxygen Evolution Catalysts. *Journal of the American Chemical Society*, 138(28):8946–8957, jul 2016. doi:10.1021/jacs.6b05196.

[62] C. Roy, B. Sebok, S. Scott, E. Fiordaliso, J. Sørensen, A. Bodin, D. Trimarco, C. Damsgaard, P. Vesborg, O. Hansen, I. Stephens, J. Kibsgaard, and I. Chorkendorff. Impact of nanoparticle size and lattice oxygen on water oxidation on NiFeO<inf>x</inf>H<inf>y</inf>. *Nature Catalysis*, 1(11): 820–829, 2018. doi:10.1038/s41929-018-0162-x.

[63] M. Wohlfahrt-Mehrens and J. Heitbaum. Oxygen evolution on Ru and RuO2 electrodes studied using isotope labelling and on-line mass spectrometry. *Journal of Electroanalytical Chemistry*, 237(2):251–260, nov 1987. doi:10.1016/0022-0728(87)85237-3.

[64] O. Diaz-Morales, F. Calle-Vallejo, C. de Munck, and M. T. M. Koper. Electrochemical water splitting by gold: evidence for an oxide decomposition mechanism. *Chemical Science*, 4(6):2334, 2013. doi:10.1039/c3sc50301a.

[65] S. Fierro, T. Nagel, H. Baltruschat, and C. Comninellis. Investigation of the oxygen evolution reaction on Ti/IrO2 electrodes using isotope labelling and on-line mass spectrometry. *Electrochemistry Communications*, 9(8):1969–1974, aug 2007. doi:10.1016/j.elecom.2007.05.008.

[66] K. Macounova, M. Makarova, and P. Krtil. Oxygen evolution on nanocrystalline RuO2 and Ru0.9Ni0.1O2-δ electrodes - DEMS approach to reaction mechanism determination. *Electrochemistry Communications*, 11(10):1865–1868, oct 2009. doi:10.1016/j.elecom.2009.08.004.

[67] J. Willsau, O. Wolter, and J. Heitbaum. Does the oxide layer take part in the oxygen evolution reaction on platinum?: A DEMS study. *Journal of Electroanalytical Chemistry*, 195(2):299–306, nov 1985. doi:10.1016/0022-0728(85)80050-4.

[68] K. A. Stoerzinger, O. Diaz-Morales, M. Kolb, R. R. Rao, R. Frydendal, L. Qiao, X. R. Wang, N. B. Halck, J. Rossmeisl, H. A. Hansen, T. Vegge, I. E. Stephens, M. T. Koper, and Y. Shao-Horn. Orientation-Dependent Oxygen Evolution on RuO2 without Lattice Exchange. *ACS Energy Letters*, 2(4):876–881, apr 2017. doi:10.1021/acsenergylett.7b00135.

[69] S. B. Scott. *Isotope-Labeling Studies in Electrocatalysis for Renewable Energy Conversion*. PhD thesis, Technical University of Denmark, 2019.

[70] A. Grimaud, O. Diaz-Morales, B. Han, W. T. Hong, Y. L. Lee, L. Giordano, K. A. Stoerzinger, M. T. Koper, and Y. Shao-Horn. Activating lattice oxygen redox reactions in metal oxides to catalyse oxygen evolution. *Nature Chemistry*, 9(5):457–465, 2017. doi:10.1038/nchem.2695.

[71] X. Lu and C. Zhao. Electrodeposition of hierarchically structured three-dimensional nickel-iron electrodes for efficient oxygen evolution at high current densities. *Nature Communications*, 6(1):1–7, mar 2015. doi:10.1038/ncomms7616.

[72] M. Bernt, A. Siebel, and H. A. Gasteiger. Analysis of Voltage Losses in PEM Water Electrolyzers with Low Platinum Group Metal Loadings. *Journal of The Electrochemical Society*, 165(5):F305–F314, mar 2018. doi:10.1149/2.0641805jes.

[73] M. Bernt and H. A. Gasteiger. Influence of Ionomer Content in IrO 2 /TiO 2 Electrodes on PEM Water Electrolyzer Performance . *Journal of The Electrochemical Society*, 163(11):F3179–F3189, aug 2016. doi:10.1149/2.0231611jes.

[74] T. Reier, H. N. Nong, D. Teschner, R. Schlögl, and P. Strasser. Electrocatalytic Oxygen Evolution Reaction in Acidic Environments - Reaction Mechanisms and Catalysts. *Advanced Energy Materials*, 7 (1):1601275, jan 2017. doi:10.1002/aenm.201601275.

[75] M. Carmo, D. L. Fritz, J. Mergel, and D. Stolten. A comprehensive review on PEM water electrolysis. *International Journal of Hydrogen Energy*, 38(12):4901–4934, apr 2013. doi:10.1016/j.ijhydene.2013.01.151.

[76] N. Danilovic, R. Subbaraman, K. C. Chang, S. H. Chang, Y. J. Kang, J. Snyder, A. P. Paulikas, D. Strmcnik, Y. T. Kim, D. Myers, V. R. Stamenkovic, and N. M. Markovic. Activity-stability trends for the oxygen evolution reaction on monometallic oxides in acidic environments. *Journal of Physical Chemistry Letters*, 5(14): 2474–2478, jul 2014. doi:10.1021/jz501061n.

[77] A. Winiwarter, L. Silvioli, S. B. Scott, K. Enemark-Rasmussen, M. Sariç, D. B. Trimarco, P. C. Vesborg, P. G. Moses, I. E. Stephens, B. Seger, J. Rossmeisl, and I. Chorkendorff. Towards an atomistic understanding of electrocatalytic partial hydrocarbon oxidation: Propene on palladium. *Energy and Environmental Science*, 12(3): 1055–1067, mar 2019. doi:10.1039/c8ee03426e.

[78] R. Frydendal, E. A. Paoli, B. P. Knudsen, B. Wickman, P. Malacrida, I. E. Stephens, and I. Chorkendorff. Benchmarking the Stability of Oxygen Evolution Reaction Catalysts: The Importance of Monitoring Mass Losses. *ChemElectroChem*, 1(12):2075–2081, dec 2014. doi:10.1002/celc.201402262.

[79] C. Roy, R. R. Rao, K. A. Stoerzinger, J. Hwang, J. Rossmeisl, I. Chorkendorff, Y. Shao-Horn, and I. E. Stephens. Trends in Activity and Dissolution on RuO2 under Oxygen Evolution Conditions: Particles versus Well-Defined Extended Surfaces. *ACS Energy Letters*, 3(9):2045–2051, sep 2018. doi:10.1021/acsenergylett.8b01178.

[80] Introduction — ixdat 0.0.1 documentation. URL `https://ixdat.readthedocs.io/en/latest/introduction.html`.

[81] A. Bagger, W. Ju, A. S. Varela, P. Strasser, and J. Rossmeisl. Electrochemical CO2 Reduction: A Classification Problem. *ChemPhysChem*, 18(22):3266–3273, nov 2017. doi:10.1002/cphc.201700736.

[82] M. T. Tang, H. Peng, P. Schlexer, M. Bajdich, and F. Abild-pedersen. Applied Catalysis B : Environmental From electricity to fuels : Descriptors for C 1 selectivity in electrochemical CO 2 reduction. *Applied Catalysis B: Environmental*, 279(July):119384, 2020. doi:10.1016/j.apcatb.2020.119384.

[83] J. Campuzano. The Chemical Physics of Solid Surfaces and Heterogeneous Catalysis. In D. King and D. Woodruff, editors, *The Chemical Physics of Solid Surfaces and Heterogeneous Catalysis, Vol. 3, Part A*. Elsevier, Amsterdam, 1990.

[84] F. J. Perez-Alonso, D. N. McCarthy, A. Nierhoff, P. Hernandez-Fernandez, C. Strebel, I. E. L. Stephens, J. H. Nielsen, and I. Chorkendorff. The Effect of Size on the Oxygen Electroreduction Activity of Mass-Selected Platinum Nanoparticles. *Angewandte Chemie*, 51:4641–4643, 2012. doi:10.1002/anie.201200586.

[85] F. Tao, S. Dag, L.-W. Wang, Z. Liu, D. R. Butcher, H. Bluhm, M. Salmeron, and G. a. Somorjai. Break-Up of Stepped Platinum Catalyst Surfaces by High CO Coverage. *Science*, 327(5967):850–853, feb 2010. doi:10.1126/science.1182122.

[86] A. K. Engstfeld, S. Brimaud, and R. J. Behm. Potential-Induced Surface Restructuring-The Need for Structural Characterization in Electrocatalysis Research. *Angewandte Chemie International Edition*, 53(47):12936–12940, nov 2014. doi:10.1002/anie.201404479.

[87] S. Nitopi, E. Bertheussen, S. B. Scott, X. Liu, A. K. Engstfeld, S. Horch, B. Seger, I. E. Stephens, K. Chan, C. Hahn, J. K. Nørskov, T. F. Jaramillo, and I. Chorkendorff. Progress and Perspectives of Electrochemical CO2 Reduction on Copper in Aqueous Electrolyte. *Chemical Reviews*, 119(12):7610–7672, 2019. doi:10.1021/acs.chemrev.8b00705.

[88] C. W. Li and M. W. Kanan. CO 2 reduction at low overpotential on Cu electrodes resulting from the reduction of thick Cu 2O films. *Journal of the American Chemical Society*, 134(17):7231–7234, 2012. doi:10.1021/ja3010978.

[89] C. W. Li, J. Ciston, and M. W. Kanan. Electroreduction of carbon monoxide to liquid fuel on oxide-derived nanocrystalline copper. *Nature*, 508(7497):504–507, 2014. doi:10.1038/nature13249.

[90] X. Feng, K. Jiang, S. Fan, and M. W. Kanan. A direct grain-boundary-activity correlation for CO electroreduction on Cu nanoparticles. *ACS Central Science*, 2(3):169–174, 2016. doi:10.1021/acscentsci.6b00022.

[91] A. Eilert, F. Cavalca, F. S. Roberts, J. Osterwalder, C. Liu, M. Favaro, E. J. Crumlin, H. Ogasawara, D. Friebel, L. G. Pettersson, and A. Nilsson. Subsurface Oxygen in Oxide-Derived Copper Electrocatalysts for Carbon Dioxide Reduction. *Journal of Physical Chemistry Letters*, 8(1):285–290, 2017. doi:10.1021/acs.jpclett.6b02273.

[92] M. Fields, X. Hong, J. K. Nørskov, and K. Chan. Role of Subsurface Oxygen on Cu Surfaces for CO2 Electrochemical Reduction. *Journal of Physical Chemistry C*, 122(28):16209–16215, 2018. doi:10.1021/acs.jpcc.8b04983.

[93] L. Wang, S. A. Nitopi, E. Bertheussen, M. Orazov, C. G. Morales-Guio, X. Liu, D. C. Higgins, K. Chan, J. K. Nørskov, C. Hahn, and T. F. Jaramillo. Electrochemical Carbon Monoxide Reduction on Polycrystalline Copper: Effects of Potential, Pressure, and pH on Selectivity toward Multicarbon and Oxygenated Products. *ACS Catalysis*, 8(8):7445–7454, 2018. doi:10.1021/acscatal.8b01200.

[94] Y. Lum and J. W. Ager. Evidence for product-specific active sites on oxide-derived Cu catalysts for electrochemical CO2 reduction. *Nature Catalysis*, 2(1):86–93, 2019. doi:10.1038/s41929-018-0201-7.

[95] S. S. Fu and G. A. Somorjai. INTERACTIONS OF \ce{O2}, CO, \ce{CO2}, AND \ce{D2} WITH THE STEPPED CU(311) CRYSTAL-FACE - COMPARISON TO CU(110). *Surface Science*, 262(1-2):68–76, 1992. doi:10.1016/0039-6028(92)90460-N.

[96] I. Bönicke, W. Kirstein, S. Spinzig, and F. Thieme. CO adsorption studies on a stepped Cu(111) surface. *Surface Science*, 313(3): 231–238, 1994. doi:10.1016/0039-6028(94)90044-2.

[97] S. Vollmer, G. Witte, and C. Wöll. Determination of site specific adsorption energies of CO on copper. *Catalysis Letters*, 77(1-3): 97–101, 2001. doi:10.1023/A:1012755616064.

[98] T. Makino and M. Okada. CO adsorption on regularly stepped Cu(410) surface. *Surface Science*, 628:36–40, 2014. doi:10.1016/j.susc.2014.05.013.

[99] A. Verdaguer-Casadevall, C. W. Li, T. P. Johansson, S. B. Scott, J. T. McKeown, M. Kumar, I. E. L. Stephens, M. W. Kanan, and I. Chorkendorff. Probing the Active Surface Sites for CO Reduction on Oxide-Derived Copper Electrocatalysts. *Journal of the American Chemical Society*, 137:9808–9811, 2015. doi:10.1021/jacs.5b06227.

[100] Multiprobe Surface Science Systems Users Guide, 2006.

[101] J. L. Needham. *Surface characterization and temperature programmed desorption of small mass-selected entities*. Master thesis, DTU, 2020.

[102] OMEGA Engineering. Thermocouple Response Time, 2019. URL `https://www.omega.com/en-us/resources/thermocouples-response-time`.

[103] OMEGA Engineering. Thermocouples - A Reference Guide, 2019. URL `https://www.omega.com/en-us/resources/thermocouples-sheath-material-and-temperature-limits`.

[104] M. L. Ng, F. Abild-Pedersen, S. Kaya, F. Mbuga, H. Ogasawara, and A. Nilsson. Low Barrier Carbon Induced CO Dissociation on Stepped

Cu. *Physical Review Letters*, 114(24):1–5, 2015. doi:10.1103/PhysRevLett.114.246101.

[105] R. J. Behm, K. Christmann, G. Ertl, and M. A. Van Hove. Adsorption of CO on Pd(100). *The Journal of Chemical Physics*, 73 (6):2984–2995, 1980. doi:10.1063/1.440430.

[106] X. Bai, W. Chen, C. Zhao, S. Li, Y. Song, R. Ge, W. Wei, and Y. Sun. Exclusive Formation of Formic Acid from CO 2 Electroreduction by a Tunable Pd-Sn Alloy. *Angewandte Chemie*, 129 (40):12387–12391, 2017. doi:10.1002/ange.201707098.

[107] T. Wei, D. Kumar, M. S. Chen, K. Luo, S. Axnanda, M. Lundwall, and D. W. Goodman. Vinyl acetate synthesis over model Pd-Sn bimetallic catalysts. *Journal of Physical Chemistry C*, 112(22): 8332–8337, 2008. doi:10.1021/jp8005266.

[108] J. Szanyi, W. K. Kuhn, and D. W. Goodman. CO adsorption on Pd(111) and Pd(100): Low and high pressure correlations. *Journal of Vacuum Science & Technology A: Vacuum, Surfaces, and Films*, 11 (4):1969–1974, jul 1993. doi:10.1116/1.578532.

[109] V. Matolin, M. Rebholz, and N. Kruse. Defect-induced dissociation of CO on palladium. *Surface Science*, 245(3):233–243, 1991. doi:10.1016/0039-6028(91)90026-O.

[110] E. Jeroro, V. Lebarbier, A. Datye, Y. Wang, and J. M. Vohs. Interaction of CO with surface PdZn alloys. *Surface Science*, 601(23): 5546–5554, 2007. doi:10.1016/j.susc.2007.09.031.